

Numerical Simulation of Transitional, Hypersonic Flows using a Hybrid Particle-Continuum Method

by

Ashley Marie Verhoff

A dissertation submitted in partial fulfillment
of the requirements for the degree of
Doctor of Philosophy
(Aerospace Engineering)
in The University of Michigan
2015

Doctoral Committee:

Professor Iain D. Boyd, Chairperson

Research Professor Michael R. Combi

Professor Kenneth G. Powell

Associate Professor Thomas E. Schwartzenruber, University of Minnesota

*“I know the plans I have for you,” declares the Lord,
“plans to prosper you and not to harm you,
plans to give you hope and a future.”*

Jeremiah 29:11

*“For my part I know nothing with any certainty,
but the sight of the stars makes me dream.”*

Vincent van Gogh

© Ashley Marie Verhoff 2015

All Rights Reserved

For my mother,
and in loving memory of my father.

ACKNOWLEDGEMENTS

This dissertation represents much more than my own personal efforts over the last several years. Without the love, encouragement, and support of so many others, I may not have even had the opportunity to attend graduate school, let alone complete my doctoral degree. I realize now that if I were to thank everyone who has helped me reach this point in my academic career, the length of this section would surely surpass the actual dissertation.

I would first like to thank my advisor, Professor Iain Boyd, for accepting me into his research group, and mentoring me through the triumphs and detours of the past five years. No matter my state of confusion or frustration before going into his office for a meeting, I always knew that I would feel better when I walked out. I'm grateful to have had an advisor with such patience and understanding in both research and personal matters. I would also like to thank Professor Michael Combi, Professor Ken Powell, and Professor Tom Schwartzentruer for making the time in their busy schedules to serve on my doctoral committee, and for their feedback and advice. I am especially grateful for Tom's willingness and ability to discuss even my most detailed questions and concerns regarding the MPC method. In addition, I thank Professor Krzysztof Fidkowski for always making himself available to discuss my CFD-related questions. Finally, this section would not be complete without recognizing the dedicated efforts of Denise Phelps, Dave McLean, Cindy Enoch, Chris Chartier, and Tom Griffin. I will miss their friendly faces and conversation.

During my first summer as a graduate student, I was very fortunate to have had

the opportunity to work with Eswar Josyula at the Air Force Research Laboratory. It was an extremely rewarding experience; I always look forward to seeing Eswar at conferences, and am appreciative of his continued mentorship. In addition, I attribute almost all of my Linux and command line knowledge to Dr. C. J. Suchyta, also from AFRL, who was very patient while I climbed that steep learning curve. I'm also very grateful for the helpful experts at NASA's Advanced Supercomputing Division and the University of Michigan's Center for Advanced Computing (CAC); I have yet to encounter a computer or programming problem that they haven't been able to solve. I would also like to acknowledge the NASA Constellation University Initiatives Project, the National Defense Science and Engineering Graduate Fellowship Program, and the National Science Foundation Graduate Research Fellowship Program for funding my research efforts. I am very honored to have had these agencies invest in my ideas and potential.

I have claimed many times that there are two people who could be "co-authors" of my dissertation, and they deserve special recognition for being such amazing colleagues, mentors, and friends. I am indebted to Marco Ceze, who has answered countless programming questions over the years, and is not only willing to listen to my problems, but also eager to offer advice. Erin Farbar has been a constant source of support and encouragement during my time at Michigan. Our coffee/tea/chocolate breaks at Pierpont Commons have always led to new perspectives on my research, career plans, and other concerns. I'm convinced that I would have left without my Ph.D. had it not been for Marco and Erin.

Between the friends that I've made in graduate school and those who have been by my side even longer, I am truly blessed. Zachary Kier and I have been through so much together, from pulling all-nighters during our senior design project at the University of Cincinnati, to navigating graduate school. Now that I'm moving on without a familiar face beside me, I'm realizing even more how much I value our friendship. There are

also a few other “bearcats” who remain some of my closest friends: Rachel Edgerly, Ryan Noble, Melissa LaBarbera, and Molly Finn Petre. You are all proof that true friendship knows no distance. In addition, graduate school would not have been nearly as enjoyable were it not for the past and present members of the Nonequilibrium Gas and Plasma Dynamics Laboratory (too many to count!), the “TacocaT” trivia team (Brandon Smith, Jon and Michelle Wiebenga, Luke Hansen, and Lauren Mackey), my former officemates (Paul Giuliano and Tim Eymann), my current officemates (Horatiu Dragnea, Kyle Hanquist, and Steve Kast), my fellow tailgaters (Eric and Lisa Muir), and my Small Church Community (especially Steve and Sarah DeWitt, and Cyril Galitzine). I am especially grateful to Cyril for taking the time to review my dissertation and provide comments; this was no easy nor short task! And who could forget firing-up the meat smoker, making cornhole boards, and painting the Michi-Van (Matt Holzel, Bojana Drincic, and Tony D’Amato)?

Lastly, I can’t begin to describe how much gratitude I have for my parents and my brother, Alan. They have always believed in me, even when I didn’t believe in myself. I learned the personal pride that work can bring from my father, who worked long hours on the General Motors factory floor for more than 35 years, and my mother, who worked extra hours on weekends to make her office run more smoothly during the week. They were my first teachers, and I owe every success to them.

TABLE OF CONTENTS

DEDICATION	ii
ACKNOWLEDGEMENTS	iii
LIST OF FIGURES	ix
LIST OF TABLES	xix
ABSTRACT	xxi
CHAPTER	
I. Introduction	1
1.1 Multiscale Nature of Transitional, Hypersonic Flows	2
1.2 Motivation	7
1.3 Scope of Dissertation	11
II. Mathematical Modeling and Numerical Simulation of Transitional, Hypersonic Flows	15
2.1 The Boltzmann Equation	15
2.1.1 Equilibrium Solution	19
2.2 Euler Equations	20
2.3 Navier-Stokes Equations	22
2.4 Alternative Solution Methods	28
2.5 Direct Simulation Monte Carlo Method	29
2.6 Hybrid Approaches	32
III. A Modular Particle-Continuum Method	37
3.1 Simulation Modules	39
3.1.1 CFD	40
3.1.2 DSMC	41

3.2	Continuum Breakdown	44
3.3	Mesh Refinement	49
3.4	Coupling Procedures	52
3.5	Hybrid Method Organization and Algorithm	62
3.6	Interim Conclusions	66
IV.	Consistent Modeling of Physical Processes	67
4.1	Transport Properties	68
4.1.1	Simple Gases	68
4.1.2	Gas Mixtures	71
4.2	Thermal Nonequilibrium	83
4.2.1	Translational-Rotational Energy Exchange	84
4.2.2	Translational-Vibrational Energy Exchange	98
4.3	Interim Conclusions	104
V.	A Comprehensive Assessment of the MPC Method	108
5.1	A Detailed Accuracy Evaluation	109
5.2	Improved Consistency of Boundary Conditions	118
5.2.1	Supersonic Outflow	118
5.2.2	Hybrid Interfaces	123
5.3	Baseline Accuracy and Computational Performance	127
5.4	Investigation of Remaining Errors	141
5.5	Interim Conclusions	146
VI.	Accurate Prediction of Rotational Nonequilibrium Effects	148
6.1	A New Rotational Nonequilibrium Detection Parameter	150
6.2	Initial Placement of Hybrid Interfaces	152
6.2.1	Simple Gas Study	152
6.2.2	Gas Mixture Study	160
6.2.3	Conclusions from Simple Gas and Gas Mixture Studies	166
6.3	MPC Results	168
6.3.1	Flow Field Properties	171
6.3.2	Surface Properties	181
6.3.3	Computational Performance	182
6.4	Interim Conclusions	186
VII.	Hybrid Simulations of Mixtures of Chemical Species	188
7.1	Multispecies Considerations	189
7.2	Verification of the MPC Method: 50% N_2 /50% N	191
7.2.1	Flow Field Properties	192

7.2.2	Surface Properties	198
7.2.3	Computational Performance	204
7.3	Verification of the MPC Method: 80% N_2 /20% O_2	205
7.3.1	Flow Field Properties	207
7.3.2	Surface Properties	214
7.3.3	Computational Performance	216
7.4	A Challenge for the MPC Method: 50% N_2 /50% H	216
7.5	Interim Conclusions	221
VIII. Conclusion		223
8.1	Summary of Dissertation	223
8.2	Unique Contributions	229
8.3	Future Work	232
8.3.1	VSS Collision Model	232
8.3.2	Generalized Chapman-Enskog Distribution	232
8.3.3	Continuum Breakdown	233
8.3.4	Mesh Refinement Algorithm	234
8.3.5	Chemical Reactions	235
8.3.6	Three-Dimensional Geometries	235
APPENDIX		237
BIBLIOGRAPHY		239

LIST OF FIGURES

Figure

1.1	Shadowgraph image of a manned re-entry capsule concept (Great Images in NASA, GPN-2000-001938).	8
1.2	Contours of Kn_{GLL} for the Mach 12, Kn_∞ 0.01 flow of N_2 over a two-dimensional cylinder.	9
1.3	Cumulative cost of simulating the Mach 12, Kn_∞ 0.01 flow of N_2 over a two-dimensional cylinder using DSMC.	10
3.1	Illustration of hybrid interface, before refinement.	49
3.2	Gradient-based refinement of continuum cell [64].	51
3.3	Illustration of hybrid interface, after refinement.	52
3.4	Particle-continuum coupling approaches.	58
3.5	Modular organization of CFD, DSMC, and MPC hybrid functions and data structures [64].	63
4.1	Viscosity collision integral dependence on translational temperature for N_2	70
4.2	Variation of viscosity with N_2/N mixture composition.	74
4.3	Velocity profile from a typical DSMC simulation of Couette flow. . .	76
4.4	Comparisons of viscosities obtained using the Gupta Mixing Rule (CFD) and the VHS collision model (DSMC).	77
4.5	Variation of viscosity with N_2/H mixture composition.	78

4.6	Rotational temperature relaxation of N_2 as predicted by CFD and DSMC, with $\phi_{rot}(E_{coll})$	90
4.7	Rotational collision number profiles of N_2 as predicted by CFD and DSMC, with $\phi_{rot}(E_{coll})$	91
4.8	Rotational temperature relaxation of 50% N_2 /50% N as predicted by CFD and DSMC, using $\phi_{rot}(E_{coll})$	93
4.9	Rotational collision number profiles of 50% N_2 /50% N as predicted by CFD and DSMC, using $\phi_{rot}(E_{coll})$	94
4.10	Rotational temperature relaxation of N_2 as predicted by CFD and DSMC, using $\phi_{rot}(E_{rel})$	95
4.11	Rotational collision number profiles of N_2 as predicted by CFD and DSMC, using $\phi_{rot}(E_{rel})$	95
4.12	Rotational temperature relaxation of 50% N_2 /50% N as predicted by CFD and DSMC, using $\phi_{rot}(E_{rel})$	96
4.13	Rotational collision number profiles of 50% N_2 /50% N as predicted by CFD and DSMC, using $\phi_{rot}(E_{rel})$	96
4.14	Rotational temperature relaxation of 80% N_2 /20% O_2 as predicted by CFD and DSMC, using $\phi_{rot}(E_{rel})$ and the particle selection methodology.	99
4.15	Rotational collision number profiles of 80% N_2 /20% O_2 as predicted by CFD and DSMC, using $\phi_{rot}(E_{rel})$ and the particle selection methodology.	99
4.16	Vibrational temperature relaxation of N_2 as predicted by CFD and DSMC.	104
4.17	Vibrational temperature relaxation of 50% N_2 /50% N as predicted by CFD and DSMC.	105
4.18	Vibrational temperature relaxation of 80% N_2 /20% O_2 as predicted by CFD and DSMC.	105
5.1	Illustration of continuum cell and constituent particle cells.	110

5.2	Contours of translational temperature errors of previous MPC results relative to full DSMC for the Mach 12, Kn_∞ 0.01 flow of N_2 over a two-dimensional cylinder; hybrid interfaces are shown as black lines.	113
5.3	Contours of rotational temperature errors of previous MPC results relative to full DSMC for the Mach 12, Kn_∞ 0.01 flow of N_2 over a two-dimensional cylinder; hybrid interfaces are shown as black lines.	113
5.4	Contours of velocity magnitude errors of previous MPC results relative to full DSMC for the Mach 12, Kn_∞ 0.01 flow of N_2 over a two-dimensional cylinder; hybrid interfaces are shown as black lines.	114
5.5	Contours of mass density errors of previous MPC results relative to full DSMC for the Mach 12, Kn_∞ 0.01 flow of N_2 over a two-dimensional cylinder; hybrid interfaces are shown as black lines. . .	114
5.6	Comparisons of probability distribution functions predicted by full DSMC and equilibrium theory in cell <i>A</i> of Fig. 5.2.	116
5.7	Comparisons of probability distribution functions predicted by full DSMC and equilibrium theory in cell <i>B</i> of Fig. 5.2.	117
5.8	Translational temperature along the stagnation streamline of the Mach 12, Kn_∞ 0.01 flow of N_2 over a two-dimensional cylinder. . .	119
5.9	Translational temperature along the $y = 0.13m$ extraction line of the Mach 12, Kn_∞ 0.01 flow of N_2 over a two-dimensional cylinder. . .	120
5.10	Illustration of a Maxwellian VDF at the outflow boundary, where u_n is the directed velocity aligned with an inward-pointing normal. . .	121
5.11	Contours of Mach number for the Mach 12, Kn_∞ 0.01 flow of N_2 over a two-dimensional cylinder.	121
5.12	Mesh and streamtraces near hybrid interfaces.	125
5.13	Contours of translational temperature errors of the current MPC results relative to full DSMC for the Mach 12, Kn_∞ 0.01 flow of N_2 over a two-dimensional cylinder; hybrid interfaces are shown as black lines.	128
5.14	Contours of rotational temperature errors of the current MPC results relative to full DSMC for the Mach 12, Kn_∞ 0.01 flow of N_2 over a two-dimensional cylinder; hybrid interfaces are shown as black lines.	128

5.15	Contours of velocity magnitude errors of the current MPC results relative to full DSMC for the Mach 12, Kn_∞ 0.01 flow of N_2 over a two-dimensional cylinder; hybrid interfaces are shown as black lines.	129
5.16	Contours of mass density errors of the current MPC results relative to full DSMC for the Mach 12, Kn_∞ 0.01 flow of N_2 over a two-dimensional cylinder; hybrid interfaces are shown as black lines. . .	129
5.17	Contours of translational temperature errors between two full DSMC simulations of the Mach 12, Kn_∞ 0.01 flow of N_2 over a two-dimensional cylinder.	131
5.18	Contours of rotational temperature errors between two full DSMC simulations of the Mach 12, Kn_∞ 0.01 flow of N_2 over a two-dimensional cylinder.	131
5.19	Contours of velocity magnitude errors between two full DSMC simulations of the Mach 12, Kn_∞ 0.01 flow of N_2 over a two-dimensional cylinder.	132
5.20	Contours of mass density errors between two full DSMC simulations of the Mach 12, Kn_∞ 0.01 flow of N_2 over a two-dimensional cylinder.	132
5.21	Surface pressure coefficient along the cylinder surface for the Mach 12, Kn_∞ 0.01 flow of N_2 over a two-dimensional cylinder.	134
5.22	Heat transfer coefficient along the cylinder surface for the Mach 12, Kn_∞ 0.01 flow of N_2 over a two-dimensional cylinder.	135
5.23	Shear stress coefficient along the cylinder surface for the Mach 12, Kn_∞ 0.01 flow of N_2 over a two-dimensional cylinder.	135
5.24	Relative errors of surface pressure coefficient along the cylinder surface for the Mach 12, Kn_∞ 0.01 flow of N_2 over a two-dimensional cylinder.	137
5.25	Relative errors of heat transfer coefficient along the cylinder surface for the Mach 12, Kn_∞ 0.01 flow of N_2 over a two-dimensional cylinder.	137
5.26	Relative errors of shear stress coefficient along the cylinder surface for the Mach 12, Kn_∞ 0.01 flow of N_2 over a two-dimensional cylinder.	138
5.27	Time history of translational temperature along the $y = 0.13m$ extraction line of the Mach 12, Kn_∞ 0.01 flow of N_2 over a two-dimensional cylinder.	143

5.28	Translational temperature along the $y = 0.13m$ extraction line, before and after the particle domains have been updated from an initial, full DSMC solution of the Mach 12, Kn_∞ 0.01 flow of N_2 over a two-dimensional cylinder.	145
6.1	Computational domain and data extraction lines.	153
6.2	Errors between full CFD and full DSMC results along the stagnation streamline for the Mach 12, Kn_∞ 0.01 flow of N_2 over a two-dimensional cylinder.	154
6.3	Continuum breakdown parameters based on a full CFD solution along the stagnation streamline for the Mach 12, Kn_∞ 0.01 flow of N_2 over a two-dimensional cylinder.	154
6.4	Errors between full CFD and full DSMC results along the 45° extraction line for the Mach 12, Kn_∞ 0.01 flow of N_2 over a two-dimensional cylinder.	158
6.5	Continuum breakdown parameters based on a full CFD solution along the 45° extraction line for the Mach 12, Kn_∞ 0.01 flow of N_2 over a two-dimensional cylinder.	158
6.6	Errors between full CFD and full DSMC results along the 90° extraction line for the Mach 12, Kn_∞ 0.01 flow of N_2 over a two-dimensional cylinder.	161
6.7	Continuum breakdown parameters based on a full CFD solution along the 90° extraction line for the Mach 12, Kn_∞ 0.01 flow of N_2 over a two-dimensional cylinder.	161
6.8	Errors between full CFD and full DSMC results along the stagnation streamline for the Mach 10, Kn_∞ 0.01 flow of 50% N_2 /50% N over a two-dimensional cylinder.	163
6.9	Continuum breakdown parameters based on a full CFD solution along the stagnation streamline for the Mach 10, Kn_∞ 0.01 flow of 50% N_2 /50% N over a two-dimensional cylinder.	163
6.10	Errors between full CFD and full DSMC results along the 45° extraction line for the Mach 10, Kn_∞ 0.01 flow of 50% N_2 /50% N over a two-dimensional cylinder.	165

6.11	Continuum breakdown parameters based on a full CFD solution along the 45° extraction line for the Mach 10, Kn_∞ 0.01 flow of 50% N_2 /50% N over a two-dimensional cylinder.	165
6.12	Errors between full CFD and full DSMC results along the 90° extraction line for the Mach 10, Kn_∞ 0.01 flow of 50% N_2 /50% N over a two-dimensional cylinder.	167
6.13	Continuum breakdown parameters based on a full CFD solution along the 90° extraction line for the Mach 10, Kn_∞ 0.01 flow of 50% N_2 /50% N over a two-dimensional cylinder.	167
6.14	Initial (upper pane) and final (lower pane) hybrid interfaces, where Kn_{rot} interfaces are shown blue, and $Kn_{ROT-NEQ}$ interfaces are shown in red.	170
6.15	Contours of translational temperature, with DSMC results shown as flooded contours, MPC results where Kn_{rot} is used as lines in the upper pane, and MPC results where $Kn_{ROT-NEQ}$ is used as lines in the lower pane.	172
6.16	Contours of rotational temperature, with DSMC results shown as flooded contours, MPC results where Kn_{rot} is used as lines in the upper pane, and MPC results where $Kn_{ROT-NEQ}$ is used as lines in the lower pane.	173
6.17	Translational and rotational temperatures along the stagnation streamline, with MPC results obtained using the original $Kn_{ROT-NEQ}$ parameter.	175
6.18	Translational and rotational temperatures along the stagnation streamline, with MPC results obtained using the new Kn_{rot} parameter. . .	175
6.19	Translational and rotational temperatures along the stagnation streamline, with MPC results obtained using the original $Kn_{ROT-NEQ}$ parameter, near the post-shock hybrid interface.	176
6.20	Translational and rotational temperatures along the stagnation streamline, with MPC results obtained using the new Kn_{rot} parameter, near the post-shock hybrid interface.	176
6.21	Translational and rotational temperatures along the stagnation streamline, with MPC results obtained using the original $Kn_{ROT-NEQ}$ parameter, near the pre-boundary layer hybrid interface.	177

6.22	Translational and rotational temperatures along the stagnation streamline, with MPC results obtained using the new Kn_{rot} parameter, near the pre-boundary layer hybrid interface.	177
6.23	Contours of translational temperature errors of the MPC method relative to full DSMC when Kn_{rot} is used, with hybrid interfaces shown as black lines.	178
6.24	Contours of rotational temperature errors of the MPC method relative to full DSMC when Kn_{rot} is used, with hybrid interfaces shown as black lines.	179
6.25	Contours of velocity magnitude errors of the MPC method relative to full DSMC when Kn_{rot} is used, with hybrid interfaces shown as black lines.	179
6.26	Contours of mass density errors of the MPC method relative to full DSMC when Kn_{rot} is used, with hybrid interfaces shown as black lines.	180
6.27	Surface pressure coefficient along the cylinder surface for the Mach 12, Kn_{∞} 0.01 flow of N_2 over a two-dimensional cylinder.	182
6.28	Heat transfer coefficient along the cylinder surface for the Mach 12, Kn_{∞} 0.01 flow of N_2 over a two-dimensional cylinder.	183
6.29	Shear stress coefficient along the cylinder surface for the Mach 12, Kn_{∞} 0.01 flow of N_2 over a two-dimensional cylinder.	183
6.30	Surface pressure coefficient errors of the MPC method relative to full DSMC when Kn_{rot} is used.	184
6.31	Heat transfer coefficient errors of the MPC method relative to full DSMC when Kn_{rot} is used.	184
6.32	Shear stress coefficient errors of the MPC method relative to full DSMC when Kn_{rot} is used.	185
7.1	Illustration of two different VDFs, where the molecular weight of particles represented by the red line is less than that of the particles represented by the blue line.	191
7.2	Initial and final hybrid interfaces for the Mach 10, Kn_{∞} 0.01 flow of 50% N_2 /50% N over a two-dimensional cylinder.	192

7.3	Contours of velocity magnitude for the Mach 10, Kn_∞ 0.01 flow of 50% N_2 /50% N over a two-dimensional cylinder.	194
7.4	Contours of translational temperature for the Mach 10, Kn_∞ 0.01 flow of 50% N_2 /50% N over a two-dimensional cylinder.	195
7.5	Contours of rotational temperature for the Mach 10, Kn_∞ 0.01 flow of 50% N_2 /50% N over a two-dimensional cylinder.	196
7.6	Contours of translational temperature errors of the MPC method relative to full DSMC for the Mach 10, Kn_∞ 0.01 flow of 50% N_2 /50% N over a two-dimensional cylinder; hybrid interfaces are shown as black lines.	199
7.7	Contours of rotational temperature errors of the MPC method relative to full DSMC for the Mach 10, Kn_∞ 0.01 flow of 50% N_2 /50% N over a two-dimensional cylinder; hybrid interfaces are shown as black lines.	199
7.8	Contours of velocity magnitude errors of the MPC method relative to full DSMC for the Mach 10, Kn_∞ 0.01 flow of 50% N_2 /50% N over a two-dimensional cylinder; hybrid interfaces are shown as black lines.	200
7.9	Contours of N_2 mass density errors of the MPC method relative to full DSMC for the Mach 10, Kn_∞ 0.01 flow of 50% N_2 /50% N over a two-dimensional cylinder; hybrid interfaces are shown as black lines.	200
7.10	Contours of N mass density errors of the MPC method relative to full DSMC for the Mach 10, Kn_∞ 0.01 flow of 50% N_2 /50% N over a two-dimensional cylinder; hybrid interfaces are shown as black lines.	201
7.11	N_2 mole fraction along the stagnation streamline for the Mach 10, Kn_∞ 0.01 flow of 50% N_2 /50% N over a two-dimensional cylinder. .	202
7.12	Surface pressure coefficient along the cylinder surface for the Mach 10, Kn_∞ 0.01 flow of 50% N_2 /50% N	202
7.13	Heat transfer coefficient along the cylinder surface for the Mach 10, Kn_∞ 0.01 flow of 50% N_2 /50% N	203
7.14	Shear stress coefficient along the cylinder surface for the Mach 10, Kn_∞ 0.01 flow of 50% N_2 /50% N	203

7.15	Initial and final hybrid interfaces for the Mach 10, Kn_∞ 0.01 flow of 80% N_2 /20% O_2 over a two-dimensional cylinder.	206
7.16	Contours of velocity magnitude for the Mach 10, Kn_∞ 0.01 flow of 80% N_2 /20% O_2 over a two-dimensional cylinder.	208
7.17	Contours of translational temperature for the Mach 10, Kn_∞ 0.01 flow of 80% N_2 /20% O_2 over a two-dimensional cylinder.	209
7.18	Contours of rotational temperature for the Mach 10, Kn_∞ 0.01 flow of 80% N_2 /20% O_2 over a two-dimensional cylinder.	210
7.19	Contours of translational temperature errors of the MPC method relative to full DSMC for the Mach 10, Kn_∞ 0.01 flow of 80% N_2 /20% O_2 over a two-dimensional cylinder; hybrid interfaces are shown as black lines.	211
7.20	Contours of rotational temperature errors of the MPC method relative to full DSMC for the Mach 10, Kn_∞ 0.01 flow of 80% N_2 /20% O_2 over a two-dimensional cylinder; hybrid interfaces are shown as black lines.	211
7.21	Contours of velocity magnitude errors of the MPC method relative to full DSMC for the Mach 10, Kn_∞ 0.01 flow of 80% N_2 /20% O_2 over a two-dimensional cylinder; hybrid interfaces are shown as black lines.	212
7.22	Contours of N_2 mass density errors of the MPC method relative to full DSMC for the Mach 10, Kn_∞ 0.01 flow of 80% N_2 /20% O_2 over a two-dimensional cylinder; hybrid interfaces are shown as black lines.	212
7.23	Contours of O_2 mass density errors of the MPC method relative to full DSMC for the Mach 10, Kn_∞ 0.01 flow of 80% N_2 /20% O_2 over a two-dimensional cylinder; hybrid interfaces are shown as black lines.	213
7.24	Surface pressure coefficient along the cylinder surface for the Mach 10, Kn_∞ 0.01 flow of 80% N_2 /20% O_2	214
7.25	Heat transfer coefficient along the cylinder surface for the Mach 10, Kn_∞ 0.01 flow of 80% N_2 /20% O_2	215
7.26	Shear stress coefficient along the cylinder surface for the Mach 10, Kn_∞ 0.01 flow of 80% N_2 /20% O_2	215

7.27	Translational temperature along the stagnation streamline for the Mach 10, Kn_∞ 0.002 flow of 50% N_2 /50% H	218
7.28	Rotational temperature along the stagnation streamline for the Mach 10, Kn_∞ 0.002 flow of 50% N_2 /50% H	219
7.29	Surface pressure coefficient along the cylinder surface for the Mach 10, Kn_∞ 0.002 flow of 50% N_2 /50% H	219
7.30	Heat transfer coefficient along the cylinder surface for the Mach 10, Kn_∞ 0.002 flow of 50% N_2 /50% H	220
7.31	Shear stress coefficient along the cylinder surface for the Mach 10, Kn_∞ 0.002 flow of 50% N_2 /20% H	220

LIST OF TABLES

Table

4.1	Comparisons of d_{ref} [Å] obtained using the simple approach and the Nelder-Mead simplex algorithm.	81
4.2	Comparisons of ω obtained using the simple approach and the Nelder-Mead simplex algorithm.	82
5.1	Ranges of previous MPC and CFD errors relative to full DSMC for the Mach 12, Kn_∞ 0.01 flow of N_2 over a two-dimensional cylinder.	115
5.2	Relative errors of previous MPC and CFD results measured in the L_2 norm for the Mach 12, Kn_∞ 0.01 flow of N_2 over a two-dimensional cylinder.	115
5.3	Ranges of current MPC and independent DSMC errors relative to full DSMC for the Mach 12, Kn_∞ 0.01 flow of N_2 over a two-dimensional cylinder.	127
5.4	Relative errors of current MPC and independent DSMC results measured in the L_2 norm for the Mach 12, Kn_∞ 0.01 flow of N_2 over a two-dimensional cylinder.	130
5.5	Computational performance statistics for the Mach 12, Kn_∞ 0.01 flow of N_2 over a two-dimensional cylinder.	140
6.1	Ranges of new MPC errors relative to full DSMC for the Mach 12, Kn_∞ 0.01 flow of N_2 over a two-dimensional cylinder.	180
6.2	Relative errors of new MPC results measured in the L_2 norm for the Mach 12, Kn_∞ 0.01 flow of N_2 over a two-dimensional cylinder.	180
6.3	Computational performance statistics for the Mach 12, Kn_∞ 0.01 flow of N_2 over a two-dimensional cylinder.	186

7.1	Ranges of errors relative to full DSMC for the Mach 10, Kn_∞ 0.01 flow of 50% N_2 /50% N over a two-dimensional cylinder.	197
7.2	Relative errors measured in the L_2 norm for the Mach 10, Kn_∞ 0.01 flow of 50% N_2 /50% N over a two-dimensional cylinder.	197
7.3	Computational performance statistics for the Mach 10, Kn_∞ 0.01 flow of 50% N_2 /50% N over a two-dimensional cylinder.	204
7.4	Ranges of errors relative to full DSMC for the Mach 10, Kn_∞ 0.01 flow of 80% N_2 /20% O_2 over a two-dimensional cylinder.	213
7.5	Relative errors measured in the L_2 norm for the Mach 10, Kn_∞ 0.01 flow of 80% N_2 /20% O_2 over a two-dimensional cylinder.	213
7.6	Computational performance statistics for the Mach 10, Kn_∞ 0.01 flow of 80% N_2 /20% O_2 over a two-dimensional cylinder.	216
A.1	Variable Hard Sphere (VHS) collision model reference diameters, d_{ref} [Å].	238
A.2	Variable Hard Sphere (VHS) collision model temperature exponents, ω	238
A.3	Molecular species constants.	238

ABSTRACT

Numerical Simulation of Transitional, Hypersonic Flows
using a Hybrid Particle-Continuum Method

by

Ashley Marie Verhoff

Chairperson: Iain D. Boyd

Analysis of hypersonic flows requires consideration of multiscale phenomena due to the range of flight regimes encountered, from rarefied conditions in the upper atmosphere to fully continuum flow at low altitudes. At transitional Knudsen numbers there are likely to be localized regions of strong thermodynamic nonequilibrium effects that invalidate the continuum assumptions of the Navier-Stokes equations. Accurate simulation of these regions, which include shock waves, boundary and shear layers, and low-density wakes, requires a kinetic theory-based approach where no *a priori* assumptions are made regarding the molecular distribution function. Because of the nature of these types of flows, there is much to be gained in terms of both numerical efficiency and physical accuracy by developing hybrid particle-continuum simulation approaches.

The focus of the present research effort is the continued development of the Modular Particle-Continuum (MPC) method, where the Navier-Stokes equations are solved numerically using computational fluid dynamics (CFD) techniques in regions of the flow field where continuum assumptions are valid, and the direct simulation Monte

Carlo (DSMC) method is used where strong thermodynamic nonequilibrium effects are present. Numerical solutions of transitional, hypersonic flows are thus obtained with increased physical accuracy relative to CFD alone, and improved numerical efficiency is achieved in comparison to DSMC alone because this more computationally expensive method is restricted to those regions of the flow field where it is necessary to maintain physical accuracy.

In this dissertation, a comprehensive assessment of the physical accuracy of the MPC method is performed, leading to the implementation of a non-vacuum supersonic outflow boundary condition in particle domains, and more consistent initialization of DSMC simulator particles along hybrid interfaces. The relative errors between MPC and full DSMC results are greatly reduced as a direct result of these improvements. Next, a new parameter for detecting rotational nonequilibrium effects is proposed and shown to offer advantages over other continuum breakdown parameters, achieving further accuracy gains. Lastly, the capabilities of the MPC method are extended to accommodate multiple chemical species in rotational nonequilibrium, each of which is allowed to equilibrate independently, enabling application of the MPC method to more realistic atmospheric flows.

CHAPTER I

Introduction

National interest in space exploration has resurged in recent years, due in large part to the successful use of several commercially-developed launch vehicles and unmanned capsules to resupply the International Space Station. NASA's current efforts to replace the retired Space Shuttle with a Space Launch System heavy-lift rocket and Orion crew capsule are being paralleled by other independent ventures funded mostly by private companies. Many of these companies have also chosen the launch vehicle and re-entry capsule architecture inspired by Apollo heritage over the winged, lifting-body configuration of the Space Shuttle. Despite this, the importance of technological advancements made in support of the Space Shuttle program, specifically in terms of aerothermodynamic modeling of the re-entry environment, cannot be overstated.

The objective of designing a reusable thermal protection system (TPS) for a more complex geometry than its predecessors demanded a high-fidelity definition of the integrated heat loads incurred by the Space Shuttle throughout its entire re-entry trajectory, a larger portion of which was spent under rarefied conditions in the upper atmosphere. Wind tunnel data, although collected at much lower enthalpies than would be experienced in flight, provided the foundation for the design methodology, while small-scale numerical simulations were used to guide the scaling of this wind tunnel data and provide some insight into the effects of finite-rate chemistry on the

flow field [61]. In contrast, following the loss of the *Columbia* vehicle during re-entry, full-scale, three-dimensional numerical simulations including real gas effects were the standard, and could be performed during the course of a single mission in order to determine whether or not the TPS had withstood catastrophic damage during launch [55]. Increased availability of computational resources and a deeper understanding of hypersonic aerothermodynamics through comparisons between flight data and design predictions have enabled a revolution in re-entry vehicle design, which is now heavily reliant on numerical simulations as an alternative to experimental measurements.

With the commercialization of spaceflight, there is widespread need to accurately simulate complex flow fields that span a range of flight regimes, from rarefied conditions at the beginning of a re-entry trajectory to fully continuum flow near the end. Even as modeling and simulation become more involved, the desire for timely solutions continues, so that there is also a need to increase the efficiency of these numerical algorithms by decreasing the computational resources required to obtain a given solution. This becomes even more important for private companies, which usually do not have access to the supercomputers that are commonplace at government and academic institutions. Therefore, it is the objective of this dissertation to detail the recent developments of a computational approach to enable physically accurate and numerically efficient simulations of transitional, hypersonic flows encountered by re-entry vehicles.

1.1 Multiscale Nature of Transitional, Hypersonic Flows

The major source of complexity associated with accurately simulating the flow field surrounding a re-entry vehicle is the multiscale nature of the physical phenomena that must be considered. At sea level conditions, there are approximately 2.5×10^{19} individual molecules of N_2 , O_2 , and other trace species in every cubic centimeter of

air. Each molecule moves, on average, 50 nanometers before colliding with another molecule, and this happens approximately once every 0.1 nanoseconds [8]. These length and time scales are much smaller than those that can be distinguished by human perception, so that air at these conditions appears to be *continuous*. In other words, the discrete nature of these air molecules can be ignored and is indeed replaced by macroscopic fluid properties such as temperature, pressure, and density that are assumed to change continuously throughout space. Conversely, in the upper atmosphere where a re-entry vehicle begins its descent trajectory, there are very few gas molecules. At an altitude of $100km$, there are approximately 6.1×10^{12} molecules per cubic centimeter [2]. The concept of a continuous fluid is no longer valid, as the role of each individual gas molecule in a given volume becomes very important to any average of molecular properties. Therefore, a re-entry vehicle experiences a decrease in density of over six orders of magnitude throughout the course of its trajectory, and the critical question of whether a *microscopic* or *macroscopic* view of the surrounding gas is more appropriate must be answered.

Analysis of multiscale problems begins with examining the relative sizes of length and time scales that are of interest. When considering any sort of fluid, one of the relevant length scales will always be the mean distance a molecule of that fluid travels between collisions. This is because molecular collisions and subsequent scattering and energy transfer are the means by which all change is propagated throughout a fluid. The atmosphere can be considered a *dilute* gas, meaning that the vast majority of collisions are binary and the average distance a molecule travels between collisions, i.e. the mean free path, is much larger than the diameters of the molecules themselves [8]. Therefore, molecules of a dilute gas spend much of their time traveling unimpeded, outside of the influence of other molecules' potential fields. The most common way of identifying the relative importance of the mean free path is the global Knudsen number, given by

$$Kn_\infty = \frac{\lambda_\infty}{L}. \quad (1.1)$$

In Eq. 1.1, λ_∞ is the freestream mean free path and L is a characteristic length scale of a vehicle or phenomenon of interest. This global parameter takes on a large value when the mean free path is relatively large, such as when considering the flow field surrounding a re-entry vehicle in the upper atmosphere. The global Knudsen number can also be large even if the mean free path is small; such is the case in microelectromechanical systems (MEMS) and processes. In both cases, the flow is termed *rarefied* because relative to the characteristic dimension, L , the gas appears to have a low density. This relative size of length scales can be seen as indicating how disruptive a hypersonic vehicle is to the unobstructed movement of and collisions between gas molecules. As $Kn_\infty \rightarrow 0$, collisions among gas molecules occur so frequently that the flow field instantaneously adjusts to any perturbation. From the perspective of the vehicle or flow feature of length scale L , the surrounding fluid is in constant equilibrium. On the contrary, a large global Knudsen number implies a greater likelihood of a given flow field being in translational nonequilibrium.

More specifically, the Knudsen number indicates how far the velocity distribution function (VDF) of molecules in a gas deviates from a normal, or Gaussian, distribution function. If the molecules of a gas are distributed according to a Gaussian, that gas is said to be in a state of *translational* equilibrium. Small deviations can be accounted for by assuming the physical validity of certain linear constitutive relations between transport processes and gradients of macroscopic fluid properties. If the VDF deviates too far from a Gaussian distribution, however, these continuum assumptions fail and the microscopic nature of the fluid must be considered. More about the details of translational and other subsets of equilibrium will be presented in Chapter II.

It is important to note that even if the global Knudsen number is small, the *local* Knudsen number may still be quite large in specific regions of the flow field.

A common example of this is the flow through a strong shock wave formed by a vehicle moving at hypersonic speed. The global, pre-shock conditions may result in a reasonably low global Knudsen number. However, the length scales associated with the extremely large gradients in the shock wave may be much smaller than the local mean free path. Such mixed rarefied/continuum flow fields are very likely to occur at transitional Knudsen numbers between 0.001 and 1.

The Knudsen number can be manipulated to yield another characterization parameter, the Damköhler number. Rather than a ratio of length scales, the Damköhler number is a ratio of the time scale associated with the convection of a fluid, and the time scale associated with a given physical or chemical process occurring in that fluid. This physical process may simply be collisions among gas molecules, so that starting with the Knudsen number, the Damköhler number is given by

$$Da_c = \frac{1}{Kn} \frac{\bar{c}}{V} = \frac{L}{\lambda} \frac{\bar{c}}{V} = \frac{\tau_f}{\tau_c}, \quad (1.2)$$

where

$$\bar{c} = \sqrt{\frac{8k_B T_{trans}}{\pi m}} \quad (1.3)$$

is the average thermal speed of the gas molecules. In Eq. 1.2, V can be either a local or a global flow speed, τ_c is the mean collision time, i.e. the mean time elapsed between consecutive molecular collisions, and τ_f is a characteristic fluid convection time. In Eq. 1.3, k_B is the Boltzmann constant, T_{trans} is the translational temperature, and m is the mass of each individual gas molecule. The Damköhler number written in this way is indicative of translational nonequilibrium. However, unlike the Knudsen number, small Damköhler numbers generally imply a greater likelihood of translational nonequilibrium.

Use of the Damköhler number is more commonplace when considering finite-rate processes that drive thermal and chemical equilibrium. Again considering the strong

shock wave formed by a hypersonic vehicle, the kinetic energy once possessed by the gas prior to passing through the shock is converted almost directly into random thermal energy, leading to a high post-shock translational temperature. This energy must then be redistributed among all internal energy modes, and can also promote dissociation of polyatomic molecules and ionization. The physical mechanism for all of these processes is collisions among molecules. In general, the relative magnitudes corresponding to common thermal relaxation and chemical processes are as follows:

$$\tau_c \approx \tau_{trans} < \tau_{rot} \ll \tau_{vib} < \tau_d < \tau_i,$$

where τ_{rot} is the characteristic relaxation time of the rotational energy mode, τ_{vib} is the characteristic relaxation time of the vibrational energy mode, τ_d is the characteristic time for a dissociative reaction to occur, and τ_i is the characteristic time for an ionization reaction to occur. The Damköhler number is, thus, generalized to be

$$Da = \frac{\tau_f}{\tau}. \quad (1.4)$$

The time scale, τ , in Eq. 1.4 now represents the characteristic time of relaxation of an internal energy mode, or the characteristic time of a chemical reaction. As $Da \rightarrow \infty$, equilibration of internal energy modes and chemical reactions occur instantaneously so that the fluid is always in a state of thermochemical equilibrium. However, as $Da \rightarrow 0$, the flow is commonly deemed “frozen” in its original state because the time required for any sort of physical or chemical process to occur is exceedingly long relative to the time available.

The computational approach that is the focus of this dissertation is applicable to steady flows only. Therefore, the local Knudsen number provides a better indication of whether a microscopic or macroscopic view of the gas is the most appropriate. Regardless of the local Knudsen number, finite-rate thermal relaxation processes are considered everywhere. This is because of the inherently small residence times of

the atmospheric gas relative to a typical hypersonic, re-entry vehicle. However, any chemical reactions that would naturally occur in the cases studied here are ignored.

1.2 Motivation

During initial development of blunt-body, re-entry capsules in support of the Mercury, Gemini, and Apollo missions, shadowgraph images were taken in order to visualize the flow fields surrounding various manned capsule concepts. Shadowgraphs are particularly useful in acquiring a qualitative understanding of where large density gradients occur in a flow field. In this technique, light is passed through a flowing fluid and, because light is refracted most through regions of large density gradients, they appear dark in the resulting images. Figure 1.1 shows one such shadowgraph in which several hallmark features of transitional, hypersonic flows are visible. The strong bow shock wave produced by the blunt-body vehicle is labeled **1**. Contrary to engineering intuition at the time, in 1951 H. Julian Allen proposed the revolutionary idea that aerodynamic heating experienced during re-entry could be minimized through the use of a blunt, rather than a slender, vehicle [3]. Instead of the weak, attached shock wave produced by slender vehicles, a blunt-body vehicle produces a strong, detached shock wave that deposits more energy into the surrounding air than the vehicle surface. As mentioned previously, because of the extremely large gradients in the shock wave produced by a blunt-body, hypersonic vehicle, and the fact that these gradients occur over a few mean free paths of the gas, it is expected that a continuum approach to simulating the shock region would yield inaccurate results.

Another region of very large gradients is the boundary layer along the forebody of the vehicle, labeled **2** in Fig. 1.1. Most re-entry vehicle shapes are characterized by a large-radius sphere in the forebody that transitions to a cone in the aftbody. The point where the forebody and aftbody meet is referred to as the *shoulder*. As the gas flows around the capsule shoulder, it must abruptly expand into the void created by the

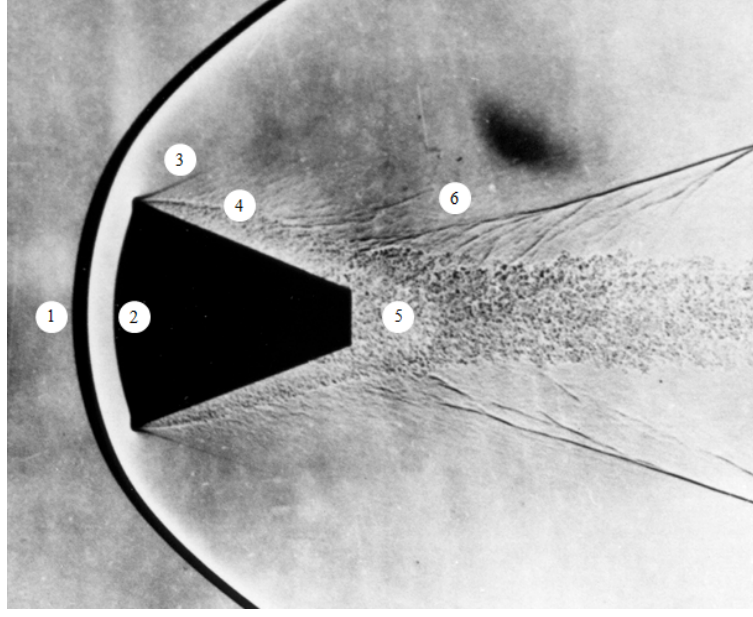


Figure 1.1: Shadowgraph image of a manned re-entry capsule concept (Great Images in NASA, GPN-2000-001938).

vehicle, leading to expansion waves and shear layers, labeled as **3** and **4**, respectively. Because of this expansion, the wake of the re-entry vehicle has a much lower density and may include a recirculation region as marked by **5** in Fig. 1.1. Flow gradients in the wake, although not as large as in the shock or boundary layer, are still likely to be on the order of the local mean free path in that region. Finally, further downstream, a recompression shock may form so that the wake flow can reaccommodate to that in the far wake; this is labeled as **6**. In all of these highlighted regions, there exists the potential for the continuum fluid assumptions to be physically inaccurate.

The computational approach that is the focus of this dissertation was developed in order to accurately and efficiently simulate transitional, hypersonic flows that are of the same mixed rarefied/continuum nature visualized in Fig. 1.1. For example, one test case that is studied extensively as part of the current development effort is that of a Mach 12 flow of N_2 over a two-dimensional cylinder at a global Knudsen number of 0.01. Even though simulation of hypersonic flow over a two-dimensional cylinder is a simplification relative to that over an actual blunt-body, re-entry vehicle, this

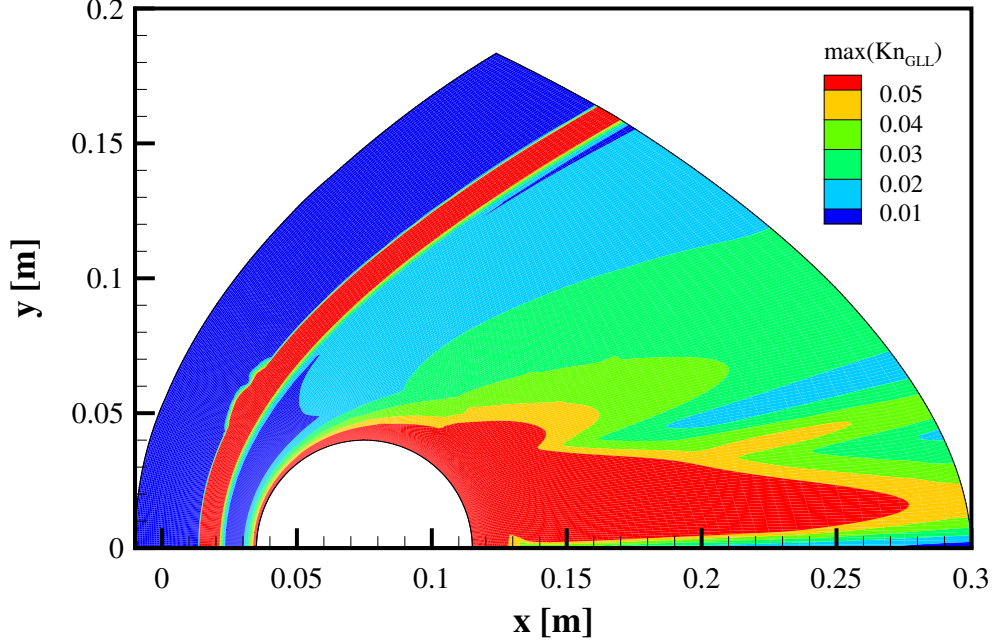


Figure 1.2: Contours of Kn_{GLL} for the Mach 12, Kn_∞ 0.01 flow of N_2 over a two-dimensional cylinder.

geometry still produces many of the same physical phenomena and facilitates a more generalized analysis. Figure 1.2 illustrates contours of the local Knudsen number based on gradient length scales throughout this flow field. More details about this gradient-length local Knudsen number will be given in Chapter III, where a value of 0.05 is proposed as the threshold between nonequilibrium and near-equilibrium regions of a flow field [14]. The same flow features that were so evident in Fig. 1.1 are also shown as having large local Knudsen numbers in Fig. 1.2, indicating that these regions are in a state of translational nonequilibrium. Therefore, according to this metric, the bow shock wave, boundary layer, and wake should be simulated using a microscopic approach, since a macroscopic analysis in which the gas is assumed to be continuous will likely be physically inaccurate.

Theoretically, a microscopic approach could be employed to simulate the entire computational domain shown in Fig. 1.2. However, microscopic approaches, as will be explained in the next chapter, are usually much more computationally intensive than a

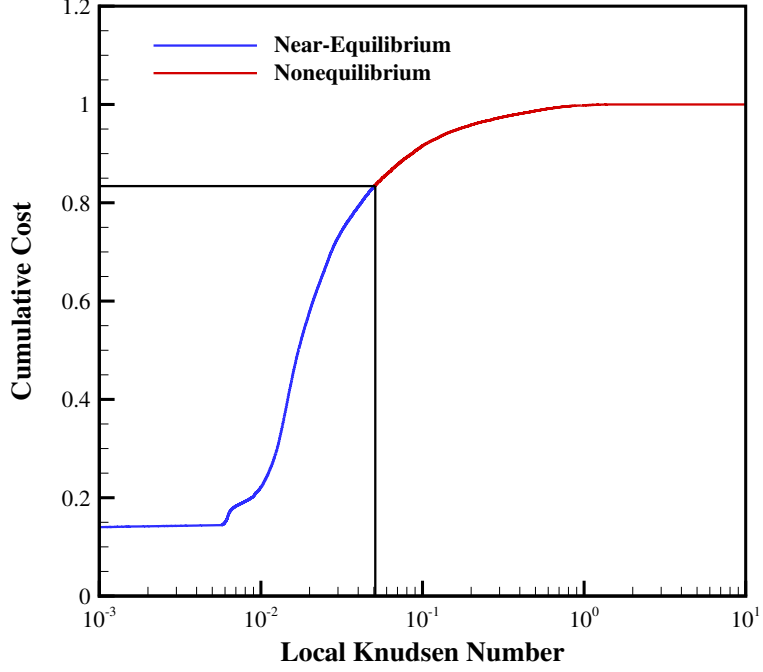


Figure 1.3: Cumulative cost of simulating the Mach 12, Kn_∞ 0.01 flow of N_2 over a two-dimensional cylinder using DSMC.

macroscopic approach. The most popular of these microscopic approaches is the direct simulation Monte Carlo (DSMC) method pioneered by G. A. Bird [8]. In the DSMC method, a large number of “simulator” particles move deterministically and collide stochastically with one another in order to mimic the movement and interactions among real gas molecules. A typical DSMC simulation involves millions of simulator particles, and the location, velocity, and internal energies of each must be tracked. In the case of the DSMC code used in this dissertation, the computational cost scales linearly with the number of simulator particles employed in a simulation. If the flow field shown in Fig. 1.2 were simulated using the DSMC method, approximately 30 million simulator particles would be needed. However, over 80% of these simulator particles are located in near-equilibrium regions of the flow field, where the local Knudsen number is less than 0.05. This is illustrated in Fig. 1.3, where the cumulative cost of this DSMC simulation is plotted against the local Knudsen number in each computational cell.

In contrast, numerical solution of the Navier-Stokes equations using computational fluid dynamics (CFD) is computationally efficient, but physically accurate in near-equilibrium regions of the flow field only. Rather than accounting for millions of simulator particles as is done in the DSMC method, a system of conservation equations is solved for macroscopic properties of mass, momentum, and energy in each computational cell of the domain of interest. Thus, because of the mixed rarefied/continuum nature of transitional, hypersonic flows, such as that illustrated by this example, there is much to be gained by developing a *hybrid* approach, where the DSMC method is used to obtain a physically accurate solution in nonequilibrium regions of the flow field, and CFD is used in near-equilibrium regions, where it is both physically accurate and numerically efficient. The development of hybrid particle-continuum methods, in which the computational domain is divided into distinct regions identified by a continuum breakdown parameter such as a local Knudsen number, and information is exchanged as the simulation evolves, is of current research interest because they provide a desirable alternative, in terms of both numerical efficiency and physical accuracy, to either DSMC or CFD alone.

1.3 Scope of Dissertation

The accurate and efficient simulation of transitional, hypersonic flows is a problem rich in physics and engineering challenges. The mixed rarefied/continuum nature of these types of flow fields requires consideration of a wide range of length and time scales. While computationally efficient, a macroscopic approach through numerical solution of the continuum conservation equations does not provide microscopic details that may be required to accurately resolve certain flow features. A molecular description of the entire flow field, however, is usually not necessary and, in many cases, proves computationally intractable. Because of this, the goal of the present research effort is the continued development and verification of a hybrid particle-continuum

method for simulating transitional, hypersonic flows.

In Chapter II, the governing equations of fluid flow are presented as a progression from first principles to the current state of research in the area of hybrid simulation techniques. The Boltzmann equation, which describes the evolution of the molecular distribution function in time and space is introduced, along with its analytical solution for equilibrium flow. In particular, emphasis is placed on the simulation of mixtures of chemical species with internal degrees of freedom. By taking moments of the Boltzmann equation, the Euler equations of inviscid flow are derived, followed by the Navier-Stokes equations that describe the behavior of near-continuum flow. Whereas many CFD methods exist for numerical solution of the Navier-Stokes equations, there is no general, analytical solution of the Boltzmann equation. Therefore, the DSMC method [8] is presented as the most mature option for simulating flow fields at any Knudsen number. Alternatives to the Navier-Stokes equations and DSMC are also discussed, and this chapter concludes with a review of various hybrid simulation approaches that have been proposed in the literature.

A comprehensive description of the Modular Particle-Continuum (MPC) method, which is the focus of this work, is presented in Chapter III. The MPC method is a hybrid framework that loosely couples state-of-the-art DSMC and CFD codes that serve as independent particle and continuum simulation modules. This modularity enables efficient extension of the existing capabilities of these component codes to the hybrid method. The functional organization of these simulation modules and the hybrid framework is illustrated in this chapter. In order to identify the computational domains where DSMC is required for physical accuracy and where CFD can be used for improved computational efficiency, several measures of continuum breakdown are employed in the MPC method. These are discussed, as well as the automatic mesh refinement algorithm used in the particle domains of the flow field. The coupling procedures required to exchange updated solution information across hybrid interfaces

are also presented, including mathematical formulae for averaging simulator particle information to yield macroscopic fluid properties, and algorithms for sampling particle information from distribution functions defined by macroscopic fluid properties. The numerical cycle of a typical hybrid simulation is also presented.

The physical models that are employed in the continuum and particle domains of an MPC hybrid simulation are discussed and verified to be consistent in Chapter IV. These physical models include the collision model that is used in full DSMC simulations and in the particle domains of hybrid simulations, and the explicit calculations of diffusion, viscosity, and heat conduction needed in full CFD simulations and in the continuum domains of hybrid simulations. In addition, models for simulating translational-rotational and translational-vibrational energy exchange processes are also presented. It is imperative that CFD and DSMC give the same solution along the domain interfaces in a hybrid simulation, which should be placed in near-equilibrium regions of the flow field. Therefore, the emphasis of this chapter is verification of the consistency of these physical models in near-equilibrium flows of both simple gases and mixtures of chemical species.

A comprehensive assessment of the physical accuracy and computational efficiency of the MPC method is presented in Chapter V. The case of a transitional, hypersonic flow over a two-dimensional cylinder is used to evaluate the MPC method relative to a full DSMC simulation in terms of cell-by-cell comparisons of flow field properties, in addition to surface properties and computational performance statistics. A number of improvements are made regarding the consistent definition of the supersonic outflow boundary condition in CFD and DSMC simulations, and the consistent exchange of information across hybrid interfaces. These changes are shown to improve the accuracy of the MPC method relative to full DSMC. However, notable discrepancies remain, and their possible causes are investigated further. For the first time, the physical accuracy of the MPC method is evaluated in the context of the statis-

tical errors between two independent, full DSMC simulations, which provides more reasonable expectations for the accuracy of the MPC method moving forward.

In Chapter VI, a new continuum breakdown parameter for predicting rotational nonequilibrium effects is proposed and evaluated alongside other continuum breakdown parameters that are currently employed by the MPC method. Detailed comparisons between full CFD and full DSMC results for hypersonic, blunt-body flows of both a simple gas and a mixture of chemical species are undertaken. The newly proposed rotational nonequilibrium parameter is shown to offer advantages where existing continuum breakdown parameters fail. This new parameter is then incorporated in the MPC hybrid method, and the resulting physical accuracy is compared to that of previous MPC simulation results in the context of a simple gas.

Extension of the MPC hybrid method to include mixtures of chemical species is described in Chapter VII. This not only enables the MPC method to simulate more realistic atmospheric flows, but is also a necessary first step towards eventually simulating chemical reactions using a hybrid method. The required modifications to the MPC method are evaluated for the hypersonic flow of a mixture of molecular and atomic nitrogen over a two-dimensional cylinder at a transitional Knudsen number. A similar case is also explored in which a mixture of molecular nitrogen and molecular oxygen is simulated. In this latter case, both constituent species experience rotational nonequilibrium effects, and are allowed to equilibrate at different rates. Finally, the case of a mixture comprised of species with widely disparate molecular weights is examined, which highlights the challenges that remain for the automatic hybrid cycle described in Chapter III.

Chapter VIII provides a summary of the conclusions drawn from the work presented in this dissertation, and the specific contributions made to the ongoing development of the MPC method and hybrid particle-continuum methods in general. Recommendations for the focus of future research efforts are also presented.

CHAPTER II

Mathematical Modeling and Numerical Simulation of Transitional, Hypersonic Flows

In this chapter, the governing equations of fluid flow and their underlying assumptions are discussed, along with various approaches to either analytically or numerically solve these equations. As introduced in Chapter I, the local Knudsen number plays a critical role in the physical validity of the assumptions made in deriving the Euler and Navier-Stokes equations of continuum flow from the Boltzmann equation, which is the kinetic underpinning of any mathematical model describing a dilute gas. In addition to discussing these individual mathematical models and numerical simulation techniques, a review of recent work in the development of hybrid approaches to simulate mixed rarefied/continuum flow fields is presented.

2.1 The Boltzmann Equation

The Boltzmann equation was first derived from kinetic theory by physical reasoning [8]. Whereas it is generally infeasible to deterministically track every molecule and its properties in a flow field of interest, the probability distribution functions (PDFs) of molecular properties, such as velocity and internal energies, serve as quantities that evolve in a manner that can be modeled mathematically. If a simple, monatomic gas

is first considered, the Boltzmann equation is given by

$$\frac{\partial}{\partial t} [nf] + c_j \frac{\partial}{\partial x_j} [nf] + \frac{\partial}{\partial c_j} [F_j nf] = \left\{ \frac{\partial}{\partial t} [nf] \right\}_{coll}, \quad (2.1)$$

which describes the rate of change of the single-particle PDF, $f(\mathbf{c}, \mathbf{x}, t)$, in a six-dimensional *phase* space that includes three physical and three velocity dimensions. The first term in Eq. 2.1 describes the time rate of change of the number of molecules of class \mathbf{c} , i.e. with velocities that deviate very slightly from \mathbf{c} , where n is the number density. This quantity is nonzero as the result of three possible actions. If molecules are convected into or out of an infinitesimal volume in physical space, the number of molecules of class \mathbf{c} in that volume changes, as modeled by the second term in Eq. 2.1. Likewise, if molecules are “convected” into or out of an infinitesimal volume in velocity space due to an acceleration, \mathbf{F} , the number of molecules of class \mathbf{c} also changes; this is modeled by the third term in Eq. 2.1, and is ignored in the present work. The fourth term describes the time rate of change of the number of molecules of class \mathbf{c} due to collisions with other molecules, and is modeled by

$$\left\{ \frac{\partial}{\partial t} [nf] \right\}_{coll} = \int_{-\infty}^{+\infty} \int_0^{4\pi} n^2 [f(\mathbf{c}', \mathbf{x}, t) f(\boldsymbol{\zeta}', \mathbf{x}, t) - f(\mathbf{c}, \mathbf{x}, t) f(\boldsymbol{\zeta}, \mathbf{x}, t)] g \sigma d\Omega d\boldsymbol{\zeta}, \quad (2.2)$$

where $f(\boldsymbol{\zeta})$ is the PDF associated with a collision partner of class $\boldsymbol{\zeta}$, and the post-collision PDFs are given by $f(\mathbf{c}')$ and $f(\boldsymbol{\zeta}')$. In Eq. 2.2, g is the relative velocity of colliding molecules, and $\sigma d\Omega$ is the differential collision cross-section, which is, in general, a function of the molecular potential of the collision partners and their relative velocity [8]. This collision term incorporates the effects of collisions with molecules of all other classes, and includes all possible differential cross-sections by integrating over the entire unit sphere.

As suggested by the collision term of the Boltzmann equation, collisions have been limited to binary interactions. This is a reasonable assumption for dilute gases, as

defined in Chapter I. In addition, derivation of the collision term requires the principle of *molecular chaos*, in which the PDFs of two molecules are assumed to be statistically independent of one another. This allows the probability of two molecules colliding to be mathematically represented by the product of their individual PDFs [8].

The integro-differential nature of the Boltzmann equation presents a challenge to general solution. This is neglecting the fact that, in the case of a gas mixture, a separate Boltzmann equation must be defined for each constituent species. In addition, description of a polyatomic species requires additional dimensions to account for the internal energy states of the molecules both before and after collision. For example, from Chang and Uhlenbeck [16], the Boltzmann equation describing the rate of change of a single-particle PDF in rotational state α , $f(\mathbf{c}, \mathbf{x}, t, \varepsilon_{rot,\alpha})$, is given by

$$\frac{\partial}{\partial t} [n_\alpha f_\alpha] + c_j \frac{\partial}{\partial x_j} [n_\alpha f_\alpha] = \sum_{\beta=0}^{\infty} \sum_{\alpha'=0}^{\infty} \sum_{\beta'=0}^{\infty} \int_{-\infty}^{+\infty} \int_0^{4\pi} (n_{\alpha'} f_{\alpha'} n_{\beta'} f_{\beta'} - n_\alpha f_\alpha n_\beta f_\beta) g_{\alpha,\beta} \sigma_{\alpha,\beta}^{\alpha',\beta'} d\Omega d\zeta. \quad (2.3)$$

Upon comparing Eqs. 2.1 and 2.3, it is evident that the complexity of the Boltzmann equation increases drastically when polyatomic species are considered, as the righthand side is now a triple summation over all possible rotational energy states, β , of the collision partner, and all possible post-collision rotational energy states. In addition to the differential collision cross-section being dependent on the relative velocity of the colliding molecules and their molecular potentials, it is now also dependent on their pre- and post-collision rotational energy states. This differential cross-section is the means by which energy is transferred between the rotational and translational energy modes. It is possible for the relative translational energy to remain unchanged by a collision while still allowing rotational energy to be exchanged between molecules. However, because of the quantum spacing between rotational energy levels, and since this spacing increases with quantum number [40], the likeli-

hood of two molecules experiencing a rotationally inelastic collision *and* being able to exchange equal amounts of quantized energy is very low. Therefore, in the current work, rotational energy is only allowed to be exchanged with the relative translational energy of the collision.

Even so, for other purposes, the rotational energy distribution function (EDF) can be assumed continuous except at cryogenic temperatures. The characteristic temperature of the rotational energy mode, θ_{rot} , is typically quite small, and the energy level spacing is of the order of $\theta_{rot}k_B$, where k_B is the Boltzmann constant. For example, in the case of molecular nitrogen, $\theta_{rot} = 2.88K$. Therefore, temperatures of interest in this work are at least an order of magnitude larger than θ_{rot} , so that assuming the rotational EDF to be continuous is valid. In addition, for large temperatures relative to θ_{rot} , the rotational energy mode is fully activated, which for diatomic molecules means that rotation contributes two degrees of freedom to the total energy content of the gas. As a result of assuming the rotational energy mode to be continuous, Eq. 2.3 can be re-written as

$$\begin{aligned} \frac{\partial}{\partial t} [n_\alpha f_\alpha] + c_j \frac{\partial}{\partial x_j} [n_\alpha f_\alpha] = \\ \int_0^{+\infty} \int_0^{+\infty} \int_0^{+\infty} \int_{-\infty}^{+\infty} \int_0^{4\pi} (n_{\alpha'} f_{\alpha'} n_{\beta'} f_{\beta'} - n_\alpha f_\alpha n_\beta f_\beta) g_{\alpha,\beta} \sigma_{\alpha,\beta}^{\alpha',\beta'} d\Omega d\zeta d\beta d\alpha' d\beta', \end{aligned} \quad (2.4)$$

where the summations have been approximated by integrals. In the case of the vibrational energy mode, for air molecules, the characteristic temperature, θ_{vib} , is typically three orders of magnitude larger than θ_{rot} . For molecular nitrogen, $\theta_{vib} = 3395K$. As such, even at relatively high temperatures, the vibrational mode is only partially activated, and the quantized nature of the vibrational EDF must be simulated. If the vibrational and rotational energy modes are assumed to be independent of one another, the same approach used to derive Eq. 2.3 can be used to derive the form of the Boltzmann equation for which the possibility of both rotational and vibrational

energies are accounted. As with rotational energy, upon collision, vibrational energy is only allowed to be exchanged with the relative translational energy of the colliding pair of molecules. Because of the larger quantum energy spacing, which is constant in accordance with the simple harmonic oscillator model, the physical reasoning behind this assumption is even more justified. In reality, the energy spacing between vibrational energy levels decreases with increasing quantum number until the dissociation energy is reached. However, chemical reactions are ignored in the present work, and the vibrational temperatures are such that the upper vibrational energy levels are not substantially populated, if at all.

2.1.1 Equilibrium Solution

Analytical solution of the Boltzmann equation is only feasible for the simplest of flow fields, namely, for a gas in equilibrium. In this case, the entire lefthand side of the Boltzmann equation is zero because the solution is steady, and there are no external forces or spatial gradients. The necessary and sufficient condition for the integral on the righthand side of Eq. 2.2 to be zero is for the single-particle PDF to have the following form:

$$f^{[0]}(c_x, c_y, c_z) = \left(\frac{m}{2\pi k_B T} \right)^{3/2} \exp \left\{ \frac{-m}{2k_B T} [(c_x - u)^2 + (c_y - v)^2 + (c_z - w)^2] \right\}. \quad (2.5)$$

This result is known as the Maxwellian distribution function. In Eq. 2.5, $\mathbf{c} = [c_x, c_y, c_z]$ is the molecular velocity vector, while $\mathbf{u} = [u, v, w]$ is the directed velocity vector of the gas as a whole. Following the same derivation presented by Vincenti and Kruger [82] for Eq. 2.5, a more general form can be found for polyatomic species, which may possess rotational and vibrational energies. This is given by

$$f^{[0]}(c_x, c_y, c_z, \varepsilon_{rot,\alpha}, \varepsilon_{vib,\beta}) = \left(\frac{m}{2\pi k_B T}\right)^{3/2} \frac{g_{rot,\alpha}}{Q_{rot} Q_{vib}} \times \exp \left\{ \frac{-m}{2k_B T} [(c_x - u)^2 + (c_y - v)^2 + (c_z - w)^2] - \frac{1}{k_B T} [\varepsilon_{rot,\alpha} + \varepsilon_{vib,\beta}] \right\}. \quad (2.6)$$

In Eq. 2.6, $\varepsilon_{rot,\alpha}$ is the rotational energy of a molecule in quantized level α , $\varepsilon_{vib,\beta}$ is the vibrational energy of a molecule in quantized level β , and Q_{rot} and Q_{vib} are the partition functions for the rotational and vibrational modes, respectively. The degeneracy of the rotational level α is given by $g_{rot,\alpha}$; the vibrational levels are not degenerate. Close inspection reveals that this expression is the product of the Maxwellian *velocity* distribution function (VDF) and an equilibrium, or Boltzmann, *energy* distribution function (EDF) for each internal energy mode, given by

$$f^{[0]}(\varepsilon_\alpha) = \frac{g_\alpha}{Q} \exp \left\{ -\frac{\varepsilon_\alpha}{k_B T} \right\}. \quad (2.7)$$

It should be noted that only one temperature is referenced here because the solution is that of thermal equilibrium. Again, a separate Maxwellian distribution function is needed to describe each constituent species in a gas mixture.

2.2 Euler Equations

The more familiar conservation equations of continuum flow can be derived by taking moments of the Boltzmann equation. Consider a molecular property, Q , that is either constant or a function of the molecular velocity, \mathbf{c} , only. Multiplying Eq. 2.1 by Q and then integrating over all of velocity space yields the following *equation of change*:

$$\frac{\partial}{\partial t} (n\overline{Q}) + \nabla \cdot (n\overline{\mathbf{c}Q}) = \Delta [Q]. \quad (2.8)$$

For ease of demonstration, and because the inclusion of internal energy is not

required at this point in the derivation, the version of the Boltzmann equation for monatomic gases has been employed. The righthand side of Eq. 2.8 is known as the *collision integral*, and is given by

$$\Delta [Q] = \int_{-\infty}^{+\infty} \int_{-\infty}^{+\infty} \int_0^{4\pi} n^2 Q [f(\mathbf{c}') f(\boldsymbol{\zeta}') - f(\mathbf{c}) f(\boldsymbol{\zeta})] g \sigma d\Omega d\boldsymbol{\zeta} d\mathbf{c}, \quad (2.9)$$

where the dependence of the distribution functions on physical space and time are implied. There are several symmetries associated with the collision integral that may be used to cast Eq. 2.9 in other forms. For example, $\Delta [Q]$ is unchanged if any of the following variable exchanges are made:

$$\begin{aligned} & \mathbf{c} \leftrightarrow \boldsymbol{\zeta} \text{ and } Q(\mathbf{c}) \leftrightarrow Q(\boldsymbol{\zeta}); \text{ or} \\ & \mathbf{c}' \leftrightarrow \boldsymbol{\zeta}' \text{ and } Q(\mathbf{c}') \leftrightarrow Q(\boldsymbol{\zeta}'); \text{ or} \\ & Q(\mathbf{c}) \leftrightarrow Q(\mathbf{c}'), \mathbf{c} \leftrightarrow \mathbf{c}', \boldsymbol{\zeta} \leftrightarrow \boldsymbol{\zeta}', f(\mathbf{c}) \leftrightarrow f(\mathbf{c}'), \text{ and } f(\boldsymbol{\zeta}) \leftrightarrow f(\boldsymbol{\zeta}'); \text{ or} \\ & Q(\boldsymbol{\zeta}) \leftrightarrow Q(\boldsymbol{\zeta}'), \mathbf{c} \leftrightarrow \mathbf{c}', \boldsymbol{\zeta} \leftrightarrow \boldsymbol{\zeta}', f(\mathbf{c}) \leftrightarrow f(\mathbf{c}'), \text{ and } f(\boldsymbol{\zeta}) \leftrightarrow f(\boldsymbol{\zeta}'). \end{aligned}$$

Incorporation of these symmetries in Eq. 2.9 and subsequent combination of the resulting forms as described by Bird [8] yields

$$\Delta [Q] = \frac{1}{2} \int_{-\infty}^{+\infty} \int_{-\infty}^{+\infty} \int_0^{4\pi} n^2 [Q(\mathbf{c}') + Q(\boldsymbol{\zeta}') - Q(\mathbf{c}) - Q(\boldsymbol{\zeta})] f(\boldsymbol{\zeta}) f(\mathbf{c}) g \sigma d\Omega d\boldsymbol{\zeta} d\mathbf{c}. \quad (2.10)$$

If the molecular quantity Q is taken to be either the mass, momentum, or energy, which are all conserved during a collision, $\Delta [Q]$ is zero. Evaluating the averages in Eq. 2.8 for each of these *collision invariants* by assuming a Maxwellian distribution function then gives

$$\frac{\partial}{\partial t} \rho + \nabla \cdot (\rho \mathbf{u}) = 0, \quad (2.11)$$

$$\frac{\partial}{\partial t} (\rho \mathbf{u}) + \nabla \cdot (\rho \mathbf{u} \mathbf{u}) + \nabla p = \mathbf{0}, \quad (2.12)$$

and

$$\frac{\partial}{\partial t}(\rho E) + \nabla \cdot (\mathbf{u}(\rho E + p)) = 0, \quad (2.13)$$

which are the Euler equations of mass, momentum, and energy conservation, respectively. In Eqs. 2.11 through 2.13, ρ is the mass density, p is the pressure, and E is the mass specific total energy.

2.3 Navier-Stokes Equations

Even though the assumption of thermodynamic equilibrium yields an analytical solution for the Boltzmann equation that can then be used to derive the Euler equations of continuum flow, such an approach is only physically valid in the limit as $Kn \rightarrow 0$. In order to obtain a more useful set of governing equations for analyzing continuum fluid flow, a small perturbation of the Maxwellian distribution function must be assumed. This approximate solution to the Boltzmann equation, called the Chapman-Enskog distribution function, was developed independently by S. Chapman (1916) and D. Enskog (1917) [17]. First consider the distribution function for a simple, monatomic gas. This distribution can be assumed to have a series representation given by

$$f = f^{[0]} + \epsilon f^{[1]} + \epsilon^2 f^{[2]} + \dots, \quad (2.14)$$

so that when the perturbation parameter, ϵ , is small, the actual distribution is well approximated by the Maxwellian distribution function. To a first-order approximation, the distribution function can be re-written as

$$f = f^{[0]} + \epsilon f^{[1]} = f^{[0]} [1 + \Phi], \quad (2.15)$$

where Φ is an unknown function. The form of Φ can be obtained by substituting Eq. 2.15 into the Boltzmann equation, simplifying, and assuming that the shear

stress tensor and heat flux vector are linear functions of the velocity and temperature gradients, respectively. These are the linear, constitutive relations of the Navier-Stokes equations, and are given by

$$\tau_{ij} = \mu \left(\frac{\partial u_i}{\partial x_j} + \frac{\partial u_j}{\partial x_i} - \frac{2}{3} \frac{\partial u_k}{\partial x_k} \delta_{ij} \right), \quad (2.16)$$

and

$$q_i = -\kappa \frac{\partial T_{trans}}{\partial x_i}, \quad (2.17)$$

where μ and κ are the familiar coefficients of viscosity and thermal conductivity, and δ_{ij} is the Kronecker delta. The rigorous derivation of these coefficients is quite involved mathematically, and is described in several texts, such as Refs. [17], [37], and [82]. A closed-form solution is available only for Maxwell molecules, which comprise a physically hypothetical gas where the coefficient of viscosity is a linear function of the temperature [82]. Determination of these coefficients for real gases usually involves integrating over an infinite series of Sonine polynomials. Fortunately, accurate approximate solutions can be obtained by considering only the first few terms in these series.

Chapman and Cowling [17] give the first-order approximate solution to the Boltzmann equation for a simple, monatomic gas as

$$\begin{aligned} f(\mathbf{c}) = f^{[0]}(\mathbf{c}) & \left[1 + (q_x^* \mathcal{C}_x + q_y^* \mathcal{C}_y + q_z^* \mathcal{C}_z) \left(\frac{2}{5} \mathcal{C}^2 - 1 \right) \right. \\ & \left. - 2 (\tau_{xy}^* \mathcal{C}_x \mathcal{C}_y + \tau_{xz}^* \mathcal{C}_x \mathcal{C}_z + \tau_{yz}^* \mathcal{C}_y \mathcal{C}_z) - \tau_{xx}^* \mathcal{C}_x^2 - \tau_{yy}^* \mathcal{C}_y^2 - \tau_{zz}^* \mathcal{C}_z^2 \right], \end{aligned} \quad (2.18)$$

where \mathbf{c} is the molecular thermal velocity normalized as

$$\mathbf{c} = \mathbf{C} \sqrt{\frac{m}{2k_B T_{trans}}}, \quad (2.19)$$

and the normalized shear stress and heat flux are given by

$$\tau_{ij}^* = \frac{1}{p} \tau_{ij} \quad (2.20)$$

and

$$q_i^* = \frac{1}{p} \sqrt{\frac{2m}{k_B T_{trans}}} q_i. \quad (2.21)$$

For a gas mixture that may include polyatomic species, the additional effects of mass diffusion and internal heat fluxes must also be considered. Like the shear stress and translational heat flux, the mass diffusion is normalized as

$$D_{i,s}^* = \sqrt{\frac{m_s}{2k_B T_{trans}}} \frac{J_{i,s}}{\rho_s}, \quad (2.22)$$

where $J_{i,s}$ is the i -component of the diffusion flux vector for species s . The diffusion flux vector is given by

$$\mathbf{J}_s = -\rho D_{sm} \nabla Y_s + Y_s \sum_{i=1}^{NS} \rho D_{im} \nabla Y_i. \quad (2.23)$$

In Eq. 2.23, Y_s and D_{sm} are, respectively, the mass fraction and effective diffusion coefficient of species s . It should also be noted that Eq. 2.23, which is known as the self-consistent effective binary diffusion (SCEBD) model [60], guarantees the sum of the diffusion fluxes will be zero. Further discussion of how the effective diffusion coefficient is calculated will be provided in Chapter IV. The rotational and vibrational heat fluxes are normalized as

$$(q_{rot,i}^*)_s = \frac{1}{\rho_s (c_{v,rot})_s T_{rot}} \sqrt{\frac{2m_s}{k_B T_{trans}}} (q_{rot,i})_s \quad (2.24)$$

and

$$(q_{vib,i}^*)_s = \frac{1}{\rho_s (c_{v,vib})_s T_{vib}} \sqrt{\frac{2m_s}{k_B T_{trans}}} (q_{vib,i})_s, \quad (2.25)$$

where $c_{v,rot}$ and $c_{v,vib}$ are, respectively, the mass specific heats of the rotational and vibrational energies at constant volume, T_{rot} is the temperature that characterizes

the energy in the rotational mode, and T_{vib} is the temperature that characterizes the energy in the vibrational mode. Using these normalized transport quantities, the *generalized* Chapman-Enskog distribution function [53, 75] for a single species s in a mixture is then given by

$$\begin{aligned}
f_s(\mathbf{c}_s, \varepsilon_{rot,s}, \varepsilon_{vib,s}) = f_s^{[0]}(\mathbf{c}_s, \varepsilon_{rot,s}, \varepsilon_{vib,s}) & \left[1 + 2(D_{x,s}^* \mathcal{C}_{x,s} + D_{y,s}^* \mathcal{C}_{y,s} + D_{z,s}^* \mathcal{C}_{z,s}) \right. \\
& + (q_{x,s}^* \mathcal{C}_{x,s} + q_{y,s}^* \mathcal{C}_{y,s} + q_{z,s}^* \mathcal{C}_{z,s}) \left(\frac{2}{5} \mathcal{C}_s^2 - 1 \right) - \tau_{xx,s}^* \mathcal{C}_{x,s}^2 - \tau_{yy,s}^* \mathcal{C}_{y,s}^2 - \tau_{zz,s}^* \mathcal{C}_{z,s}^2 \\
& + \left((q_{rot,x}^*)_s \mathcal{C}_{x,s} + (q_{rot,y}^*)_s \mathcal{C}_{y,s} + (q_{rot,z}^*)_s \mathcal{C}_{z,s} \right) \left(\frac{\varepsilon_{rot,s} - \bar{\varepsilon}_{rot,s}}{k_B T_{rot}} \right) \\
& + \left((q_{vib,x}^*)_s \mathcal{C}_{x,s} + (q_{vib,y}^*)_s \mathcal{C}_{y,s} + (q_{vib,z}^*)_s \mathcal{C}_{z,s} \right) \left(\frac{\varepsilon_{vib,s} - \bar{\varepsilon}_{vib,s}}{k_B T_{vib}} \right) \\
& \left. - 2(\tau_{xy,s}^* \mathcal{C}_{x,s} \mathcal{C}_{y,s} + \tau_{xz,s}^* \mathcal{C}_{x,s} \mathcal{C}_{z,s} + \tau_{yz,s}^* \mathcal{C}_{y,s} \mathcal{C}_{z,s}) \right].
\end{aligned} \tag{2.26}$$

As was done in the derivation of the Euler equations, the Navier-Stokes equations of mass, momentum, and energy conservation are derived by evaluating Eq. 2.8 for the collision invariants, assuming a generalized Chapman-Enskog distribution. Separate rotational and vibrational energy equations can also be derived to allow for nonequilibrium between energy modes [16]. The resulting set of Navier-Stokes equations that is used in the current work is given by

$$\frac{\partial}{\partial t} \mathbf{U} + \frac{\partial}{\partial x} (\mathbf{F} - \mathbf{F}_v) + \frac{\partial}{\partial y} (\mathbf{G} - \mathbf{G}_v) = \mathbf{S}, \tag{2.27}$$

where

$$\mathbf{U} = \begin{bmatrix} \rho_1 & \cdots & \rho_{NS} & \rho u & \rho v & \rho E & \rho e_{rot} & \rho e_{vib} \end{bmatrix}^T \tag{2.28}$$

is the vector of conserved variables. The mass densities of all species in the gas mixture are defined by $\rho_1 \cdots \rho_{NS}$, and the mass specific rotational and vibrational energies are defined as

$$e_{rot} = \sum_{i=1}^{NS} \frac{\rho_i}{\rho} c_{v,rot,i} T_{rot} \quad (2.29)$$

and

$$e_{vib} = \sum_{i=1}^{NS} \frac{\rho_i}{\rho} c_{v,vib,i} T_{vib}. \quad (2.30)$$

The total energy per unit volume is then given by

$$\rho E = \sum_{i=1}^{NS} \rho_i (c_{v,trans})_i T_{trans} + \frac{1}{2} \rho (u^2 + v^2) + \sum_{i=1}^{NS} \rho_i h_i^0 + \rho e_{rot} + \rho e_{vib}, \quad (2.31)$$

where $(c_{v,trans})_i$ is the mass specific heat of the translational energy at constant volume for species i , and h_i^0 is the enthalpy of formation for this species. The vector of source terms, \mathbf{S} , is given by

$$\mathbf{S} = \begin{bmatrix} 0 & \cdots & 0 & 0 & 0 & 0 & S_{trans-rot} & S_{trans-vib} \end{bmatrix}^T. \quad (2.32)$$

More about the translational-rotational and translational-vibrational source terms will be discussed in Chapter IV. The inviscid flux vector, \mathbf{F} , and diffusive flux vector, \mathbf{F}_v , in the x direction are defined as follows, where the flux vectors in the other directions are defined in a similar manner:

$$\mathbf{F} = \begin{bmatrix} \rho_1 u \\ \vdots \\ \rho_{NS} u \\ \rho u^2 + p \\ \rho uv \\ (\rho E + p) u \\ \rho e_{rot} u \\ \rho e_{vib} u \end{bmatrix} \quad (2.33)$$

$$\mathbf{F}_v = \begin{bmatrix} -J_{x,1} \\ \vdots \\ -J_{x,NS} \\ \tau_{xx} \\ \tau_{xy} \\ \tau_{xx}u + \tau_{xy}v - q_{trans,x} - q_{rot,x} - q_{vib,x} - \sum_{i=1}^{NS} (J_{x,i}h_i) \\ -q_{rot,x} - \sum_{i=1}^{NS} (J_{x,i}e_{rot,i}) \\ -q_{vib,x} - \sum_{i=1}^{NS} (J_{x,i}e_{vib,i}) \end{bmatrix} \quad (2.34)$$

Using computational fluid dynamics (CFD) techniques, the above Navier-Stokes equations can be discretized and numerically integrated to yield a flow field solution that is accurate within the constraints of the previously stated continuum assumptions. Specifically, CFD is a physically appropriate simulation method for low Knudsen numbers only, where the molecular properties can be accurately described by a Chapman-Enskog distribution function. Their range of applicability can be extended through the use of boundary conditions that allow for the higher Knudsen number effects of velocity slip and temperature jump [47]. However, such measures serve to correct for strong nonequilibrium effects near a wall only, leaving the continuum prediction of other flow features lacking in accuracy, such as the internal structure of a strong bow shock wave. Despite the limitations of the Navier-Stokes equations, obtaining numerical solutions of these equations using CFD has been well studied and is computationally efficient. In addition, for most transitional, hypersonic flow fields of interest, CFD yields a reasonable solution throughout the majority of the simulation domain. More details about the methods used to obtain numerical solutions of the Navier-Stokes equations in the present work will be presented in Chapter III.

2.4 Alternative Solution Methods

Continuing with a second- and third-order perturbation of the Maxwellian equilibrium distribution function yields the Burnett and super-Burnett equations, respectively. However, derivation of these distribution functions and corresponding extended hydrodynamic equations is even more mathematically esoteric, involving higher-order constitutive closure relations [37]. In addition, these equations have been shown to provide only marginal improvement over the Navier-Stokes equations, and the nature of the series expansion limits their applicability to regions where a first-order approximation is already adequate [17, 82]. Therefore, higher-order approximate solutions to the Boltzmann equation are not widely used.

Grad [31] proposed an alternative series expansion to that assumed in the previous section. For small Knudsen numbers, Grad's Thirteen Moment equations are equivalent to the Burnett equations, but only yield an accurate approximation of the true molecular distribution function at relatively small Mach numbers [17]. For solution of the internal structure of strong, one-dimensional shock waves, Mott-Smith [52] suggested that the distribution function be described by a linear combination of Maxwellian distribution functions characterized by the upstream and downstream conditions. Although fairly successful for a limited number of applications, the complexity associated with these moment methods, both in their formulation and numerical solution, usually outweighs any potential benefits over the Navier-Stokes equations.

Approaches to analytically solve modified versions of the Boltzmann equation have also been proposed, many of which assume a simplified form of the collision term in Eq. 2.2. For example, Bhatnagar, Gross, and Krook [5] proposed that the collision term be modeled as

$$\left\{ \frac{\partial}{\partial t} [nf] \right\}_{coll} = n\nu (f^{[0]} - f), \quad (2.35)$$

which is known as the B-G-K approximation, and describes the relaxation of a nonequilibrium distribution towards a local Maxwellian. In Eq. 2.35, ν is a collision frequency that is often defined as the ratio between the pressure and coefficient of viscosity [17, 82]. Although the B-G-K approximation simplifies the Boltzmann equation significantly, it remains an integro-differential equation. If a series representation is again assumed for the distribution function and substituted into this modified Boltzmann equation, as was done in the derivation of the Chapman-Enskog distribution function, the result is very similar except that the Prandtl number is found to be unity. For real monatomic gases, the Prandtl number is closer to $2/3$.

2.5 Direct Simulation Monte Carlo Method

Because of the limited success achieved in attempting to extend the Navier-Stokes equations, and the intractability of obtaining an analytical, nonequilibrium solution of the Boltzmann equation, this section describes a reliable numerical approach for simulating higher Knudsen number flows. The obvious choice for numerical solution of the Boltzmann equation is to employ CFD techniques to discretize all pertinent phase space dimensions and integrate to obtain the evolution of the distribution function, which is the lone dependent variable. However, there are a number of difficulties associated with this approach in terms of both numerical formulation and computational requirements. For example, accounting for the dimensions of physical *and* velocity space that must be simulated, and, as noted in Section 2.1, the complexity and number of simultaneous Boltzmann equations that must be solved when any real gas is considered, the problem quickly becomes unmanageable. As expected, evaluation of the collision term is especially involved.

Advantage of the molecular nature of gases was taken by G. A. Bird when he proposed the direct simulation Monte Carlo (DSMC) method in 1963 [6, 8]. In the DSMC method, the movement of and collisions between the real molecules in a gas

are simulated by the deterministic movement of and probabilistic collisions between a large number—usually millions—of representative simulator particles. These particles have associated positions, velocities, and internal energies. The Boltzmann equation is not solved directly, but even so, in the limit of an infinite number of simulator particles, the DSMC method has been shown to yield flow field predictions that converge to the true solutions of the Boltzmann equation [85]. The primary assumption of the DSMC method is that the movement of these simulator particles can be decoupled from their collisions. For this assumption to be valid, simulator particles are moved along their individual velocity vectors through a time step that is less than the local mean collision time. As in CFD, physical space is discretized into computational cells through which particle movement is tracked. After the particles are moved and boundary conditions are applied, potential collision partners are selected from within the same computational cell. Therefore, in addition to requiring that the time step be less than the local mean collision time, the dimensions of each computational cell must be less than the local mean free path. The collision selection process is grounded in kinetic theory and, as such, the DSMC method is also limited by the same underlying assumptions of the Boltzmann equation. Specifically, these include the assumption of molecular chaos and a dilute gas.

In a collision, mass, momentum, and energy are conserved. Collisions that occur such that there is no exchange of energy between the translational motion of the particles and their rotational and vibrational modes are defined as *elastic* collisions. In the case of an *inelastic* collision, momentum is conserved in that the velocity of the center of mass of the colliding pair remains unchanged, while there is a redistribution of the relative translational and internal energies. As the simulator particles move and collide over many time steps, the local distribution function of particle properties evolves from an initially prescribed state to one that is physically representative of the true flow field. Thus, there are no *a priori* assumptions about the shape of the

distribution function relative to a Maxwellian, as is done in the derivation of the Navier-Stokes equations.

Although inherently unsteady, a steady flow field solution is obtained with the DSMC method by waiting until the total number of simulator particles reaches a steady state and then collecting samples of particle properties within each computational cell. Macroscopic fluid properties are then calculated as averages of these particle properties, where the statistical scatter is inversely proportional to the square root of the number of samples. In general, the accuracy of the DSMC method is dependent on both the number of particles in each computational cell and the total number of time steps over which samples are collected. Fallavollita, *et al.* [24] found that the error associated with a DSMC simulation asymptotes as the number of samples increases towards infinity, where the asymptotic value decreases with an increasing number of particles per cell. This is very dependent on whether or not the simulator particles possess statistically independent properties. It is usually recommended that each computational cell contain at least 20 particles per cell [8, 18]. It should also be noted that, because the time step and computational cell size greatly impact the validity of the assumptions made in the formulation of the DSMC method, their values relative to the local mean collision time and mean free path, respectively, play a critical role in the physical accuracy of a DSMC simulation.

Like the Boltzmann equation, the DSMC method is physically appropriate for analyzing the complete range of Knudsen numbers. However, because of the restrictions on both time step and cell size, the DSMC method becomes computationally demanding in highly collisional flow fields. Most of the computational time required to perform a DSMC simulation is spent in collision partner selection and collision mechanics. As will be further discussed in Chapter III, the computational cost of the specific implementation of the DSMC method used in this work is directly proportional to the number of simulator particles.

2.6 Hybrid Approaches

As can be surmised from the mathematical models and numerical simulation techniques described thus far in this chapter, there are advantages and disadvantages that must be reconciled in each case. The mixed rarefied/continuum nature of transitional, hypersonic flows makes the choice of which approach to use even more difficult. Whereas numerical solution of the Navier-Stokes equations throughout the entire flow field is computationally efficient, the nonequilibrium effects that are present where the local Knudsen number is relatively large invalidate the linear constitutive relations assumed in Section 2.3. However, even if it is computationally feasible to simulate an entire flow field of this type with the DSMC method, this is not an efficient use of computational resources. In many regions of the flow field, the local molecular property distribution function predicted by the DSMC method can be accurately approximated by a Chapman-Enskog distribution and, therefore, more efficiently simulated using CFD. Because of this, the development of hybrid methods for simulating transitional, hypersonic flows is an active area of current research.

The most prevalent hybrid approach in the literature involves coupling the numerical solution of the Navier-Stokes equations using CFD in near-equilibrium regions of a flow field with the DSMC method in regions of thermodynamic nonequilibrium. Both CFD and DSMC are well developed and reliable simulation techniques, and models exist for both methods that encompass a wide range of physical phenomena. Therefore, although they are very different approaches, their relative maturity makes these methods strong candidates for implementation in a hybrid framework. Wadsworth and Erwin [83, 84] proposed a strongly-coupled, hybrid particle-continuum method which they demonstrated for both one-dimensional shock waves and the two-dimensional, pressure-driven flow through a slit. The *strongly-coupled* qualifier is used here because boundary values for each computational method were updated and employed by the other method during each global time step. However, as expected, some amount of

time-averaging of the DSMC solution was required to prevent spurious propagation of statistical scatter into the continuum domains. For simplicity, the boundaries between computational domains were static throughout the simulation, although the value of the shear stress was proposed as an indicator of nonequilibrium effects. Emphasis was placed on exploring the consistent and conservative exchange of flux-based information across these boundaries. Gains in computational efficiency over full DSMC simulations were observed in both one-dimensional and two-dimensional cases; these gains were strongly dependent on the relative sizes of the DSMC domains used.

Hash and Hassan [35, 36] explored the advantages and disadvantages of different coupling techniques in the context of a loosely-coupled, hybrid particle-continuum method. Although more details regarding these studies will be provided in Chapter III, the flux-based coupling approach was found to be problematic along hybrid interfaces that are either aligned with the macroscopic velocity or located in low Mach number regions of the flow field. This is due to the level of statistical scatter that is passed from the DSMC domains to the CFD domains. A novel coupling approach proposed by Roveda, *et al.* [62] employs several layers of ghost cells along hybrid interfaces in order to reduce the level of statistical scatter. Although the cloning of particles for each layer of ghost cells does not result in additional statistically independent samples, if a large number of ghost cells are used such that independent collisions can occur on each level, the cloned particles quickly lose their identities.

Statistical scatter is a drawback inherent to the DSMC method, and becomes even more challenging to overcome when attempting to incorporate the DSMC method in a hybrid simulation approach. Because of this, an “information preserving” DSMC (IP-DSMC) method has been proposed where each particle is assigned an average velocity in addition to its own molecular velocity [25]. By tracking a macroscopic velocity, a significant reduction in statistical scatter is achieved. Wang and Boyd [87] developed a hybrid approach that strongly couples this IP-DSMC method and a CFD

Navier-Stokes solver. Hybrid results for the cases of hypersonic flow over a blunted cone tip, and hypersonic external flow around a hollow-cylinder flare were compared to full CFD and full DSMC simulations. Because of the presence of shock waves and other strong nonequilibrium effects, and the limitations of the IP-DSMC method, the hybrid approach was not able to reproduce the full DSMC results. The IP-DSMC method was later modified to enable more accurate simulation of nonequilibrium effects [86], but the computational expense of this hybrid approach was found to be, at best, on the order of a full DSMC simulation, and actually required more memory, making it unpractical.

Similarities between the coupling procedures used across different levels of adaptive mesh refinement (AMR) algorithms and those required in a hybrid particle-continuum method were recognized by Garcia, *et al.* [27] when developing an adaptive mesh *and* algorithm refinement (AMAR) method. In this approach, CFD is employed throughout the simulation domain and some estimate of numerical error is used to automatically refine the computational mesh. The DSMC method is then used at the level of highest refinement, where computational cell dimensions may be comparable to the local mean free path of the flow. A buffer region surrounds the DSMC domain, and new simulator particles are generated using macroscopic information obtained from CFD cells in this region. Simulator particles that cross hybrid interfaces while the DSMC domain is being updated, in turn, provide the flux information required by the CFD domain. This enables a strongly-coupled scheme that is algorithmically very similar to AMR procedures, and facilitates the straightforward development of a hybrid method from an existing AMR framework.

A loosely-coupled, hybrid particle-continuum method that is applicable to three-dimensional, unstructured computational meshes was proposed and demonstrated by Wu, *et al.* [91]. This hybrid method was shown to reproduce full DSMC results for the hypersonic flow over a two-dimensional wedge. Excellent agreement was also

achieved for the three-dimensional simulation of two parallel jets exhausting into a near-vacuum when results were compared to published experimental measurements. However, simulation of the former test case using the proposed hybrid method required a larger computational expense than the corresponding full DSMC simulation. As noted by Schwartzentruber [64], this may be due to the fact that after being initialized by a full Navier-Stokes solution, simulator particles are allowed to move and collide in the DSMC regions until a steady-state is reached, after which samples are collected until statistical fluctuations have been substantially reduced. Although this is one way of providing steady boundary conditions to the CFD domains, it does not promote numerical efficiency. An alternative approach to reducing this statistical scatter will be described in Chapter III.

Another subtle, yet potentially problematic, characteristic of the hybrid cycle proposed by Wu, *et al.* [91] is that after the DSMC domains are updated, information is provided to the CFD domains in the form of updated boundary conditions *before* re-positioning of the hybrid interfaces. During the initial development of the hybrid method that is the focus of this dissertation, Schwartzentruber [64] found that transferring information from the DSMC domains to the CFD domains before verifying that the hybrid interfaces are placed in near-equilibrium regions of the flow can lead to incorrect predictions of post-shock flow properties. It's also interesting to note that in this hybrid approach, newly generated particles along hybrid interfaces are sampled from a Maxwellian distribution function, even though the CFD domains are simulated using a Navier-Stokes solver. Although sampling from a Maxwellian is simpler and requires fewer operations, this severely restricts the placement of hybrid interfaces to regions of the flow field that can accurately be described by an equilibrium distribution function.

In an uncoupled hybrid particle-continuum approach very similar to that presented in this dissertation, Stephani, *et al.* [73] initialized a local DSMC simulation

with a three-dimensional CFD solution of a hypersonic flow over a flat plate with discrete surface roughness. DSMC simulator particle information was sampled from generalized Chapman-Enskog distributions for a five-species air mixture exhibiting both rotational and vibrational nonequilibrium. In addition, a detailed comparison of transport coefficients predicted by the continuum and particle models was performed in order to verify consistency of the information transferred from the initial Navier-Stokes solution to the DSMC domain. However, because of the uncoupled nature of this approach, where the locations of the hybrid interfaces were predetermined and stationary throughout the simulation, and updated boundary information did not have to be transferred from the DSMC domain to the CFD domain, many of the potential issues associated with an automated and adaptive hybrid approach were avoided. Although this hybrid approach is not readily applicable to general flow fields, the investigations regarding consistent physical models and particle generation are of importance to any hybrid particle-continuum method.

CHAPTER III

A Modular Particle-Continuum Method

In the case of hypersonic, blunt-body flows at transitional Knudsen numbers, there are likely to be localized regions of thermodynamic nonequilibrium effects that invalidate the continuum assumptions of the Navier-Stokes equations. Accurate simulation of these regions, which may include strong shock waves, boundary and shear layers, and low-density wakes, requires a kinetic theory-based approach where no *a priori* assumptions are made regarding the VDF or internal EDFs of the constituent molecules. The most popular of these approaches is the DSMC method [8]. Although the DSMC method is physically accurate for all Knudsen numbers, restrictions on both time step and cell size make the approach computationally demanding for high-density regions of the flow field. However, it is in these high-density, near-continuum regions of the flow field where CFD techniques are well suited for efficient numerical solution of the Navier-Stokes equations. Because of the mixed rarefied/continuum nature of hypersonic, transitional Knudsen number flows, it is advantageous in terms of both numerical efficiency and physical accuracy to develop and employ a hybrid particle-continuum method.

The purpose of this dissertation is to describe recent efforts to verify and further develop the Modular Particle-Continuum (MPC) method, which was first introduced and demonstrated by Schwartzentruber, *et al.* [66]. The MPC method is a hybrid

framework that loosely couples the LeMANS finite volume CFD solver [50] with the MONACO DSMC code [23]. Because of the modular nature of the MPC code, almost all modifications required to extend the capabilities of the method have been limited to the hybrid data structure and functions. This has allowed for both LeMANS and MONACO to be maintained separately from the hybrid code, and enables many of the state-of-the-art capabilities of each of the simulation modules to be incorporated in the MPC method.

The MPC method is initialized with a full CFD solution from LeMANS, from which several continuum breakdown parameters that indicate failure of the Navier-Stokes equations are computed. Based on the values of these continuum breakdown parameters, the simulation domain is divided into distinct particle and continuum regions where DSMC and CFD are used sequentially to obtain a numerically efficient and physically accurate solution. Information is exchanged between particle and continuum regions in the form of updated boundary conditions as the solution evolves. Because use of the DSMC method is restricted to regions of the flow field where it is necessary to maintain physical accuracy, it has been the goal of this hybrid approach to achieve solutions of hypersonic, transitional Knudsen number flows that are accurate to within $\pm 5\%$ of a full DSMC solution, and to do so at a reduced computational cost.

During the initial development of the MPC hybrid method, Schwartzentruber, *et al.* demonstrated its numerical efficiency and physical accuracy relative to full DSMC and full CFD in a number of applications, including one-dimensional shock waves [65], two-dimensional and axisymmetric, steady, hypersonic, blunt-body flows [66, 68], and shock-boundary layer interaction flows [67]. All of these simulations were performed in serial, and were limited to simple gases. The MPC method was later parallelized by Deschenes and Boyd [20] by using the Message Passing Interface (MPI) and METIS [43] graph partitioning. For optimal parallel efficiency, each com-

putational cell is assigned a weight based on the number of particles per cell prior to simulation of the particle domains. A different weighting scheme is used prior to simulating the continuum domains, where cells that will be updated or are otherwise involved are given a weight of unity, and particle cells are given a weight of zero. The ability to simulate rotational nonequilibrium effects in simple gases and vibrationally excited single-species flows was also incorporated in the MPC method by Deschenes, *et al.* [21, 22]. These were the capabilities of the MPC method prior to the contributions of this dissertation, and the details presented in this chapter represent the state of the code at that time unless explicitly stated.

This chapter first describes the individual CFD and DSMC simulation modules that comprise the MPC hybrid method. Details of how regions of nonequilibrium are identified from an initial, continuum solution, subsequent mesh refinement of the particle regions, and consistent exchange of information between the particle and continuum regions are also presented. Finally, the organizational structure of the MPC method, and the hybrid cycle that is typical of the simulations presented in this dissertation are described.

3.1 Simulation Modules

As with the MPC hybrid method, the LeMANS finite volume CFD solver and the MONACO DSMC code continue to be developed at the University of Michigan. Additional details of each of these codes, which serve as independent simulation modules of the MPC method, are provided in this section. LeMANS and MONACO themselves are also used to generate full CFD and full DSMC simulation results for comparison with MPC hybrid results.

3.1.1 CFD

LeMANS is a finite volume CFD code capable of numerically solving the steady, laminar Navier-Stokes equations on axisymmetric, two-dimensional, and three-dimensional, body-fitted meshes. All simulations presented in this dissertation employ structured meshes because of the requirements of the MPC method, even though LeMANS is formulated to handle unstructured meshes. Parallel simulations are performed using the Message Passing Interface (MPI) and METIS [43] graph partitioning. The Steger-Warming Flux Vector Splitting (FVS) scheme [72] is used to discretize the inviscid fluxes of the Navier-Stokes equations for proper upwinding of characteristic information. In order to achieve second-order spatial accuracy, the linear variation of primitive variables in each cell is reconstructed according to the MUSCL approach [78]. The minmod limiter is used to prevent oscillatory behavior near shock waves. Because the original Steger-Warming FVS scheme is quite dissipative, a modified approach is employed everywhere except in the vicinity of shock waves [49]. A pressure switch enables automatic and seamless transition between the original and modified schemes. The viscous fluxes are discretized according to a central difference scheme that uses both cell-centered macroscopic properties and information interpolated to cell nodes to calculate face-based derivatives [41].

Temporal integration is performed using the Backward Euler scheme and either a point- or line-implicit relaxation method. Because of improved convergence rates, the line-implicit method is used in the full CFD simulations presented in this dissertation. However, point-implicit time integration is used in the continuum regions of MPC hybrid simulations. Not only is the improvement in convergence rate negligible when the line-implicit method is used in the MPC simulations, but the point-implicit method allows the particle domains to be completely ignored while the continuum domains are being updated. In the case of a full CFD simulation, the time step is initialized to a relatively small value and incremented each iteration as long as the

L_2 norm decreases and until a maximum Courant-Friedrichs-Lewy (CFL) number is reached. Because the boundary conditions of the continuum domains are changed during every cycle of a hybrid simulation, this incrementing procedure is repeated each time the continuum domains are updated.

LeMANS is capable of simulating weakly ionized, hypersonic flows, accounting for excitation of vibrational energy modes and rotational nonequilibrium effects. Finite-rate chemistry is another capability of the LeMANS code. Although this functionality is not explored in the present work, it will be important for future development of the MPC hybrid method. More details regarding the physical models employed in the continuum domains of hybrid simulations and in full CFD simulations will be given in Chapter IV, and more information on the development of the LeMANS code itself can be found in Ref. [63].

3.1.2 DSMC

MONACO is a general, cell-based implementation of the DSMC method capable of using axisymmetric, two-dimensional, and three-dimensional, body-fitted meshes. Cell-based particle weights and local time-stepping can be used in order to reduce the computational cost of simulating a flow field that may include a wide range of densities. However, a constant time step is specified throughout the entire simulation domain, and cell-based particle weighting is limited to avoid reliance on dependent samples in full DSMC simulations and in particle regions of MPC hybrid simulations presented here. MONACO is also parallelized using the Message Passing Interface (MPI), and graph partitioning with METIS [43] is optimized for the number of particles in each computational cell.

At the start of each full DSMC simulation, the computational domain is populated according to a Maxwellian VDF defined by ambient macroscopic properties provided by the user. The number of particle pairs in each cell selected to be tested for collision

is calculated using Bird’s No Time Counter (NTC) method [8]. Because a limited number of potential collision pairs are analyzed in each particle cell, the computational cost of a DSMC simulation using the NTC method is directly proportional to the number of simulator particles rather than its square. According to the NTC method, the number of particle pairs selected to be tested for collision is given by

$$N_{pairs} = \frac{1}{2} N \bar{N} W_c (\sigma_{Tg})_{max} \frac{\Delta t}{V_c}. \quad (3.1)$$

In Eq. 3.1, N is the instantaneous number of particles in a given cell, \bar{N} is the time-averaged number of particles, W_c is the number of real molecules represented by each simulator particle, Δt is the time step, and V_c is the volume of the cell. The parameter $(\sigma_{Tg})_{max}$ represents the maximum volume swept out by two colliding particles’ total cross-section per unit time. However, this parameter does not affect the collision rate because the probability of each of these pairs actually colliding is calculated as

$$P_{coll} = \frac{\sigma_{Tg}}{(\sigma_{Tg})_{max}}, \quad (3.2)$$

so that this parameter is eventually canceled. In practice, this parameter is initialized to a relatively large value and updated if it is exceeded by any value of σ_{Tg} encountered in the simulation. The total collision cross-section and other collision parameters will be further discussed in Chapter IV.

Once the number of potential collision pairs is determined, particles are randomly paired within a computational cell, hence, the requirement of DSMC cells having dimensions less than the local mean free path. MONACO employs subcells to facilitate collision pair selection. Subcells are created in each particle cell as needed, such that the dimensions of each subcell are a fraction of the local mean free path. Preference for a particle’s potential collision partner is given to those particles that are co-located in the same subcell, with particles in adjacent subcells being considered

next if needed. Thus, even if the actual computational cell is larger than the local mean free path, the accuracy of the collision selection process is maintained. The probability of a given pair colliding is compared to a random fraction as part of an acceptance-rejection procedure. If the random fraction is less than P_{coll} , the collision occurs.

Colliding particle pairs that include at least one molecular species may undergo either elastic or inelastic collisions. In both cases, the velocity of the center of mass of the collision pair is conserved during collision. However, if a collision is inelastic, there is an exchange of energy between internal energy mode(s)—either rotational or vibrational or both—and the relative translational energy of the colliding pair. An acceptance-rejection procedure is again used in conjunction with internal energy exchange probabilities determined by models that will be described in Chapter IV. If a collision pair is selected to undergo an inelastic collision, energy is redistributed according to the Borgnakke-Larsen internal energy exchange model [10], which acts to equilibrate the translational and internal energy modes according to their respective degrees of freedom.

For the DSMC simulations presented in this dissertation, the resultant relative translational energy is used to scatter the particles isotropically, in accordance with the Variable Hard Sphere (VHS) collision model. Angular preference of the post-collision relative translational energy may be incorporated by using the Variable Soft Sphere (VSS) collision model instead, which is another option in MONACO. After the collision step of the DSMC method is complete, the particles are then advected according to their individual velocity vectors, boundary conditions are enforced, and the cycle is repeated. Once the total number of simulator particles in the simulation reaches a steady state, samples of particle properties are collected in each computational cell so that macroscopic properties may be calculated. More detailed information about MONACO can be found in Ref. [23].

3.2 Continuum Breakdown

Accurate determination of continuum breakdown is the mechanism for achieving the optimal balance between physical accuracy and numerical efficiency that is the underlying goal of the MPC hybrid method. If hybrid interfaces are not located in regions of near-equilibrium, the CFD module will be used beyond its range of applicability and physical accuracy will deteriorate. In contrast, being too conservative in the placement of the hybrid interfaces leads to excessive use of the DSMC method in regions that can be accurately simulated using a more economical continuum approach.

The MPC method is initialized with a mesh-independent CFD solution obtained with LeMANS. Although this continuum solution is known to be inaccurate in certain regions of the flow field, it serves as an initial guess that can be obtained efficiently with CFD. Starting with a solution that is close to the correct DSMC result also circumvents the initial transient period that is needed in full DSMC simulations before sampling can begin. Several continuum breakdown parameters are then calculated using this initial continuum solution in order to determine which regions of the flow field should be simulated using DSMC to achieve the desired level of physical accuracy, and which regions are more efficiently simulated using CFD. Again, even if these indicators of continuum breakdown were perfect, this initial identification of particle and continuum domains would be imperfect. However, this is mitigated by periodically recalculating these continuum breakdown parameters as the solution is updated throughout the course of the hybrid simulation. This will become evident in the description of the hybrid cycle presented in Section 3.5.

Various continuum breakdown parameters have been proposed in the literature, most of which rely upon gradients of macroscopic properties obtained from a continuum solution. The physical basis for these continuum breakdown parameters originates in the Chapman-Enskog approximate solution of the Boltzmann equation. The

Chapman-Enskog distribution function is a first-order perturbation of the Maxwellian equilibrium distribution function, and this perturbation, for a mixture of chemical species with internal energy modes, contains terms involving gradients of composition, temperature, and velocity. These gradients drive the physical processes of mass diffusion, thermal conduction, and viscosity, respectively. When these nonequilibrium phenomena occur over length scales of the order of the local mean free path, a Chapman-Enskog distribution function cannot be maintained and the Navier-Stokes equations can no longer accurately represent the state of the flow field.

For detecting the onset of nonequilibrium effects in expanding flows, Bird [7] proposed the following parameter:

$$P = \tau_c \left| \frac{D(\ln \rho)}{Dt} \right|. \quad (3.3)$$

In Eq. 3.3, τ_c is the mean collision time, ρ is the mass density, and $D() / Dt$ is the substantial derivative. Simplifying this expression for steady flows yields

$$P = M \sqrt{\frac{\pi \gamma}{8}} \frac{\lambda}{\rho} \left| \frac{d\rho}{ds} \right|, \quad (3.4)$$

where M is the local Mach number, γ is the ratio of specific heats, λ is the local mean free path, and s is the distance along a streamline. A strong correlation was found between this parameter and the degree of nonequilibrium exhibited by several expanding nozzle flow cases. This correlation also suggested a threshold value of 0.05, so that when $P \geq 0.05$, the normal and parallel translational temperatures in the gas expansion deviated by more than 10%. Boyd, *et al.* [14] later suggested the use of a local Knudsen number to determine the physical applicability of the Navier-Stokes equations, and compared the efficacy of this new parameter to Bird's P parameter in both one-dimensional shock waves and hypersonic, blunt-body flows. This gradient-length local Knudsen number is calculated as

$$Kn_{GLL-Q} = \lambda \left| \frac{\nabla Q}{Q} \right|, \quad (3.5)$$

where Q was initially either translational temperature or mass density. Both continuum breakdown parameters were found to accurately indicate the failure of the Navier-Stokes equations within the one-dimensional shock waves. However, Bird's P parameter was unable to predict the nonequilibrium effects near the stagnation point of the two-dimensional cylinder case examined. Comparison of Eqs. 3.4 and 3.5 reveals that they are approximately equal when Q is taken to be the mass density except for the factor involving the Mach number in Bird's P parameter. No matter how large the gradients in the boundary layer of the cylinder or near its stagnation point, the velocities near the surface decrease to zero and so does Bird's P parameter.

As part of their proposed method for sampling particle velocities from a Chapman-Enskog VDF, Garcia and Alder [26] used the following breakdown parameter:

$$B = \max \left(|\tau_{ij}^*|, |q_i^*| \right), \quad (3.6)$$

where τ_{ij}^* and q_i^* are the normalized stress tensor and heat flux, respectively, that were introduced in Chapter II. Stephani, *et al.* [75] later included normalized mass diffusion and internal heat fluxes in the B parameter formulation when proposing an extension of this particle property sampling procedure to gas mixtures with internal energies. Entropy generation was also investigated as a possible indicator of continuum breakdown by Camberos and Chen [15]. The disadvantage of all of these parameters, however, is their reliance on an empirically-determined threshold value. A truly rigorous procedure for predicting failure of the Navier-Stokes equations would involve comparison of the actual particle distribution function with the Chapman-Enskog distribution function. However, for a hybrid approach such as the MPC method, this would negate any potential efficiency gains. A larger portion—if not the entirety—of the computational domain would need to be populated with

DSMC simulator particles and, after waiting for steady state to be reached, many samples would be needed to obtain a smooth representation of the actual molecular distribution function in each cell.

Since the gradient-length local Knudsen number has been vetted against Bird's P parameter, and has been the focus of numerous independent studies, such as those presented in Refs. [39], [46], and [88], the gradient-length local Knudsen number is used to predict failure of the Navier-Stokes equations in the MPC hybrid method. Wang and Boyd [88] expanded the definition of the gradient-length local Knudsen number to include the velocity magnitude. However, in this work, rather than normalizing the gradient of the velocity magnitude by the velocity, which will approach zero near solid boundaries, the following formulation is used, where a is the local speed of sound:

$$Kn_{GLL-|V|} = \lambda \left| \frac{\nabla|V|}{\max(a, |V|)} \right|. \quad (3.7)$$

By careful comparison of full CFD and full DSMC simulation results, it was determined that when the maximum value of the gradient-length local Knudsen number based on translational temperature, mass density, and velocity magnitude exceeds a threshold of 0.05, the difference between the predicted solutions exceeds $\pm 5\%$ [14, 88]. Therefore, since the first efforts to develop the MPC hybrid method, the goal has been to obtain hybrid results that are accurate to within $\pm 5\%$ of a full DSMC solution. In addition to the gradient-length local Knudsen number, Schwartzenuber, *et al.* [66] found that it was necessary to use another continuum breakdown parameter specifically indicative of rotational nonequilibrium in the post-shock region of hypersonic, blunt-body flows. This supplementary parameter is given by

$$Kn_{ROT-NEQ} = \frac{1}{2} \frac{T_{trans} - T_{rot}}{T_{rot}}, \quad (3.8)$$

and is a relative difference between the translational and rotational temperatures,

with a coefficient determined by Deschenes, *et al.* [22] such that the same threshold value of 0.05 could continue being used. As shown, this parameter is non-negative only when the translational temperature exceeds the rotational temperature, which occurs in the post-shock region of a blunt-body flow where the kinetic energy is first converted to random thermal energy prior to relaxation of the internal energy modes. It is necessary to consider this additional breakdown parameter because of the rapid relaxation processes in the forebody, while the relatively slow expansion in the wake prevents substantial rotational nonequilibrium effects in that region. When the MPC method was extended to be able to simulate rotational nonequilibrium effects and vibrational excitation in simple gases, Deschenes, *et al.* [21, 22] also included the gradient-length local Knudsen numbers based on the rotational temperature and vibrational energy.

Therefore, prior to the work performed in this dissertation, continuum breakdown was determined by calculating

$$Br = \max \left(Kn_{GLL-T_{trans}}, Kn_{GLL-\rho}, Kn_{GLL-|V|}, Kn_{GLL-T_{rot}}, Kn_{ROT-NEQ}, Kn_{GLL-e_{vib}} \right) \quad (3.9)$$

in each computational cell. If Br exceeds the threshold value of 0.05, then the solution in that particular computational cell is obtained using DSMC. Otherwise, CFD is used in that cell because the solution should be within acceptable error of the corresponding DSMC solution. In practice, after the continuum breakdown parameters are calculated, the computational cells are labeled and a smoothing procedure is performed in an attempt to remove any small, isolated particle or continuum regions in the flow field. Although the empirical nature of these continuum breakdown parameters allows for some flexibility in the placement of the hybrid interfaces that separate particle and continuum domains, five additional layers of particle cells are included in the interest of hybrid simulations being conservative rather than inaccurate.

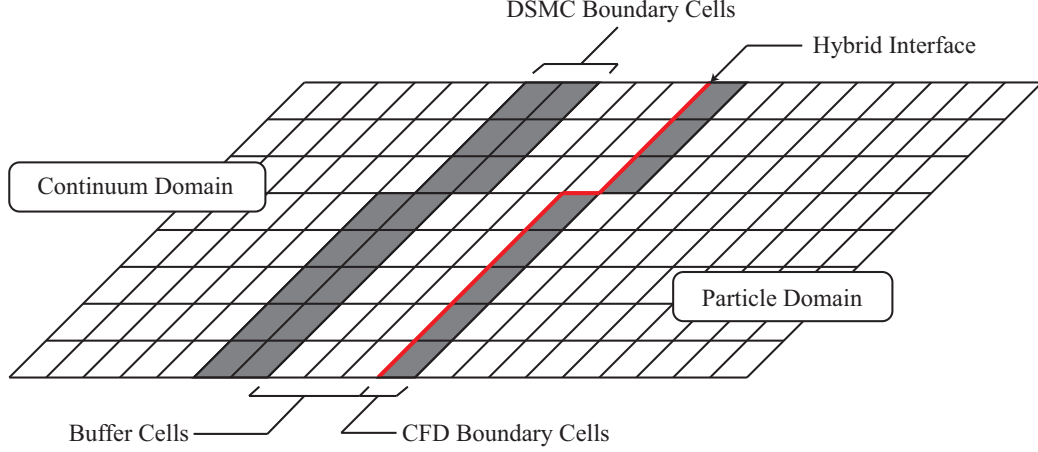


Figure 3.1: Illustration of hybrid interface, before refinement.

The particle domain is then extended into the continuum domain by a user-defined number of “buffer” cells. This not only provides more confidence in the boundary conditions provided to the DSMC module, but also enables the particle regions to expand by updating the solution in regions more extensive than indicated by the continuum breakdown parameters. An illustration of the hybrid interface and associated terminology is shown in Fig. 3.1. Typically, two layers of DSMC boundary, i.e. reservoir, cells are created on the continuum side of the buffer cells in order to generate simulator particles that will either travel into the particle domain or be removed after each time step. One layer of ghost cells is also created on the particle side of the hybrid interface so that boundary conditions can be provided to the continuum module in a manner that is consistent with the standard LeMANS code.

3.3 Mesh Refinement

The MPC method relies on two layers of computational meshes. The continuum mesh layer is the same mesh on which the initial CFD solution is obtained, and is usually much coarser than what is required by the DSMC method. Therefore, once the continuum breakdown parameters are calculated and each cell is assigned to either a particle or continuum domain, this coarse mesh must be selectively refined. Because

the advection and collision steps of simulator particles in the DSMC method are decoupled, the computational mesh must be comprised of cells that have dimensions that are less than the local mean free path. This requirement is most important in the direction of macroscopic gradients in the flow field. Therefore, in the interest of computational efficiency, refinement of cells along the dimension that is perpendicular to the steepest gradients is relaxed slightly. Schwartzentruber, *et al.* [68] used the following equation to dictate the refinement of computational cells in particle regions of a hybrid simulation:

$$r_f = l_f \left[F\lambda \left(3 \left| \hat{n}_f \cdot \frac{\nabla Q}{|\nabla Q|} \right| + 1 \right) \right]^{-1}. \quad (3.10)$$

In Eq. 3.10, r_f is the refinement factor of cell face f , which has length l_f and unit normal \hat{n}_f . The macroscopic property Q is the same macroscopic property identified to give the largest value for the gradient-length local Knudsen number. By calculating the dot product of the face unit normal vector and the normalized gradient vector, the alignment of the cell face relative to flow field gradients is determined. Consider the computational cell in Fig. 3.2. The gradient vector of property Q is pointing nearly opposite the face normal vector \hat{n}_1 so that the refinement factor r_1 , when rounded to the nearest integer, becomes $l_1 (4F\lambda)^{-1}$. If the user-defined constant F has a value of unity, this continuum cell will be refined to include two particle cells along the face with dimension l_1 . Following the same procedure for the face with dimension l_2 , it can be shown that this face will have a refinement factor, r_2 , of four. Because the DSMC module of the MPC hybrid method employs subcells for collision partner selection if a particle cell is deemed too large, the factor F used in the simulations presented here has a value of 1.5.

Neither LeMANS nor MONACO can accommodate hanging nodes in computational meshes. Therefore, once each continuum cell is assigned a refinement factor along each dimension, the refinement factors associated with all of its neighboring

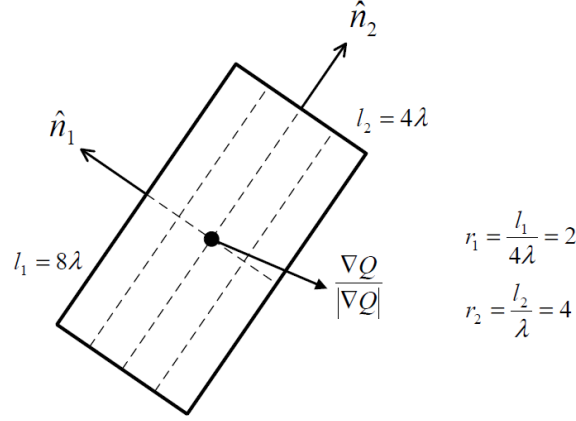


Figure 3.2: Gradient-based refinement of continuum cell [64].

cells are examined and the largest refinement is used along each line of cells in the mesh. This eliminates any hanging nodes at the expense of over-refining the particle mesh in some areas. It should also be noted that the continuum mesh undergoes this refinement procedure only once at the beginning of a hybrid simulation. In terms of numerical efficiency, a hybrid particle-continuum approach is a viable alternative to full DSMC only for a specific class of simulations, namely, transitional, hypersonic flows. If the MPC method were employed to simulate a flow field that is considered nonequilibrium throughout the majority of the domain, there may be no reduction in computational cost. For optimal efficiency, the MPC method should be viewed as a correction to the initial continuum solution, where CFD is capable of accurately simulating the entire flow field except for isolated regions such as the shock wave, boundary layer, and wake. Thus, the assumption that the continuum mesh need only be refined once is substantiated for simulations of interest.

The result of this refinement process is a fine, particle mesh layer as illustrated in Fig. 3.3. The MPC method employs both mesh layers by numerically solving the Navier-Stokes equations on the coarser mesh in the continuum domains, and by moving and colliding simulator particles and sampling on the fine mesh in the particle domains. The particle mesh layer is also exported to be used to obtain a consistent,

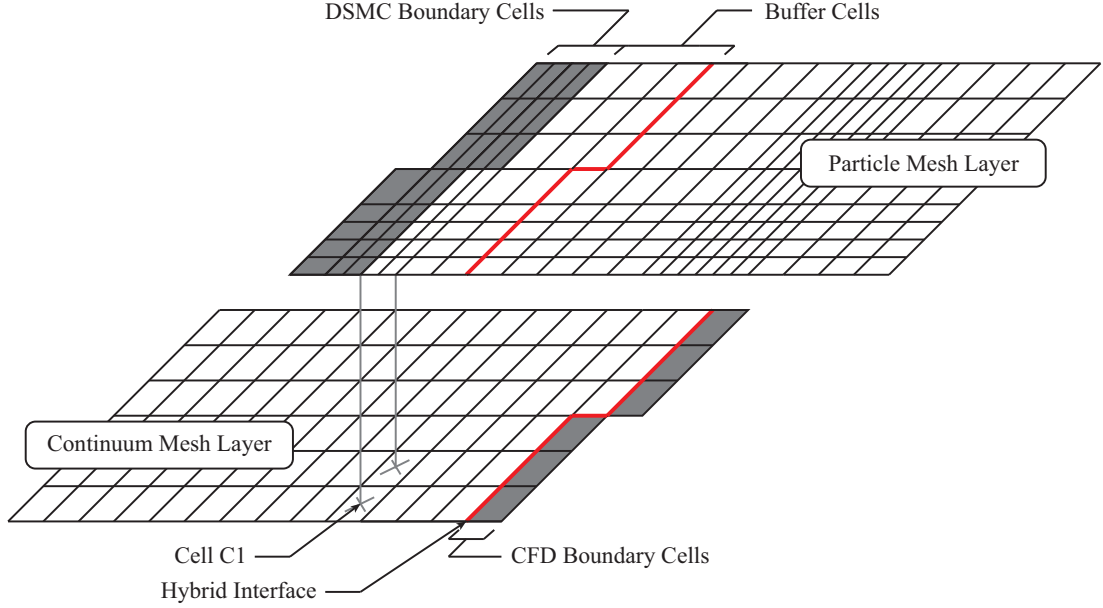


Figure 3.3: Illustration of hybrid interface, after refinement.

full DSMC solution for verification of the hybrid method. These mesh layers allow for direct cell-by-cell comparisons of CFD, DSMC, and MPC hybrid results, as will be discussed in Chapter V.

3.4 Coupling Procedures

Once the particle domains of the initial CFD solution are identified, the macroscopic information in these regions must be consistently translated into simulator particle information for use in the DSMC method. As discussed in Chapter II, the Navier-Stokes equations can be derived by assuming a first-order perturbation of the Maxwellian distribution function, substituting into the Boltzmann equation, and approximating the solution using various constitutive relations. This first-order perturbation of a Maxwellian distribution function is the Chapman-Enskog distribution function, and for a simple, monatomic gas, this distribution function is completely defined by the translational temperature, directed velocity components, mass density, temperature gradient, stress tensor, viscosity coefficient, and coefficient of thermal

conductivity. By sampling velocities from a Chapman-Enskog distribution defined in each continuum cell, and assigning these velocities to newly generated simulator particles, the DSMC method is initialized in the particle regions with the full CFD solution.

Garcia and Alder [26] proposed an efficient procedure for sampling particle velocities from a known Chapman-Enskog distribution function, and this is the approach taken in the MPC hybrid method. For ease of explanation, the Chapman-Enskog distribution function is repeated here as

$$f(\mathbf{c}) = f^{[0]}(\mathbf{c}) \Gamma(\mathbf{C}), \quad (3.11)$$

where $f^{[0]}(\mathbf{c})$ is the Maxwellian distribution function, and

$$\begin{aligned} \Gamma(\mathbf{C}) = & \left[1 + (q_x^* \mathcal{C}_x + q_y^* \mathcal{C}_y + q_z^* \mathcal{C}_z) \left(\frac{2}{5} \mathcal{C}^2 - 1 \right) \right. \\ & \left. - 2 (\tau_{xy}^* \mathcal{C}_x \mathcal{C}_y + \tau_{xz}^* \mathcal{C}_x \mathcal{C}_z + \tau_{yz}^* \mathcal{C}_y \mathcal{C}_z) - \tau_{xx}^* \mathcal{C}_x^2 - \tau_{yy}^* \mathcal{C}_y^2 - \tau_{zz}^* \mathcal{C}_z^2 \right]. \end{aligned} \quad (3.12)$$

Given the macroscopic properties from an initial CFD solution, Garcia and Alder's B parameter is calculated, followed by an amplitude parameter, A , given by

$$A = 1 + 30B. \quad (3.13)$$

A candidate thermal velocity, \mathbf{C}_{try} , is sampled from the corresponding Maxwellian VDF, and using the acceptance-rejection method, is tested against a random fraction, R_f . The candidate thermal velocity is only accepted if

$$R_f \leq \frac{\Gamma(\mathbf{C}_{try})}{A}, \quad (3.14)$$

and when this condition is met, the newly generated particle is assigned the following velocity:

$$\mathbf{c} = \mathbf{u} + \left(\frac{2k_B T_{trans}}{m} \right)^{1/2} \mathbf{C}_{try}. \quad (3.15)$$

In a similar manner, rotational energies are sampled from a Boltzmann energy distribution defined by a macroscopic temperature. If the rotational energy mode is assumed to be in equilibrium with the translational energy mode, particles are assigned rotational energies calculated from

$$\varepsilon_{rot} = -k_B T_{trans} \ln(R_f). \quad (3.16)$$

Otherwise, the rotational temperature is used in place of the translational temperature. Whereas the rotational energy distribution function can be assumed continuous except at cryogenic temperatures, due to the large quantum spacing between vibrational energy levels, the discrete nature of the vibrational energy distribution function cannot be ignored. This large quantum spacing also leads to a high level of statistical scatter when attempting to sample particle vibrational energies in regions exhibiting low temperatures. Therefore, rather than sampling from a Boltzmann distribution, newly generated simulator particles are assigned the *average* vibrational energy corresponding to the continuum solution. If a simple harmonic oscillator is assumed, and N_{max} vibrational levels are considered, the partition function for the vibrational energy mode is written as

$$Q_{vib} = \sum_{i=0}^{N_{max}} \exp(-i\theta_{vib}/T_{vib}). \quad (3.17)$$

The mass specific vibrational energy is then obtained by

$$e_{vib} = \frac{k_B T_{vib}^2}{m} \frac{\partial \ln(Q_{vib})}{\partial T_{vib}} = \frac{k_B \theta_{vib}}{m} \left[\left(1 - \exp\left(\frac{-\theta_{vib}}{T_{vib}}\right) \right) \sum_{i=0}^{N_{max}} i \exp\left(\frac{-i\theta_{vib}}{T_{vib}}\right) \right]. \quad (3.18)$$

In Eqs. 3.17 and 3.18, θ_{vib} is the characteristic temperature of the vibrational energy mode, and N_{max} is determined such that the probability of a simulator particle being in a higher level is less than 1×10^{-8} .

In addition to populating newly labeled particle cells according to macroscopic properties from the continuum solver, simulator particles must also be generated

along the boundaries of particle regions. This provides a means for transferring boundary condition information from the continuum regions to the particle regions in a hybrid particle-continuum method. In DSMC, there are two approaches commonly used to generate particles along a computational boundary. Particles can be created along the cell faces adjacent to the boundary, with velocities sampled from a biased VDF such that the correct particle flux is achieved. During the advection step of the DSMC algorithm, particles are then moved by random fractions of the full time step. This is how particles are generated at the inflow boundary of a full DSMC simulation using MONACO. Particle velocities here are sampled from a biased Maxwellian VDF because of the uniform, freestream conditions specified at the inflow boundary. Alternatively, several “reservoir” cells can be created adjacent to the boundary, and populated with particles whose velocities are sampled from an unbiased VDF. These particles are then moved a complete time step along with all other particles in the simulation, and any particles that reside in these reservoir cells at the end of the advection step are removed from the simulation. This reproduces the correct flux of particles into the computational domain.

Because both approaches are equivalent, and the algorithm for populating entire cells with new simulator particles is also required for the initialization of particle domains at the onset of the simulation, the latter approach is employed in the MPC method. In general, two continuum cells adjacent to the buffer region are labeled as DSMC boundary/reservoir cells, as illustrated in Fig. 3.3. The time step used in the particle regions is specified such that simulator particles are unlikely to cross multiple cells during a given time step. However, particles with velocities sampled from the high-energy tails of the VDF may travel beyond the immediate neighbors of the cell in which they are generated. In order to accurately capture the effect of such particles on the influx at hybrid interfaces, two reservoir cells are used. The likelihood of a particle traversing more than two cells in a single time step is extremely rare,

so it is generally unnecessary to include more than two reservoir cells. It should also be noted that these reservoir cells are the *continuum* cells, which are usually much coarser than the *particle* cells.

Given the acceptance-rejection procedure proposed by Garcia and Alder [26], the transfer of information from the continuum domains to the particle domains is achieved in a straightforward manner. Because of the statistical scatter inherent to the DSMC method, the transfer of information from the particle domains to the continuum domains is more challenging. Hash and Hassan [35] investigated the use of several coupling approaches in the context of a hybrid DSMC/Navier-Stokes method. The Marshak condition [30], which was the first documented mechanism for coupling the DSMC method and a Navier-Stokes solver, involves the summation of the half-fluxes calculated on each side of a hybrid interface and subsequent solution for the net flux. Two other candidate coupling approaches involve extrapolation of either the net fluxes or flow properties to the hybrid interfaces [83, 84]. Because extrapolation of net fluxes involves calculating higher-order moments of DSMC particle information, which are highly susceptible to statistical scatter, Hash and Hassan [35] focused on comparing the Marshak condition and flow property extrapolation procedure. For one-dimensional Couette flow simulations, the Marshak condition was found to be more efficient and less sensitive to the number of DSMC simulator particles per cell than the flow property extrapolation technique. However, a later study involving simulations of hypersonic flow over an axisymmetric planetary probe revealed additional problems for the Marshak condition [36]. When a hybrid interface is located in a region of the flow where the Mach number is low, the flux across that hybrid interface is also small and may be of the order of the statistical scatter of the DSMC method itself. Even at high Mach numbers, fluxes across hybrid interfaces that are aligned with the directed velocity of the flow will also be susceptible to relatively high statistical scatter.

The work performed by Hash and Hassan [35, 36] highlights one of the major difficulties of developing a hybrid particle-continuum method, and exemplifies the disadvantages of employing flux-based coupling schemes. The use of state-based coupling, which is analogous to the reservoir particle generation approach previously described, is favored over flux-based coupling because of the decreased level of statistical scatter associated with volume-based averages as compared to fluxal quantities. The flux-based and state-based coupling approaches are illustrated in Figs. 3.4(a) and 3.4(b), respectively.

Hadjiconstantinou, *et al.* [34] determined the relationship between the error associated with fluxal quantities, E_{flux} , and that associated with volume-based averages, E_{state} , as being

$$E_{flux} \propto \frac{E_{state}}{Kn}. \quad (3.19)$$

Since the local Knudsen number at the hybrid interfaces will be approximately 0.05, the error incurred by using flux-based coupling is estimated to be over an order of magnitude greater than if state-based coupling is used. An additional benefit of a state-based coupling approach is that it is aligned with the modular nature of the MPC method. Particle information is sampled in order to update the macroscopic solution in each CFD boundary cell. These boundary cells then serve the same purpose as the “ghost” cells that are employed to enforce boundary conditions in the LeMANS code. Thus, no modifications of the LeMANS boundary condition algorithms are required for them to be used in the MPC hybrid method.

The mass density of each species in a given cell is calculated in DSMC as

$$\rho_i = \frac{N_i M_i W_c}{V_c N_A}, \quad (3.20)$$

where N_i is the number of simulator particles of species i in the cell, M_i is the molecular weight, and N_A is Avogadro’s number. Note that even though extension

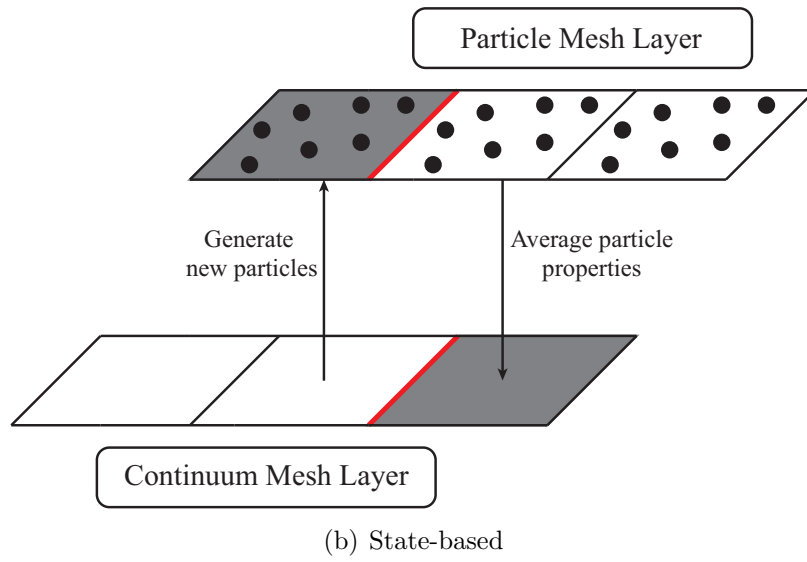
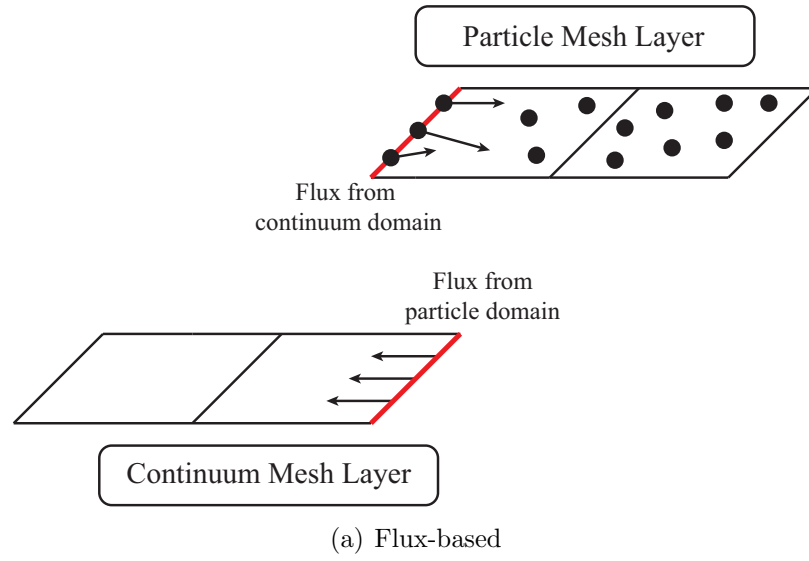


Figure 3.4: Particle-continuum coupling approaches.

of the MPC hybrid method to include mixtures of chemical species is an objective of the current work, the equations presented here for averaging particle properties have been generalized in anticipation of the developments that will be described in Chapter VII. The x -component of the average velocity for each species is given in DSMC by

$$u_i = \frac{\sum_{j=1}^{N_i} c_{x,j}}{N_i}. \quad (3.21)$$

In Eq. 3.21, $c_{x,j}$ is the x -component of the velocity of each individual simulator particle. If a gas mixture comprised of NS species is being considered, the x -component of the mixture average velocity is then calculated as

$$u = \frac{\sum_{i=1}^{NS} N_i M_i u_i}{\sum_{i=1}^{NS} N_i M_i}. \quad (3.22)$$

The remaining velocity components are calculated in a similar manner. The translational temperature is obtained in DSMC from the following:

$$T_{trans} = \left(\frac{N_s}{N_s - 1} \right) \frac{1}{3R_u N} \left\{ \sum_{i=1}^{NS} M_i N_i \left[\left(\frac{\sum_{j=1}^{N_i} c_{x,j}^2 + c_{y,j}^2 + c_{z,j}^2}{N_i} \right) - u_i^2 - v_i^2 - w_i^2 \right] \right\}. \quad (3.23)$$

In Eq. 3.23, R_u is the universal gas constant, N is the total number of particles in the cell, and N_s is the total number of samples, that is, the sum of all particles of all species taken over all sampling time steps. Roveda, *et al.* [62] proposed the coefficient $N_s/(N_s - 1)$ in order to combat the effect of a small number of DSMC samples artificially decreasing the translational temperature. This is a general result for correcting a variance calculated for a sample rather than an entire population, and is necessary because the DSMC method is only simulating a fraction of the real

molecules in a gas. The rotational temperature of molecular species is calculated in DSMC as

$$T_{rot} = \frac{\sum_{\substack{i=1 \\ i=mol.}}^{NS} M_i \left(\sum_{j=1}^{N_i} e_{rot,j} \right)}{R_u \sum_{\substack{i=1 \\ i=mol.}}^{NS} N_i}, \quad (3.24)$$

where e_{rot} is the mass specific rotational energy, and the summations include molecular species only. Similarly, the vibrational temperature is calculated as

$$T_{vib} = \left[\sum_{\substack{i=1 \\ i=mol.}}^{NS} \frac{N_i \theta_{vib,i}}{\ln \left(1 + \frac{\theta_{vib,i} R_i}{e_{vib,i}} \right)} \right] \left[\sum_{\substack{i=1 \\ i=mol.}}^{NS} N_i \right]^{-1}, \quad (3.25)$$

where the mass specific vibrational energy of species i is given by

$$e_{vib,i} = \frac{\sum_{j=1}^{N_i} e_{vib,j}}{N_i}. \quad (3.26)$$

As the hybrid solution evolves from the initial continuum solution, updated boundary conditions must be provided to the continuum domains after relatively few DSMC time steps. Macroscopic properties in the particle domains must also be used to periodically recalculate the continuum breakdown parameters so that the hybrid interfaces may be adjusted according to the most current flow field solution. In order to reduce the statistical scatter associated with the macroscopic averages of particle properties, the subrelaxation average proposed by Sun and Boyd [76] is employed. This subrelaxation average is calculated as

$$\overline{Q}_j = (1 - \theta) \overline{Q}_{j-1} + \theta Q_j. \quad (3.27)$$

In Eq. 3.27, Q_j is an instantaneous average over a computational cell at time step j , and \overline{Q}_{j-1} is the subrelaxation average at the previous time step. This latter quantity is initialized with the full CFD solution obtained with LeMANS. For simulations

presented here, θ is assigned a value of 0.001, which has been shown to effectively reduce the fluctuations in macroscopic fluid properties that must be passed from the particle domains to the continuum domains [65]. However, the subrelaxation average may be polluted by the same time history that reduces its statistical scatter. Because of this, \overline{Q}_j is corrected every $1/\theta$ time steps as follows:

$$\overline{Q}'_j = \overline{Q}_j + \frac{(1 - \theta)^{1/\theta}}{1 - (1 - \theta)^{1/\theta}} (\overline{Q}_j - \overline{Q}_{j-1/\theta}). \quad (3.28)$$

The subrelaxation average of mass density, directed velocity, translational temperature, and rotational temperature are calculated at every DSMC time step until the hybrid interfaces stop moving and a steady state is reached. Deschenes [19] demonstrated that use of the subrelaxation average to update the vibrational temperature leads to random walk errors that tend to amplify the statistical scatter in this quantity. The statistical scatter associated with the vibrational energy mode is already high relative to the translational and rotational energy modes because of the quantized nature of its probability distribution function. Therefore, the subrelaxation average must be calculated for the vibrational energy instead of the temperature.

It should be noted that whether transferring information from the continuum domains to the particle domains or *vice versa*, all state variables are specified without regard to the Mach number of the flow normal to the hybrid interface. This has the potential to cause problems when the interface is located in subsonic regions of the flow field by disallowing flow transients to exit the numerical domain. Hash and Hassan [36] noted such issues in their loosely-coupled hybrid simulations of an axisymmetric planetary probe. However, in their work, the most accurate results were eventually obtained when a blend of over-constrained and characteristic boundary conditions were used. These problems are not observed in results obtained using the MPC method, and this is believed to be due to the use of a flux vector splitting scheme in the continuum module. Since the direction in which characteristic information is

propagating is inherently considered in this scheme, as long as the properties in the CFD boundary cells are close to their correct values, specifying the full state should be a reasonable alternative to employing subsonic boundary conditions. As for the particle domains, the subrelaxation average tends to dampen any numerical oscillations that may result from specifying all boundary variables.

3.5 Hybrid Method Organization and Algorithm

Great importance has been placed on the modularity of the MPC hybrid method throughout its development. As the independent MONACO and LeMANS codes continue to be developed and maintained as state-of-the-art simulation tools, so do the DSMC and CFD modules of the MPC method, with the capabilities of the hybrid framework advancing in succession. The modular organization of the functions and data structures of the DSMC and CFD modules, and of the hybrid framework that serves to couple them in the MPC method, is illustrated in Fig. 3.5.

In the continuum module, computational mesh and solution information is stored in face, node, and cell data structures. The MPC method is initialized by a CFD solution and mesh that are imported in this manner. For each coarse, continuum cell, there is a corresponding hybrid data cell that stores additional information that is pertinent to the MPC method. This information includes the cell’s identity—whether it is in a (p)article or (c)ontinuum domain, if it is a boundary cell, or if it is a buffer cell—along with the refinement level of each cell dimension, which can be used to determine the number of particle cells in that continuum cell, and the indices of its constituent particle cells. In addition, macroscopic properties required for updating the subrelaxation average in each continuum cell is also stored in this data structure. Therefore, given any continuum cell, its hybrid data cell can be accessed for use in the MPC method.

Each particle cell has its own data structure in accordance with the MONACO

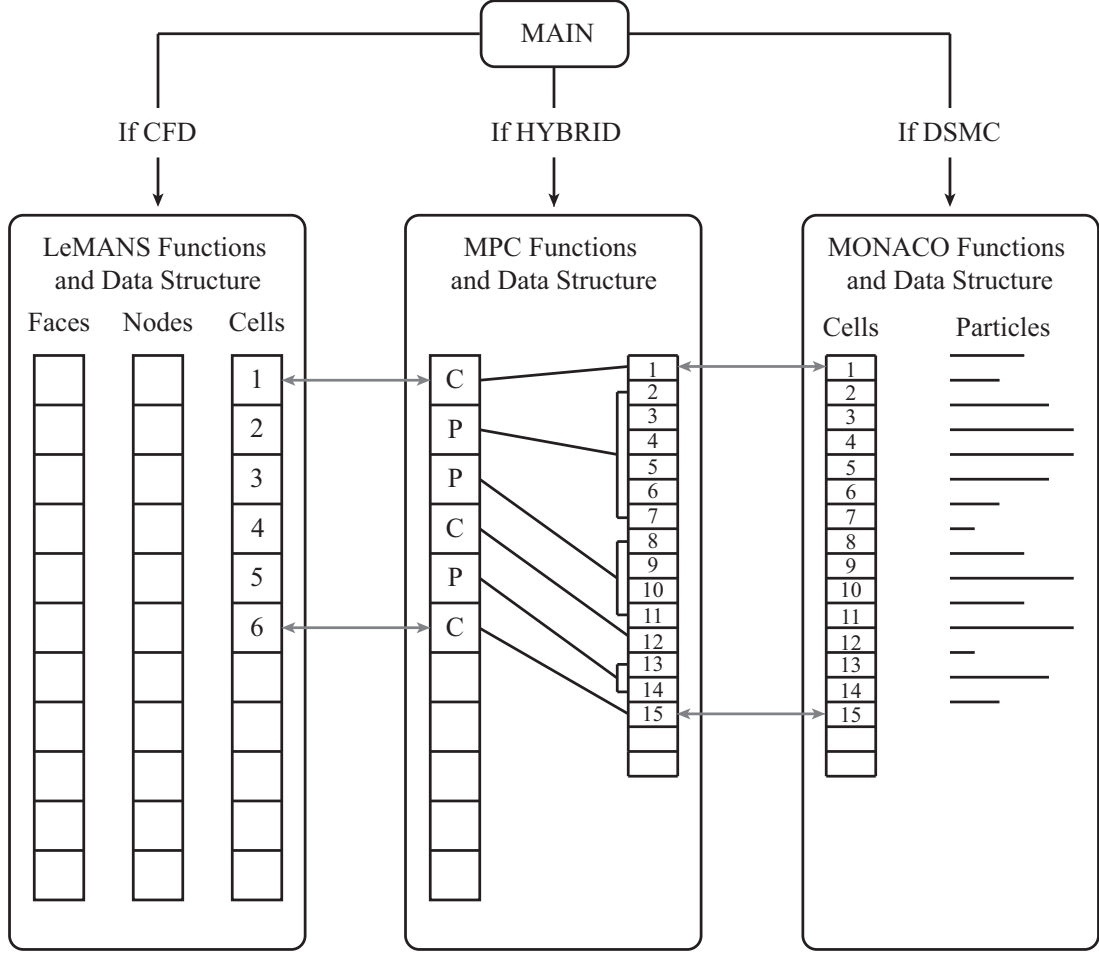


Figure 3.5: Modular organization of CFD, DSMC, and MPC hybrid functions and data structures [64].

code, which includes cell geometry, connectivity, and sampled particle information. The DSMC simulator particles located in each particle cell are organized by a linked list of pointers. A separate array outside of the particle cell data structure is used to identify the continuum cell to which a given particle cell belongs. In this way, whether the particle or continuum regions of the flow field are being updated, the hybrid data cell to which each computational cell corresponds is easily accessible.

A standard hybrid simulation using the MPC method proceeds as follows:

1. Obtain a grid-independent CFD solution of the flow field using LeMANS.
2. Calculate the continuum breakdown parameters, Br , based on the initial CFD

solution in each computational cell. If $Br \geq 0.05$, assign the cell to the particle domain; otherwise, assign the cell to the continuum domain.

3. Smooth hybrid domain interfaces, and extend particle regions an additional five cells in all directions. Assign buffer cells, DSMC boundary/reservoir cells, and CFD boundary cells.
4. Populate newly labeled particle cells with DSMC simulator particles consistent with the continuum solution. Allow these particles to move and collide for 1,010 time steps while updating the subrelaxation average at each time step. Note that this number of time steps must be greater than $1/\theta$ so that the old time history can be removed from the subrelaxation average before continuum breakdown parameters are recalculated.
5. Copy the subrelaxation average to the CFD data structure. Recalculate the continuum breakdown parameters based on the updated solution, and adjust the hybrid interfaces accordingly.
IF the continuum domains have not been updated yet, **AND** the relative number of DSMC cells changes by less than 1%, continue to Step 6.
ELSE IF the continuum domains have been updated **AND** the relative number of DSMC cells changes by less than 1%, skip to Step 7.
ELSE return to Step 4 for another update of the particle domains.
6. Update continuum domains with 400 iterations, using the most recent solution in CFD boundary cells. Recalculate the continuum breakdown parameters and adjust hybrid interfaces accordingly. Return to Step 4 .
7. Remove buffer cells and lock hybrid interfaces because the hybrid solution has reached a steady state.
8. Update particle domains while sampling particle information as in a standard

DSMC simulation, i.e. without using the subrelaxation average, for 10,000 time steps.

9. Copy the sampled particle information to the CFD data structure. Update continuum domains with 200 iterations. Note that the purpose of this step is to allow any statistical scatter previously introduced by the particle domains to leave the continuum domains.

IF the desired number of samples have been accrued in the particle domains, the simulation is finished.

ELSE return to Step 8 for additional sampling.

This automated hybrid algorithm differs slightly from that used previously by Deschenes [19] by requiring fewer user-defined parameters to influence the course of the simulation. For example, the hybrid interfaces are locked automatically after they stop moving upon recalculation of the continuum breakdown parameters, whereas this was previously dictated by the user. The number of implicit CFD iterations performed in each hybrid cycle continues to be a simulation input. This is because, in terms of efficiency, the number of processors requested for a hybrid simulation is usually better suited for the number of DSMC simulator particles rather than the number of CFD cells. As such, the time spent performing interprocessor communication begins to overrun the time spent actually updating the continuum domains, leading to each CFD iteration requiring more computational effort than each DSMC time step. Therefore, the efficiency of the MPC method can quickly diminish if too many CFD iterations are performed. By monitoring the L_2 norm during continuum domain updates, it can be seen that, in the cases presented here, a two order-of-magnitude reduction occurs within the first 400 iterations, but it usually takes many more iterations to achieve a further order-of-magnitude decrease. The number of CFD iterations performed during each hybrid cycle could very easily be automatically determined by tracking the L_2 norm, but with the numerical efficiency of the MPC

method being very sensitive to the total number of CFD iterations, this continues to be defined by the user.

3.6 Interim Conclusions

Recent efforts to improve the physical accuracy of the MPC hybrid method and extend its capabilities to more realistic atmospheric flows are described in the remaining chapters of this dissertation. Although the overall algorithm remains largely unchanged, to enable these improvements, a number of significant modifications have been made to the CFD and DSMC modules and the hybrid framework presented here. Where appropriate, these most recent developments will be discussed in detail, and evaluated against previous results.

CHAPTER IV

Consistent Modeling of Physical Processes

The accurate exchange of information across hybrid interfaces requires the use of consistent physical models in the particle and continuum domains of a hybrid simulation. Hybrid interfaces are placed in near-equilibrium regions of the flow field, where both CFD and DSMC are appropriate simulation methods. As such, it is imperative that the manner in which a physical process is modeled in the continuum module gives results that are consistent with the corresponding model in the particle module, and *vice versa*, along the hybrid interfaces. The use of consistent physical models helps to ensure accurate information exchange, so that any differences between results obtained using CFD, DSMC, and the MPC hybrid method are due to the limitations of the numerical approaches only.

In this chapter, models for simulating various physical processes in CFD and DSMC are discussed and verified to be consistent in near-equilibrium flows of both simple gases and mixtures of chemical species. As is evident from Chapter III, CFD and DSMC are two very different simulation techniques. Physically accurate models are employed when possible. However, the ability to simulate physical processes in a consistent manner and, therefore, obtain meaningful comparisons among hybrid, full DSMC, and full CFD results takes precedence.

4.1 Transport Properties

A gas that is in thermodynamic equilibrium exhibits no spatial or temporal variations in its macroscopic properties. This is an idealized view, however, as any flow field of practical interest will include a vehicle or disturbance that imposes gradients in the composition of the gas, its directed velocity, and/or temperature. On a microscopic level, molecules facilitate the transport of mass, momentum, and energy from one region of the flow field to another through their motion and collisions, leading to the macroscopic transport phenomena of diffusion, viscosity, and heat conduction. As described in Chapter II, closure of the Navier-Stokes equations requires the assumption of several constitutive relations involving these transport processes. Whereas the diffusivity, viscosity, and heat conduction are explicitly calculated in CFD simulations, molecular transport is an indirect result of collision models used in the DSMC method. This section describes the choice of macroscopic transport models and particle collision models used in CFD, DSMC, and MPC simulations of both simple gases and mixtures of chemical species.

4.1.1 Simple Gases

The Variable Hard Sphere (VHS) collision model proposed by Bird [8] is used in the full DSMC simulations and in the particle module of MPC hybrid simulations presented in this dissertation. Colliding particles are assumed to scatter isotropically, and unlike the hard sphere collision model, the VHS model allows the collision cross-section to vary with the translational temperature, T_{trans} , as follows:

$$\sigma_T = \sigma_{T,ref} \left(\frac{T_{ref}}{T_{trans}} \right)^{\omega-1/2}. \quad (4.1)$$

In Eq. 4.1, $\sigma_{T,ref}$ is a reference collision cross-section that is calculated at a reference translational temperature, T_{ref} . The temperature exponent, ω , is unique to each

collision class, and will be discussed extensively throughout this section. In practice, Eq. 4.1 is not explicitly calculated in a DSMC simulation; the collision cross-section is calculated as a function of the relative collision velocity, which, in turn, is a function of the translational temperature. The actual equation that is used to determine the collision cross-section of a particle pair will be presented later in this chapter. The collision cross-section can also be written in terms of the collision diameter, d , as

$$\sigma_T = \pi d^2. \quad (4.2)$$

Except at very low temperatures, the collision cross-sections of molecules that comprise a real gas decrease as the relative velocity between colliding molecules increases [8]. By allowing the collision cross-section to vary as shown in Eq. 4.1, the VHS model serves to reproduce the dependence of the macroscopic viscosity on the translational temperature. This power law relationship is given by

$$\mu = \mu_{ref} \left(\frac{T_{trans}}{T_{ref}} \right)^\omega, \quad (4.3)$$

where μ_{ref} is the viscosity at T_{ref} . In the case of simple gases, Eq. 4.3 is used to calculate the viscosity in the continuum module of the MPC method and in full CFD simulations, where the reference viscosity is calculated from

$$\mu_{ref} = \frac{15 (mk_B \pi T_{ref})^{1/2}}{2 (5 - 2\omega) (7 - 2\omega) \sigma_{T,ref}}. \quad (4.4)$$

In Eq. 4.4, m is the mass of each individual molecule, and k_B is the Boltzmann constant. The reference temperature in these equations can be chosen arbitrarily as long as a reference viscosity can be calculated with confidence at that temperature. For all collision classes simulated here, a reference temperature of $300K$ is chosen.

A physically accurate value for the ω parameter in the above equations can be obtained from the relationship between the viscosity collision integrals, $\Omega^{(2,2)}$, and the translational temperature. As will soon be shown, collision integrals provide the con-

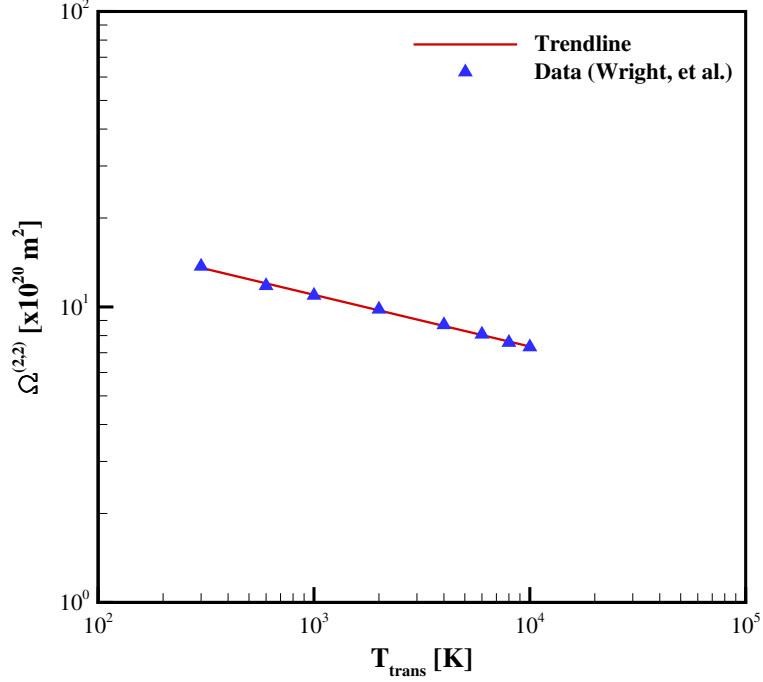


Figure 4.1: Viscosity collision integral dependence on translational temperature for N_2 .

nection between molecular collision dynamics and macroscopic transport properties. Collision integrals for a 13-species air mixture were compiled from various sources by Wright, *et al.* [90]. The errors associated with the collision integral data for the N_2 - N_2 collision class, which are used in several simple gas and gas mixture simulations in this dissertation, are estimated to be less than 10% for temperatures between 300K and 10,000K. A log-log plot of these data against translational temperature is shown in Fig. 4.1, and it is no coincidence that the trend follows a power law similar to Eq. 4.3. A first-order Chapman-Enskog approximation to the rigorous derivation of viscosity from kinetic theory is given by

$$\mu = \frac{5}{16} \sqrt{\frac{k_B T_{trans} m}{\pi}} \frac{1}{\Omega^{(2,2)}(T_{trans})}. \quad (4.5)$$

The derivation of Eq. 4.5 is given by Hirschfelder, *et al.* [37], but the viscosity collision integral notation used here is that of Wright, *et al.* [90]. If the power law

relationship from Eq. 4.3 is substituted into Eq. 4.5, close inspection reveals that the sum of ω for the N_2 - N_2 collision class and the slope of the trendline in Fig. 4.1 is equal to 0.5. This is true of all simple gases, so that a physically realistic ω is obtained directly from known viscosity collision integral data. The reference viscosity is then calculated using Eq. 4.5, and the reference collision cross-section is calculated using Eq. 4.4. These VHS model parameters are used in DSMC, CFD, and MPC simulations to ensure consistent calculation of viscosity, and are given for all collision classes relevant to this work in Appendix A.

As is the case with viscosity, there is no explicit calculation of heat conduction in the DSMC method. Energy is transferred within a gas, and between a gas and a surface, through molecular collisions. Full thermal accommodation is assumed in all DSMC simulations presented here. In CFD, the thermal conductivity for each energy mode is calculated from Eucken's relation [82] as

$$\kappa_{trans} = \frac{5}{2} \mu c_{v,trans}, \quad (4.6)$$

$$\kappa_{rot} = \mu c_{v,rot}, \quad (4.7)$$

and

$$\kappa_{vib} = \mu c_{v,vib}. \quad (4.8)$$

In Eqs. 4.6 through 4.8, $c_{v,trans}$, $c_{v,rot}$, and $c_{v,vib}$ are, respectively, the mass specific heats of the translational, rotational, and vibrational energies at constant volume.

4.1.2 Gas Mixtures

In the case of gas mixtures, the use of the VHS collision model in DSMC is not strictly correct. Although this model has been shown to reproduce the correct macroscopic viscosity coefficient, an additional scattering parameter that leads to the

Variable Soft Sphere (VSS) collision model [8] is required to accurately reproduce the diffusion coefficient in gas mixtures. The inclusion of this additional parameter increases the complexity of the matching procedure used to obtain consistent viscosity results in CFD and DSMC. Because this work represents an initial effort in extending the MPC method to include gas mixtures, results presented here are obtained using the VHS collision model rather than the VSS collision model. As will become clear in Chapter VII, at least for the gas mixtures examined in this dissertation, minimal diffusion effects are observed and are generally limited to the shock wave and boundary layer.

In CFD, a mass diffusion flux for each component species of a gas mixture is modeled using a modified form of Fick’s Law. An “effective” diffusion coefficient can be calculated for each species i as if species i were interacting with only one other imaginary species. This imaginary species represents an average of the remaining components of the gas mixture. An approximation for the effective diffusion coefficient of a given species i is given by Bird, *et al.* [9] as

$$\frac{1 - x_i}{D_{im}} = \sum_{j \neq i}^{NS} \frac{x_j}{\mathcal{D}_{ij}}, \quad (4.9)$$

and is used here. In Eq. 4.9, x_i is the mole fraction of species i , D_{im} is the effective diffusion coefficient of species i within the mixture of NS species, and \mathcal{D}_{ij} is the binary diffusion coefficient of the i - j species pair. This approximation and the diffusion flux calculation given in Eq. 2.23 were shown by Sutton and Gnoffo [77] to give accurate results for Earth re-entry simulations. The binary diffusion coefficient of the i - j species pair is obtained, to a first-order Chapman-Enskog approximation, from

$$\mathcal{D}_{ij} = \frac{k_B T_{trans}}{p \Delta_{ij}^{(1)}(T_{trans})}, \quad (4.10)$$

where p is the pressure and

$$\Delta_{ij}^{(1)}(T_{trans}) = \frac{8}{3} \sqrt{\frac{2M_i M_j \pi}{R_u T_{trans} (M_i + M_j)}} \Omega_{ij}^{(1,1)}(T_{trans}). \quad (4.11)$$

In Eq. 4.11, M_i and M_j are the molecular weights of species i and j , respectively, R_u is the universal gas constant, and $\Omega_{ij}^{(1,1)}(T_{trans})$ is the diffusion collision integral for the i - j collision class at T_{trans} .

The Gupta Mixing Rule [32], which was derived for weakly or nonionized flows, is used to approximate the viscosity and thermal conductivities of gas mixtures in CFD. This relatively simple formulation was shown by Palmer and Wright [57] to be both computationally efficient and physically accurate in the temperature range of interest relative to the mixture viscosity derived from a first-order Chapman-Enskog approximation. The Gupta Mixing Rule for mixture viscosity is given by

$$\mu = \sum_i^{NS} \frac{m_i x_i}{\sum_{j=1}^{NS} x_j \Delta_{ij}^{(2)}(T_{trans})}, \quad (4.12)$$

where

$$\Delta_{ij}^{(2)}(T_{trans}) = \frac{16}{5} \sqrt{\frac{2M_i M_j \pi}{R_u T_{trans} (M_i + M_j)}} \Omega_{ij}^{(2,2)}(T_{trans}). \quad (4.13)$$

The Gupta Mixing Rule reduces to Eq. 4.5 in the case of a simple gas, and similar to Eq. 4.11, Eq. 4.13 requires viscosity collision integral data for each collision class in the mixture. The VHS collision model is still used in the particle module of the MPC method and in full DSMC simulations of gas mixtures, and the model parameters for collision classes involving like molecules can be determined by following the procedure detailed for simple gases. However, the increased complexity of the Gupta Mixing Rule in CFD requires modification to the matching procedure for collision classes involving different species.

By inspection of Eqs. 4.12 and 4.13, it is clear that there is no longer a straightforward relationship between the VHS model parameter ω and the viscosity collision

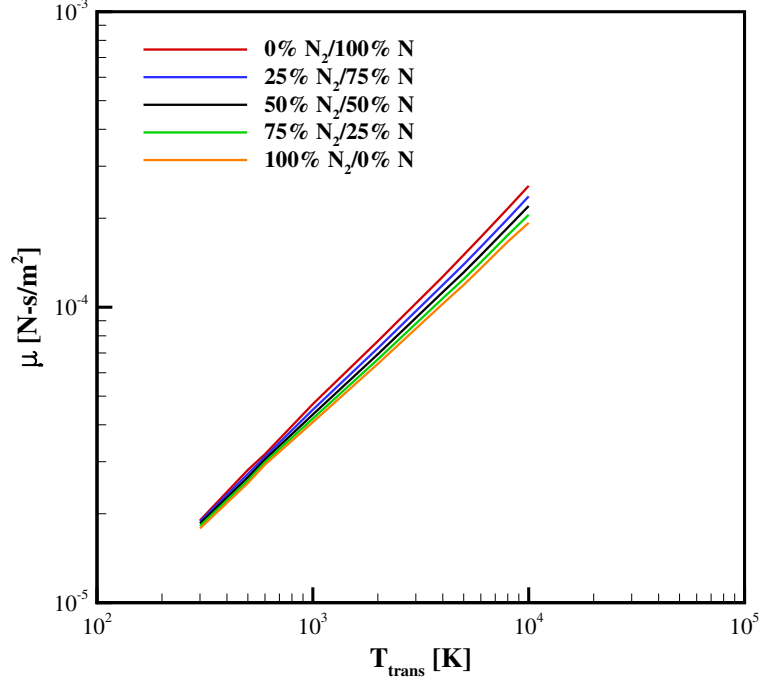


Figure 4.2: Variation of viscosity with N_2/N mixture composition.

integral data. To further illustrate, the viscosities of several mixtures of N_2 and N are plotted versus temperature in Fig. 4.2. Given the variation of line slope with mixture composition, the slope of the 50%/50% molar concentration is chosen to provide the ω value for the N_2 - N collision class that is required for any mixture of N_2 and N . With this ω value and a reference viscosity calculated from Eq. 4.12, the reference cross-section for the N_2 - N collision class is calculated by assuming an average particle mass for m in Eq. 4.4.

Because of the heuristic nature of this procedure, further verification is sought to ensure that these VHS model parameters produce viscosity results in DSMC that are consistent with those predicted by the Gupta Mixing Rule in CFD. For a 50% N_2 /50% N (by mole) mixture, DSMC is used to simulate a number of Couette flows at various temperatures in the range of interest for this work. In performing these DSMC simulations, the VHS model parameters are indirectly verified by comparing the “measured” viscosities to the corresponding viscosities calculated in CFD. The

shear stress of the gas in each of these Couette flow simulations is determined by collecting momentum data from the DSMC simulator particles that cross each horizontal cell face. The viscosity can then be deduced from this shear stress and the imposed velocity gradient.

In order to perform a true comparison of the viscosities obtained from these DSMC simulations, which inherently allow for velocity slip, and viscosities calculated using the Gupta Mixing Rule, a slight adjustment must be made. As illustrated by Vincenti and Kruger [82], the slope of the velocity profile in a Couette flow (dy/du) where velocity slip is ignored is smaller than that in a real gas. Therefore, following their suggested correction, the viscosities determined in these Couette flow simulations are related to the viscosities predicted by the Gupta Mixing Rule by

$$\mu_{CFD} \approx \mu_{DSMC} (1 + 2Kn_{\infty}). \quad (4.14)$$

As illustrated by one example in Fig. 4.3, the velocity profiles in these Couette flow simulations are nearly linear. In each simulation, the wall velocities are specified such that the Mach numbers of these flows are approximately 0.1. At such low Mach numbers, it is reasonable to assume that the temperature and density remain constant throughout the channel. Full momentum accommodation is assumed at the channel walls. In addition, the Knudsen number of each of these Couette flow simulations, as defined by the channel height, h , is maintained at a value of 0.01. In order to minimize nonequilibrium effects near the channel walls, it would be preferable to perform these simulations at a lower Knudsen number. However, the computational expense of these simulations is already quite large, and further increasing the density of the flow would make them unmanageable as a verification tool. Statistical errors are calculated in order to estimate the uncertainty associated with a finite number of particles and sampling time steps. Formulae for the velocity and shear stress errors are given by Sun and Boyd [76] and Hadjiconstantinou, *et al.* [34], and these uncertainties are

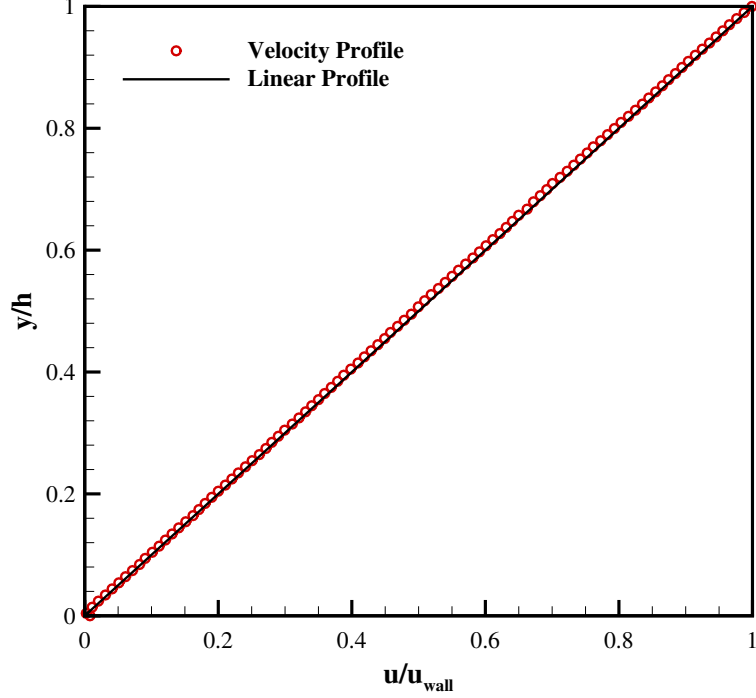


Figure 4.3: Velocity profile from a typical DSMC simulation of Couette flow.

then propagated throughout the calculation to yield an overall error associated with the DSMC viscosity. The results from this verification study are plotted in Fig. 4.4, where it is shown that this procedure for determining VHS model parameters yields viscosity results that are consistent with the Gupta Mixing Rule for this 50% N_2 /50% N mixture.

Although this simple approach to matching VHS model parameters in DSMC to the Gupta Mixing Rule in CFD is accurate for the 50% N_2 /50% N mixture, the same may not be true for other gas mixtures. For example, another gas composition that will be examined in the context of the MPC hybrid method is a mixture of 50% N_2 /50% H (by mole). Whereas molecular and atomic nitrogen have molecular weights that differ by a factor of two, the ratio of the molecular weight of N_2 to that of H is 28. A mixture of chemical species with such disparate molecular weights further tests the modifications made to the MPC method to accommodate gas mixtures, which will be described in Chapter VII.

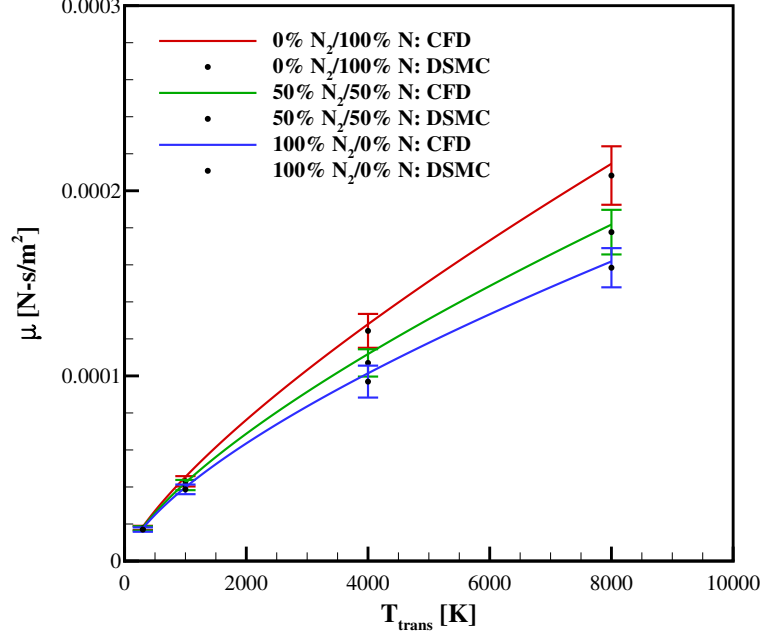


Figure 4.4: Comparisons of viscosities obtained using the Gupta Mixing Rule (CFD) and the VHS collision model (DSMC).

The first indication that this mixture may pose challenges for the simplified approach is a comparison between the Gupta Mixing Rule viscosities calculated for N_2 , H , and a 50% N_2 /50% H mixture. This comparison is plotted in Fig. 4.5. Unlike the 50% N_2 /50% N mixture viscosity, which is bounded by the viscosities of its constituents, the viscosity of the 50% N_2 /50% H mixture is very close to the viscosity of pure N_2 over the temperature range of interest. At higher temperatures, the viscosity of the mixture exceeds that of both N_2 and H . It is questionable whether the same assumptions that are made when deriving VHS model parameters for the N_2 - N collision class remain valid for the N_2 - H collision class. These suspicions are confirmed by performing simulations of Couette flows comprised of 50% N_2 /50% H using the VHS parameters obtained in the same way as described for the N_2 / N mixture. It should also be noted that the viscosity collision integral data for the N_2 - H and H - H collision classes do not follow the temperature power law relationship as closely as the viscosity collision integral data for the N_2 - N_2 , N_2 - N , and N - N collision classes. This leads to the slightly nonlinear behavior of the pure H and N_2 / H mixture viscosities

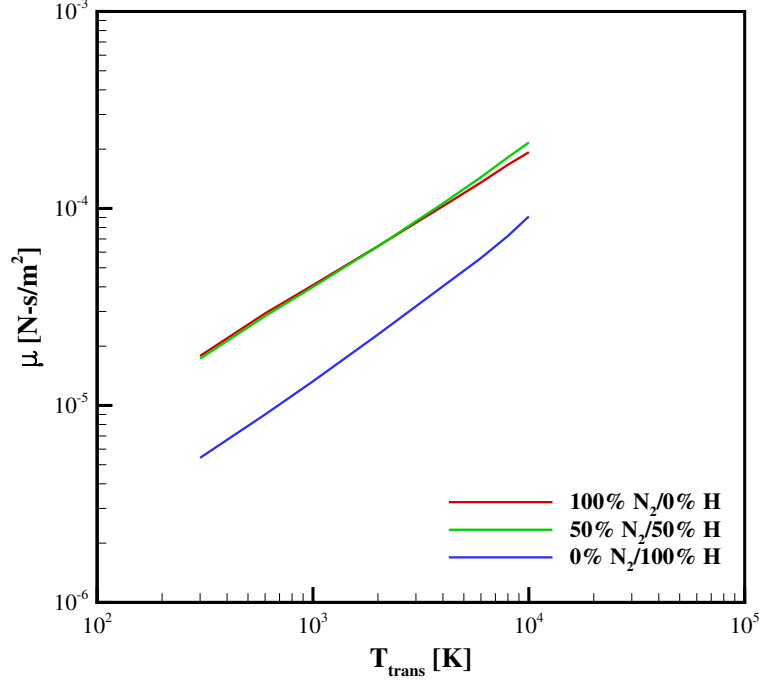


Figure 4.5: Variation of viscosity with N_2/H mixture composition.

plotted in Fig. 4.5. Despite this, Stallcop, *et al.* [70] claim that the viscosity collision integral data for the $H-H$ collision class are accurate to three or four significant figures. No numerical accuracy estimate is provided for the N_2-H viscosity collision integral data [71].

A more rigorous approach to calculating VHS model parameters that are consistent with the Gupta Mixing Rule is explored for the collision classes referenced in this work. Stephani, *et al.* [74] outlined such an approach by employing the Nelder-Mead simplex algorithm [54] to obtain VHS model parameters for a five-species air mixture. The Nelder-Mead simplex algorithm minimizes a given function of n variables by evaluating that function at $n + 1$ points in space, forming a simplex whose shape is then altered as new points are tested and the minimum is approached.

First, an equation that relates the viscosity collision integrals for each collision class to their corresponding VHS model parameters must be derived. The definition of the viscosity collision integral as given by Hirschfelder, *et al.* [37], but again re-cast

in the notation of Wright, *et al.* [90], is

$$\Omega^{(2,2)} = \frac{1}{2\pi} \int_0^\infty \left\{ \exp[-\gamma^2] \gamma^7 Q^{(2)}(g) \right\} d\gamma, \quad (4.15)$$

where

$$\gamma = \left[\frac{\frac{1}{2}m^*g^2}{k_B T_{trans}} \right]^{1/2} \quad (4.16)$$

and

$$Q^{(2)}(g) = 2\pi \int_0^\infty \left\{ [1 - \cos^2(\chi(g, b))] b \right\} db. \quad (4.17)$$

In the above equations, g is the relative collision velocity, and m^* is the reduced mass defined by

$$m_{ij}^* = \frac{m_i m_j}{m_i + m_j}. \quad (4.18)$$

Although the subscripts are omitted in Eq. 4.16, m^* is understood to be a collision-specific parameter. The parameter $Q^{(2)}$ is better known as the viscosity cross-section [8]. In Eq. 4.17, χ is the collision deflection angle and is, in general, a function of g and the impact parameter, b , which is the distance of closest approach of the centers of two colliding particles. However, in the case of the VHS collision model, this is greatly simplified to

$$Q^{(2)} = \frac{2}{3} \sigma_T. \quad (4.19)$$

The viscosity collision integrals are thus seen to be a function of various collision parameters through the relationship given in Eq. 4.15, but what is still needed is a link between these collision parameters and the reference diameter and ω temperature exponent specified in the VHS collision model. As previously mentioned, the VHS collision model is able to reproduce the macroscopic viscosity of a real gas by allowing the collision cross-sections of DSMC simulator particles to vary with the relative

collision velocity. The explicit relationship between the collision diameter of class i - j and the relative velocity between colliding particles is given as

$$d_{ij} = \left[d_{ref,ij}^2 \left(\frac{2k_B T_{ref}}{m^* g^2} \right)^{\omega_{ij}-1/2} \frac{1}{\Gamma(5/2 - \omega_{ij})} \right]^{1/2}. \quad (4.20)$$

A direct relationship between the viscosity collision integrals and VHS model parameters can now be derived by differentiating Eq. 4.16 with respect to g , substituting this result and Eq. 4.20 into Eq. 4.15, and integrating. Accounting for differences in notation, this result matches that derived by Stephani, *et al.* [74] and is as follows:

$$\Omega_{ij}^{(2,2)} = \frac{d_{ref,ij}^2}{6} \left(\frac{T_{ref}}{T_{trans}} \right)^{\omega_{ij}-1/2} \frac{\Gamma(9/2 - \omega_{ij})}{\Gamma(5/2 - \omega_{ij})}. \quad (4.21)$$

It is the objective of the Nelder-Mead simplex algorithm to find a minimum of a given function. Thus, the function to be minimized in order to find the optimal VHS model parameters is

$$f(d_{ref,ij}, \omega_{ij}) = \left| \left(\Omega_{ij}^{(2,2)} \right)_{analytical} - \left(\Omega_{ij}^{(2,2)} \right)_{observed} \right|, \quad (4.22)$$

where the *analytical* viscosity collision integral is that calculated using Eq. 4.21 and candidate values of $d_{ref,ij}$ and ω , and the *observed* viscosity collision integral is that obtained through observation, whether experimental or otherwise. In fact, viscosity collision integral data over the entire range of temperatures of interest in this work should be incorporated in the minimization. Therefore, the final function to be minimized is actually obtained by summing the values of Eq. 4.22 at every available data point in the temperature range of interest. This approach can be thought of as minimizing the distance between a vector comprised of the analytical viscosity collision integral data and a vector comprised of the observed data. Stephani, *et al.* [74] found that employing the actual mixture transport coefficients as elements in these vectors achieved more consistent results than when the collision integrals themselves were used. However, this results in the calculation of slightly different optimal VHS model

Table 4.1: Comparisons of d_{ref} [Å] obtained using the simple approach and the Nelder-Mead simplex algorithm.

Collision Class	Simple Approach	Nelder-Mead	Error
N_2-N_2	3.99	4.00	0.25%
$N-N$	3.36	3.35	0.30%
N_2-N	3.69	3.65	1.10%
$H-H$	3.35	3.44	2.62%
N_2-H	3.51	3.58	1.96%
O_2-O_2	3.85	3.76	2.39%
N_2-O_2	3.79	3.68	2.99%

parameters for each mixture composition. In reality, the binary collision interactions between gas molecules, and, in turn, the collision integrals, should be independent of macroscopic mixture composition.

The implementation of the Nelder-Mead simplex algorithm used in this work initializes $d_{ref,ij}$ to a random number between two and four angstroms, which should encompass a physically realizable range for the collision diameter, and initializes ω_{ij} to a random number between 0.5 (hard sphere molecule) and one (Maxwell molecule). The same results are repeatedly obtained after numerous calls to the simplex algorithm, indicating the final, optimized VHS model parameters are independent of their starting points. This also lends confidence to the assumption that the minimum found by the algorithm is global rather than local.

Table 4.1 compares the reference diameters calculated using the simple approach initially used for the N_2-N collision class, and those calculated using the more rigorous Nelder-Mead simplex algorithm. The relative errors between these results are also presented, indicating that even for the N_2-H collision class, the simple approach is quite accurate. Table 4.2 compares the ω temperature exponents calculated using each method, where the necessity of a rigorous approach such as the Nelder-Mead simplex algorithm is demonstrated by the large error associated with the N_2-H collision class. For all other collision classes, there is fairly close agreement between the temperature exponents obtained using the different approaches. In general, curve-fitting a linear

Table 4.2: Comparisons of ω obtained using the simple approach and the Nelder-Mead simplex algorithm.

Collision Class	Simple Approach	Nelder-Mead	Error
N_2-N_2	0.675	0.679	0.59%
$N-N$	0.746	0.737	1.22%
N_2-N	0.701	0.700	0.14%
$H-H$	0.801	0.799	0.25%
N_2-H	0.716	0.793	9.71%
O_2-O_2	0.683	0.677	0.89%
N_2-O_2	0.690	0.713	3.23%

trendline to the viscosity collision integral data plotted on a logarithmic scale is found to be quite sensitive to scatter and the data points that are included.

As a result of these comparisons, both the temperature exponent and the reference diameter as calculated with the Nelder-Mead simplex algorithm for the N_2-H collision class are used here. The VHS model parameters for the remaining collision classes are those calculated using the simple approach. The VHS model parameters for all collision classes simulated in this dissertation are given in Appendix A. In addition, since the simple approach agrees with the Nelder-Mead simplex algorithm for the N_2-N_2 , N_2-N , and $N-N$ collision classes, and mixtures involving these VHS model parameters are verified to be consistent with the Gupta Mixing Rule through DSMC simulations of Couette flows, it is assumed the same is true for the remaining collision classes. This is a reasonable assumption, and obviates the need to perform additional costly Couette flow simulations.

The Gupta Mixing Rule is also used to approximate the thermal conductivity of each energy mode of a gas mixture. Palmer and Wright [56] compared several methods for calculating mixture thermal conductivities and found that the Gupta Mixing Rule was both computationally efficient and physically accurate relative to both first- and second-order approximate solutions of the Boltzmann equation. The mixture thermal conductivity of the translational energy mode is given by

$$\kappa_{trans} = \frac{15}{4} k_B \sum_{i=1}^{NS} \frac{x_i}{\sum_{j=1}^{NS} \alpha_{ij} x_j \Delta_{ij}^{(2)} (T_{trans})}, \quad (4.23)$$

where

$$\alpha_{ij} = 1 + \frac{\left(1 - \frac{M_i}{M_j}\right) \left(0.45 - 2.54 \frac{M_i}{M_j}\right)}{\left(1 + \frac{M_i}{M_j}\right)^2}, \quad (4.24)$$

and $\Delta_{ij}^{(2)}$ is again calculated as in Eq. 4.13. The mixture thermal conductivities for the rotational and vibrational energy modes are calculated as

$$\kappa_{rot} = k_B \sum_{i=1}^{NS} \frac{x_i}{\sum_{j=1}^{NS} x_j \Delta_{ij}^{(1)} (T_{trans})}, \quad (4.25)$$

and

$$\kappa_{vib} = \frac{k_B}{R_u} \sum_{i=1}^{NS} \frac{(c_{v,vib})_i M_i x_i}{\sum_{j=1}^{NS} x_j \Delta_{ij}^{(1)} (T_{trans})}. \quad (4.26)$$

4.2 Thermal Nonequilibrium

As described in Chapter I, due to the small residence times of a hypersonic flow relative to a vehicle or phenomenon of interest, accurate simulation may require consideration of the finite rates at which thermal relaxation occurs. For instance, consider a strong shock wave caused by a hypersonic vehicle. After passing through the shock, the kinetic energy once possessed by the gas is converted into random thermal energy, leading to a high post-shock translational temperature. Subsequent collisions between gas molecules then enable distribution of this energy among the internal energy modes until thermal equilibrium is reached. However, this relaxation process requires a finite amount of time, during which other temperature-dependent processes may occur, such as chemical reactions. Therefore, as the physics of a hypersonic flow

field increase in complexity, the importance of accurately simulating thermal relaxation also increases. In this section, the CFD and DSMC models used to simulate the exchange of energy between the translational and internal energy modes are discussed.

4.2.1 Translational-Rotational Energy Exchange

Translational-rotational energy exchange models have been investigated for simple gases in the context of the MPC hybrid method by Deschenes, *et al.* [22]. However, more detailed comparisons have led to the current choice of translational-rotational energy exchange models not only for simple gases, but also for mixtures of chemical species. Rotational nonequilibrium is simulated in CFD by solving a rotational energy conservation equation in addition to the standard set of Navier-Stokes equations. Energy transfer between the translational and rotational energy modes is usually modeled using Jeans' equation [42] given by

$$\frac{dE_{rot}}{dt} = \frac{E_{rot}^* - E_{rot}}{Z_{rot}\tau_c}. \quad (4.27)$$

In Eq. 4.27, E_{rot}^* is the energy of the rotational mode if it were in equilibrium with the translational mode, E_{rot} is the instantaneous rotational energy, and Z_{rot} is the rotational collision number. The denominator of the righthand side of this equation is equivalent to the characteristic relaxation time of the rotational energy mode, τ_{rot} . Jeans' equation can be rewritten in terms of the translational and rotational temperatures to yield the following source term for a gas comprised of NS species, to be used in the rotational energy conservation equation:

$$S_{trans-rot} = \sum_{i=1}^{NS} \rho_i (c_{v,rot})_i \frac{T_{trans} - T_{rot}}{Z_{rot,i}\tau_{c,i}}. \quad (4.28)$$

The continuum module of the MPC method and full CFD simulations employ Parker's model [59] to calculate the rotational collision number for use in Eq. 4.28. In this model, the rotational collision number is assumed to be a function of the

translational temperature only, and is calculated as

$$Z_{rot} = \frac{(Z_{rot})_{\infty}}{1 + \frac{\pi^{3/2}}{2} \left(\frac{T^*}{T_{trans}} \right)^{1/2} + \left(\frac{\pi^2}{4} + \pi \right) \frac{T^*}{T_{trans}}}, \quad (4.29)$$

where $(Z_{rot})_{\infty}$ and T^* are species-specific constants. The values used for the molecular species simulated in this dissertation are given in Appendix A.

Prior to discussing the use of a consistent translational-rotational energy exchange model in DSMC, an important distinction must be made between the rotational collision number defined in the context of continuum methods and the rotational collision number defined in the context of particle methods. Whereas Z_{rot} is defined as described above for continuum methods, i.e.

$$Z_{rot}^{cont} = \frac{\tau_{rot}}{\tau_c}, \quad (4.30)$$

the rotational collision number has a slightly different interpretation in DSMC. In the Borgnakke-Larsen internal energy exchange model [10] used in DSMC, colliding simulator particles are chosen to undergo a translational-rotational energy exchange event with average probability $\langle \phi_{rot} \rangle$. Intuitively, Eq. 4.30 suggests that, on average, Z_{rot}^{cont} collisions are required prior to a given particle being selected to relax and, therefore, $\langle \phi_{rot} \rangle$ should be the reciprocal of Z_{rot}^{cont} . However, due to the inefficiency of the equilibration process achieved by the Borgnakke-Larsen internal energy exchange model, $\langle \phi_{rot} \rangle$ must be greater than $1/Z_{rot}^{cont}$ to ensure that the actual fraction of particles that experiences a relaxation event is $1/Z_{rot}^{cont}$ [33]. The relationship between the probability and the fraction of particles that undergoes internal energy relaxation is also dependent on the selection methodology, as will become apparent.

Lumpkin, *et al.* [48] recognized this discrepancy and derived the following conversion factor, where ζ_{rot} is the number of rotational degrees of freedom:

$$Z_{rot,ij}^{part} = \frac{1}{\langle \phi_{rot,ij} \rangle} = Z_{rot,i}^{cont} \left(1 + \frac{\zeta_{rot,i} + \zeta_{rot,j}}{5 - 2\omega_{ij}} \right)^{-1}. \quad (4.31)$$

This conversion factor is valid for relating $Z_{rot,i}^{cont}$ to the probability used in a *pair* selection procedure, where *both* colliding particles are chosen to either undergo internal energy relaxation or experience an elastic collision. This is the type of selection methodology originally implemented in MONACO. Haas, *et al.* [33] derived a different conversion factor to be used in DSMC codes in which the probability of a rotationally inelastic collision is used to either accept or reject each particle *individually*. This latter particle selection methodology enables different molecular species in a gas mixture to relax at different rates. If the pair selection procedure were used to simulate the rotational relaxation of a mixture of N_2 and O_2 , for example, the question would arise as to which Z_{rot}^{cont} should be used in Eq. 4.31, since both particles will exchange rotational energy with the translational energy mode. The particle selection procedure that is implemented in MONACO to allow for constituent species in a gas mixture to relax independently of one another is discussed later in this section.

In order to achieve consistency with Parker’s model in CFD, Boyd proposed a variable probability rotational relaxation model [12] to be used in DSMC simulations. This particular model was derived by assuming that the instantaneous probability of a simulator particle undergoing a translational-rotational energy exchange event due to a collision is a function of the relative translational energy of the colliding pair, E_{rel} . Given that Parker’s model relates the rotational collision number to the translational temperature only, this is a reasonable assumption. A DSMC model that is consistent with Parker’s model must, on average, reproduce the same Z_{rot}^{cont} given by Eq. 4.29 under equilibrium conditions. In mathematical terms, and assuming perfect efficiency for the Borgnakke-Larsen internal energy exchange model, the following relationship must hold:

$$\langle \phi_{rot} \rangle = \frac{1}{Z_{rot}^{cont}} = \frac{1}{\Gamma(5/2 - \omega)} \left[\frac{1}{k_B T_{trans}} \right]^{5/2 - \omega} \int_0^\infty \left\{ \phi_{rot} E_{rel}^{3/2 - \omega} \exp \left[\frac{-E_{rel}}{k_B T_{trans}} \right] \right\} dE_{rel}. \quad (4.32)$$

In the interest of clarity, a simple gas has been considered and the collision-class subscripts removed. Since the instantaneous probability of translational-rotational energy exchange, ϕ_{rot} , is assumed to be a function of the relative translational energy of the colliding pair, it is part of the integrand on the righthand side of Eq. 4.32. By integrating over the equilibrium distribution function for relative translational energy, as biased by the collision selection process in DSMC, an average probability $\langle \phi_{rot} \rangle$ under equilibrium conditions is obtained. If Z_{rot}^{cont} as defined in Eq. 4.29 is then substituted into Eq. 4.32, the instantaneous probability is given by

$$\phi_{rot} = \frac{1}{(Z_{rot})_\infty} \times \left[1 + \frac{\Gamma(\frac{1}{2}\zeta)}{\Gamma(\frac{1}{2}\zeta - \frac{1}{2})} \left(\frac{k_B T^*}{E_{rel}} \right)^{1/2} \frac{\pi^{3/2}}{2} + \frac{\Gamma(\frac{1}{2}\zeta)}{\Gamma(\frac{1}{2}\zeta - 1)} \frac{k_B T^*}{E_{rel}} \left(\frac{\pi^2}{4} + \pi \right) \right]. \quad (4.33)$$

In Eq. 4.33, ζ is the number of degrees of freedom corresponding to the relative translational energy, as biased by the collision selection process, which is equal to $5 - 2\omega$ in this formulation. However, because the probability of internal energy relaxation is *not* equivalent to the fraction of particles that must relax, Eq. 4.33 must include the aforementioned conversion factor. The final form of the instantaneous probability of translational-rotational energy exchange to be used in DSMC simulations in order to be consistent with Parker's model in CFD is then calculated as

$$\phi_{rot,ij} = \left(1 + \frac{\zeta_{rot,i} + \zeta_{rot,j}}{5 - 2\omega_{ij}}\right) \frac{1}{(Z_{rot})_{\infty}} \times \left[1 + \frac{\Gamma\left(\frac{1}{2}\zeta\right)}{\Gamma\left(\frac{1}{2}\zeta - \frac{1}{2}\right)} \left(\frac{k_B T^*}{E_{rel}}\right)^{1/2} \frac{\pi^{3/2}}{2} + \frac{\Gamma\left(\frac{1}{2}\zeta\right)}{\Gamma\left(\frac{1}{2}\zeta - 1\right)} \frac{k_B T^*}{E_{rel}} \left(\frac{\pi^2}{4} + \pi\right)\right]. \quad (4.34)$$

This equation is written in terms of a general gas mixture where a particle of species i and a particle of species j may undergo rotational energy relaxation upon colliding with one another. With the appropriate subscripts, this same equation is used to calculate the translational-rotational energy exchange probabilities of all collision pairs in a gas mixture.

The drawback of Boyd's DSMC model is that equipartition of energy is not inherently maintained because of the preferential acceptance of collision pairs with lower relative translational energies to undergo rotational-translational energy exchange. Since this preferential treatment does not include the rotational energy mode, the Borgnakke-Larsen internal energy exchange model [10] tends to redistribute more of the energy to the translational mode than is appropriate to maintain equipartition of energy. Thus, the cell-based average of these instantaneous probabilities, calculated for each collision class from all pairs regardless of actual translational-rotational energy exchange, must be used.

This averaging procedure is not necessary if the instantaneous probabilities are assumed to be functions of the total collision energy of the particle pair. Boyd, therefore, proposed an alternative translational-rotational energy exchange model, the derivation of which is quite similar to the previous with the exception that the equilibrium distribution function for the total collision energy is used instead of that for the relative translational energy in Eq. 4.32 [11]. The instantaneous probability defined in this way has the same form as Eq. 4.34 except E_{rel} is replaced by E_{coll} , i.e. the sum of the relative translational energy of the colliding pair and the rotational

energies of both particles, and ζ is now $5 - 2\omega_{ij} + \zeta_{rot,i} + \zeta_{rot,j}$.

The latter of these DSMC models was successfully used in past MPC simulations of simple gases exhibiting rotational nonequilibrium [22]. In the interest of being thorough, isothermal heat bath simulations of N_2 are again performed to verify consistency of this DSMC model and Parker’s model in CFD. It is important to note that in the DSMC heat bath simulations, the particle velocities are re-sampled from a Maxwellian VDF at the beginning of each time step. This additional consideration enables a better approximation of the continuous VDF by a finite number of simulator particles and, in turn, yields a constant translational temperature of $10,000K$ throughout the simulation. The rotational temperature is initialized to $1,000K$, and particle collisions enable the eventual equilibration of the rotational energy mode at a rate dictated by the translational-rotational energy exchange model. Excitation of the vibrational energy mode is neglected in these heat bath simulations. Figure 4.6 shows a comparison of the rotational temperature relaxation process predicted by Parker’s model in CFD and that predicted by Boyd’s $\phi_{rot}(E_{coll})$ model in DSMC. The greatest difference between these two profiles is approximately $207K$, or 3.2% of the CFD rotational temperature *at that time* of $6,429K$. This is sizable considering the simplicity of the current simulation relative to simulations of interest, which include mixtures of chemical species in rotational and vibrational nonequilibrium.

This discrepancy is further investigated by comparing the profiles of the rotational collision numbers used in each of the isothermal heat bath simulations. These results are plotted in Fig. 4.7. Because this particular DSMC model assumes that the probability of translational-rotational energy exchange is a function of the total collision energy of the particle pair, there is a degree of ambiguity in the choice of an appropriate average temperature to be used in Parker’s model. Three logical approaches to incorporate both the translational and rotational temperatures in an average temperature to be used in Eq. 4.29 are explored. The first, which is given by

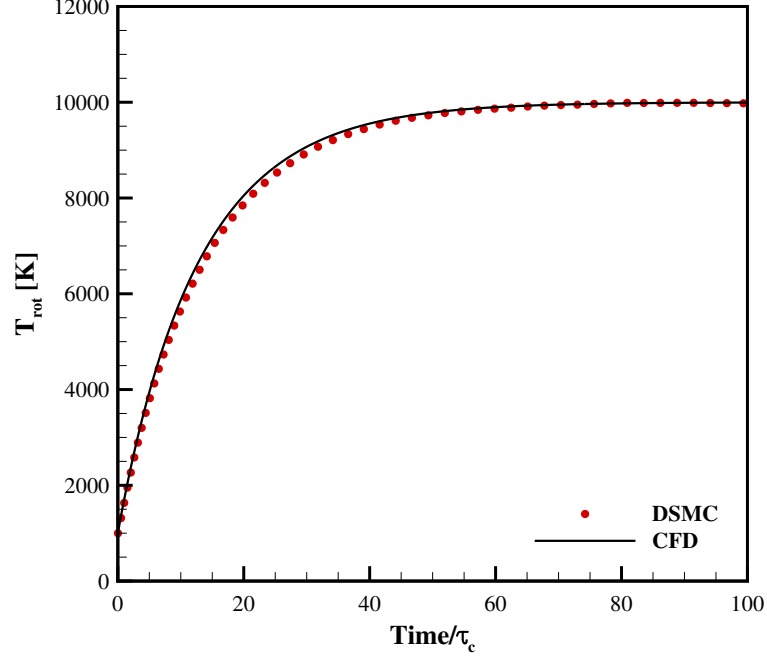


Figure 4.6: Rotational temperature relaxation of N_2 as predicted by CFD and DSMC, with $\phi_{rot}(E_{coll})$.

$$T_{ave,1} = \frac{(5 - 2\omega_{ij}) T_{trans} + 2T_{rot}}{7 - 2\omega_{ij}}, \quad (4.35)$$

is a weighted average based on the degrees of freedom of the relative translational energy and the average number of rotational degrees of freedom between the colliding pair. The second approach is similar, but the weight of the rotational temperature is based on the total number of degrees of freedom in the rotational energy mode. This average temperature is calculated as

$$T_{ave,2} = \frac{(5 - 2\omega_{ij}) T_{trans} + 4T_{rot}}{9 - 2\omega_{ij}}. \quad (4.36)$$

A final approach to calculate a relevant average temperature is given by

$$T_{ave,3} = \frac{3T_{trans} + 2T_{rot}}{5}, \quad (4.37)$$

where the degrees of freedom in the translational energy mode are no longer biased by the collision selection process in DSMC. The results of each of these approaches

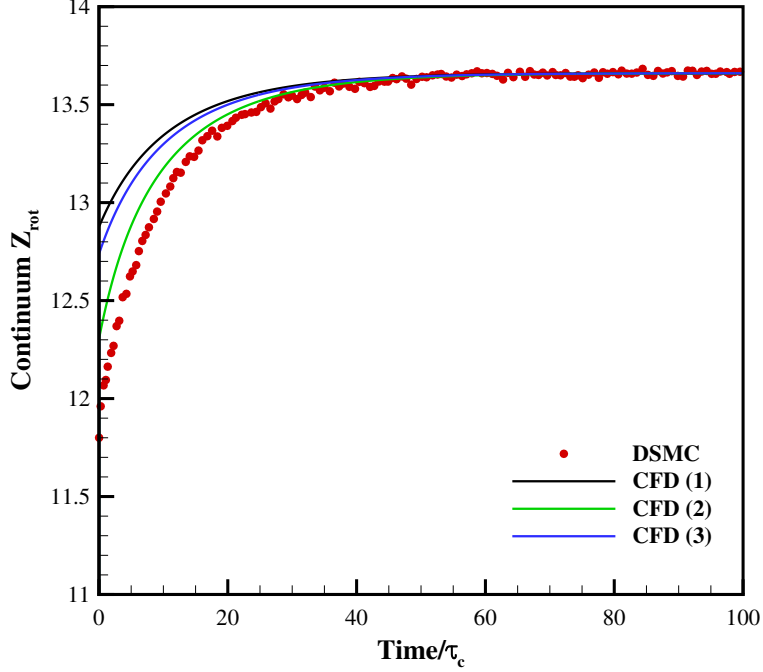


Figure 4.7: Rotational collision number profiles of N_2 as predicted by CFD and DSMC, with $\phi_{rot}(E_{coll})$.

are labeled as **CFD (1)**, **CFD (2)**, and **CFD (3)**, respectively, in Fig. 4.7.

As is evident, the rotational collision number profiles predicted by Parker’s model in CFD and Boyd’s $\phi_{rot}(E_{coll})$ model in DSMC cannot be brought into agreement, even for a simple gas. None of the proposed average temperatures are found to be capable of replicating the complex relationship between the total collision energy and rotational collision number exhibited by Boyd’s $\phi_{rot}(E_{coll})$ model. The use of different average temperatures yields a negligible effect on the rotational temperature relaxation process, which is why there is only one CFD profile shown in Fig. 4.6.

Because one of the aims of the current work is to advance the capability of the MPC hybrid method to include mixtures of chemical species, isothermal heat bath simulations of 50% N_2 /50% N (by mole) are also performed. For the sake of clarity, the characteristic rotational relaxation time of species i , which results from that species’ molecules undergoing relaxation events with all other atoms and molecules in the mixture, is calculated as

$$\tau_{rot,i} = \left[\sum_{j=1}^{NS} \frac{\nu_{ij}}{Z_{rot,ij}} \right]^{-1}, \quad (4.38)$$

where ν_{ij} is the collision rate between particles of species i and particles of species j . Note that in Eq. 4.38, the possibility of having Z_{rot} vary with different collision partners has been included for generality. This definition is derived directly from writing Eq. 4.27 for each species in a mixture:

$$\frac{dE_{rot,i}}{dt} = \frac{E_{rot,i}^* - E_{rot,i}}{\tau_{rot,i}} = \rho_i (c_{v,rot})_i (T_{trans} - T_{rot}) \sum_{j=1}^{NS} \frac{1}{Z_{rot,ij} \tau_{c,ij}}. \quad (4.39)$$

The mixture average rotational relaxation time can then be given by

$$\tau_{rot} = \frac{\sum_{\substack{i=1 \\ i=mol.}}^{NS} x_i}{\sum_{\substack{i=1 \\ i=mol.}}^{NS} x_i / \tau_{rot,i}}, \quad (4.40)$$

which is of the same form suggested by Gnoffo, *et al.* [29] for the vibrational energy mode. Only polyatomic species are included in the summations in Eq. 4.40. The mixture average rotational collision number is then calculated by dividing this overall rotational relaxation time by the mean collision time of polyatomic species only. Thus, the collision numbers that are plotted in the following figures showing the rotational relaxation process of a gas mixture are calculated as

$$Z_{rot} = \frac{\sum_{\substack{i=1 \\ i=mol.}}^{NS} x_i / \tau_{c,i}}{\sum_{\substack{i=1 \\ i=mol.}}^{NS} x_i / \tau_{rot,i}}. \quad (4.41)$$

In Fig. 4.8, the rotational temperature relaxation predicted by Parker's model is compared to that predicted by Boyd's $\phi_{rot}(E_{coll})$ model for a mixture of 50% N_2 /50% N (by mole). In the simple gas case, the use of an average temperature in Parker's model based on the degrees of freedom of the relative translational energy and the

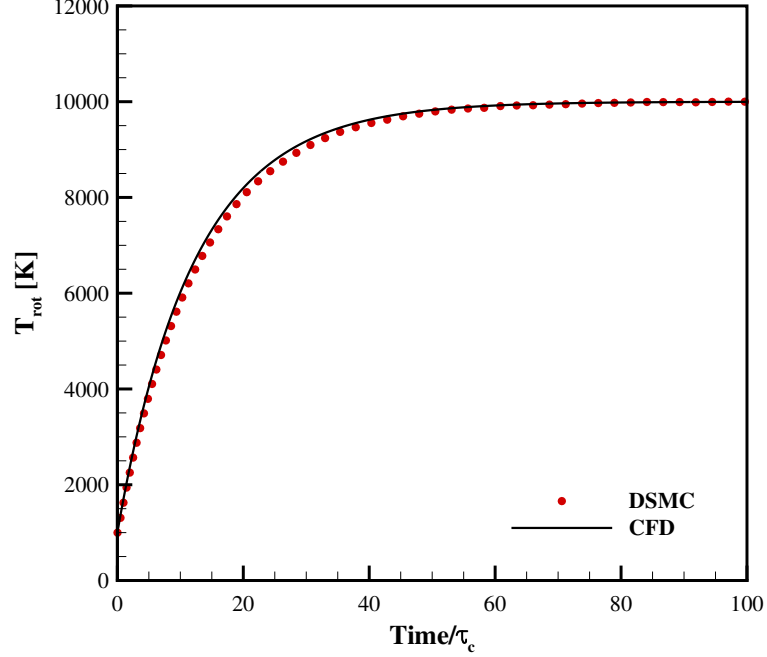


Figure 4.8: Rotational temperature relaxation of 50% N_2 /50% N as predicted by CFD and DSMC, using $\phi_{rot}(E_{coll})$.

total number of rotational degrees of freedom yields the best agreement with DSMC. Therefore, Eq. 4.36 is used to calculate the relevant temperature for N_2 - N_2 collisions, and Eq. 4.35 is used to calculate the relevant temperature for N_2 - N collisions. The maximum error is approximately $207K$, or 3.7% of the rotational temperature at that time ($5,534K$), so the level of agreement between CFD and DSMC that was seen in the simple gas is maintained for the gas mixture. Again, large errors in the rotational collision number profiles are exhibited, as seen in Fig. 4.9.

With the objective of reducing these errors, Boyd's original model, which assumes that the probability of translational-rotational energy exchange is a function of the relative translational energy only, is revisited. Again, isothermal heat bath simulations of N_2 are performed in order to verify consistency with Parker's model in CFD. The rotational temperature relaxation processes are shown in Fig. 4.10, along with the theoretical result as found by integrating Eq. 4.27. In this case, the maximum error has been reduced to approximately $29K$, or 2.6% of the CFD rotational tem-

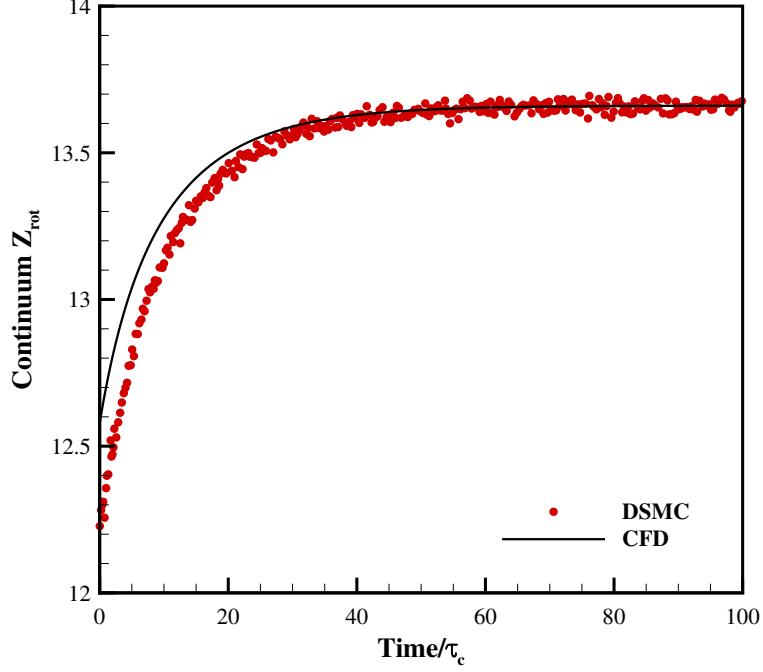


Figure 4.9: Rotational collision number profiles of 50% N_2 /50% N as predicted by CFD and DSMC, using $\phi_{rot}(E_{coll})$.

perature at that time (1,108K). In addition, the rotational collision number profiles predicted by DSMC and CFD are in much better agreement, as shown in Fig. 4.11, because the relevant temperature in Parker's model is the translational temperature.

In order to verify that this level of agreement is maintained for mixtures of chemical species, isothermal heat bath simulations of 50% N_2 /50% N (by mole) are also performed. Comparisons of Parker's model in CFD and Boyd's $\phi_{rot}(E_{rel})$ model in DSMC are shown in terms of the rotational temperature and collision number in Figs. 4.12 and 4.13, respectively. Again, the theoretical rotational temperature relaxation process according to Eq. 4.27 is plotted alongside the CFD and DSMC results, and all are in excellent agreement. The maximum error between the CFD and DSMC results in this case is approximately 33K, which is 0.4% of the CFD rotational temperature at that time (9,340K).

Because of the improved consistency achieved in these latter results, all subsequent hybrid simulations in which rotational nonequilibrium effects are present employ

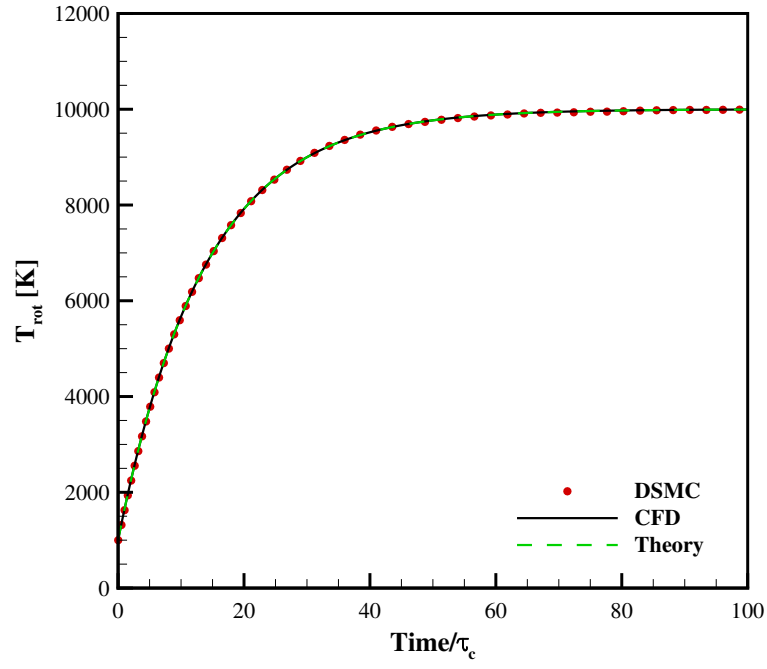


Figure 4.10: Rotational temperature relaxation of N_2 as predicted by CFD and DSMC, using $\phi_{\text{rot}}(E_{\text{rel}})$.

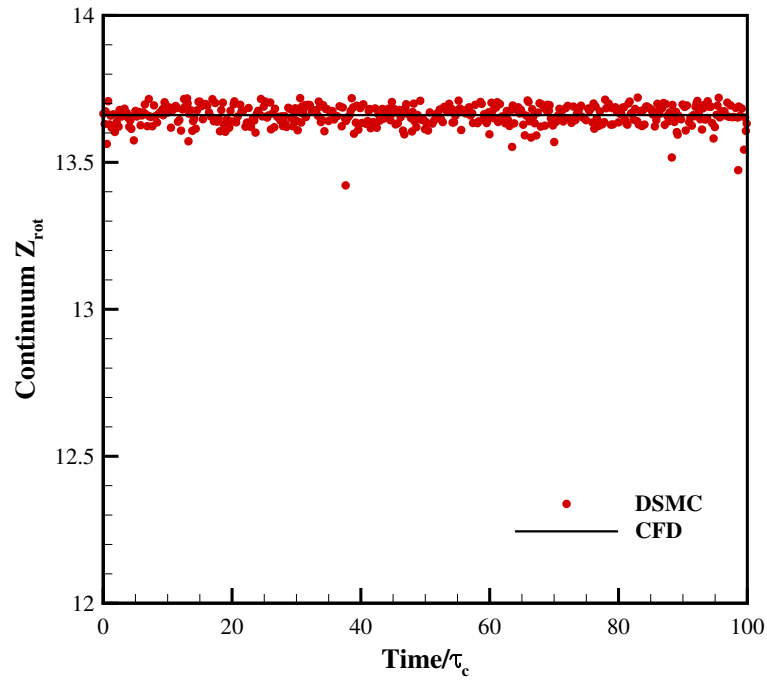


Figure 4.11: Rotational collision number profiles of N_2 as predicted by CFD and DSMC, using $\phi_{\text{rot}}(E_{\text{rel}})$.

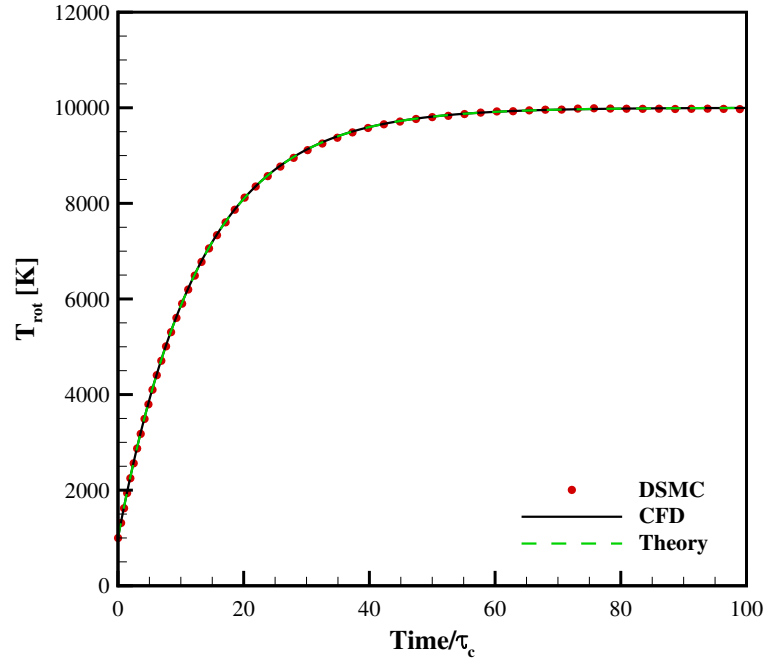


Figure 4.12: Rotational temperature relaxation of 50% N_2 /50% N as predicted by CFD and DSMC, using $\phi_{rot}(E_{rel})$.

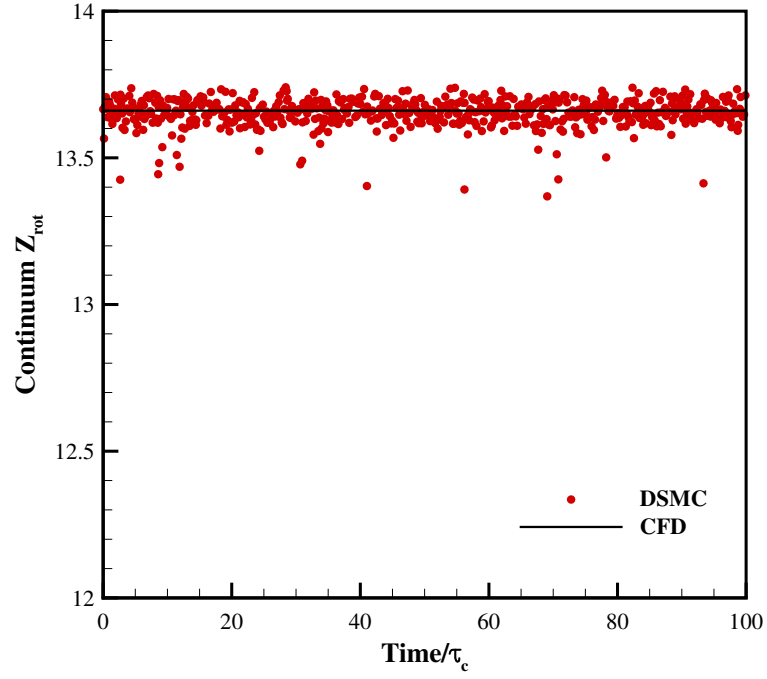


Figure 4.13: Rotational collision number profiles of 50% N_2 /50% N as predicted by CFD and DSMC, using $\phi_{rot}(E_{rel})$.

Boyd’s model in particle domains, where the probability of rotational-translational energy exchange is assumed to be a function of the relative translational energy only. Such a model will provide better agreement with CFD at the hybrid interfaces in terms of the macroscopic rotational temperature *and* rotational collision number, and will alleviate concerns about inconsistency between the translational-rotational energy exchange models. This is important not only in its own right, but also when moving forward to flows with more complex physics in the future.

In order to simulate general gas mixtures in which several species may be in rotational nonequilibrium and equilibrate at different rates, the particle selection procedure proposed by Zhang and Schwartzentruber [92] is implemented in MONACO. This procedure is equivalent to that proposed by Haas, *et al.* [33], but is simpler to implement and is more recognizable as playing the same role for the particle selection methodology that Eq. 4.31 plays for the pair selection methodology. As detailed in Ref. [92], each individual particle in a collision pair is sequentially examined to determine whether or not a translational-rotational energy exchange event occurs. Both particles have an equal probability of being examined first, which is important because double relaxation is prohibited. In other words, if the first particle is determined to undergo rotational energy relaxation, then the second particle is not even considered. The first particle is accepted to relax with probability given by

$$\phi_{rot,1} = \frac{1}{Z_{rot,1}^{cont}} \left(1 + \frac{\zeta_{rot,1}}{5 - 2\omega_{12}} \right). \quad (4.42)$$

Similarities between Eq. 4.31 and Eq. 4.42 are evident. In the case of Eq. 4.42, however, the subscripts correspond to the first and second particles in a colliding pair rather than the species numbers. Using the acceptance-rejection method, if this first particle is chosen to undergo a rotational energy relaxation event, the Borgnakke-Larsen internal energy exchange model is employed to redistribute the relative translational energy between colliding particles and the rotational energy of the first particle

only. If the first particle is not chosen, the second particle is accepted to relax with probability given by

$$\phi_{rot,2} = \frac{1}{Z_{rot,2}^{cont}} \left(1 + \frac{\zeta_{rot,2}}{5 - 2\omega_{12}} \right) \left(\frac{1}{1 - \phi_{rot,1}} \right), \quad (4.43)$$

which is the conditional probability given that the first particle was not chosen to undergo rotational relaxation. If the second particle is chosen to be examined first, then Eq. 4.42 and Eq. 4.43 are also used in sequence, but with the subscripts exchanged.

The particle and pair selection methodologies are verified to yield the same relaxation rates for the isothermal heat bath simulations of N_2 and the mixture of 50% N_2 /50% N (by mole) that were already presented. To verify that the particle selection methodology is consistent with Parker’s model in CFD for a mixture of species that relax independently of one another, the rotational relaxation of an 80% N_2 /20% O_2 (by mole) mixture is simulated under the same initial conditions that were specified for the previous heat bath simulations. Figure 4.14 illustrates this relaxation process as simulated using CFD and DSMC. Both profiles are in excellent agreement with each other, exhibiting a maximum rotational temperature difference of approximately 26K, which is 1.4% of the CFD rotational temperature at that time (1,913K). For reference, the theoretical rotational relaxation profile is also shown in Fig. 4.14. The agreement between the rotational collision numbers plotted in Fig. 4.15 reiterates that the particle selection methodology has been implemented correctly and yields DSMC results that are consistent with CFD.

4.2.2 Translational-Vibrational Energy Exchange

Consistent simulation of translational-vibrational energy exchange in CFD and DSMC for simple gases was previously investigated by Deschenes and Boyd [21]. Therefore, this section provides a review of these models as they apply to simple gases, and a discussion of how they are extended to mixtures of chemical species. As

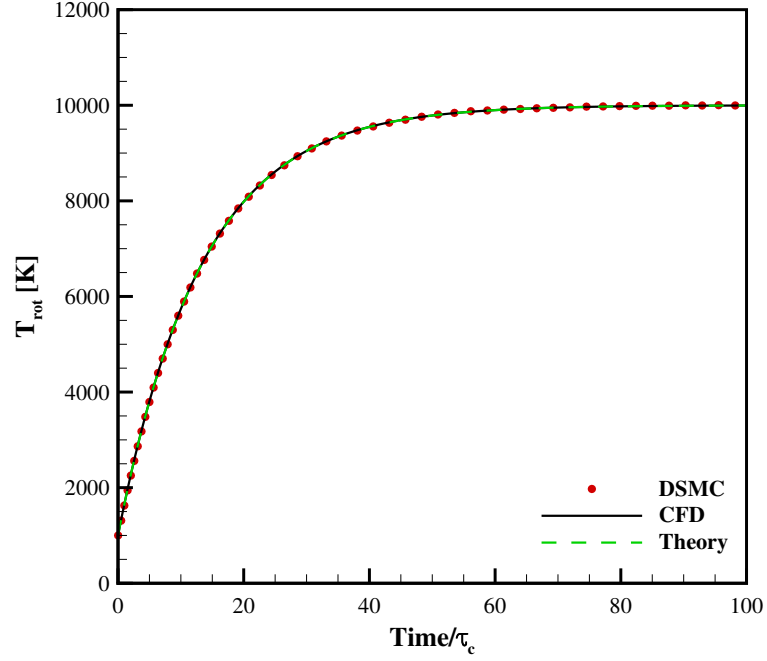


Figure 4.14: Rotational temperature relaxation of 80% N_2 /20% O_2 as predicted by CFD and DSMC, using $\phi_{rot}(E_{rel})$ and the particle selection methodology.

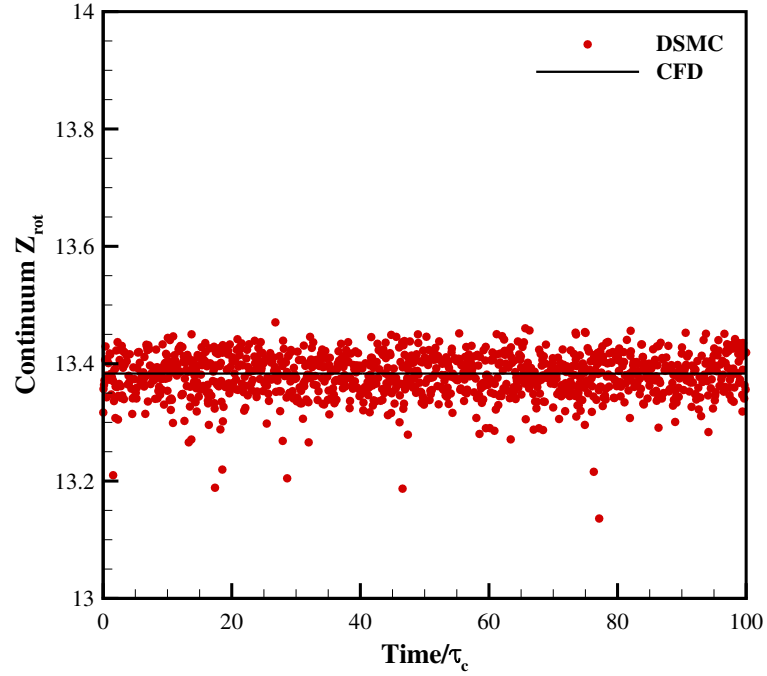


Figure 4.15: Rotational collision number profiles of 80% N_2 /20% O_2 as predicted by CFD and DSMC, using $\phi_{rot}(E_{rel})$ and the particle selection methodology.

was the case for rotational nonequilibrium, vibrational excitation in CFD is simulated by solving a separate vibrational energy equation along with the standard Navier-Stokes conservation equations. The source term accounting for the exchange of energy between the vibrational and translational modes is based on the theory presented by Landau and Teller [44]. Although developed independently, the Landau-Teller equation, as given by

$$\frac{dE_{vib}}{dt} = \frac{E_{vib}^* - E_{vib}}{\tau_{vib}}, \quad (4.44)$$

is of the exact same form as Jeans' equation [42] given by Eq. 4.27. For a gas mixture comprised of NS species, this source term is written as

$$S_{trans-vib} = \sum_{i=1}^{NS} \rho_i \frac{e_{vib,i}^* - e_{vib,i}}{\tau_{vib,i}}. \quad (4.45)$$

The procedure for calculating $\tau_{vib,i}$ such that contributions from all collision classes are included is given later in this section. Unlike the rotational energy mode, where a constant number of degrees of freedom can be assumed for all temperatures except cryogenic, the number of degrees of freedom in the vibrational energy mode is temperature-dependent. For a simple harmonic oscillator, the number of vibrational degrees of freedom is calculated as

$$\zeta_{vib}(T_{vib}) = \frac{2\theta_{vib}/T_{vib}}{\exp[\theta_{vib}/T_{vib}] - 1}, \quad (4.46)$$

where T_{vib} is the vibrational temperature and θ_{vib} is the characteristic temperature of the vibrational energy mode. For the molecular species considered in this dissertation, characteristic vibrational temperatures are given in Appendix A. Because of this nonlinear relationship between the degrees of freedom and temperature, Eq. 4.31 cannot be used to convert between the continuum and particle definitions of the vibrational collision number as was done for the rotational energy mode. Instead, Gimelshein, *et al.* [28] proposed the following relationship between Z_{vib}^{cont} and Z_{vib}^{part} :

$$Z_{vib,ij}^{part} = Z_{vib,ij}^{cont} \left[1 + \frac{[\zeta_{vib}(T_{trans})]^2 \exp[\theta_{vib}/T_{trans}]}{2(5 - 2\omega_{ij})} \right]^{-1}. \quad (4.47)$$

Using the theory developed by Landau and Teller and available experimental data up to temperatures of approximately $8,000K$, Millikan and White [51] developed curve-fits to calculate vibrational relaxation times as a function of pressure and translational temperature. These relaxation times are used in the continuum module of the MPC simulations and in full CFD simulations presented in this dissertation, and are calculated as

$$\tau_{vib,ij}^{MW} = \frac{1}{p[atm]} \exp \left[A_{ij} \left(T_{trans}^{-1/3} - B_{ij} \right) - 18.42 \right], \quad (4.48)$$

where

$$A_{ij} = 1.16 \cdot 10^{-3} \theta_{vib}^{4/3} \sqrt{M_{ij}^*} \quad (4.49)$$

and

$$B_{ij} = 0.015 (M_{ij}^*)^{1/4}. \quad (4.50)$$

In the previous equations, M^* is the reduced mass, but calculated with molecular weights rather than particle masses. When temperatures exceed approximately $5,000K$, the vibrational relaxation times predicted by Millikan and White begin to under predict experimental data. In order to decrease the rate of vibrational relaxation at high temperatures, Park proposed the following additive correction [58] to Eq. 4.48:

$$\tau_i^P = \frac{1}{n_i (5.81 \cdot 10^{-21}) \sqrt{8k_B T_{trans} / (\pi m_i)}}. \quad (4.51)$$

Similar to Eq. 4.38 for the rotational energy mode, the overall vibrational relaxation time of a given species i to be used in Eq. 4.45 is then given by

$$\tau_{vib,i} = \left[\sum_{j=1}^{NS} \frac{1}{\tau_{vib,ij}^{MW} + \tau_i^P} \right]^{-1}. \quad (4.52)$$

The manner in which the contributions of other species are included when determining the vibrational relaxation time of an individual species differs from those proposed by other researchers, such as in Refs. [29] and [45]. Here, Park’s correction term is added to the relaxation time associated with each collision class and then an overall relaxation time is calculated. Other approaches have been proposed in which a “mixture rule” is used to calculate the overall relaxation time of a given species and only then is Park’s correction term added. However, as will be illustrated shortly, the current procedure yields vibrational relaxation times that are consistent with DSMC. In addition, this procedure parallels that used to calculate rotational relaxation times for a gas mixture.

To be consistent with the Millikan and White curve-fit data in CFD, Boyd proposed a translational-vibrational energy exchange model for DSMC by assuming the probability of a vibrationally inelastic collision is a function of the relative velocity between colliding particles [13]. However, adiabatic heat bath simulations of N_2 performed by Deschenes and Boyd [21] showed large errors between the vibrational relaxation process predicted by the Millikan and White curve-fit data and that of Boyd’s DSMC model. Such errors are attributed to mathematical approximations that were required to derive the DSMC model. As a result of these discrepancies, Deschenes, *et al.* [21] proposed using a cell-based pressure and translational temperature in DSMC to calculate the vibrational relaxation time for each collision class according to Millikan and White curve-fit data. The sum of this relaxation time and Park’s correction factor for the collision partner undergoing vibrational relaxation is then converted to a particle-based vibrational relaxation time with the Gimelshein correction factor as follows:

$$\tau_{vib,ij}^{part} = (\tau_{vib,ij}^{MW} + \tau_i^P) \left[1 + \frac{[\zeta_{vib}(T_{trans})]^2 \exp[\theta_{vib}/T_{trans}]}{2(5 - 2\omega_{ij})} \right]^{-1}. \quad (4.53)$$

The probability that a particle of species i will undergo a translational-vibrational energy exchange event by colliding with a particle of species j is then given by

$$\langle \phi_{vib,ij} \rangle = \frac{1}{\tau_{vib,ij}^{part} \nu_{ij}}, \quad (4.54)$$

and this is used instead of a collision-dependent probability. This model is shown to give good agreement with CFD when used in DSMC simulations of adiabatic heat baths of N_2 . In MONACO, a particle selection methodology that allows for double relaxation is employed to determine whether or not colliding particles undergo a translational-vibrational energy exchange event, in accordance with the procedure proposed by Bergemann and Boyd [4].

For completeness, just as was done for verification of the translational-rotational energy exchange models, isothermal heat bath simulations of N_2 are again performed, assuming that the translational and rotational energy modes are in equilibrium with one another at $10,000K$. The relaxation process that occurs as the vibrational temperature is equilibrated from its initial value of $1,000K$ is shown in Fig. 4.16. The CFD and DSMC results are in excellent agreement; the maximum error is calculated to be $25K$, which is approximately 0.3% of the CFD vibrational temperature at that time ($7,836K$). Comparison of these results and Fig. 4.10 illustrates the order-of-magnitude difference between the relaxation rates exhibited by the rotational and vibrational energy modes. In addition, isothermal heat bath simulations of two gas mixtures that are considered in this dissertation are also performed to verify consistency for gas mixtures. The results for the 50% N_2 /50% N (by mole) mixture are plotted in Fig. 4.17, where the continuum and particle models are shown to yield consistent results. In this case, the maximum error is calculated to be $32K$, which is approximately 0.3% of the CFD vibrational temperature at that time ($9,178K$). Like-

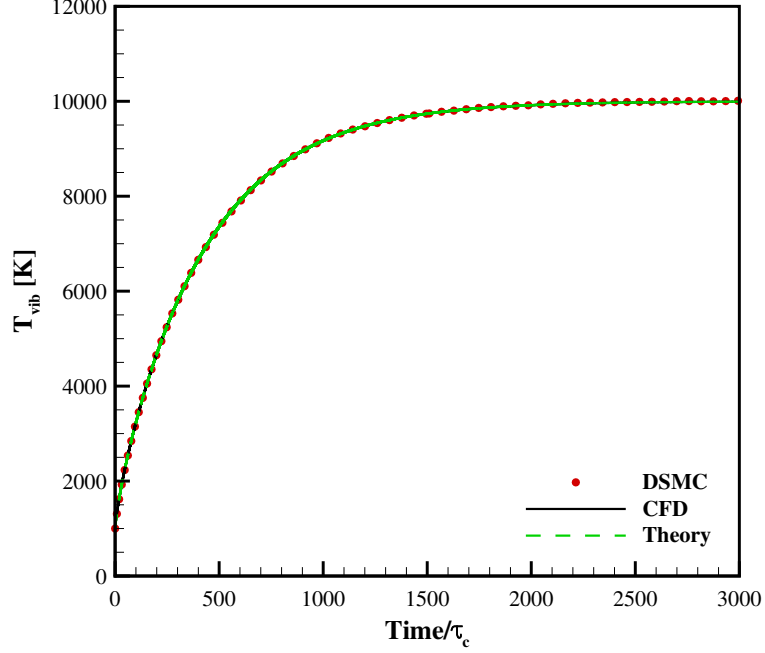


Figure 4.16: Vibrational temperature relaxation of N_2 as predicted by CFD and DSMC.

wise, the vibrational relaxation processes predicted by CFD and DSMC for an 80% N_2 /20% O_2 (by mole) mixture are in excellent agreement, as shown in Fig. 4.18. The largest difference between CFD and DSMC is calculated to be $31K$, which is approximately 1.2% of the CFD vibrational temperature at that time ($2,629K$). Theoretical results obtained by integrating Eq. 4.44 are also shown in Figs. 4.16 and 4.17, and lend confidence to the numerical results. Theoretical results are not included for the 80% N_2 /20% O_2 mixture results because there is not an analytical result for the vibrational temperature in this case.

4.3 Interim Conclusions

In this chapter, the physical models used for simulating transport and thermal relaxation processes in CFD, DSMC, and the MPC method were discussed. Most importantly, these models were verified to be consistent in near-equilibrium flows of both simple gases and mixtures of chemical species. First, a review of the VHS col-

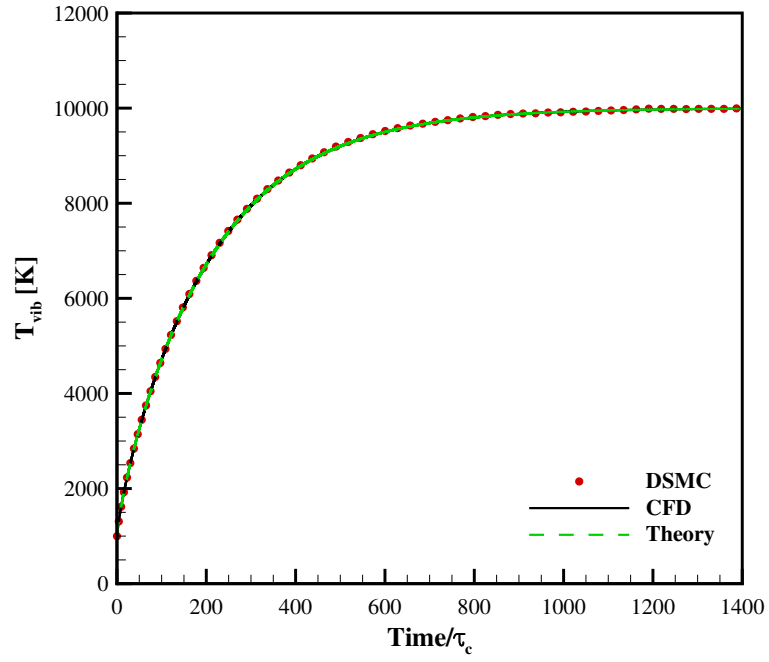


Figure 4.17: Vibrational temperature relaxation of 50% N_2 /50% N as predicted by CFD and DSMC.

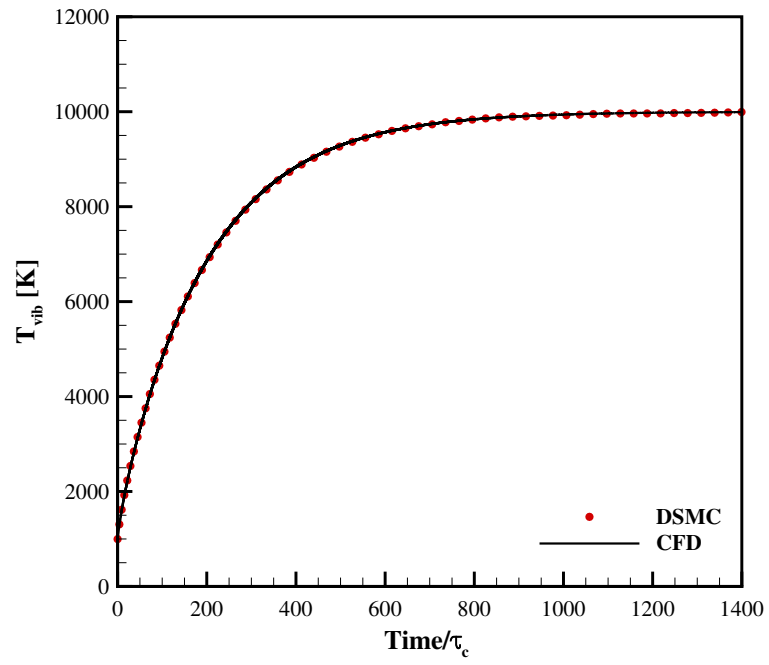


Figure 4.18: Vibrational temperature relaxation of 80% N_2 /20% O_2 as predicted by CFD and DSMC.

lision model used in DSMC, and the explicit calculations of viscosity and thermal conductivities required in CFD, were presented as they apply to simple gases. For the simulation of gas mixtures using CFD, the explicit calculation of the diffusion flux was discussed, along with the Gupta Mixing Rule, which is used to approximate the mixture viscosity and thermal conductivities. An in-depth discussion was presented regarding how VHS collision model parameters should be determined so as to give viscosity predictions that are consistent with the Gupta Mixing Rule. A simple approach was proposed and shown through DSMC simulations of various Couette flows to yield consistent viscosity results for a number of simple gases and gas mixtures. However, this simple approach failed when a mixture comprised of species with very different molecular weights was considered; this was confirmed through comparisons with a more rigorous approach that employs the Nelder-Mead simplex algorithm. As such, this more rigorous approach is recommended for calculating VHS and VSS collision model parameters in the future.

Models for the consistent simulation of thermal nonequilibrium effects were also discussed. Previous MPC simulations employed a DSMC model for translational-rotational energy exchange in which the probability of two colliding particles experiencing an inelastic collision was assumed to be dependent on the total collision energy. To achieve utmost consistency with Parker’s model in CFD, however, it was shown that this probability should be a function of the relative collision energy only. This was verified through isothermal heat bath simulations of N_2 and a mixture of N_2 and N . Extension of the MPC method to accurately simulate mixtures of polyatomic species in rotational nonequilibrium, and to allow these constituent species to equilibrate independently of one another, was also discussed. The pair selection procedure for determining which colliding pairs will experience an inelastic collision was replaced with a more versatile particle selection methodology. Again, subsequent isothermal heat bath simulations of a mixture of N_2 and O_2 using DSMC and CFD

were verified to be consistent. Translational-vibrational energy exchange models and their associated “mixture rules” were also verified to be consistent through isothermal heat bath simulations of the aforementioned simple gas and gas mixtures.

CHAPTER V

A Comprehensive Assessment of the MPC Method

Prior to extending the capabilities of the MPC hybrid method, a detailed and consistent evaluation of its physical accuracy relative to a full DSMC simulation is performed. Previously reported comparisons between the MPC method and full DSMC simulation results were made along streamlines and other flow field extraction lines only, leading to accuracy verification that is quite limited in scope. A preferred approach for evaluating the errors incurred by employing the MPC method rather than performing a full DSMC simulation is to compare macroscopic fluid properties on a cell-by-cell basis. Such comparisons are presented and discussed here for a transitional, hypersonic flow over a two-dimensional cylinder. This provides a more comprehensive understanding of both the location and magnitude of errors that are occurring in the flow field, and therefore, more insight into what challenges remain unresolved.

As a result of this detailed accuracy assessment, several improvements are made to the MPC method that was described in Chapter III. These improvements specifically address the consistent treatment of the outflow boundary conditions imposed in the MPC and full DSMC simulations, and the consistent exchange of information across the interfaces that separate particle and continuum domains in a hybrid simulation. New simulation results are generated and evaluated in terms of physical accuracy.

Further investigation into the potential causes of remaining errors, and the level of error that should be expected in these simulations is also presented. In addition, the MPC hybrid method is also compared to full DSMC and full CFD in terms of computational performance metrics, including memory usage requirements that are reliably obtained using commercial profiling software.

5.1 A Detailed Accuracy Evaluation

As described in Chapter III, the MPC method employs two computational mesh layers by numerically solving the Navier-Stokes equations on a coarse mesh in the continuum domains, and by moving and colliding simulator particles and sampling on a fine mesh in particle domains. Because the particle mesh is merely a refined version of the continuum mesh, a direct comparison between MPC simulation results and those from full DSMC is obtained in a straightforward manner by mapping the CFD solution on to the fine mesh in the continuum domains of the flow field. For example, consider the continuum cell $C1$, which is comprised of four particle cells after refinement of the original CFD mesh, as illustrated in Fig. 5.1. If cell $C1$ is labeled as being part of the continuum domain in a hybrid simulation, and has therefore been refined only to eliminate hanging nodes in the computational mesh, the final MPC hybrid solution is constant across this cell. The solution can then be copied to each of the constituent particle cells without interpolation or loss of accuracy. By repeating this for all cells in the continuum domains of the hybrid simulation, these results can be compared to the full DSMC simulation results on a cell-by-cell basis without confining the MPC method to using the same mesh as that used in the full DSMC simulation. Although this type of comparison is usually forgone for a global mathematical norm, such a detailed accuracy evaluation is critical while developing a new numerical technique.

Using this procedure, a detailed accuracy evaluation of the MPC method is per-

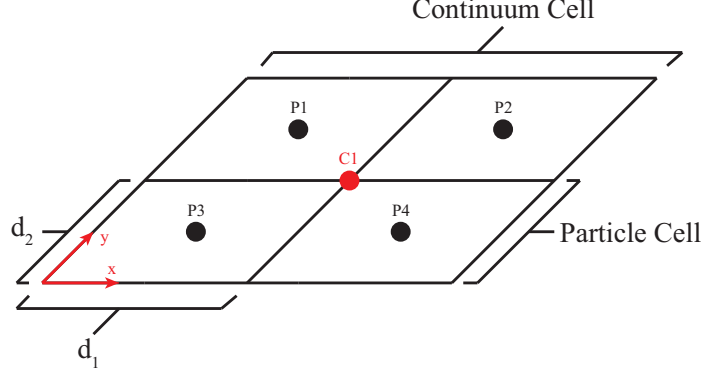


Figure 5.1: Illustration of continuum cell and constituent particle cells.

formed by simulating a Mach 12 flow of N_2 over a two-dimensional cylinder at a global Knudsen number of 0.01. This case was previously simulated using the MPC hybrid method in Ref. [22]. Although excitation of the vibrational energy mode is neglected in this simulation, rotational energy nonequilibrium is allowed. The global Knudsen number is based on the freestream VHS mean free path so that the freestream density is $7.752 \times 10^{-5} kg/m^3$. The freestream velocity is $3,608 m/s$, the freestream temperature is $217.45 K$, and an isothermal wall boundary condition is used with a specified temperature of $1,000 K$. In the full DSMC simulation, a constant numerical weight of 3×10^{12} is required in order to maintain a minimum of 20 particles per cell throughout the computational domain. However, reduced cell-based numerical weights are used near the cylinder surface so that a larger number of particles collide with the cylinder, thus reducing the statistical scatter in the surface properties. This is especially problematic in the low-density wake. In order to make consistent comparisons of computational requirements and to ensure that the same level of statistical scatter is present in both simulations, these same cell-based weights are used in the hybrid simulation, and sampling of particle properties occurs over the same number of time steps in both simulations.

A constant time step of $1 \times 10^{-8} s$ is used in the full DSMC simulation and in particle regions of the hybrid simulation. This is, at most, one-third of the local mean

collision time, and a local CFL number is calculated in each particle cell to verify that no simulator particle traverses more than one cell in a given time step. The maximum time step used in the continuum regions of the hybrid simulation is ten times larger than that in the particle regions. Subcells are used in the full DSMC simulation and in the particle domains of the MPC simulation, mitigating any shortcomings of the gradient-based mesh refinement procedure described in Section 3.3. In addition to verifying that these numerical parameters are aligned with the “best practices” of the DSMC method, consistent physical models are used to achieve the best possible agreement between MPC and full DSMC results. These models were detailed in Chapter IV. Finally, as was commonplace in previous MPC simulations, DSMC is forced to be used within $5mm$ of the cylinder surface in order to expand the particle regions automatically identified by the continuum breakdown parameters described in Chapter III. This additional requirement will be eliminated upon development of a new rotational nonequilibrium parameter that will be the focus of Chapter VI.

The relative errors between MPC and full DSMC results for this case are calculated as

$$\epsilon = \frac{Q_{MPC}}{Q_{DSMC}} - 1, \quad (5.1)$$

where Q represents relevant macroscopic properties. As illustrated by the error contours in Figs. 5.2 through 5.5, although the majority of the flow field is in excellent agreement with full DSMC, there remain localized regions of errors in excess of the aforementioned goal of $\pm 5\%$. The labels in Fig. 5.2 indicate that DSMC is used in the region surrounding the bow shock wave, and in the region surrounding the boundary layer and low-density wake; CFD is used in the remainder of the computational domain. Although these labels are not included in subsequent plots of flow field properties, the regions where DSMC and CFD are employed can be inferred by comparison with Fig. 5.2. Due to the small velocity magnitudes near the stagnation

point and in the wake, even small discrepancies between MPC and full DSMC appear as sizable errors. Therefore, it is not surprising to see such large errors between the velocity magnitudes in these regions. In addition, because of the very steep flow field gradients in the bow shock wave, even small differences in the location of the shock may lead to large relative errors. The disagreement between the rotational temperatures predicted by the MPC method and full DSMC in the far wake is unexpected. However, although this disagreement appears extensive, the errors in this region do not exceed 6%. The disagreement exhibited in both velocity magnitude and mass density along the outflow boundary near the axis of symmetry is also surprising, as this should be a relatively benign area of the flow field. The full ranges of errors for various macroscopic fluid properties are given under the “Previous MPC Results” heading in Table 5.1. For comparison, the ranges of errors calculated from the results of a full CFD simulation are also included in this table. In addition to the error defined in Eq. 5.1, the relative error measured in the L_2 norm is given by

$$(\epsilon)_{L_2} = \frac{\|Q - Q_{DSMC}\|_{L_2}}{\|Q_{DSMC}\|_{L_2}}, \quad (5.2)$$

where the L_2 norm is defined as

$$\|Q\|_{L_2} = \sqrt{\sum_{i=1}^{NC} Q_i^2}. \quad (5.3)$$

In Eq. 5.3, NC is the total number of computational cells. This measure of error provides a single, average value that is indicative of the overall agreement between two flow field solutions. For various macroscopic fluid properties of interest, this relative error is calculated and provided in Table 5.2. Again, the relative error measured in the L_2 norm is also calculated for the full CFD solution.

Before exploring other causes for the higher than anticipated errors, the possibility of shock unsteadiness is first eliminated in both the full DSMC solution and

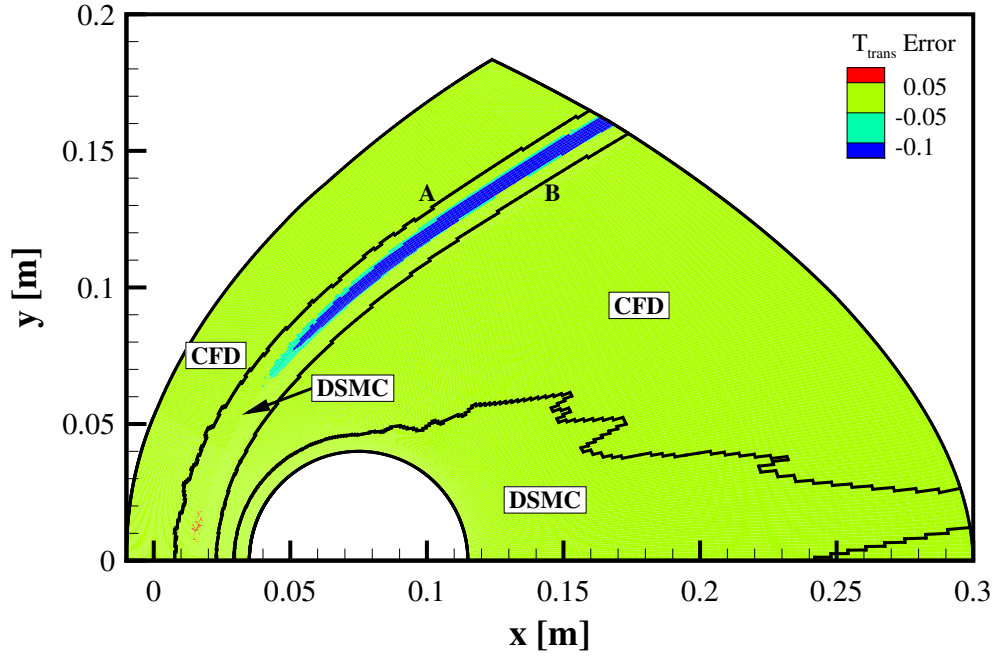


Figure 5.2: Contours of translational temperature errors of previous MPC results relative to full DSMC for the Mach 12, Kn_∞ 0.01 flow of N_2 over a two-dimensional cylinder; hybrid interfaces are shown as black lines.

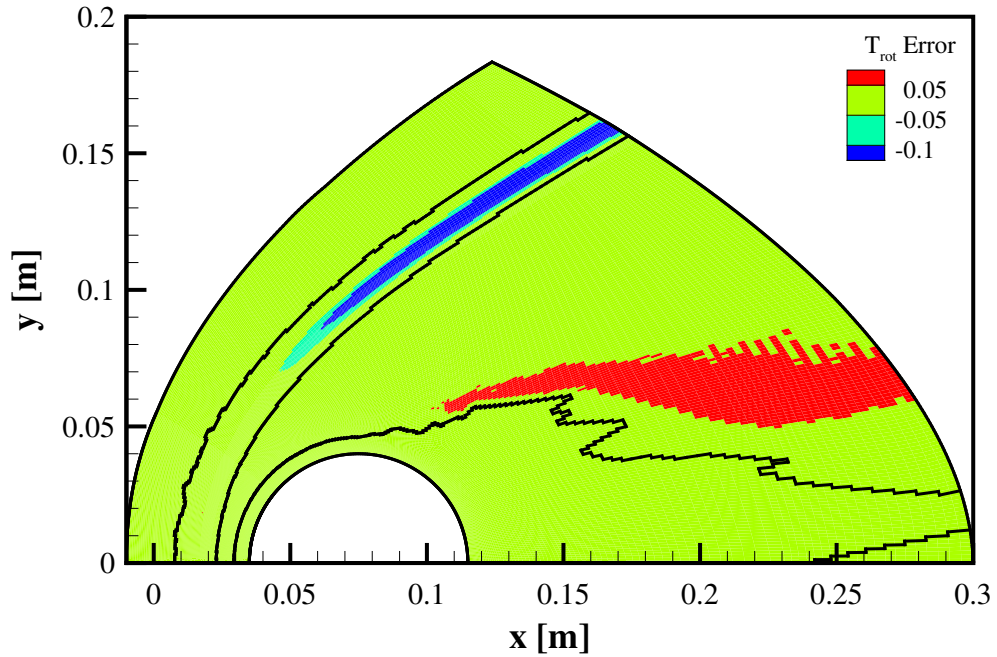


Figure 5.3: Contours of rotational temperature errors of previous MPC results relative to full DSMC for the Mach 12, Kn_∞ 0.01 flow of N_2 over a two-dimensional cylinder; hybrid interfaces are shown as black lines.

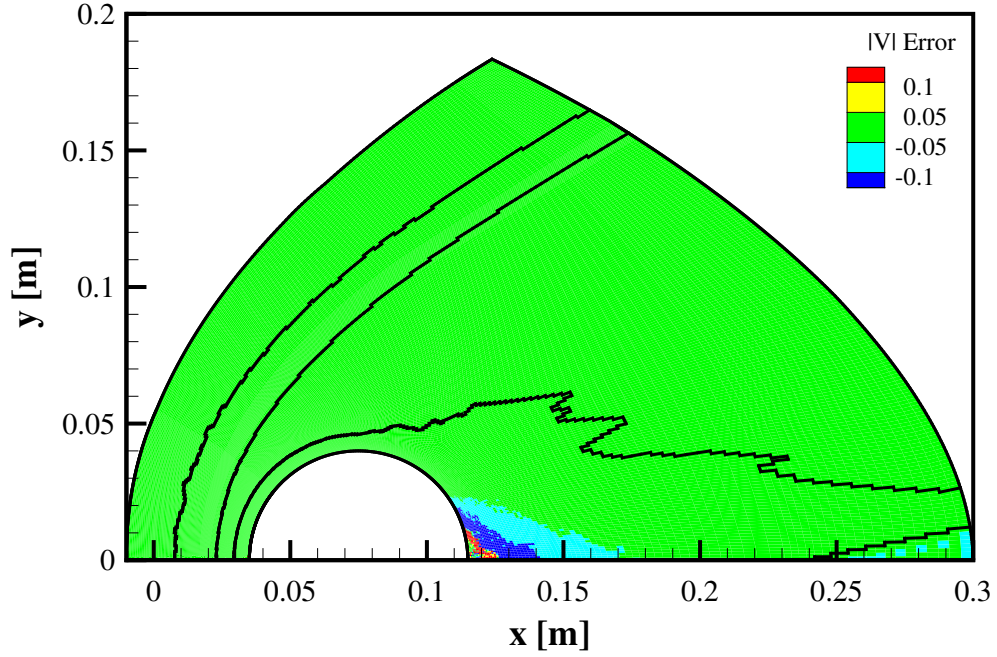


Figure 5.4: Contours of velocity magnitude errors of previous MPC results relative to full DSMC for the Mach 12, Kn_∞ 0.01 flow of N_2 over a two-dimensional cylinder; hybrid interfaces are shown as black lines.

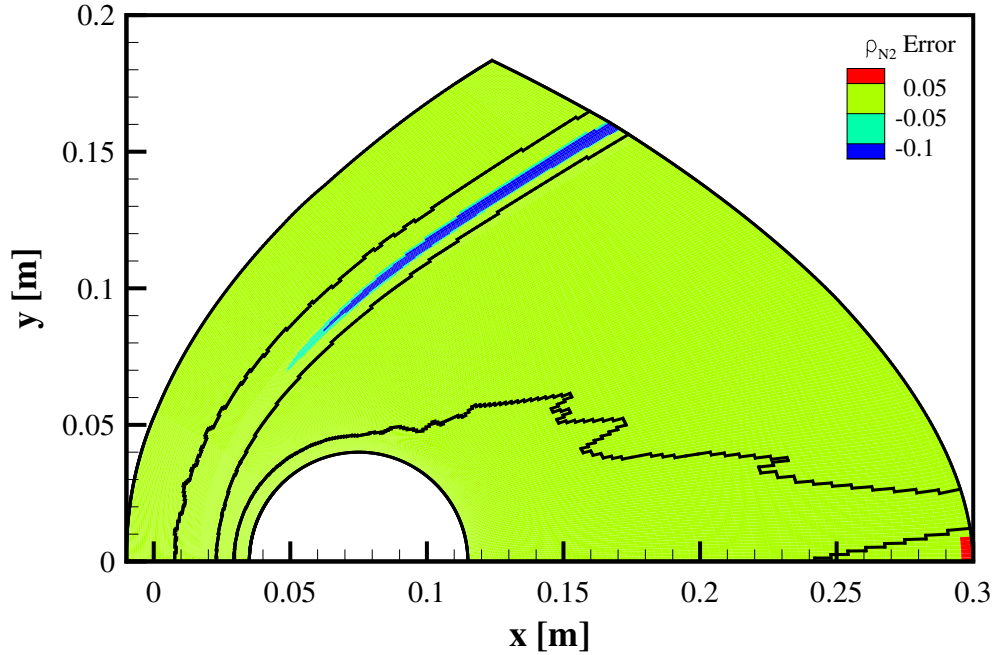


Figure 5.5: Contours of mass density errors of previous MPC results relative to full DSMC for the Mach 12, Kn_∞ 0.01 flow of N_2 over a two-dimensional cylinder; hybrid interfaces are shown as black lines.

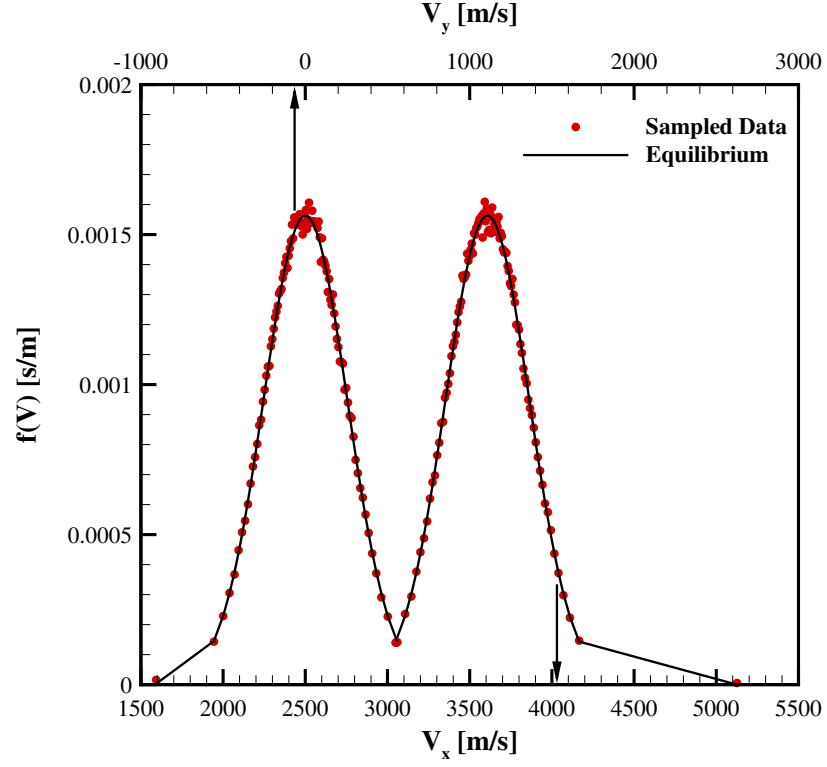
Table 5.1: Ranges of previous MPC and CFD errors relative to full DSMC for the Mach 12, Kn_∞ 0.01 flow of N_2 over a two-dimensional cylinder.

Property	Previous MPC Results	CFD Results
T_{trans}	$-0.43 \leq \epsilon \leq 0.07$	$-0.72 \leq \epsilon \leq 0.81$
T_{rot}	$-0.34 \leq \epsilon \leq 0.06$	$-0.71 \leq \epsilon \leq 0.13$
ρ_{N2}	$-0.38 \leq \epsilon \leq 0.07$	$-0.08 \leq \epsilon \leq 0.66$

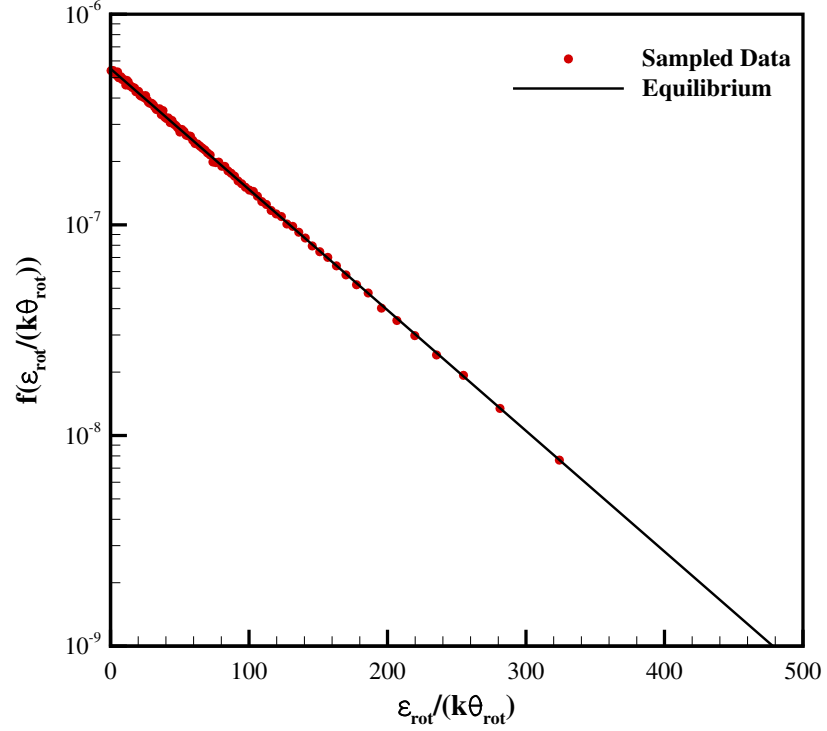
Table 5.2: Relative errors of previous MPC and CFD results measured in the L_2 norm for the Mach 12, Kn_∞ 0.01 flow of N_2 over a two-dimensional cylinder.

Property	Previous MPC Results	CFD Results
T_{trans}	0.012	0.037
T_{rot}	0.015	0.072
$ V $	0.006	0.034
ρ_{N2}	0.013	0.088

the CFD solution used to initialize the MPC simulation. In addition, because of the empirical nature of the continuum breakdown parameters, it is also prudent to verify that the hybrid interfaces are placed in regions of near-continuum. Velocity and rotational energy samples are collected from a full DSMC simulation at the two locations indicated by letters *A* and *B* in Fig. 5.2. The particle cell labeled *A* lies adjacent to the pre-shock hybrid interface, and cell *B* lies adjacent to the post-shock hybrid interface. The probability distribution functions, as derived from DSMC simulator particle samples collected in each cell, are shown in Figs. 5.6 and 5.7, respectively. At both locations, the sampled VDFs and rotational EDFs are in excellent agreement with the calculated equilibrium distributions. Therefore, it is concluded that the hybrid interfaces are conservatively placed in the upper shock wave region. In addition, the number of DSMC boundary/reservoir cells is also increased from two to ten with negligible change to the solution. With these potential sources of error eliminated, the assumptions of certain boundary conditions, specifically, those imposed along the computational domain outflow and the hybrid interfaces, are examined for consistency.

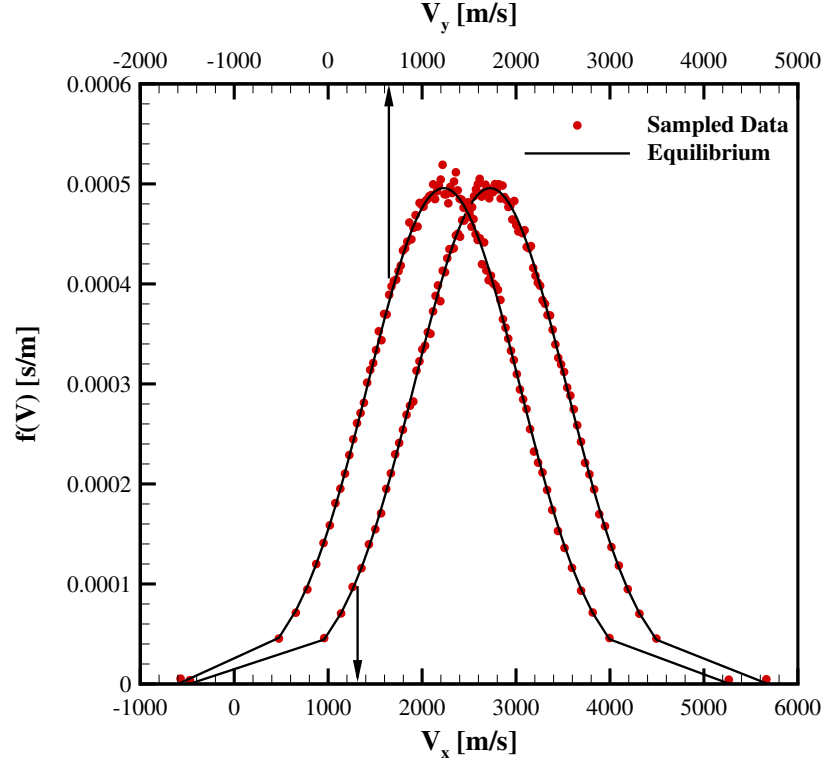


(a) Velocity

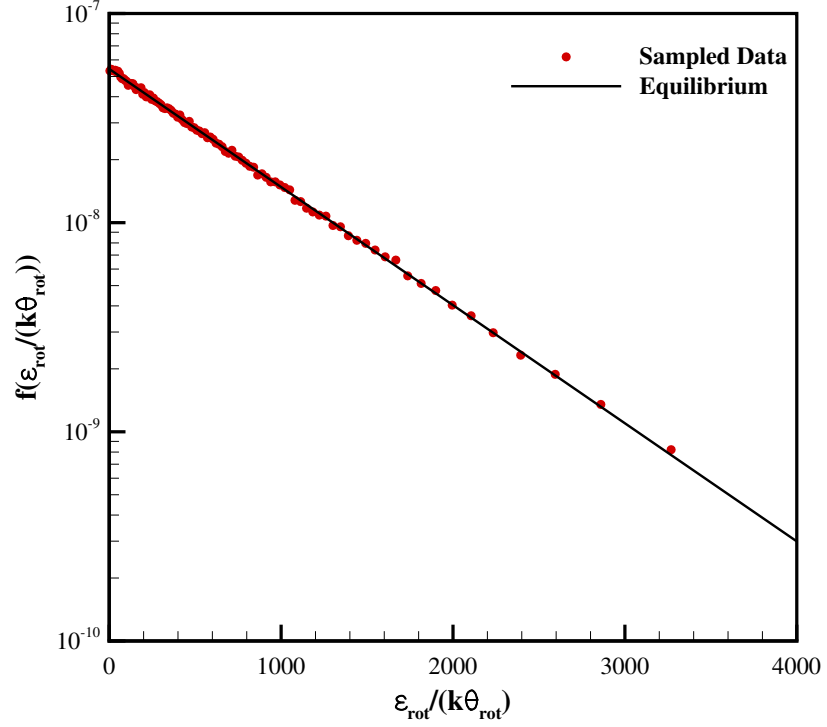


(b) Rotational energy

Figure 5.6: Comparisons of probability distribution functions predicted by full DSMC and equilibrium theory in cell A of Fig. 5.2.



(a) Velocity



(b) Rotational energy

Figure 5.7: Comparisons of probability distribution functions predicted by full DSMC and equilibrium theory in cell B of Fig. 5.2.

5.2 Improved Consistency of Boundary Conditions

To enable valid comparisons between results obtained using the MPC method and those obtained using full DSMC, every effort must be made to maintain as much consistency between simulation techniques as possible. This not only points towards the use of consistent physical models, as was the focus of Chapter IV, but the consistent enforcement of numerical boundary conditions along the boundaries of the computational domain and hybrid interfaces. Because of the fundamental differences between CFD and DSMC, this is not always trivial.

5.2.1 Supersonic Outflow

Along the stagnation streamline, the MPC method is able to accurately predict the location of the bow shock wave, as seen by comparing the translational temperature profiles in Fig. 5.8. The shock wave is at its maximum strength when it intersects the stagnation streamline, which means that the limitations of the continuum assumptions of the Navier-Stokes equations are especially pronounced in this region of the flow field. This might also suggest an increased level of difficulty in obtaining an accurate solution with the MPC method. However, in the forebody flow, the shock wave is stabilized by the two-dimensional cylinder. The high density in this region and resulting high rate of collisions among gas molecules also enables the post-shock flow to equilibrate rapidly. As the flow expands after accommodating the body, the bow shock curves due to its interaction with the expansion waves formed in the wake. The interaction of the shock wave and expansion waves results in the upper shock wave region being a challenge for the MPC method to simulate accurately.

As the path of the bow shock wave is traced from the axis of symmetry upward, the MPC method predicts a shock wave location that is further downstream of that predicted by the full DSMC simulation. This shift in shock wave location is shown in Fig. 5.9, where the translational temperature profiles have been extracted along

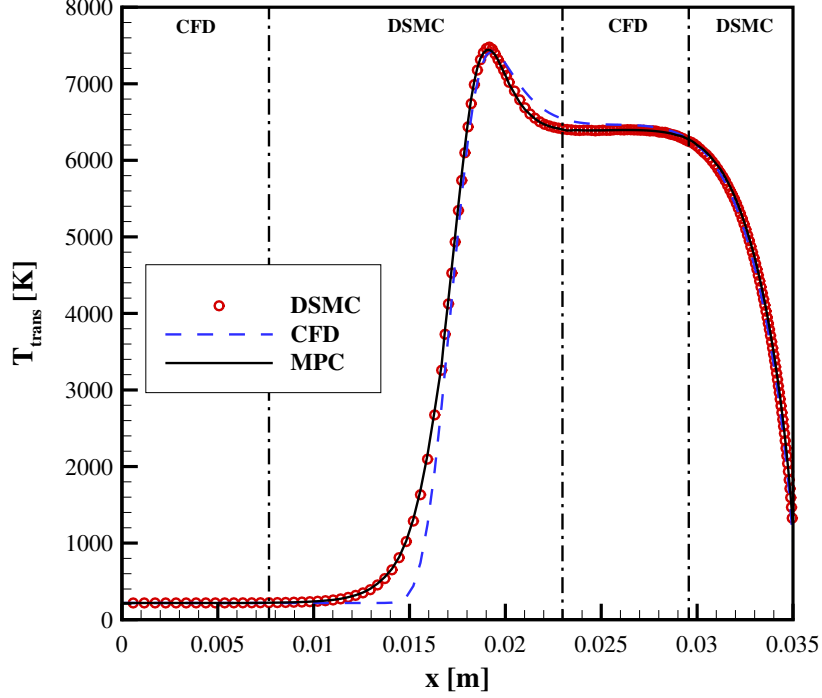


Figure 5.8: Translational temperature along the stagnation streamline of the Mach 12, Kn_∞ 0.01 flow of N_2 over a two-dimensional cylinder.

a horizontal line at $y = 0.13m$. Differences between the bow shock wave locations predicted by the MPC method and full DSMC, which lead to the large errors in the upper shock wave regions of Figs. 5.2 through 5.5, along with those errors observed along the outflow boundary near the axis of symmetry, indicate that the inconsistent treatment of the outflow boundary may be more problematic than previously assumed.

Prior to this work, the full DSMC simulations used for comparison with MPC results imposed a vacuum outflow boundary condition. Such a condition stipulates that any simulator particles that encounter the outflow boundary be removed from the simulation and no new particles be generated. If the average velocity magnitude of outgoing particles is sufficiently high, this is a valid assumption because the probability of particles entering the domain through the exit is low. Simulator particles that are generated along an inflow or outflow domain are sampled from a biased Maxwellian VDF. In order to truncate the low-probability tails of this distribution,

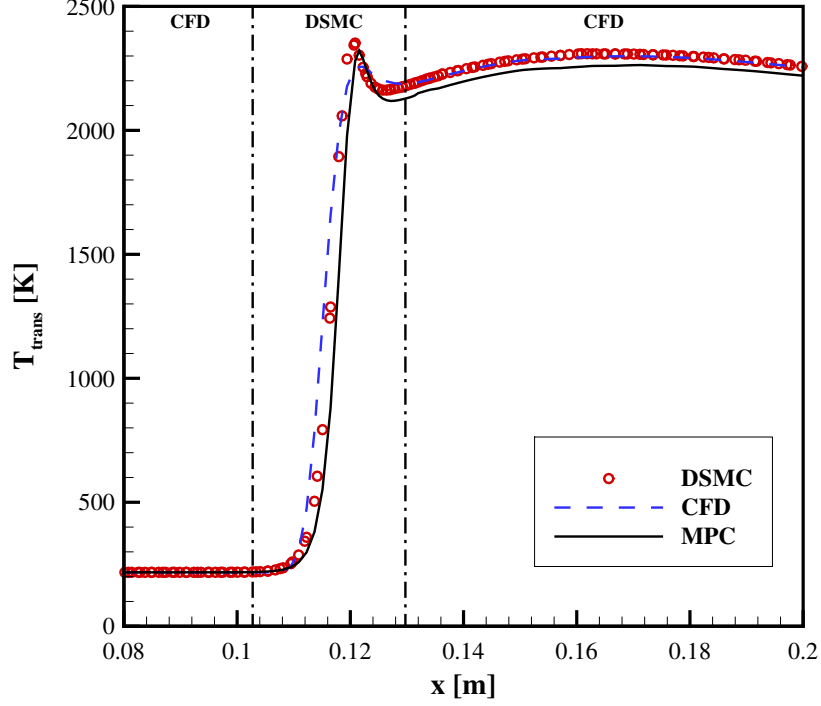


Figure 5.9: Translational temperature along the $y = 0.13m$ extraction line of the Mach 12, Kn_∞ 0.01 flow of N_2 over a two-dimensional cylinder.

samples are limited to

$$u_n - 3\beta \leq c_i \leq u_n + 3\beta,$$

where u_n is the directed velocity of the gas aligned with an inward-pointing normal, β is the most probable particle speed, $\sqrt{2RT_{trans}}$, and c_i is a given velocity sample. Therefore, if the directed velocity aligned with an inward-pointing normal is greater than -3β , as depicted in Fig. 5.10, then there should be particles entering the domain along the outflow boundary because positive velocities are then included in the truncated distribution. Even though there are particles entering the outflow, this is not equivalent to a subsonic boundary condition where characteristic information must be specified at the outflow boundary. The flow is supersonic along the entire outflow boundary, as seen by the contours of Mach number in Fig. 5.11.

For the case presented here, the Mach number of the flow near the axis of symmetry is low enough such that there should be simulator particles that enter the outflow

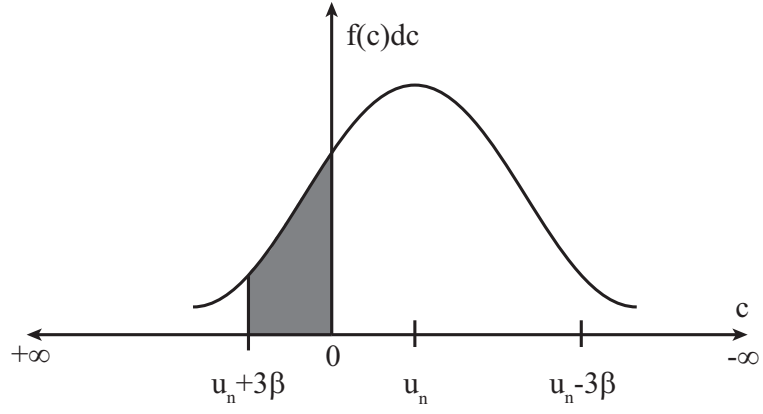


Figure 5.10: Illustration of a Maxwellian VDF at the outflow boundary, where u_n is the directed velocity aligned with an inward-pointing normal.

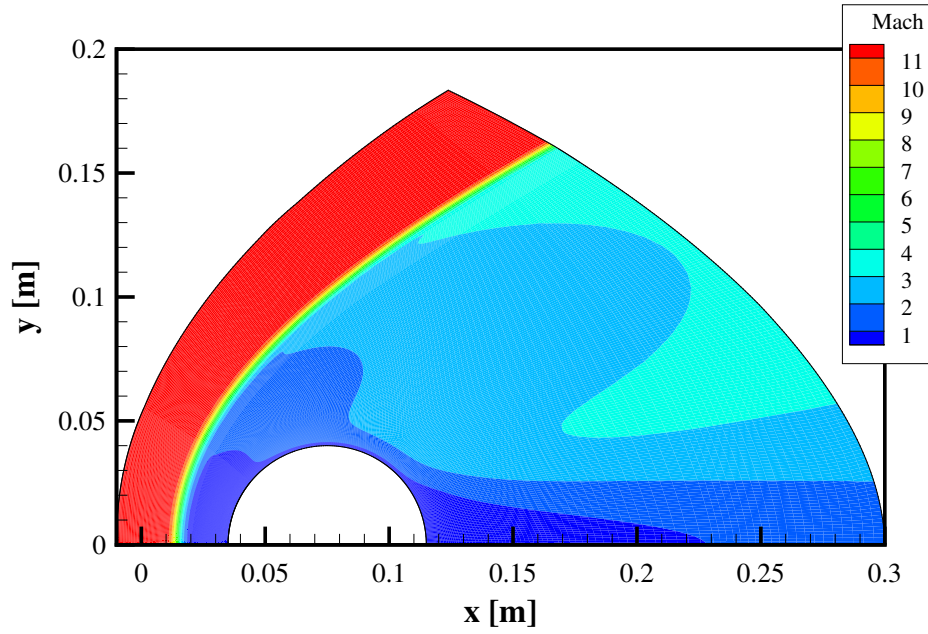


Figure 5.11: Contours of Mach number for the Mach 12, Kn_∞ 0.01 flow of N_2 over a two-dimensional cylinder.

boundary. Use of a vacuum outflow boundary condition is even more suspect when considering the normal velocity along the entire outflow boundary is lower than the Mach number would suggest. In addition to being physically questionable, neglecting the particles that enter through the outflow is inconsistent with the CFD module of the MPC method, which employs a zeroth-order extrapolation of macroscopic properties along the outflow boundary. Intuitively, incorrect simulation of the outflow as a vacuum in DSMC would have the effect of moving the shock wave downstream of that predicted by CFD, as shown in Fig. 5.9. Although the shock wave is located even further downstream in the MPC results, this may be due to compounding effects of initializing the hybrid simulation with the CFD solution and then correcting the nonequilibrium regions with a DSMC module that assumes a vacuum outflow boundary condition. However, the greatest improvement resulting from the use of a consistent outflow boundary condition in DSMC is expected to be seen near the axis of symmetry where the Mach number is lowest.

To predict the flux of particles entering the domain through the outflow boundary, cell-based averages of particle properties, including translational temperature, directed velocity, and number density, are calculated. Cell-based translational temperatures are already calculated throughout the flow field for use in the translational-vibrational energy exchange model described in Section 4.2.2. Using these cell-based averages along the domain outflow, the number of new particles entering the domain is then given by

$$\Gamma_s = \frac{\Delta t A n_s}{W_c} \sqrt{\frac{k_B T_{trans}}{2\pi m_s}} \left[s_n \sqrt{\pi} (1 - \text{Erf}(-s_n)) + e^{-s_n^2} \right]. \quad (5.4)$$

In Eq. 5.4, Δt is the time step, A is the area of the cell face along the outflow boundary, n_s is the number density of species s , W_c is the numerical weight of each simulator particle, k_B is the Boltzmann constant, m_s is the particle mass of species s , s_n is the ratio of u_n and the most probable particle speed, and $\text{Erf}()$ is the error

function. Once the number of new particles is known, properties are sampled from a biased Maxwellian VDF and Boltzmann internal EDFs, again defined using cell-based averages of macroscopic properties along the outflow boundary.

5.2.2 Hybrid Interfaces

A further improvement made to the MPC hybrid method concerns the boundary conditions along the hybrid interfaces. The consistent transfer of information across the hybrid interfaces is achieved not only through the placement of the hybrid interfaces and the use of consistent physical models, but also the mechanics of how information is communicated between the continuum and particle domains. In an MPC simulation, the particles entering the domain along the hybrid interfaces should be *indistinguishable* from those that would have crossed an imaginary interface placed in the same position in a full DSMC simulation. Even when the hybrid interfaces are accurately positioned and consistent physical models are used, however, because the particle mesh is more refined than the continuum mesh, there remain subtle differences between a full DSMC simulation and an MPC simulation.

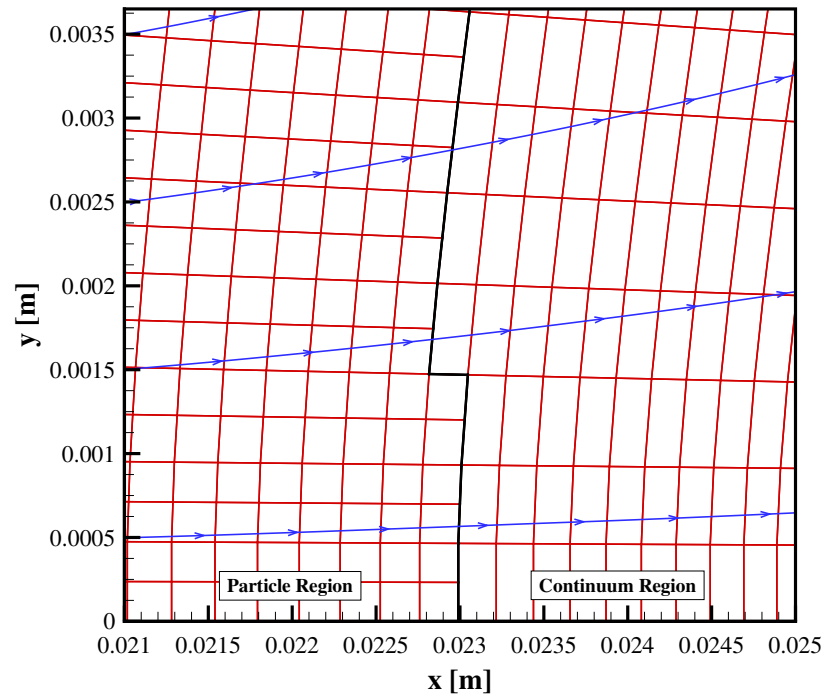
For instance, compare Fig. 5.12(a), which shows the mesh along a hybrid interface that intersects the stagnation streamline, to Fig. 5.12(b), which gives a view of the mesh in the upper shock wave region where the aforementioned errors are particularly pronounced. In both figures, the hybrid interface, shown as the black line, is aligned with the shock wave. When new particles are generated in the DSMC boundary cells, the macroscopic properties used to define the Chapman-Enskog VDF from which their velocities are sampled are taken from the larger, continuum cells. In addition, internal energies are sampled from Boltzmann distributions defined by macroscopic temperatures from these cells. Inherent to this procedure is the assumption that these macroscopic properties do not vary substantially across the continuum cells, even if they were comprised of smaller particle cells as in a full DSMC simulation. This

assumption is more acceptable near the axis of symmetry, where the streamtraces are aligned with the flow field gradients and macroscopic properties are not expected to vary as much in the vertical direction. However, this is not true in the upper shock wave region, where, in addition to the gradients perpendicular to the bow shock, the strength of the shock wave is decreasing with distance away from the cylinder due to its interaction with the expanding flow in the wake. Therefore, in order to make the manner in which new particles are generated along the hybrid interfaces more consistent with full DSMC, the gradients of the flow in the DSMC boundary cells must be considered.

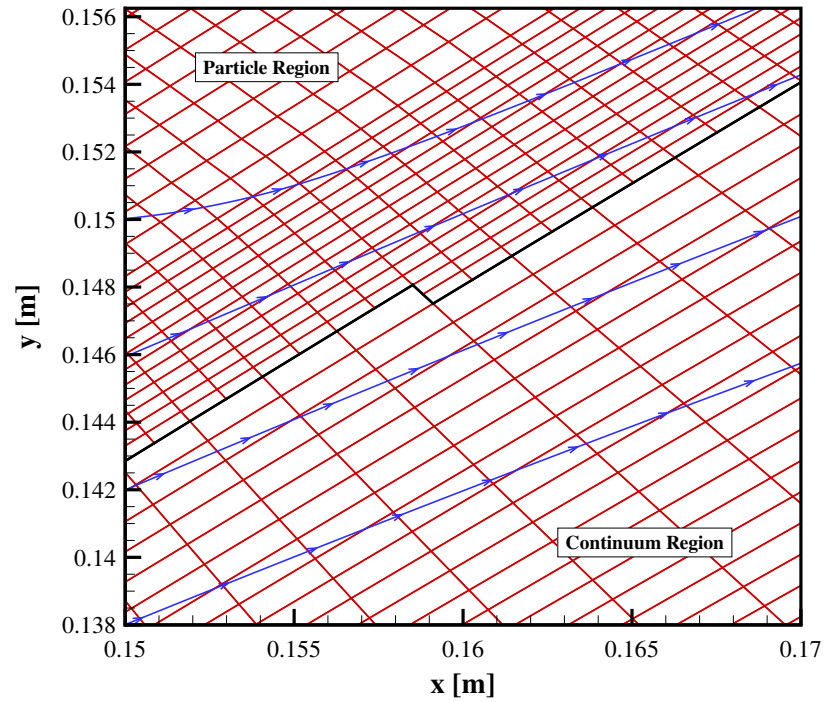
In the case of a full DSMC simulation, macroscopic properties would be allowed to vary over distances characterized by the more refined particle mesh layer. On the continuum side of the hybrid interfaces, however, knowledge of the solution is limited to constant macroscopic properties in each continuum cell and their corresponding gradients. In order to improve the consistency of the particle generation procedure in the MPC method relative to what would naturally occur in a full DSMC simulation, macroscopic properties in the DSMC boundary cells are interpolated to the smaller particle cells that comprise them in the refined mesh layer. Consider again the continuum cell shown in Fig. 5.1, which has been refined to include four particle cells. Macroscopic properties known at $C1$ and their gradients centered around this point can be used to linearly interpolate for properties at the center of each constituent particle cell. For example, the mass density at $P3$ is calculated from

$$\rho_{P3} = \rho_{C1} + (x_{P3} - x_{C1})\frac{\partial\rho_{C1}}{\partial x} + (y_{P3} - y_{C1})\frac{\partial\rho_{C1}}{\partial y}. \quad (5.5)$$

Using the translational temperature, mass density, and velocity components centered at $P3$, velocities can then be assigned to newly generated particles using the procedure outlined by Garcia and Alder [26]. In the case presented here, the rotational temperature is also linearly interpolated for use in assigning rotational energies



(a) Forebody, near the axis of symmetry



(b) Upper shock wave region

Figure 5.12: Mesh and streamtraces near hybrid interfaces.

to new particles. The gradient of mass density is also employed to bias the probability expression for determining the location of newly generated particles. For example, the x location of a new particle generated in cell $P3$ is calculated according to the following probability, which is comprised of a uniform distribution (first term) and that imposed by the density gradient (second term):

$$P(x)dx = \left[\frac{1}{d_1} + \frac{\partial \rho_{C1}}{\partial x} \frac{1}{\rho_{P3} d_1} (x - x_{P3}) \right] dx. \quad (5.6)$$

The dimensions of the particle cell $P3$ are labeled in Fig. 5.1, and it should be noted that when the density gradient is zero, the uniform distribution is recovered. This probability is the same as referenced by Wijesinghe [89]. As is standard practice, the cumulative distribution function is then obtained by integrating Eq. 5.6 from one side of cell $P3$, which is at $x = 0$, to the x -coordinate of a candidate particle location, x_i . This cumulative distribution function is given by

$$F(x_i) = \frac{x_i}{d_1} + \frac{\partial \rho_{C1}}{\partial x} \frac{1}{\rho_{P3} d_1} \left(\frac{x_i}{2} - x_{P3} \right) x_i. \quad (5.7)$$

Upon generating a random fraction, R_f , the x -coordinate of a newly generated simulator particle is found to be

$$x_i = \frac{d_1}{\gamma_x} \left\{ \frac{\gamma_x}{2} - 1 + \left[\left(1 - \frac{\gamma_x}{2} \right)^2 + 2\gamma_x R_f \right]^{1/2} \right\}, \quad (5.8)$$

where

$$\gamma_x = \frac{\partial \rho_{C1}}{\partial x} \frac{d_1}{\rho_{P3}}. \quad (5.9)$$

The y -coordinate is calculated in a similar manner. With this procedure, and the example geometry shown in Fig. 5.1, if the gradient of density is positive in the x direction, then $\rho_{P3} \leq \rho_{C1}$ and $\rho_{C1} \leq \rho_{P4}$. Therefore, more particles are generated in particle cell $P4$ than in particle cell $P3$, and a newly generated particle is more likely to be placed on the righthand side of particle cell $P3$ than on the lefthand side.

Table 5.3: Ranges of current MPC and independent DSMC errors relative to full DSMC for the Mach 12, Kn_∞ 0.01 flow of N_2 over a two-dimensional cylinder.

Property	Current MPC Results	Other DSMC Results
T_{trans}	$-0.26 \leq \epsilon \leq 0.07$	$-0.04 \leq \epsilon \leq 0.05$
T_{rot}	$-0.19 \leq \epsilon \leq 0.06$	$-0.03 \leq \epsilon \leq 0.03$
ρ_{N2}	$-0.23 \leq \epsilon \leq 0.03$	$-0.02 \leq \epsilon \leq 0.02$

5.3 Baseline Accuracy and Computational Performance

With these improvements made to the MPC hybrid method and the DSMC code to which hybrid results are compared, the test case presented earlier is repeated. The error contours from this new simulation are presented in Figs. 5.13 through 5.16, and the numerical ranges are given under the “Current MPC Results” heading in Table 5.3. Both the ranges of errors seen in this most recent simulation and their extent in the upper shock region have been reduced substantially relative to the previous results. The relative errors measured in the L_2 norm have also been reduced, as shown in Table 5.4. The region of excessive positive error in T_{rot} near the outflow boundary remains, despite the improved consistency of the outflow boundary conditions and hybrid interfaces. Again, the relative errors in this region do not exceed 6%. The improved agreement in the upper shock region is due in large part to the improved consistency of the coupling procedures along the hybrid interfaces, whereas the use of consistent outflow boundary conditions reduced the errors along the outflow boundary near the axis of symmetry, where the Mach number is lowest. However, the level of accuracy achieved by the MPC method for this test case still does not meet the original objective of allowing no more than $\pm 5\%$ error relative to full DSMC. An investigation of these remaining errors is presented in the next section.

Inherent to the DSMC method is a certain level of statistical scatter resulting from the use of a relatively small number of simulator particles to represent all molecules that would be present in a real gas, and the finite number of samples that are collected

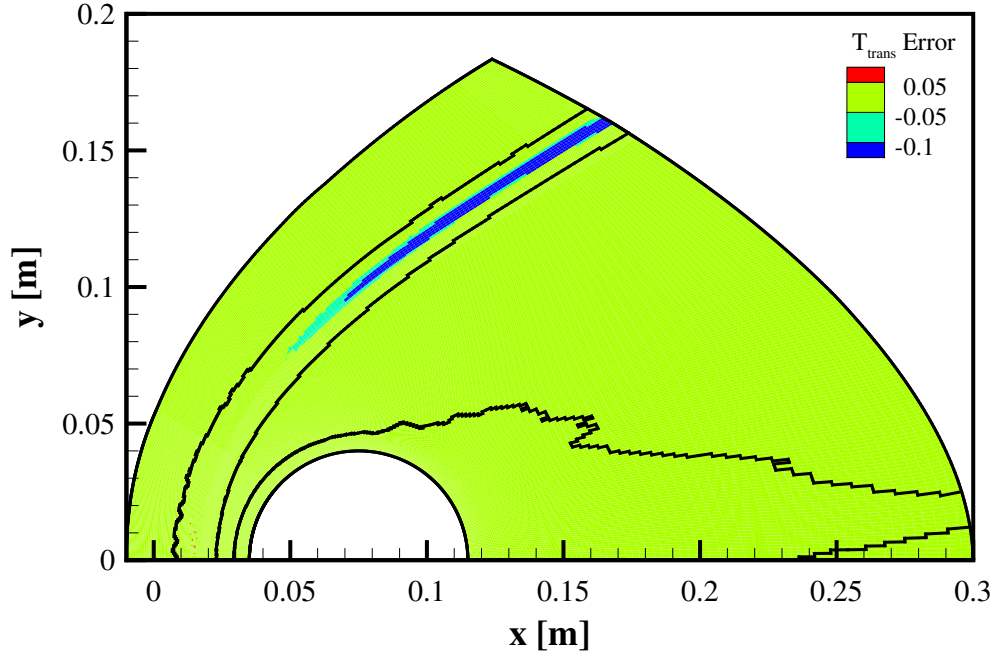


Figure 5.13: Contours of translational temperature errors of the current MPC results relative to full DSMC for the Mach 12, Kn_∞ 0.01 flow of N_2 over a two-dimensional cylinder; hybrid interfaces are shown as black lines.

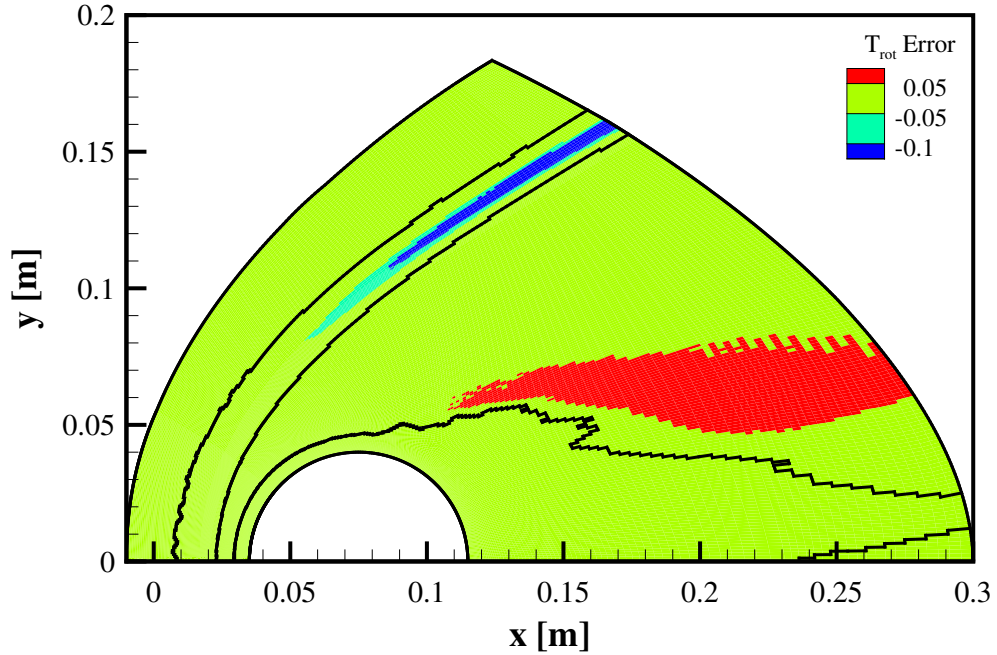


Figure 5.14: Contours of rotational temperature errors of the current MPC results relative to full DSMC for the Mach 12, Kn_∞ 0.01 flow of N_2 over a two-dimensional cylinder; hybrid interfaces are shown as black lines.

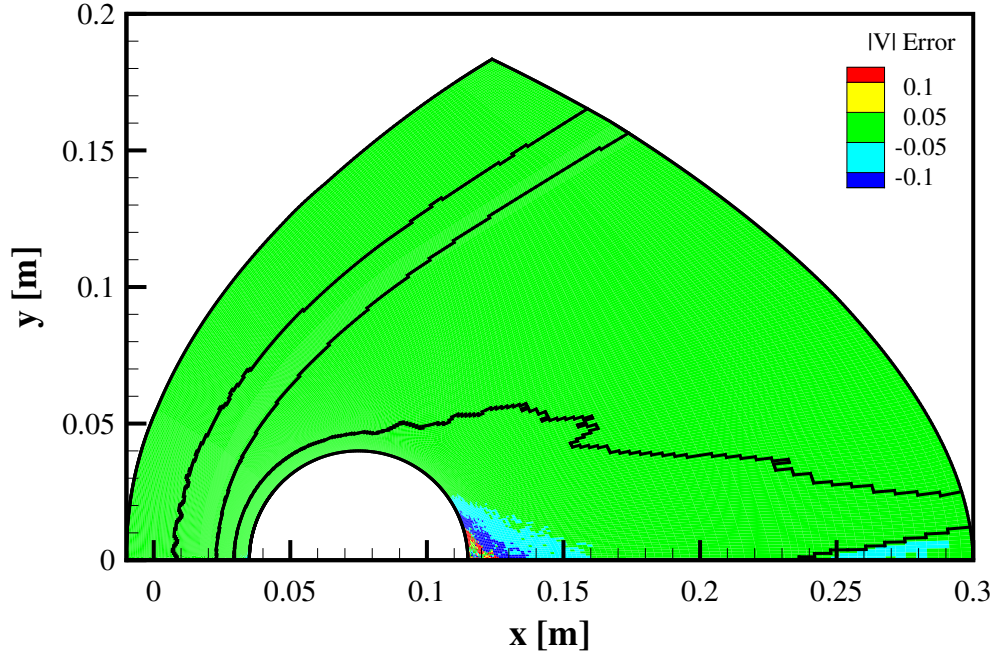


Figure 5.15: Contours of velocity magnitude errors of the current MPC results relative to full DSMC for the Mach 12, Kn_∞ 0.01 flow of N_2 over a two-dimensional cylinder; hybrid interfaces are shown as black lines.

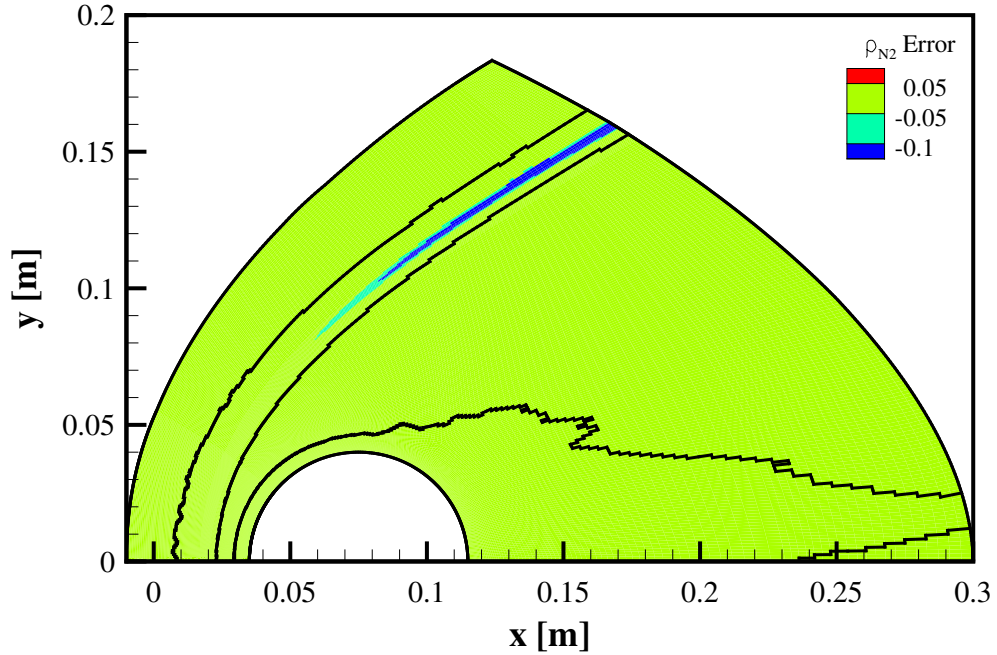


Figure 5.16: Contours of mass density errors of the current MPC results relative to full DSMC for the Mach 12, Kn_∞ 0.01 flow of N_2 over a two-dimensional cylinder; hybrid interfaces are shown as black lines.

Table 5.4: Relative errors of current MPC and independent DSMC results measured in the L_2 norm for the Mach 12, Kn_∞ 0.01 flow of N_2 over a two-dimensional cylinder.

Property	Current MPC Results	Other DSMC Results
T_{trans}	0.009	0.002
T_{rot}	0.013	0.002
$ V $	0.005	0.001
ρ_{N2}	0.007	0.001

from which macroscopic averages may be calculated. Therefore, the errors plotted in Figs. 5.13 through 5.16 should be contextualized by the level of statistical error that can be expected in the given DSMC simulation. Quantification of this statistical error is obtained by repeating the full DSMC simulation of the current test case, but with a different sequence of random numbers. Comparison of the two full DSMC simulation results yields the error contours plotted in Figs. 5.17 through 5.20. The numerical ranges of these errors are also included in Table 5.3, and the relative errors measured in the L_2 norm are given in Table 5.4. Although the differences between the MPC hybrid results and those obtained using DSMC cannot be explained by statistical scatter alone, these results do suggest that the original goal of the MPC method to maintain a physical accuracy of $\pm 5\%$ is too stringent to be met under what would be considered standard simulation conditions.

Despite these flow field errors, the first priority of the MPC hybrid method has always been the accurate prediction of surface properties. After all, these are the simulation results that are most useful to designers of hypersonic vehicles as they determine the requirements of the thermal protection system, vehicle structure, and control surfaces. In a previous study of two-dimensional, blunt-body flow using the MPC method, accurate simulation of the shock wave structure with DSMC was forgone because the resulting surface properties were found to be unaffected [67]. This, in turn, led to a reduction in computational cost because the particle regions were limited to the boundary layer and wake. Therefore, the fact that there remain re-

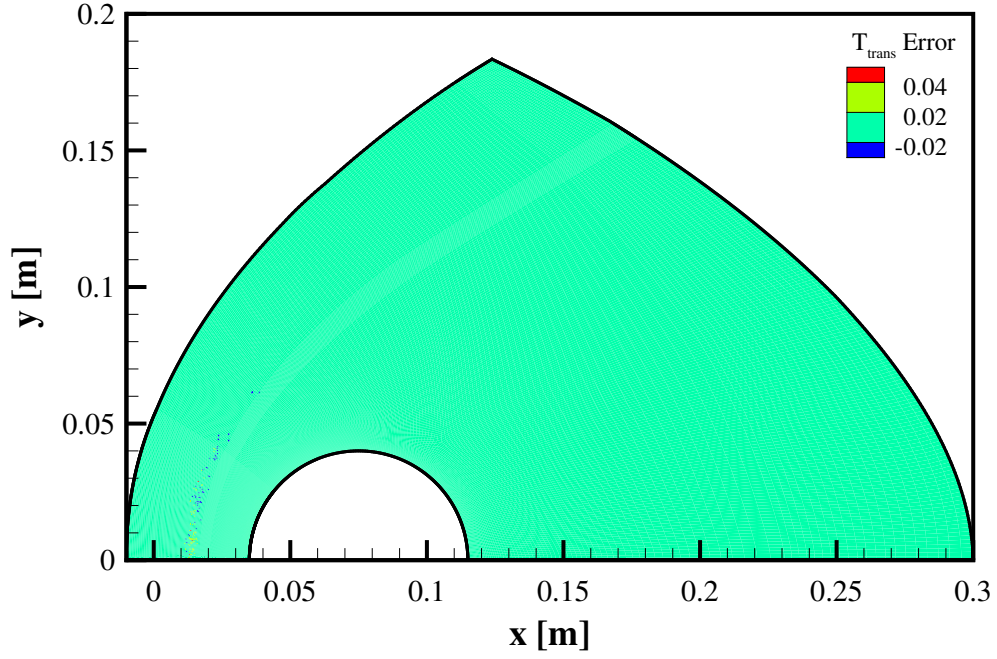


Figure 5.17: Contours of translational temperature errors between two full DSMC simulations of the Mach 12, Kn_∞ 0.01 flow of N_2 over a two-dimensional cylinder.

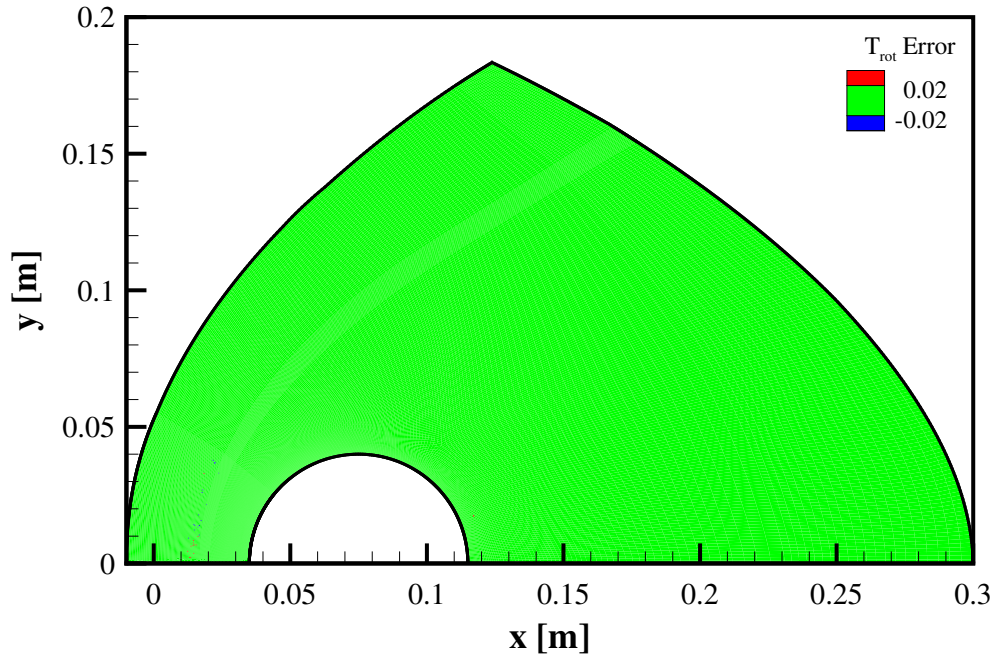


Figure 5.18: Contours of rotational temperature errors between two full DSMC simulations of the Mach 12, Kn_∞ 0.01 flow of N_2 over a two-dimensional cylinder.

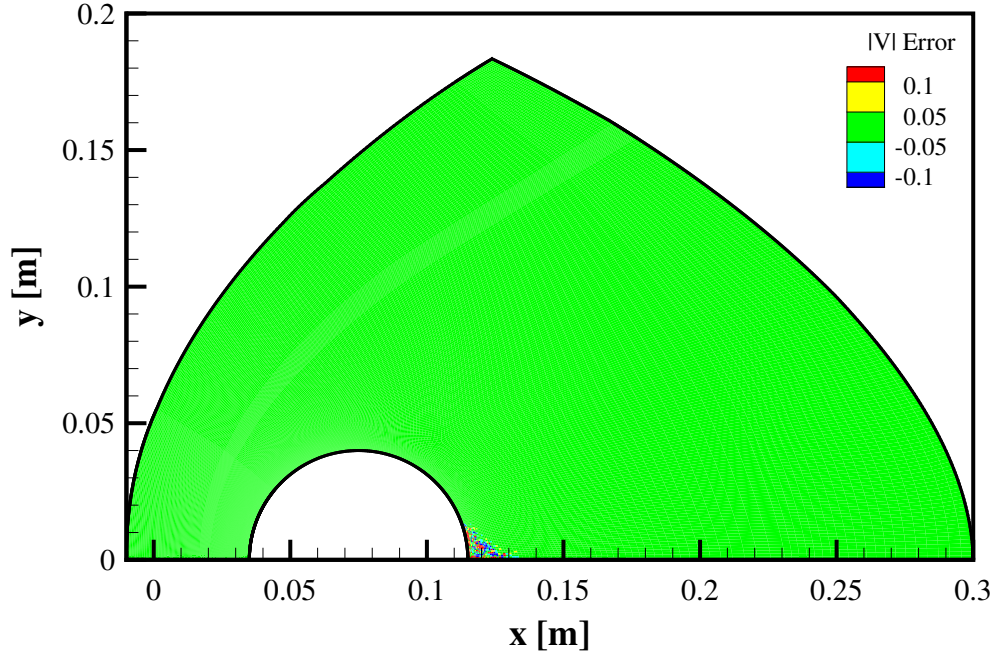


Figure 5.19: Contours of velocity magnitude errors between two full DSMC simulations of the Mach 12, Kn_∞ 0.01 flow of N_2 over a two-dimensional cylinder.

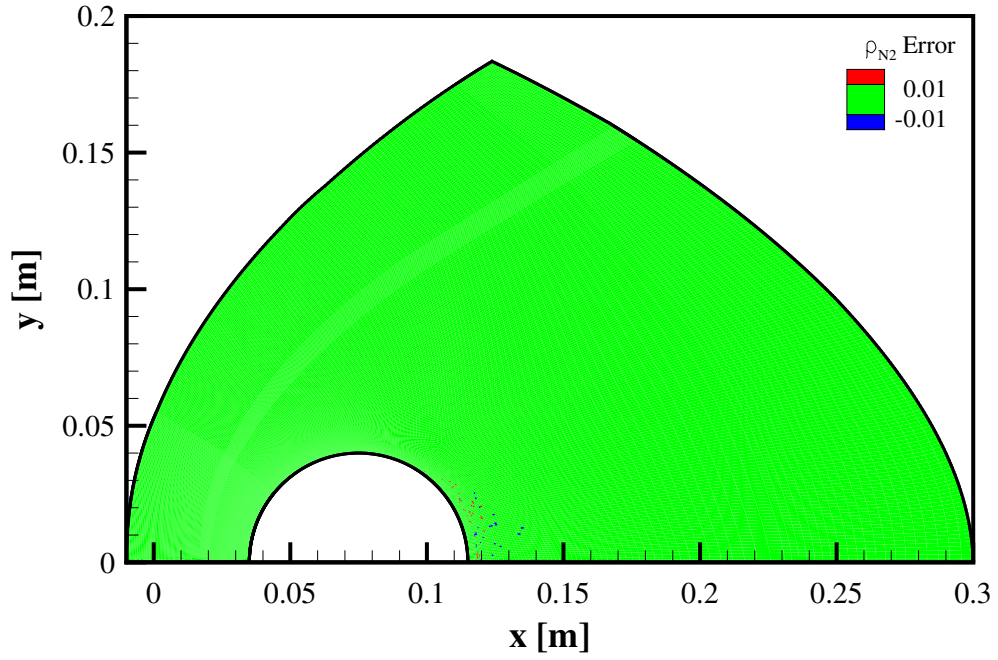


Figure 5.20: Contours of mass density errors between two full DSMC simulations of the Mach 12, Kn_∞ 0.01 flow of N_2 over a two-dimensional cylinder.

gions of large error in the flow field may not be a critical detriment to the continued development of the MPC hybrid method, as long as the surface properties retain an acceptable level of accuracy. The surface properties that are calculated to evaluate the physical accuracy of the MPC method include the surface pressure coefficient, C_p , the heat transfer coefficient, C_h , and the shear stress coefficient, C_τ , which are calculated as follows:

$$C_p = \frac{p}{\frac{1}{2}\rho_\infty V_\infty^2}, \quad (5.10)$$

$$C_h = \frac{q}{\frac{1}{2}\rho_\infty V_\infty^3}, \quad (5.11)$$

$$C_\tau = \frac{|\tau|}{\frac{1}{2}\rho_\infty V_\infty^2}. \quad (5.12)$$

The surface properties predicted by full CFD, full DSMC, and MPC hybrid simulations of this test case are plotted in Figs. 5.21 through 5.23, where an angular position of 0° corresponds to the front stagnation point. Qualitatively, there is very good agreement between MPC and full DSMC results. The profile of surface pressure coefficient predicted by DSMC appears to be almost exactly reproduced by the MPC method. The results obtained using CFD agree reasonably well with DSMC and MPC until an angular position of approximately 80° , after which point CFD overpredicts the surface pressure coefficient. As expected, Fig. 5.22 shows that the profile of heat flux coefficient predicted by full CFD is everywhere greater than that given by full DSMC. The continuum approach forces the temperature near the cylinder wall to match the isothermal boundary condition, which leads to higher temperature gradients and, in turn, larger heat fluxes. The MPC method seems to slightly underpredict the heat flux coefficient in the wake. Figure 5.23 illustrates that, because of the no-slip condition enforced by CFD, the continuum prediction of the shear stress

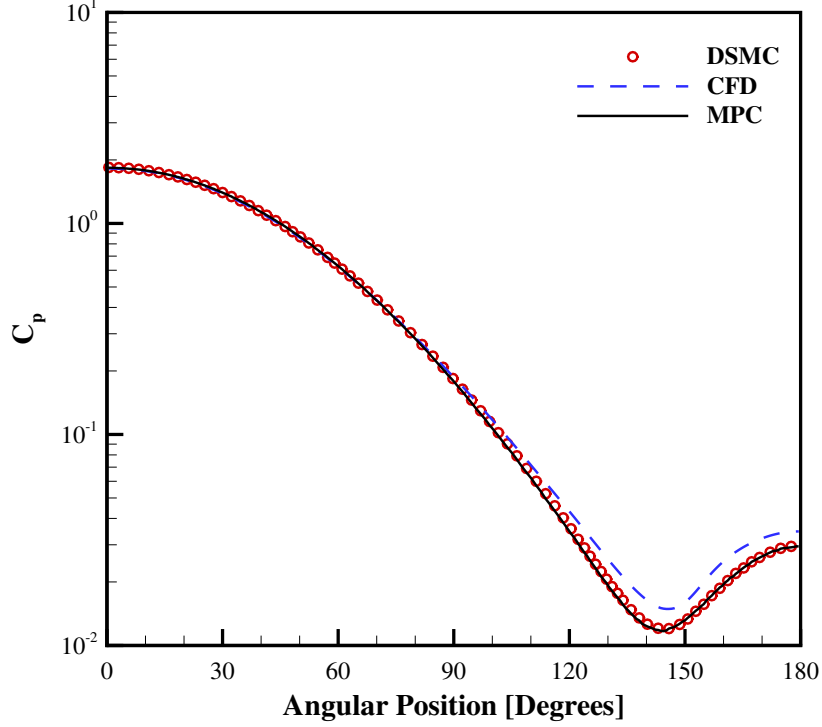


Figure 5.21: Surface pressure coefficient along the cylinder surface for the Mach 12, Kn_∞ 0.01 flow of N_2 over a two-dimensional cylinder.

coefficient exceeds those of the full DSMC and hybrid simulations, starting at an angular position of approximately 60° . The size of the wake region is also predicted to be larger in the continuum solution, as is evident by the sudden change in slope of the shear stress coefficient profile, which is based on the absolute value of wall shear stress. The MPC method is able to accurately reproduce the location of incipient separation in the wake, which is predicted by DSMC to occur at an angular position of approximately 163° .

Like the flow field properties, however, a quantitative comparison of these surface properties illustrates what are in some locations sizable differences between MPC and full DSMC. The errors in the surface properties predicted by the MPC method, calculated relative to the full DSMC results using Eq. 5.1, are plotted in Figs. 5.24 through 5.26. Again, so that these errors may be viewed in the proper context, the errors between surface properties predicted by the two independent DSMC simula-

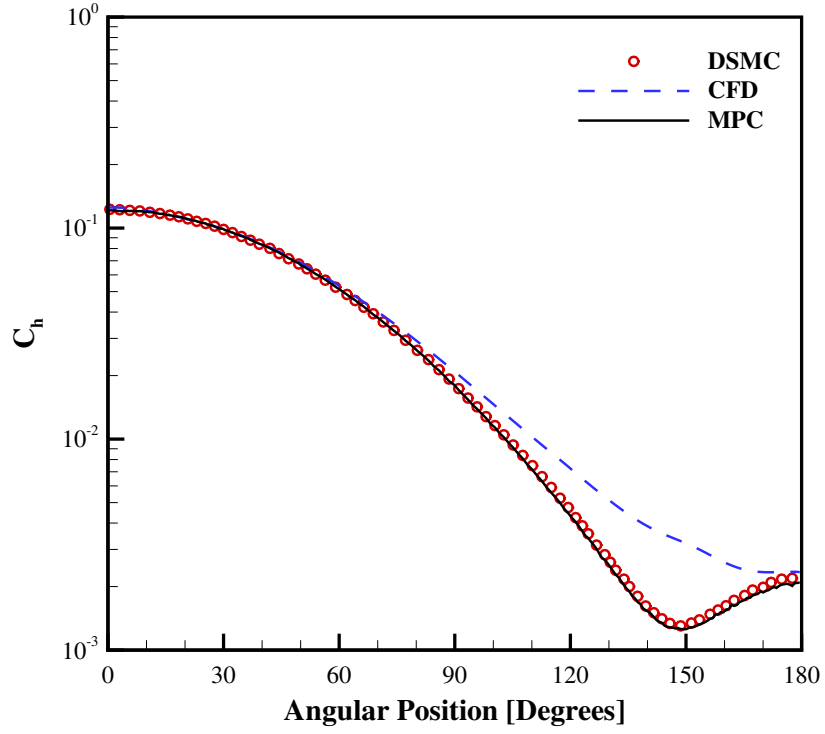


Figure 5.22: Heat transfer coefficient along the cylinder surface for the Mach 12, Kn_∞ 0.01 flow of N_2 over a two-dimensional cylinder.

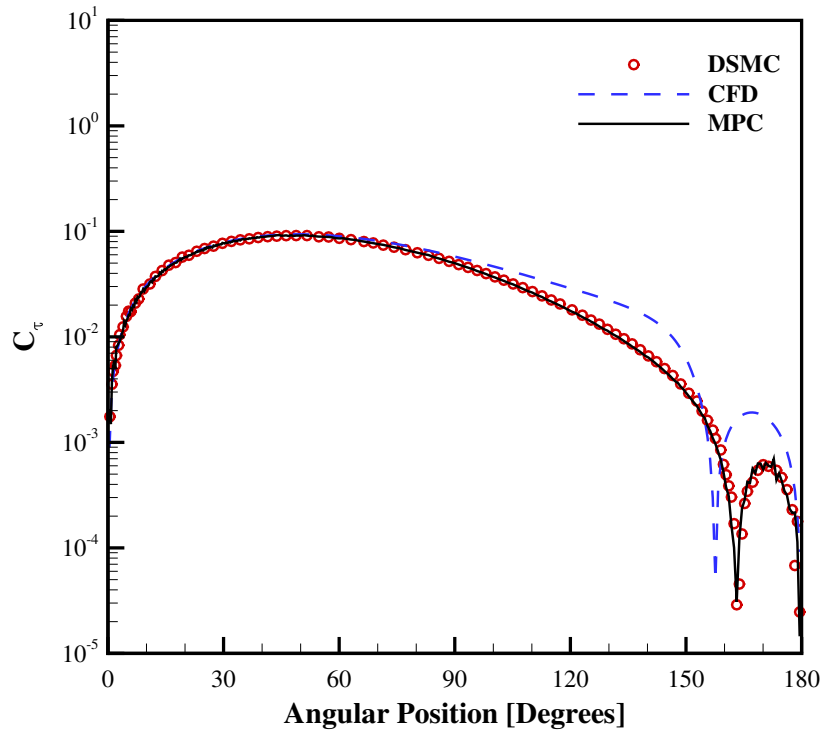


Figure 5.23: Shear stress coefficient along the cylinder surface for the Mach 12, Kn_∞ 0.01 flow of N_2 over a two-dimensional cylinder.

tions are also shown in these figures. Figure 5.24 indicates that the highest level of accuracy that should be expected for the surface pressure coefficient is $\pm 2\%$. The MPC method is able to achieve this level of accuracy in the forebody and in the wake, but predicts a systematically lower pressure coefficient between the angular positions of 60° and 150° . In the case of the heat transfer coefficient, the level of error between the two independent DSMC simulations increases slightly for increasing angular position, as seen in Fig. 5.25. This is to be expected because there are fewer particles colliding with the cylinder surface in the low-density wake than in the forebody. Also, the level of statistical scatter is observed to be greater for the heat transfer coefficient than for the surface pressure coefficient. This is also not surprising, as calculation of the heat transfer coefficient requires higher-order moments of particle thermal velocities. Like the surface pressure coefficient, the MPC method yields a systematic underprediction of the heat transfer coefficient after an angular position of approximately 80° . In Fig. 5.26, very large errors are seen between the shear stress coefficient profiles predicted by the two independent DSMC simulations, and between the MPC hybrid method and full DSMC simulation results. These surface property errors are a direct result of the large velocity errors plotted in Figs. 5.15 and 5.19. Near the stagnation point and in the wake, the directed velocity of the flow approaches zero, leading to statistical scatter that is of the same order of magnitude as the sampled average itself. This results in extremely large errors, whether considering full DSMC or the MPC hybrid method. Possible causes for the increased level of error associated with the MPC method relative to full DSMC will be discussed in the next section of this chapter.

By limiting the use of the DSMC method to nonequilibrium regions of the flow field, the MPC hybrid method achieves a solution for this test case at a reduced computational cost. Whereas a full DSMC simulation requires approximately 28.5 million particles, the particle domains of the hybrid solution require approximately

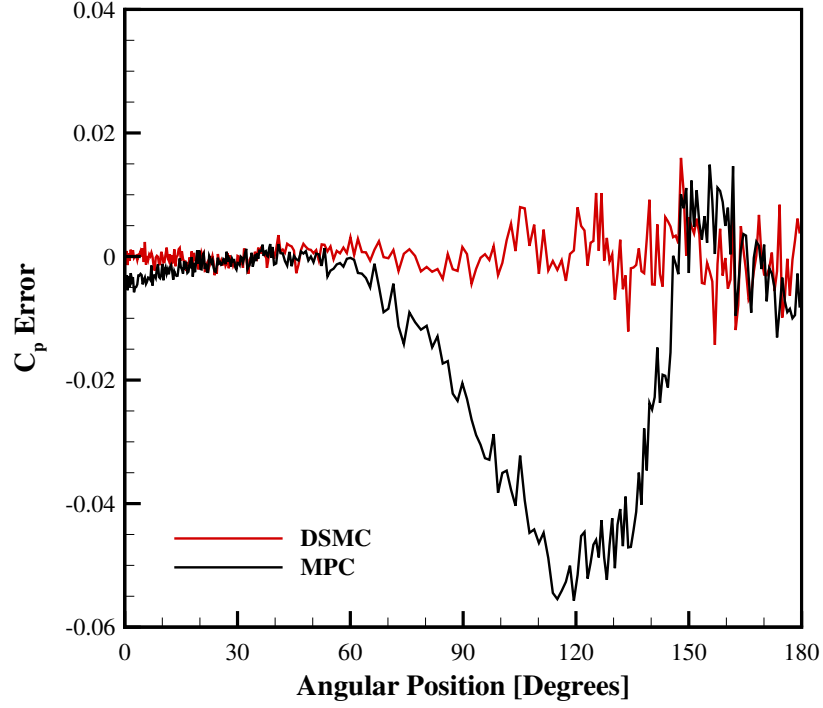


Figure 5.24: Relative errors of surface pressure coefficient along the cylinder surface for the Mach 12, Kn_∞ 0.01 flow of N_2 over a two-dimensional cylinder.

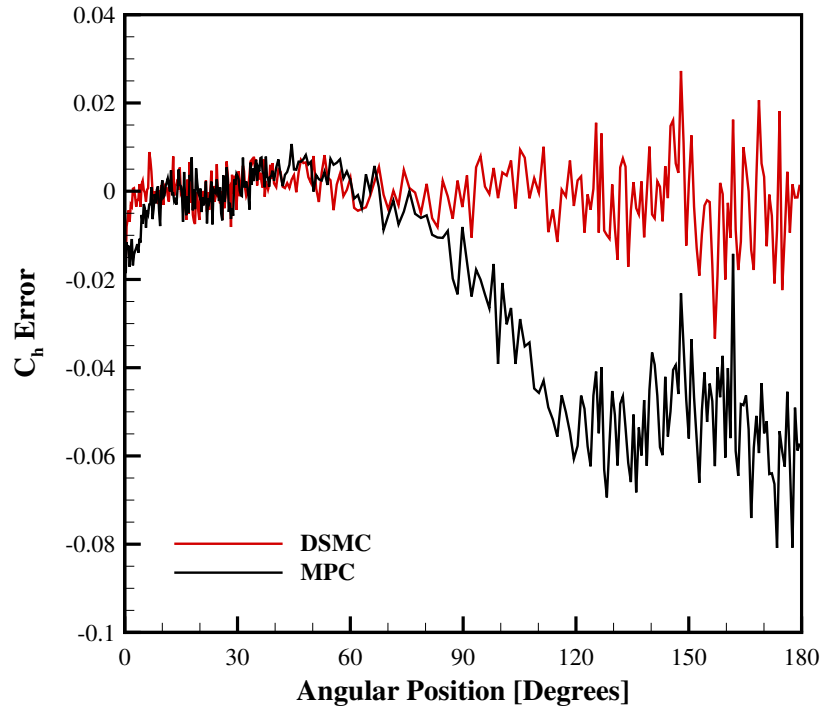


Figure 5.25: Relative errors of heat transfer coefficient along the cylinder surface for the Mach 12, Kn_∞ 0.01 flow of N_2 over a two-dimensional cylinder.

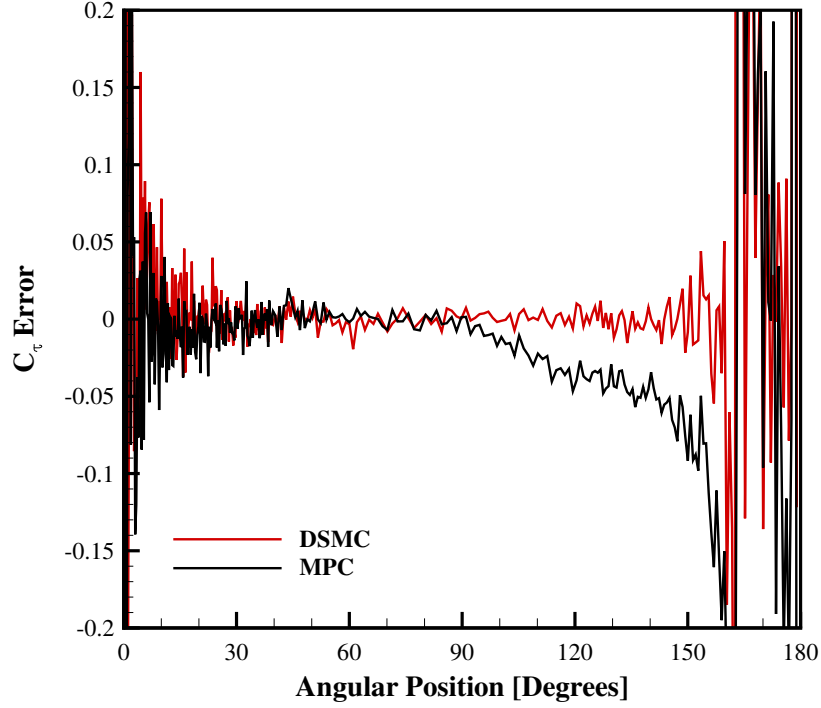


Figure 5.26: Relative errors of shear stress coefficient along the cylinder surface for the Mach 12, Kn_∞ 0.01 flow of N_2 over a two-dimensional cylinder.

12.2 million particles. It should be stressed that the same cell-based numerical weights are used in both the full DSMC and MPC simulations, and in both cases, particle information is sampled for 100,000 time steps. If the computational cost of updating the continuum regions of the flow field is assumed to be negligible compared to simulating the particle regions, and since the computational cost of a DSMC simulation is directly proportional to the number of simulator particles, this results in an ideal speedup factor of 2.34.

Simulation of this test case using DSMC requires approximately 34.7 hours of computing time on 22 processors, which equates to a total computational cost of 763 hours. Using nearly the same number of particles per processor, the MPC hybrid simulation requires approximately 31.2 hours of computing time on 10 processors, resulting in a total computational cost of 312 hours. After taking into account the cost of the initial CFD simulation obtained prior to the hybrid simulation, which requires approximately 5.7 hours of computing time on four processors prior to convergence of

the L_2 norm, the actual speedup factor of the MPC simulation is 2.27. This is slightly less than the ideal speedup factor. Even though the hybrid interfaces are automatically locked after only 4,040 DSMC time steps, whereas the DSMC simulation must run for 80,000 time steps before a steady state is reached and sampling commences, the computational cost of updating the continuum domains is not negligible.

As suggested by the number of processors used to obtain the full CFD and full DSMC simulation results, different parallel scaling metrics are important for each simulation technique. For example, Scalabrin [63] found that the LeMANS CFD solver maintains nearly ideal parallel efficiency as long as each processor is assigned at least 10,000 cells. The MONACO DSMC code maintains nearly ideal parallel efficiency when each processor is assigned at least one million simulator particles. Therefore, in a case such as the one examined here, where a grid-independent CFD solution requires approximately 41,100 cells, and more than 28 million particles are needed for a full DSMC simulation, the number of processors required to efficiently obtain a hybrid solution may be uncertain. As was suggested by Deschenes and Boyd [20], the number of processors requested is such that the same number of DSMC simulator particles per processor is used in both the MPC and full DSMC simulations. However, what was not previously noted is that this may result in a reduced parallel efficiency when updating the continuum domains of a hybrid simulation. For example, in the MPC hybrid simulation discussed here, the continuum regions include approximately 21,000 cells so that each processor is assigned half as many cells than is required for optimal parallel efficiency. This results in the computational cost of each iteration performed by the CFD module being larger than the cost of each DSMC time step.

The computational benefits of the MPC method are expected to be even more pronounced for three-dimensional simulation domains. For example, it is estimated that more than 14 million cells would be required to perform a three-dimensional simulation of the current test case using DSMC. This is calculated by determining the

Table 5.5: Computational performance statistics for the Mach 12, Kn_∞ 0.01 flow of N_2 over a two-dimensional cylinder.

	CFD	DSMC	MPC
Normalized CPU Time	1.0	33.2	14.6
Normalized Memory	1.0	11.5	6.51
# Particles	-	28.5×10^6	12.2×10^6
# Continuum Cells	41,122	-	20,967
# Particle Cells	-	58,809	32,775
# Processors	4	22	10
Sampling/Total DSMC Steps	-	100,000/180,000	100,000/104,040

dimensions of a comparable square domain from the number of particle cells needed in the two-dimensional simulation, and cubing this result to obtain the number of cells in the corresponding volume. If the average number of simulator particles per cell in the current full DSMC simulation is maintained in the three-dimensional simulation, approximately 7 billion particles would be required. Based on the number of particle cells in the current MPC simulation, this same estimation procedure predicts that approximately 2 billion particles would be needed in the corresponding three-dimensional simulation. Therefore, it is reasonable to expect a speedup factor of 3.5 if this test case were simulated in three dimensions, a further improvement over the current speedup factor in two dimensions.

In order to obtain accurate measurements of the memory requirements of full CFD, full DSMC, and MPC hybrid simulations of this test case, the Allinea MAP [1] parallel memory profiling software was employed. The MPC hybrid method is found to use a maximum of approximately $1.84GB$ of memory throughout the course of this simulation, while the full DSMC simulation required a maximum of $3.24GB$ of memory—a reduction of 43%. A summary of various computational performance metrics for those simulations presented in this section is given in Table 5.5.

5.4 Investigation of Remaining Errors

In this section, the remaining errors between the full DSMC and MPC hybrid solutions are further investigated. Although the developments discussed in Section 5.2 have improved the accuracy of the MPC method relative to full DSMC, there are a number of factors that may prevent the MPC method, or any hybrid particle-continuum method for that matter, from achieving the same level of accuracy as a full DSMC simulation. Making use of all available continuum information in the DSMC boundary cells to interpolate macroscopic properties to the constituent particle cells and, in turn, position newly generated particles, did improve the consistency of the information exchange across the hybrid interfaces. However, this is merely an approximation to what would naturally occur in a full DSMC simulation. Solution of this problem would require the same computational mesh to be used by CFD, DSMC, and MPC hybrid simulations, which would severely diminish the numerical efficiency of the hybrid approach. The use of subcells, which is commonplace in DSMC simulations, further adds to the computational mesh size discrepancy along the hybrid interfaces. In addition, on a practical level, because of the large gradients in the bow shock waves of these hypersonic, blunt-body flows, even small differences in their positions can lead to surprisingly large errors. Likewise, relatively low values for properties such as the velocity magnitude near the stagnation point and in the wake will lead to large statistical errors not only in the flow field properties in these regions, but also in surface properties, such as the shear stress coefficient.

To investigate potential causes for the large errors in the upper shock region, this Mach 12, Kn_∞ 0.01 case is again simulated using the MPC hybrid method, but with the continuum breakdown threshold value reduced from 0.05 to 0.01. This results in the entire domain, except for the freestream before the shock wave, being simulated using DSMC. The final MPC results of this test compare very well with full DSMC simulation results, with errors on the order of the statistical scatter, suggesting that

the source of the remaining flow field errors lies in the post-shock hybrid interface. It was initially believed that subsonic boundary conditions may be required along this post-shock hybrid interface. However, the fact that these large errors predominantly occur in the upper shock and not in the forebody region, where the shock wave is strongest, indicates this is not a problem, unless errors near the forebody are being propagated upwards along the shock wave.

Further analysis of the evolution of this hybrid simulation, where DSMC is used everywhere downstream of the shock wave, reveals what appears to be a different path to steady state than that observed with the simulation results presented here. A time history of the evolving translational temperature along a horizontal extraction line at $y = 0.13m$ is shown in Fig. 5.27. When there is no post-shock continuum region and the particle region is allowed to evolve without any post-shock hybrid interface imposing a boundary condition, the translational temperature first fluctuates (profile **MPC t1**), and then attains values greater than in the initial solution provided by CFD (profile **MPC t2**), before finally decreasing to its final value as more samples are taken (profile **MPC Final**). The final MPC profile plotted in Fig. 5.27 is in excellent agreement with that obtained from a full DSMC simulation. When there is a post-shock continuum region, however, with a fixed DSMC boundary condition downstream of the shock, this same transient process is not allowed.

To verify the information exchange procedures along the hybrid interfaces, especially downstream of the shock wave, a series of additional tests are performed. First, the transfer of updated boundary condition information from the particle regions to the continuum regions is evaluated. The MPC hybrid method is initialized with a full CFD solution, and particle and continuum simulation domains are identified according to the standard algorithm. The particle regions are held constant, however, while the continuum domains are updated. As expected, there is no change to the solution in the continuum domains, indicating accurate implementation of the CFD

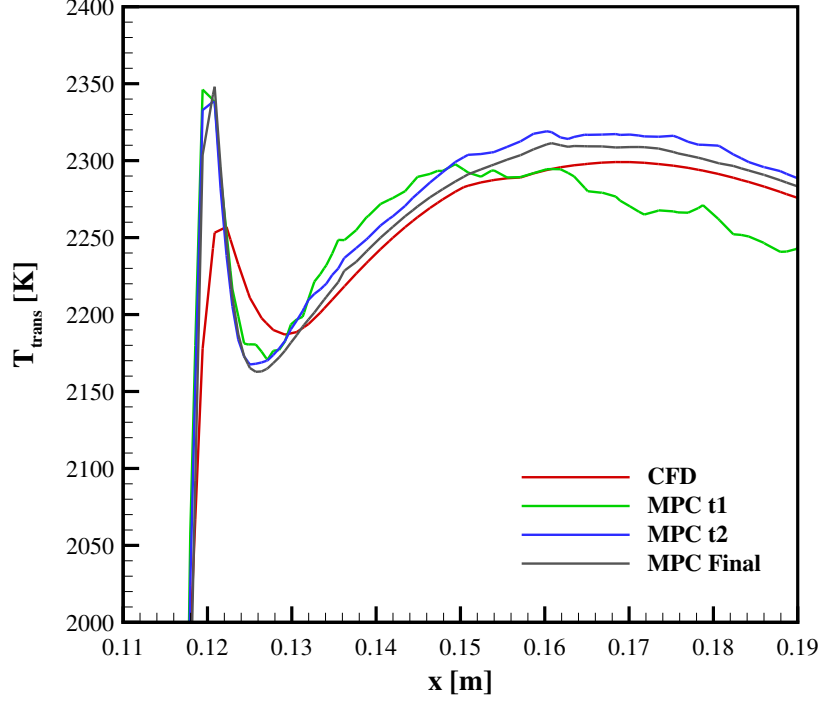


Figure 5.27: Time history of translational temperature along the $y = 0.13m$ extraction line of the Mach 12, Kn_∞ 0.01 flow of N_2 over a two-dimensional cylinder.

boundary conditions along the hybrid interfaces.

The second test required initializing the MPC hybrid method with a full DSMC solution of the flow field, and identifying particle and continuum domains from this solution. Unlike the normal manner in which the MPC method is initialized, placement of these hybrid interfaces is determined by the trusted full DSMC solution, and should therefore enable consistent information exchange between continuum and particle domains. The particle regions are then updated while the continuum regions are held constant, which allows the transfer of updated boundary condition information from the continuum regions to the particle regions to be verified. It should be noted that the computational mesh used to obtain the initial DSMC solution is refined no further by the MPC hybrid method. The DSMC simulator particles are allowed to move and collide for approximately 4,000 time steps in the regions identified to be in nonequilibrium, and then particle properties are sampled for an additional 10,000

time steps. Ideally, this procedure would result in an unchanged solution in the updated particle domains, as was seen for the continuum domains in the previous test. However, the solution in the particle regions does change, and in a manner that cannot be explained by statistical scatter alone. For example, consider Fig. 5.28, which shows the translational temperature extracted along a horizontal line at $y = 0.13m$. The red line represents the initial, full DSMC simulation result, whereas the black line represents the translational temperature after the particle domains have been further updated. There is a noticeable decrease in the post-shock translational temperature, which also shifts the shock wave location downstream.

Figure 5.28 illustrates the mechanism by which the MPC method under predicts the post-shock translational temperature relative to a full DSMC solution. This under prediction is much more noticeable in a typical MPC simulation, where the solution is initialized with CFD, the mesh in the particle regions is refined, and subcells are used, as illustrated previously in Fig. 5.9. However, even when the MPC method is initialized with a full DSMC solution, subsequent updating of the particle regions changes that solution. This is believed to be due to a number of factors. Although there is no change in the computational cell size across hybrid interfaces in this test, the use of subcells in the particle domains does cause a virtual change in the level of grid refinement between the DSMC boundary cells and the interior cells of the particle domain. Also, determination of a steady state during a standard MPC hybrid simulation involves tracking the change in the locations of the hybrid interfaces. Initially, the number of cells that comprise the particle domains increases upon recalculation of the continuum breakdown parameters until there is little change, after which point the hybrid interfaces are locked. Such an approach is less effective in areas of the flow field that evolve more slowly due to the inherently transient nature of the DSMC method. For example, the locations of the hybrid interfaces may not change in a given area because the DSMC solution is evolving on a longer time scale.

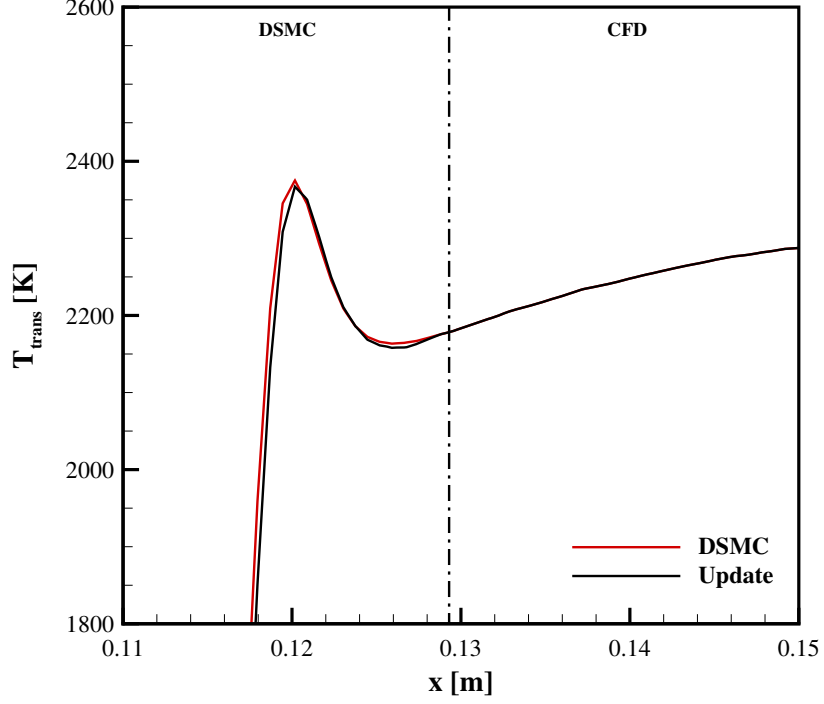


Figure 5.28: Translational temperature along the $y = 0.13m$ extraction line, before and after the particle domains have been updated from an initial, full DSMC solution of the Mach 12, Kn_∞ 0.01 flow of N_2 over a two-dimensional cylinder.

Flow field errors that remain in the wake and in the upper shock region are most likely due to this effect.

On the topic of coupling procedures, there is also concern regarding the smoothness of the hybrid interfaces themselves. Although a smoothing procedure is employed to eliminate isolated particle and continuum regions, the hybrid interfaces may still exhibit sharp features that would not be encountered along a typical inflow or outflow boundary. Every effort has been made to align the computational mesh with the bow shock wave, which in turn, promotes smooth hybrid interfaces in this region. However, as illustrated by the hybrid interface encompassing the boundary layer and wake, mesh topology alone is not a reliable solution. In the future, additional iterations of the smoothing algorithm should mitigate this effect, but most likely, a more sophisticated smoothing algorithm will be needed to adjust the initial hybrid

interfaces such that there is a smooth transition between particle and continuum simulation domains.

5.5 Interim Conclusions

In this chapter, the accuracy and computational performance of the MPC hybrid method relative to full DSMC was evaluated in a detailed and consistent manner. By mapping the continuum solution on to the more refined particle mesh layer and making cell-by-cell comparisons between flow field solutions obtained using DSMC and the MPC method, a comprehensive understanding of both the location and magnitude of errors is achieved. Higher than anticipated errors in the upper shock wave region and along the outflow boundary near the symmetry axis in a test case of hypersonic, blunt-body flow suggested several improvements should be made to the original hybrid method. Specifically, these improvements involved the implementation of consistent supersonic outflow boundary conditions, and the use of additional continuum information in the DSMC boundary cells along hybrid interfaces for more accurate particle generation. These improvements were shown to decrease both the range and extent of errors throughout the flow field. Further investigation of the statistical scatter associated with the full DSMC solution of this particular flow field indicates that the original goal of obtaining MPC hybrid results that are accurate to within $\pm 5\%$ is unreasonable. Instead, the goal of the MPC hybrid method should be to achieve a physical accuracy that is within the statistical scatter associated with a corresponding full DSMC simulation.

The level of error that remains after the aforementioned improvements were made cannot be substantiated by statistical scatter alone, and may be attributed to several other factors. These include differences in mesh refinement between the particle and continuum domains along the hybrid interfaces, where information must be exchanged between the DSMC and CFD modules of the MPC method. The use of more refined

cells and subcells in the particle regions allows macroscopic fluid properties to vary over much smaller distances than what is possible in the adjacent continuum cells. In addition, the transient nature of the DSMC method itself poses challenges for the automated MPC algorithm, especially in regions of the flow field that evolve more slowly due to reduced collisionality of simulator particles, such as the wake. Nevertheless, the accuracy achieved by the MPC method is on the order of the statistical scatter of DSMC throughout the majority of the flow field. In terms of surface properties, the MPC method is able to reproduce full DSMC results to within $\pm 10\%$ except in regions where statistical scatter overshadows the particle average of interest, as is the case near the stagnation point and in the wake.

CHAPTER VI

Accurate Prediction of Rotational Nonequilibrium Effects

During the initial development of the MPC hybrid method, the ability to simulate rotational nonequilibrium effects in the continuum module had not yet been incorporated. Therefore, not only did the hybrid interfaces need to be placed in regions of translational equilibrium, but also in regions where it could be accurately assumed that the translational and rotational energy modes were in equilibrium. In the one-dimensional shock wave study that was first performed using the MPC method [65], the gradient-length local Knudsen number with a threshold value of 0.05 was found to accurately position the pre-shock and post-shock hybrid interfaces, despite its inability to directly account for thermal nonequilibrium effects. However, it was noted in Ref. [65] that an additional parameter may be needed in future MPC hybrid simulations to specifically indicate regions of rotational nonequilibrium so that the particle module would be used rather than the continuum module. In a more recent study of transitional, hypersonic flow over a two-dimensional cylinder, Schwarzen-truber, *et al.* [66] proposed the following parameter to be used in conjunction with the gradient-length local Knudsen number based on mass density, translational temperature, and velocity magnitude:

$$Kn_{ROT-NEQ} = 5 \times \frac{T_{trans} - T_{rot}}{T_{rot}}. \quad (6.1)$$

The parameter in Eq. 6.1 is reminiscent of the translational-rotational energy exchange source term of the rotational energy conservation equation introduced in Chapter II, and further detailed in Chapter IV. Because the difference between the translational and rotational temperatures drives the exchange of energy between these modes in the continuum module, it was proposed that this difference should also be used to predict rotational nonequilibrium. However, it does not capture the possibility of a nonequilibrium rotational EDF. The $Kn_{ROT-NEQ}$ parameter was found to be critical for accurately predicting the location of the post-shock hybrid interface in transitional, hypersonic, blunt-body flows. In order to avoid the use of another parameter, attempts were made to enlarge the particle region surrounding the shock by reducing the Kn_{GLL} threshold value. However, the resulting locations of the other hybrid interfaces were far too sensitive to the threshold value for this to be a viable option. Therefore, this new parameter was employed with the same threshold value of 0.05 so that hybrid interfaces were placed in regions where the relative difference between the translational and rotational temperatures was less than 1%.

Later, when a separate rotational energy equation was included in LeMANS [38], and the MPC method was extended to simulate rotational nonequilibrium effects in simple gases [22], the matter of predicting thermal nonequilibrium was revisited. Because the continuum domain accounted for differences between the translational and rotational temperatures, the coefficient in Eq. 6.1 was relaxed to a factor of 0.5. An additional gradient-length local Knudsen number was also calculated with respect to the rotational temperature because of the presence of the rotational temperature gradient in the calculation of the rotational heat flux. However, extensive parametric studies concerning the coefficient in Eq. 6.1 and the threshold value appropriate for

these additional thermal nonequilibrium parameters were not published. It was also commonplace to manually enlarge the particle region surrounding the boundary layer of a transitional, hypersonic, blunt-body flow to achieve better agreement between surface properties predicted by the MPC method and those of full DSMC simulations.

Because of the ambiguity associated with this original $Kn_{ROT-NEQ}$ parameter, and in order to improve the *automatic* detection of both translational and thermal nonequilibrium effects in the MPC method, a new rotational nonequilibrium parameter is proposed in this chapter. This new parameter is evaluated in the context of transitional, hypersonic, blunt-body flows involving both a simple gas and a mixture of chemical species. Finally, the accuracy of the MPC method when employing this new parameter relative to a full DSMC simulation is determined, and compared to the accuracy achieved by the MPC method with the original $Kn_{ROT-NEQ}$ parameter.

6.1 A New Rotational Nonequilibrium Detection Parameter

Although the gradient-length local Knudsen number is empirical and, therefore, not guaranteed to be capable of predicting translational nonequilibrium in all cases, one of its benefits is that it is physically intuitive. When the gradient-length local Knudsen number has a small value, it is known that a continuum approach such as CFD is a physically accurate simulation technique. However, when the the gradient-length local Knudsen number has a large value, the results from a continuum approach become less accurate and a kinetic theory-based approach must be used. It is desirable for a thermal nonequilibrium detection parameter to invoke the same physical intuition as the gradient-length local Knudsen number.

As described in Chapter IV, the product of the rotational collision number, Z_{rot} , and the mean collision time, τ_c , is the characteristic relaxation time of the rotational energy mode, τ_{rot} . If rotational nonequilibrium effects were ignored altogether, then τ_{rot} would be equivalent to τ_c because *every* collision would allow for the translational

and rotational energies to be redistributed according to the degrees of freedom associated with each mode. However, in reality, only one out of every Z_{rot} collisions results in translational-rotational energy exchange, and rotational nonequilibrium is a direct consequence of this collision inefficiency. It is reasonable, therefore, that any reliable means of detecting rotational nonequilibrium effects should include these characteristic quantities. The new parameter that is proposed and evaluated in this chapter is

$$Kn_{rot} = \lambda_{rot} \left| \frac{\nabla T_{rot}}{T_{rot}} \right| = (\tau_{rot}) \sqrt{\frac{8RT_{trans}}{\pi}} \left| \frac{\nabla T_{rot}}{T_{rot}} \right| = (Z_{rot}) \lambda \left| \frac{\nabla T_{rot}}{T_{rot}} \right|, \quad (6.2)$$

which is the same as the gradient-length local Knudsen number evaluated as a function of T_{rot} , except for the presence of the rotational collision number. This is not the same as simply using a different threshold value for $Kn_{GLL}(T_{rot})$ because the rotational collision number is a function of the translational temperature. The product of Z_{rot} and λ has the physical significance of being the average distance a simulator particle travels prior to undergoing a rotationally inelastic collision. Therefore, a *rotational* mean free path is being used to represent the microscopic length scale of interest in this new parameter.

In the interest of thoroughness, the efficacy of the current continuum breakdown parameters should also be evaluated periodically as the capabilities of the MPC hybrid method continue to be developed. As such, this new parameter is evaluated alongside those currently used to detect continuum breakdown. The results of this analysis, as applied to simulations of both a simple gas and a mixture of chemical species, are presented in the next section. Because the original $Kn_{ROT-NEQ}$ rotational energy nonequilibrium parameter was originally employed to extend the post-shock hybrid interface further downstream, the bow shock region is the focus of the following analysis. However, it will also be shown that the newly proposed parameter given

in Eq. 6.2 is also capable of automatically determining an appropriate location for the hybrid interface that demarcates the boundary layer in a transitional, hypersonic, blunt-body flow.

6.2 Initial Placement of Hybrid Interfaces

As was done in Ref. [14], where the gradient-length local Knudsen number was first proposed for detecting failure of the continuum assumptions of the Navier-Stokes equations, the errors between full CFD and full DSMC simulations are calculated and compared to current measures of continuum breakdown employed in the MPC method and the newly proposed Kn_{rot} parameter. This is done not only to determine an appropriate threshold value for this new rotational nonequilibrium parameter, but also to re-evaluate the efficacy of the gradient-length local Knudsen number in consideration of recent extensions to the MPC hybrid method.

6.2.1 Simple Gas Study

The first case used to investigate the prediction of rotational nonequilibrium effects using the new parameter given in Eq. 6.2 is that of a Mach 12, Kn_∞ 0.01 flow of N_2 over a two-dimensional cylinder. This is the same case simulated in Chapter V. For simplicity of evaluation, the specific cases studied in this chapter ignore excitation of the vibrational energy mode. In order to determine whether or not a given continuum breakdown parameter is effective, the regions of the flow field in which the continuum and molecular descriptions differ must first be identified. Because previously noted failures of the gradient-length local Knudsen number have occurred in the fore body, full CFD and full DSMC simulation results are compared along the stagnation streamline and two additional extraction lines, as illustrated in Fig. 6.1.

The error, ϵ , between full CFD and full DSMC simulation results is defined as

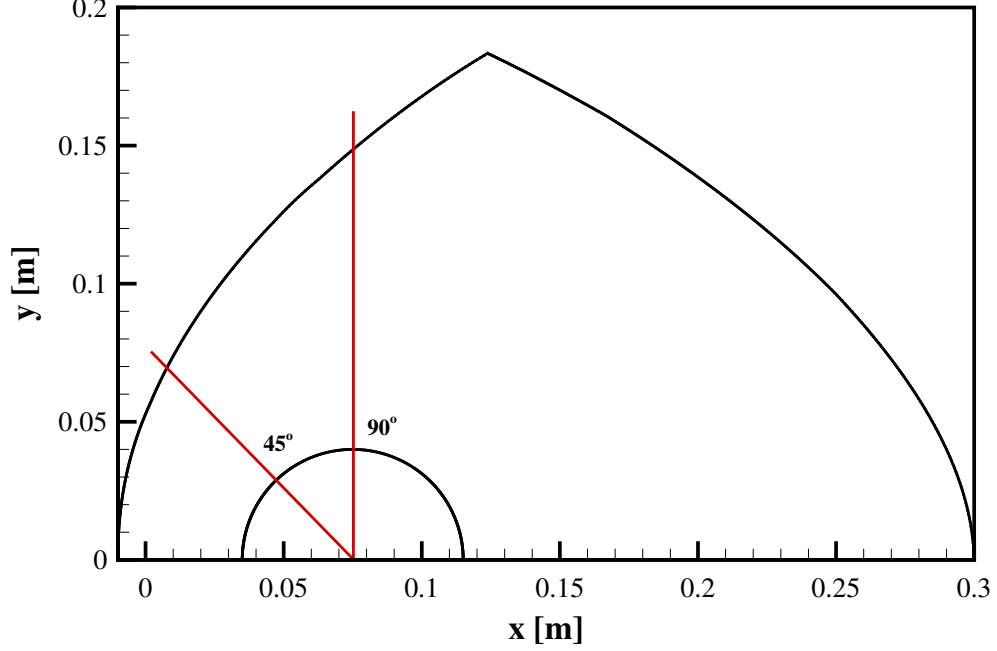


Figure 6.1: Computational domain and data extraction lines.

$$\epsilon = \frac{Q_{CFD}}{Q_{DSMC}} - 1, \quad (6.3)$$

where Q is any macroscopic property of interest. The errors in translational temperature, rotational temperature, velocity magnitude, and mass density along the stagnation streamline are plotted against the distance from the cylinder surface, normalized by the cylinder radius, in Fig. 6.2. Two dashed black lines are also plotted to indicate the upper and lower error bounds of $\pm 5\%$. Note that even though this level of accuracy was found to be too strict in Chapter V due to the statistical error associated with the DSMC method, because this was the accuracy goal used during the original assessment of the gradient-length local Knudsen number, it will continue to be used here.

According to Fig. 6.2, the hybrid interfaces should intersect the stagnation streamline such that DSMC is used between 0.319 and 0.646 radii from the cylinder surface to accurately simulate the strong nonequilibrium effects in the shock wave. There should also be a particle region enclosing the surface of the cylinder in order to ac-

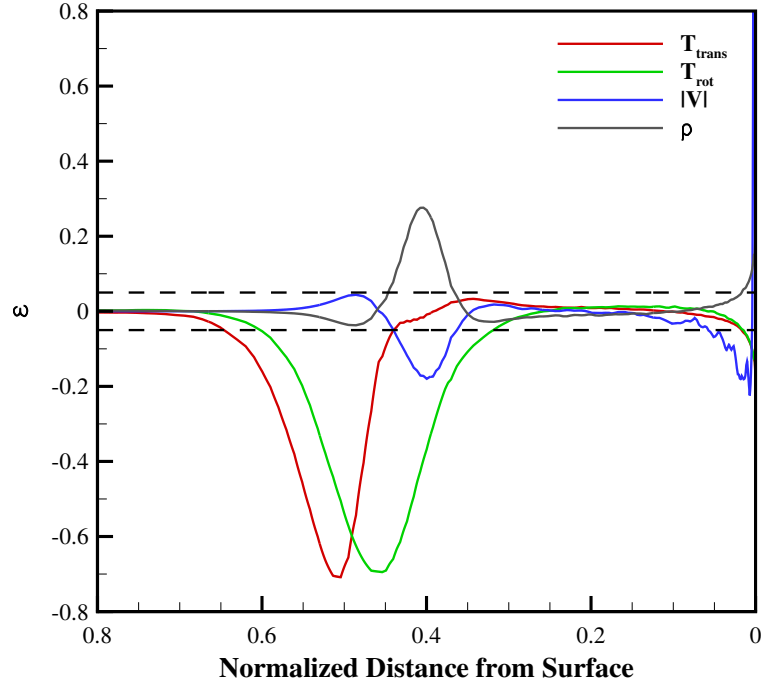


Figure 6.2: Errors between full CFD and full DSMC results along the stagnation streamline for the Mach 12, Kn_∞ 0.01 flow of N_2 over a two-dimensional cylinder.

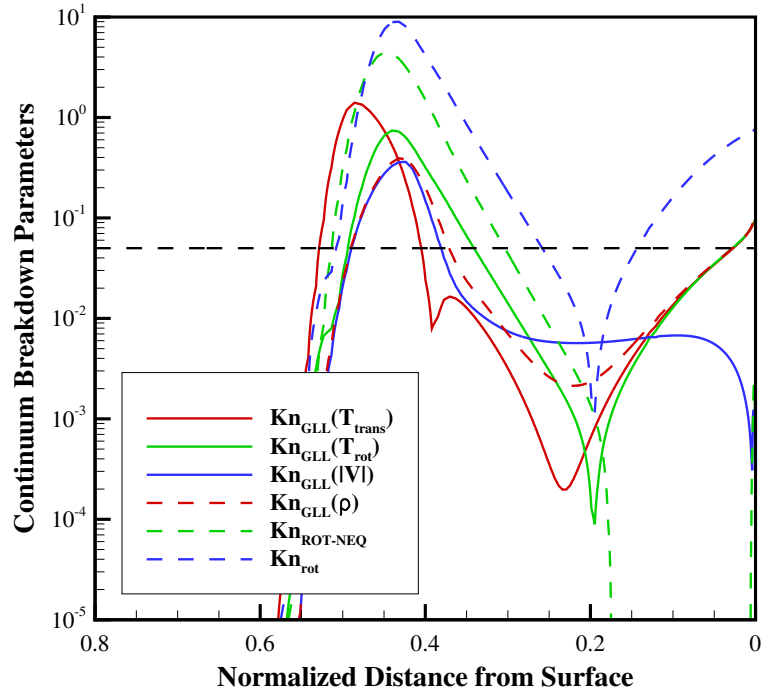


Figure 6.3: Continuum breakdown parameters based on a full CFD solution along the stagnation streamline for the Mach 12, Kn_∞ 0.01 flow of N_2 over a two-dimensional cylinder.

curately simulate the boundary layer, which extends to 0.057 radii from the cylinder surface. The values of the various continuum breakdown parameters currently employed in the MPC hybrid method, and the new Kn_{rot} parameter, are plotted along the stagnation streamline in Fig. 6.3. These continuum breakdown parameters are calculated from the full CFD solution of this flow field. Therefore, in an MPC hybrid simulation, these results would be used for initial placement of the hybrid interfaces.

Due to the underestimation of the shock thickness by the Navier-Stokes equations, the location upstream of the shock wave where the differences between CFD and DSMC first exceed $\pm 5\%$ is not accurately predicted by the continuum breakdown parameters shown in Fig. 6.3. In this test case, the value of the gradient-length local Knudsen number based on translational temperature exceeds the threshold value of 0.05 at a normalized distance of 0.529 from the cylinder surface. This would place the pre-shock hybrid interface much further downstream than required for accurate and consistent exchange of information between the particle and continuum domains. The inability of the gradient-length local Knudsen number to accurately predict the onset of continuum breakdown at the shock front has been noted by Wang and Boyd [88], and if the initial hybrid interfaces were not adjusted as the hybrid solution evolved, this would lead to inaccurate results. However, because these continuum breakdown parameters are re-calculated periodically throughout the simulation, and the hybrid interfaces are moved accordingly, this has not posed a problem for past simulations. As will be shown later in this chapter, the pre-shock hybrid interface will be automatically repositioned to a near-equilibrium region as the simulation evolves, obviating any concerns about the initial placement of this hybrid interface. Thus, the location of the pre-shock hybrid interface as predicted by the initial CFD solution will not be discussed further.

Whereas the pre-shock hybrid interface moves upstream substantially during the course of a hybrid simulation, the post-shock and boundary layer hybrid interfaces

experience minimal change. Therefore, their initial placement relative to regions in which full CFD and full DSMC simulation results disagree gives greater insight to the effectiveness of these continuum breakdown parameters. According to Fig. 6.2, the post-shock hybrid interface should be placed at a maximum of 0.319 radii from the cylinder surface in order to envelope the shock wave in a particle region. Fig. 6.3 illustrates that without some indicator of rotational nonequilibrium effects, the post-shock hybrid interface would be located at a normalized distance of 0.341, where significant errors between CFD and DSMC are present. Thus, an additional parameter is required. The value of the $Kn_{ROT-NEQ}$ parameter decreases below 0.05 at a normalized distance of 0.304, placing the post-shock hybrid interface in an appropriate position slightly downstream of the shock.

Because of the isothermal boundary condition enforced at the cylinder surface in the CFD simulation, the value of the $Kn_{ROT-NEQ}$ parameter in the boundary layer is much smaller than the threshold value of 0.05. The gradient-length local Knudsen number also fails to position the boundary layer hybrid interface upstream of the location where CFD and DSMC begin to deviate by more than $\pm 5\%$. Whereas the error in the velocity magnitude exceeds the lower error bound at a normalized distance of 0.057, the gradient-length local Knudsen number based on the rotational temperature exceeds the threshold value of 0.05 at a normalized distance of 0.028—much too close to the cylinder surface.

Focusing now on the value of Kn_{rot} along the stagnation streamline, even though an appropriate threshold value has yet to be determined, it can be seen from Fig. 6.3 that this new parameter offers an advantage over the original $Kn_{ROT-NEQ}$ parameter near the surface of the cylinder. An optimal choice for the threshold value for this new parameter would maintain a similar position for the post-shock hybrid interface while increasing the size of the boundary layer particle region relative to the other continuum breakdown parameters. When the value of $Kn_{ROT-NEQ}$ decreases below

0.05 downstream of the shock wave, the Kn_{rot} parameter has a value of approximately 0.2. Near the cylinder surface, Kn_{rot} takes this value at a normalized distance of 0.090, which would enlarge the particle region surrounding the boundary layer such that the hybrid interface is placed in a near-equilibrium region of the flow field, based on the level of agreement exhibited in Fig. 6.2. Therefore, comparison of the full CFD and full DSMC results along the stagnation streamline, along with the values of the various continuum breakdown parameters, shows that the new Kn_{rot} parameter with a threshold value of 0.2 may be an effective alternative to $Kn_{ROT-NEQ}$.

The errors between full CFD and full DSMC along the 45° extraction line are plotted in Fig. 6.4. Again, the strong nonequilibrium effects in the shock wave and the boundary layer are apparent in this plot. A notable difference between Fig. 6.4 and Fig. 6.2 is the profile of velocity magnitude error near the cylinder surface. The no-slip boundary condition is enforced along the entire cylinder surface in the CFD simulation, whereas DSMC inherently allows for velocity slip. At the stagnation point, the velocity magnitude must go to zero in both simulations, so that the scatter associated with the DSMC solution can be of the same order as the velocity itself. This leads to large oscillations in Fig. 6.2 near the cylinder surface. The velocity tangent to the cylinder surface at the point where it intersects the 45° extraction line is nonzero according to the full DSMC results, leading to no oscillations in the velocity magnitude error near the cylinder surface in Fig. 6.4.

According to the errors plotted in Fig. 6.4, the rotational temperature predicted by CFD is the last macroscopic property to come into agreement with DSMC downstream of the shock wave. This occurs at a normalized distance of 0.472 from the cylinder surface. The inability of CFD to accurately simulate the nonequilibrium effects in the boundary layer is confirmed by errors in all macroscopic properties of interest exceeding $\pm 5\%$ at nearly the same distance from the cylinder surface. The error in translational temperature exceeds the lower error bound at a normalized distance of

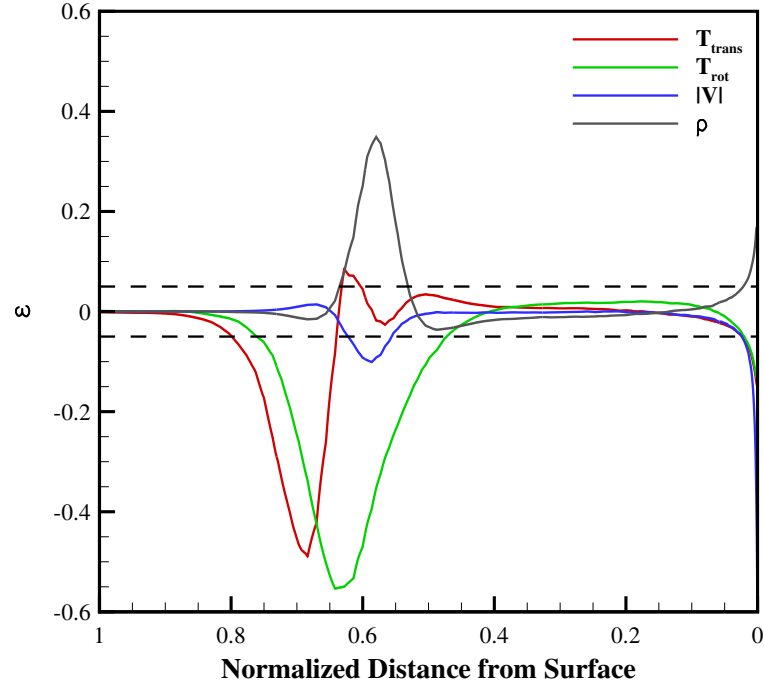


Figure 6.4: Errors between full CFD and full DSMC results along the 45° extraction line for the Mach 12, Kn_∞ 0.01 flow of N_2 over a two-dimensional cylinder.

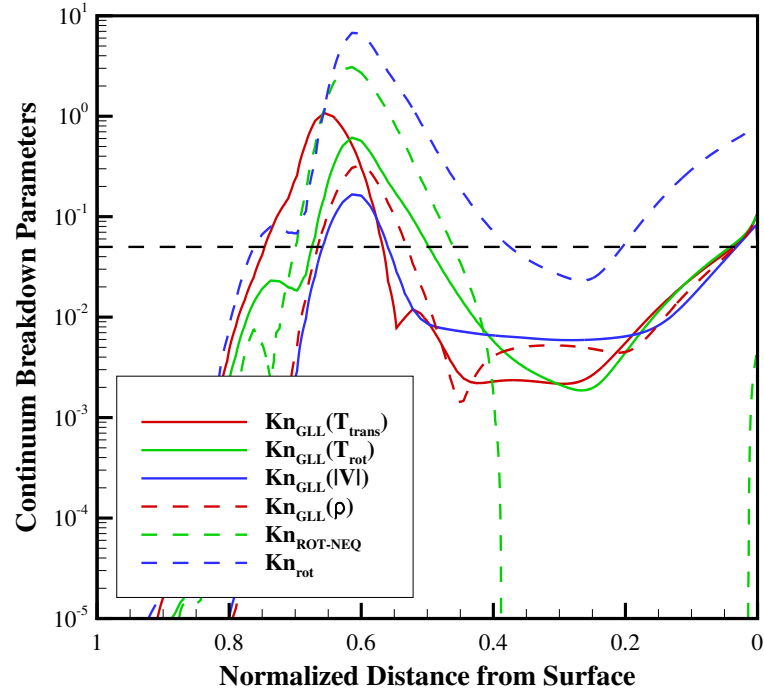


Figure 6.5: Continuum breakdown parameters based on a full CFD solution along the 45° extraction line for the Mach 12, Kn_∞ 0.01 flow of N_2 over a two-dimensional cylinder.

0.024. As was the case along the stagnation streamline, the original $Kn_{ROT-NEQ}$ parameter accurately predicts the location of the post-shock hybrid interface at a distance of 0.461 radii from the cylinder surface, but fails to predict the need for a particle region in the boundary layer. This is illustrated in Fig. 6.5. However, the value of $Kn_{GLL}(T_{rot})$ exceeds the threshold value of 0.05 at a normalized distance of 0.042 from the cylinder surface, which does provide a conservative estimate of the thickness of the boundary layer region. Therefore, according to these results alone, the combination of the gradient-length local Knudsen number and $Kn_{ROT-NEQ}$ is sufficient for accurately positioning hybrid interfaces in near-equilibrium regions of the flow field along the 45° extraction line. Use of the new Kn_{rot} parameter (with a threshold value of 0.2) in place of $Kn_{ROT-NEQ}$ would only serve to provide a more conservative estimate of rotational nonequilibrium, as the post-shock and boundary layer hybrid interfaces would be placed at normalized distances of 0.452 and 0.127, respectively.

Figure 6.6 shows the errors between full CFD and full DSMC simulation results along the 90° extraction line. As was the case with the other extraction lines, the rotational temperature predicted by CFD is the last macroscopic property to come into agreement with DSMC in the post-shock region at a normalized distance of 1.29 from the cylinder surface. Strong nonequilibrium effects in the boundary layer are first indicated by the error in velocity magnitude, which exceeds the lower error bound approximately 0.102 radii from the cylinder surface. The $Kn_{ROT-NEQ}$ parameter and the gradient-length local Knudsen number are able to accurately predict the initial placement of the post-shock and boundary layer hybrid interfaces at normalized distances of 1.28 and 0.127, respectively. Again, the new Kn_{rot} parameter provides a more conservative measure of rotational nonequilibrium, predicting that the post-shock hybrid interface be located at a normalized distance of 1.27 from the cylinder and the boundary layer hybrid interface be placed approximately 0.326 cylinder radii

from the surface.

Based on these simple gas simulation results, the benefit of using the Kn_{rot} rotational nonequilibrium parameter instead of the $Kn_{ROT-NEQ}$ is most evident along the stagnation streamline. In order to present a more complete evaluation of this new parameter, and because one of the main objectives of the current work is to extend the MPC method's capabilities to include mixtures of chemical species, a gas comprised of 50% N_2 /50% N (by mole) is examined in the next section.

6.2.2 Gas Mixture Study

The second flow field of interest in this evaluation of the new Kn_{rot} rotational nonequilibrium parameter is that of a Mach 10, Kn_∞ 0.01 flow of a 50% N_2 /50% N (by mole) gas mixture over a two-dimensional cylinder. The mixture mean free path is calculated as

$$\lambda = \sum_{i=1}^s \frac{n_i}{n} \left\{ \sum_{j=1}^s \left[\pi d_{ref,ij}^2 n_j \left(\frac{T_{ref}}{T_{trans}} \right)^{\omega_{ij}-1/2} \left(1 + \frac{m_i}{m_j} \right)^{1/2} \right] \right\}^{-1}, \quad (6.4)$$

in accordance with the VHS collision model. With a freestream temperature of $217.45K$, and the reference collision diameters given in Appendix A, this results in freestream densities of $4.522 \times 10^{-5} kg/m^3$ and $2.261 \times 10^{-5} kg/m^3$ for N_2 and N , respectively. The freestream velocity is $3,594 m/s$, and the cylinder surface employs an isothermal boundary condition where the temperature is maintained at $1,000K$. It should be noted that calculation of the new Kn_{rot} rotational nonequilibrium parameter for gas mixtures employs the mixture average rotational relaxation time as calculated using Eq. 4.40, and the specific gas constant, R , calculated for the mixture.

The full CFD solution is verified to be grid-independent on a computational mesh comprised of approximately 41,100 cells. This same mesh is used to obtain the full DSMC solution after being refined to comply with DSMC cell size requirements using the automatic refinement algorithm outlined in Chapter III. A constant time step of

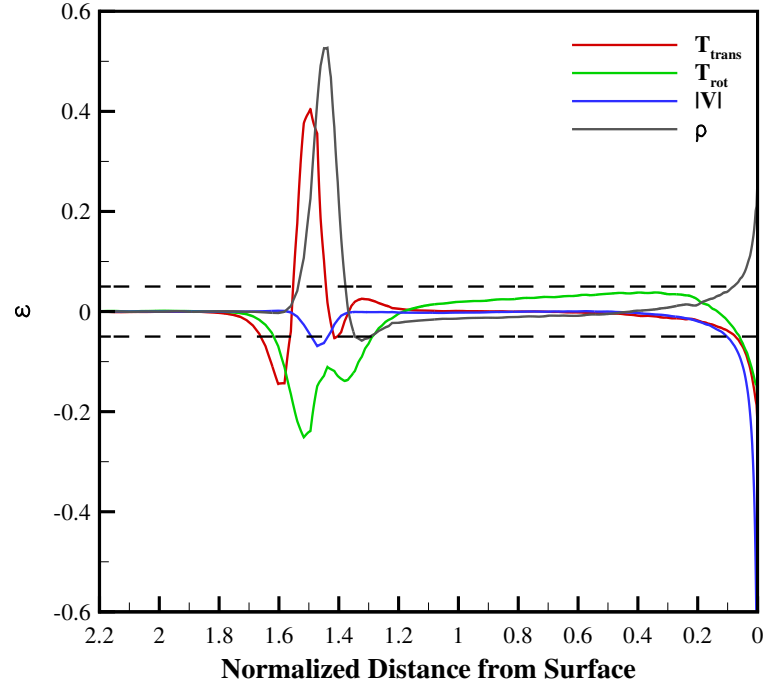


Figure 6.6: Errors between full CFD and full DSMC results along the 90° extraction line for the Mach 12, Kn_∞ 0.01 flow of N_2 over a two-dimensional cylinder.

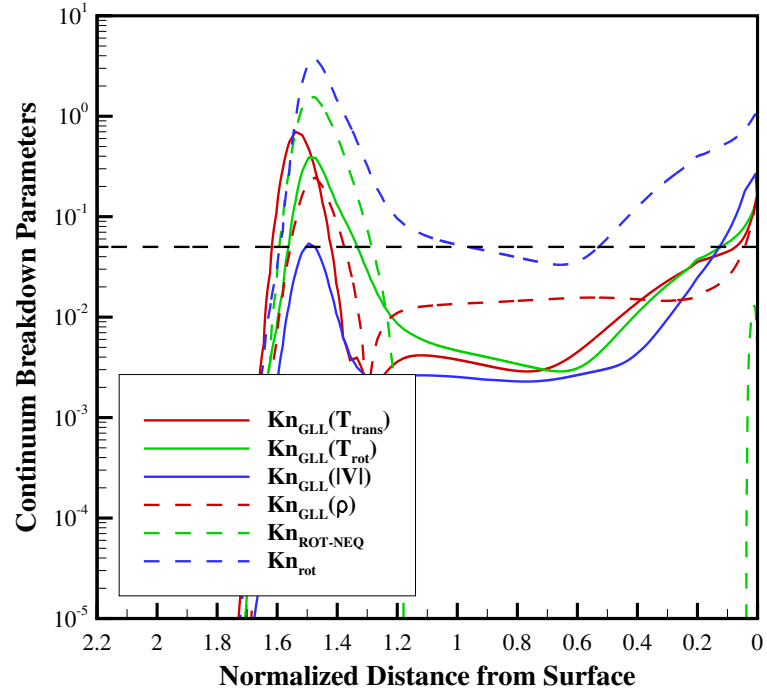


Figure 6.7: Continuum breakdown parameters based on a full CFD solution along the 90° extraction line for the Mach 12, Kn_∞ 0.01 flow of N_2 over a two-dimensional cylinder.

$1 \times 10^{-8} s$ is used in the full DSMC simulation; this time step is verified to be less than the local mean collision time throughout the flow domain. The maximum time step employed in the full CFD simulation is $1 \times 10^{-7} s$. In order to maintain a minimum of 40 particles per cell (approximately 20 particles of each species per cell), a constant numerical weight of 2×10^{12} is specified everywhere except near the cylinder surface, where reduced cell-based numerical weights are used. Vibrational excitation is again ignored in these simulations so that the merit of each of the rotational nonequilibrium parameters can be clearly determined. The CFD and DSMC simulations compared here employ consistent physical models, which have been detailed in Chapter IV.

Following the same procedure as described in the previous section, the errors between the full CFD and full DSMC simulation results for this flow field, along with the initial predictions of continuum breakdown based on the full CFD solution, are calculated along the stagnation streamline and two additional extraction lines. Figure 6.8 shows the errors in various macroscopic properties along the stagnation streamline. Again, the initial placement of the pre-shock hybrid interface is not discussed.

According to Fig. 6.8, the post-shock hybrid interface should be located no more than 0.377 radii from the cylinder surface, as this is the approximate location where the rotational temperature predicted by CFD comes back into agreement with that predicted by DSMC. The error in velocity magnitude indicates that the boundary layer hybrid interface should be located at least 0.077 cylinder radii from the surface. Looking now at Fig. 6.9, where the various continuum breakdown parameters are plotted along the stagnation streamline, the value of $Kn_{ROT-NEQ}$ crosses the threshold indicated by the dashed black line at a normalized distance of 0.372. The new Kn_{rot} parameter takes the value of 0.2 at a normalized distance of 0.375, so either one of these rotational nonequilibrium parameters could be used to predict the location of the post-shock hybrid interface. Note that if the gradient-length local Knudsen num-

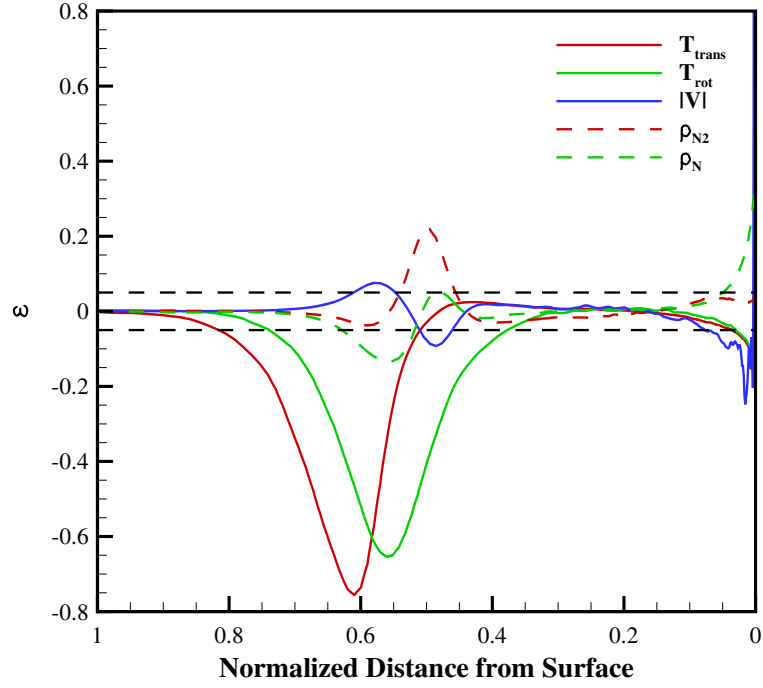


Figure 6.8: Errors between full CFD and full DSMC results along the stagnation streamline for the Mach 10, Kn_∞ 0.01 flow of 50% N_2 /50% N over a two-dimensional cylinder.

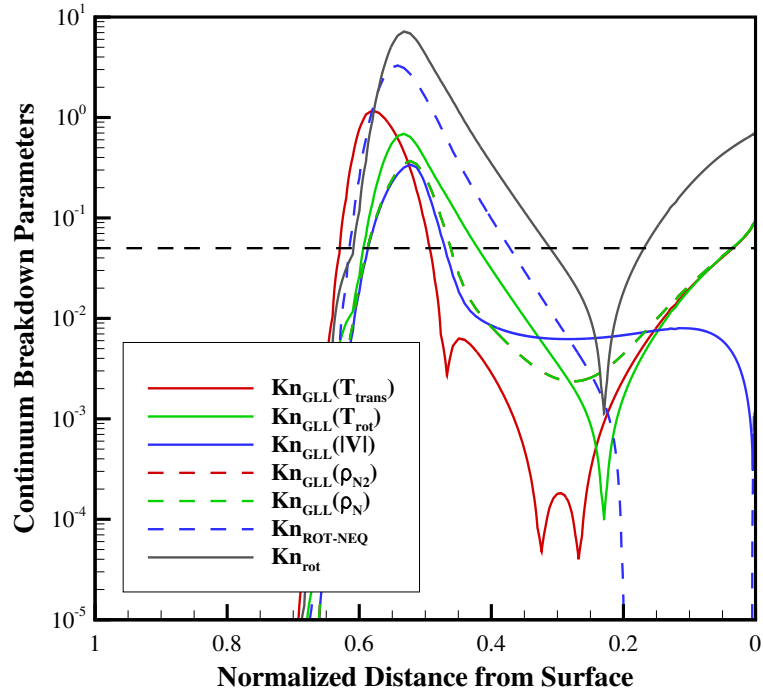


Figure 6.9: Continuum breakdown parameters based on a full CFD solution along the stagnation streamline for the Mach 10, Kn_∞ 0.01 flow of 50% N_2 /50% N over a two-dimensional cylinder.

ber is the only continuum breakdown parameter considered, the post-shock hybrid interface would be located within the shock wave at a normalized distance of 0.421.

Neither the gradient-length local Knudsen number nor the $Kn_{ROT-NEQ}$ parameter are capable of accurately predicting the thickness of the boundary layer along the stagnation streamline. The first indication of strong nonequilibrium effects near the surface is when the value of $Kn_{GLL}(T_{rot})$ exceeds 0.05 at a normalized distance of 0.035 from the cylinder surface. The Kn_{rot} parameter takes on a value of 0.2 at a normalized distance of 0.103, which is a conservative estimate of where the hybrid interface should be placed so that DSMC can be used in the boundary layer rather than CFD.

Similar conclusions can be drawn by analyzing the full CFD and full DSMC results along the 45° extraction line. The errors between these two solutions and the values of the continuum breakdown parameters are shown in Fig. 6.10 and Fig. 6.11, respectively. Again, the Kn_{rot} parameter with a threshold value of 0.2 predicts that the boundary layer hybrid interface be placed at a normalized distance of 0.142 from the cylinder surface, which is conservative considering the errors in macroscopic properties do not exceed $\pm 5\%$ until a normalized distance of 0.071. The gradient-length local Knudsen number provides a more accurate estimate of continuum breakdown than $Kn_{ROT-NEQ}$, but still under predicts the thickness of the boundary layer along the 45° extraction line. The new Kn_{rot} parameter is also more accurate at predicting the location of the post-shock hybrid interface at a normalized distance of 0.552, as compared to the $Kn_{ROT-NEQ}$ parameter, which places the interface at a normalized distance of 0.556. As can be seen in Fig. 6.10, the error in rotational temperature falls within the target accuracy range downstream of the shock at a normalized distance of 0.554 from the cylinder surface.

Lastly, the errors between the full CFD and full DSMC results along a 90° extraction line are plotted in Fig. 6.12. According to these results, the post- shock hybrid

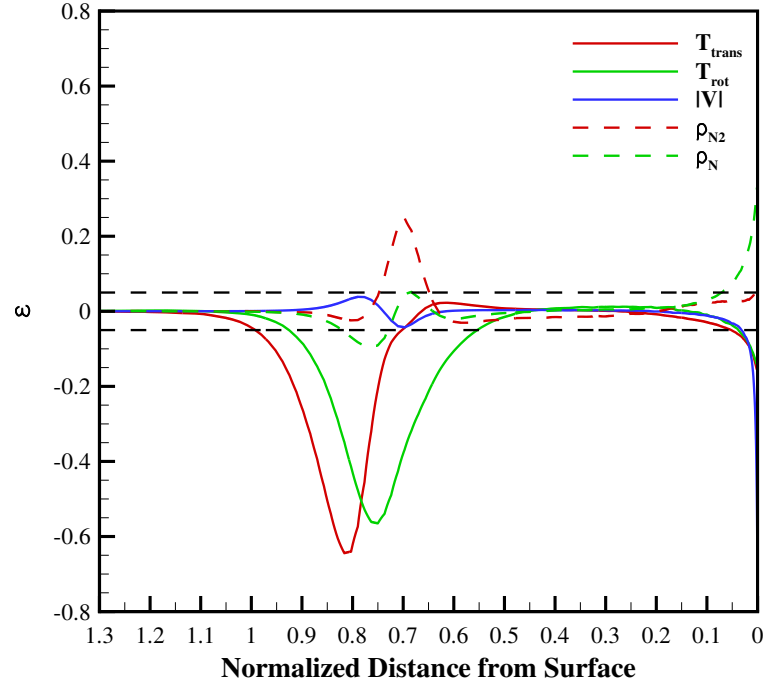


Figure 6.10: Errors between full CFD and full DSMC results along the 45° extraction line for the Mach 10, Kn_∞ 0.01 flow of 50% N_2 /50% N over a two-dimensional cylinder.

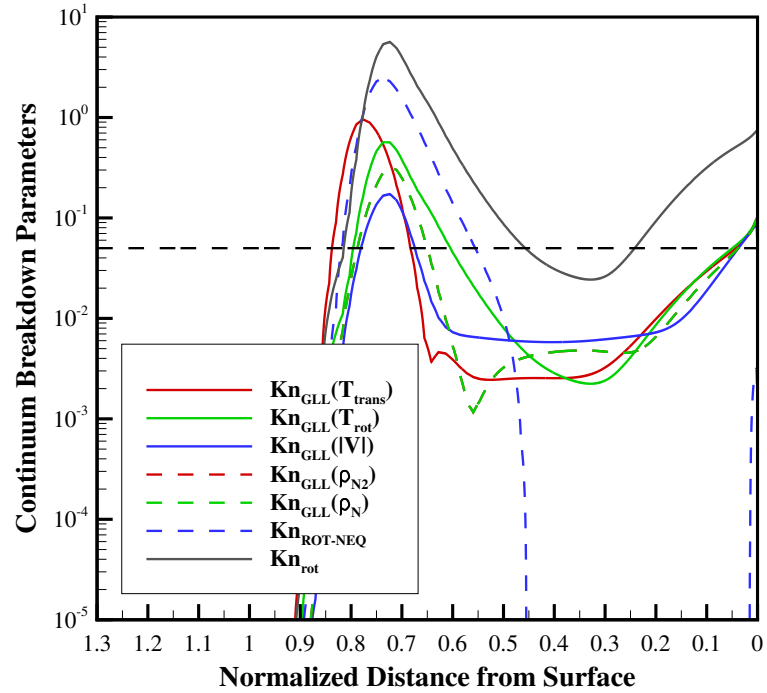


Figure 6.11: Continuum breakdown parameters based on a full CFD solution along the 45° extraction line for the Mach 10, Kn_∞ 0.01 flow of 50% N_2 /50% N over a two-dimensional cylinder.

interface should be located at a maximum of 1.496 radii from the cylinder surface. Additionally, the boundary layer hybrid interface should be located at least 0.188 radii from the cylinder surface. Upon comparing these error profiles to the continuum breakdown parameters plotted in Fig. 6.13, it is evident that none of the continuum breakdown parameters that have been used in the past accurately predict the correct placement of either the post-shock or the boundary layer hybrid interfaces. The value of $Kn_{ROT-NEQ}$ decreases below the threshold value of 0.05 at a normalized distance of 1.512, where the errors between CFD and DSMC still exceed the target error range of $\pm 5\%$. The Kn_{rot} parameter decreases below a value of 0.2 at a normalized distance of 1.506. Although this is more conservative than $Kn_{ROT-NEQ}$, this position is still in a region of nonequilibrium, as dictated by the initial CFD solution. However, use of the Kn_{rot} parameter and a threshold value of 0.2 does provide a reasonable measure of nonequilibrium in the boundary layer. According to this parameter, the hybrid interface should be placed at a distance of 0.344 radii from the cylinder surface, which is upstream of the location where errors in macroscopic properties exceed $\pm 5\%$. The gradient-length local Knudsen number places this hybrid interface too close to the cylinder surface at a normalized distance of 0.142.

6.2.3 Conclusions from Simple Gas and Gas Mixture Studies

As just exhibited, a great deal of information can be derived by performing careful comparisons of the errors between CFD and DSMC results, and the values of various continuum breakdown parameters, throughout a given flow field of interest. This is precisely the methodology followed by Boyd, *et al.* [14] when the gradient-length local Knudsen number was originally proposed and investigated, and is an integral component of verifying any hybrid DSMC/CFD approach. Although this evaluation of the new Kn_{rot} rotational nonequilibrium parameter is by no means exhaustive, it does provide insight into its effectiveness and advantages over the original $Kn_{ROT-NEQ}$

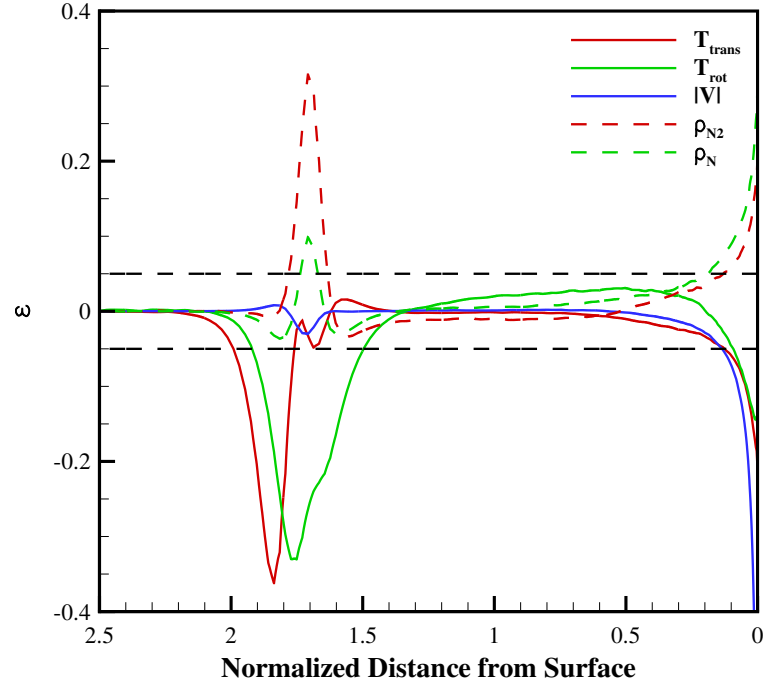


Figure 6.12: Errors between full CFD and full DSMC results along the 90° extraction line for the Mach 10, Kn_∞ 0.01 flow of 50% N_2 /50% N over a two-dimensional cylinder.

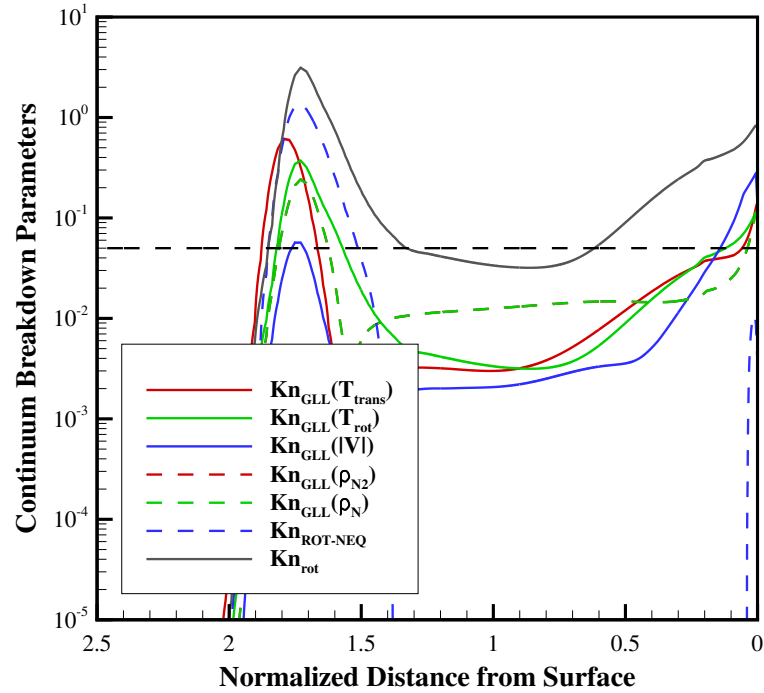


Figure 6.13: Continuum breakdown parameters based on a full CFD solution along the 90° extraction line for the Mach 10, Kn_∞ 0.01 flow of 50% N_2 /50% N over a two-dimensional cylinder.

parameter and gradient-length local Knudsen number. For example, in neither the simple gas study nor the gas mixture study was the gradient-length local Knudsen number able to accurately predict the thickness of the boundary layer over the entire fore body. This is an important finding of this study, as the gradient-length local Knudsen number has been the cornerstone of continuum breakdown prediction in the MPC hybrid method since its inception. Manually increasing the thickness of the particle domain that envelopes the boundary layer proved useful in past simulations using the MPC method, but in the interest of furthering both the generality and the applicability of the MPC hybrid method, such shortcomings must be identified and corrected.

The original $Kn_{ROT-NEQ}$ parameter is fairly effective at predicting the correct location of the post-shock hybrid interface, for which it was intended, without being overly conservative. This is more true for the simple gas study than it is for the gas mixture study, where the failures have been highlighted in the previous section. In many cases, Kn_{rot} takes on a value of 0.2 at the same approximate distance from the cylinder surface as $Kn_{ROT-NEQ}$ takes on a value of 0.05 to indicate where the post-shock hybrid interface should be located. It should also be noted that a larger threshold value for Kn_{rot} would still be appropriate for most of the fore body region in the simple gas case. However, for all but one of the six extraction lines examined here, a threshold value of 0.2 enables a conservative estimate for the initial placement of both the post-shock and boundary layer hybrid interfaces.

6.3 MPC Results

This new Kn_{rot} parameter, in conjunction with the gradient-length local Knudsen number, is employed to demarcate particle and continuum regions of an MPC hybrid simulation of the Mach 12, Kn_∞ 0.01 simple gas case examined in Section 6.2.1. After hybrid results are obtained, they are not only compared to full CFD and full

DSMC simulation results, but also those from a hybrid solution obtained by using the original $Kn_{ROT-NEQ}$ parameter. Unlike the results presented in Chapter V, hybrid interface locations are determined solely by these continuum breakdown parameters, i.e. DSMC is not forced to be used within a certain distance of the cylinder surface.

Many of the same conclusions from the previous section can be drawn from the initial placement of the hybrid interfaces when using each rotational nonequilibrium parameter. These initial hybrid interfaces are plotted in the upper pane of Fig. 6.14, where the red interfaces are obtained with the original $Kn_{ROT-NEQ}$ parameter and the blue interfaces are obtained with the new Kn_{rot} parameter. It can be seen that the particle region enveloping the bow shock wave is comparable in size, whether employing the Kn_{rot} or the $Kn_{ROT-NEQ}$ parameter. The new parameter predicts the same initial post-shock hybrid interface location for which the original parameter was first proposed, and as the simulation progresses, adjusts the post-shock hybrid interface to a more conservative location slightly downstream of the final post-shock hybrid interface predicted by the $Kn_{ROT-NEQ}$ parameter. The final positions of the hybrid interfaces in this simulation are plotted in the lower pane of Fig. 6.14.

The difference between the pre-boundary layer hybrid interface locations is much more evident. The new Kn_{rot} parameter predicts a thicker nonequilibrium boundary layer region that neither the $Kn_{ROT-NEQ}$ parameter nor the gradient-length local Knudsen number is able to consistently predict. This expanded particle region in the fore body then smoothly transitions to a slightly larger near-wake region in which DSMC is also used. As alluded to in the previous section, the largest difference between the initial and final hybrid interfaces is the position of the pre-shock hybrid interface. Again, this is why the initial location of the pre-shock hybrid interface as calculated by the full CFD solution is not as concerning as that for the post-shock and boundary layer hybrid interfaces.

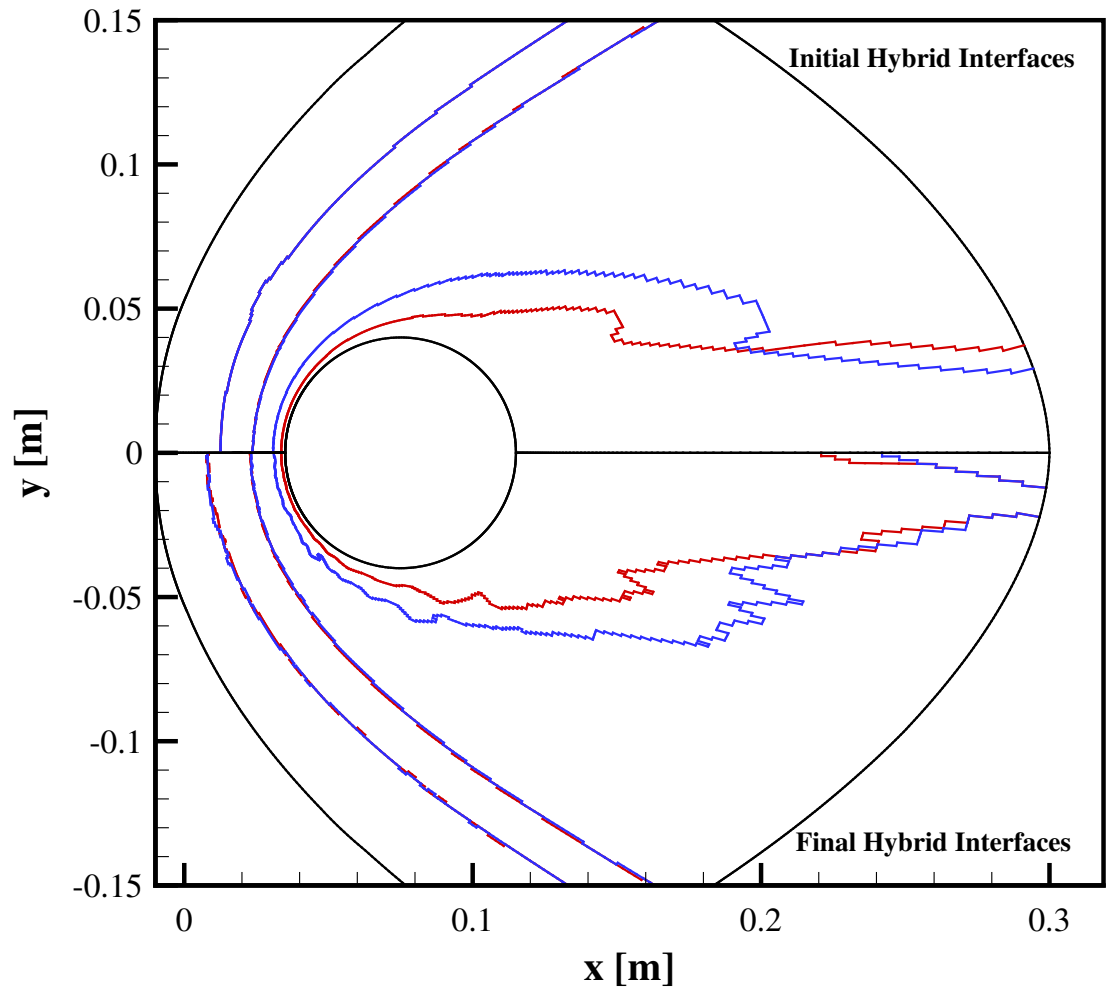


Figure 6.14: Initial (upper pane) and final (lower pane) hybrid interfaces, where Kn_{rot} interfaces are shown blue, and $Kn_{ROT-NEQ}$ interfaces are shown in red.

6.3.1 Flow Field Properties

Various flow field properties are first compared in order to evaluate the ability of the MPC method to reproduce results from a full DSMC simulation when the new Kn_{rot} parameter is employed to predict regions of strong rotational nonequilibrium effects. A comparison of the contours of translational temperature is plotted in Fig. 6.15, where DSMC results are shown as flooded contours, MPC hybrid results using the new Kn_{rot} parameter are shown as lines in the upper pane, and MPC hybrid results using the original $Kn_{ROT-NEQ}$ parameter are shown as lines in the lower pane. The differences between these two sets of MPC results are much more subtle than those between the MPC and full CFD results discussed in Chapter V, for example. However, because of the subsonic region in the fore body of the cylinder, incorrect placement of the pre-boundary layer hybrid interface has far-reaching effects upstream, which leads to disagreement between the translational temperature profiles within the diffuse shock wave. There are also differences between contours of translational temperature in the near-wake. The same observations can be made from the contours of rotational temperature plotted in Fig. 6.16.

Because the gradient-length local Knudsen number was initially supplemented by the $Kn_{ROT-NEQ}$ parameter in order to extend the post-shock hybrid interface downstream to a region of near-equilibrium, a closer examination of the translational and rotational temperatures along the stagnation streamline is warranted. First, translational and rotational temperatures given by DSMC, CFD, and the MPC hybrid method employing the $Kn_{ROT-NEQ}$ parameter are plotted in Fig. 6.17. The hybrid interfaces that demarcate particle and continuum regions in the MPC method are also shown as vertical black lines. The onset of the shock wave predicted by the MPC method is preceded by that predicted by full DSMC. Within the particle region enveloping the shock wave, the hybrid results for the translational and rotational temperatures lie between those given by the full CFD and full DSMC solutions. In

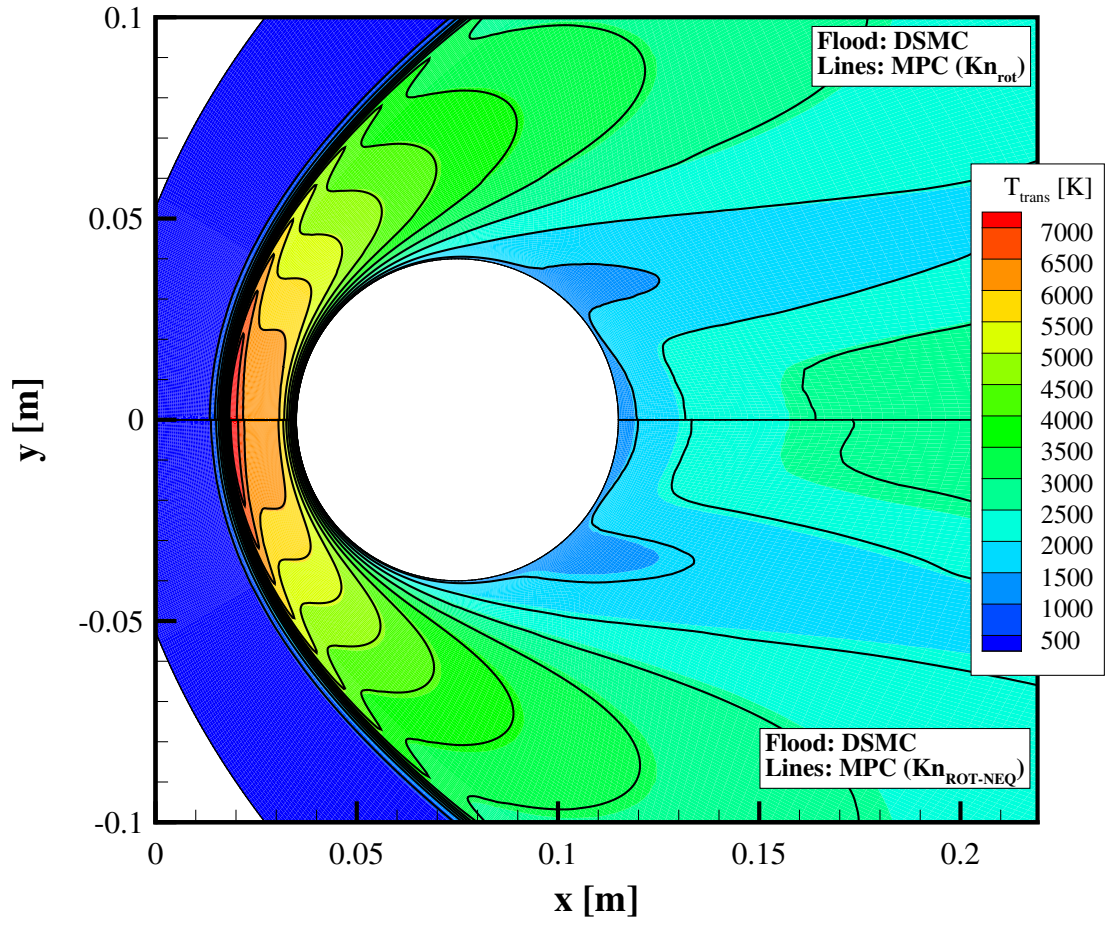


Figure 6.15: Contours of translational temperature, with DSMC results shown as flooded contours, MPC results where Kn_{rot} is used as lines in the upper pane, and MPC results where $Kn_{\text{ROT-NEQ}}$ is used as lines in the lower pane.

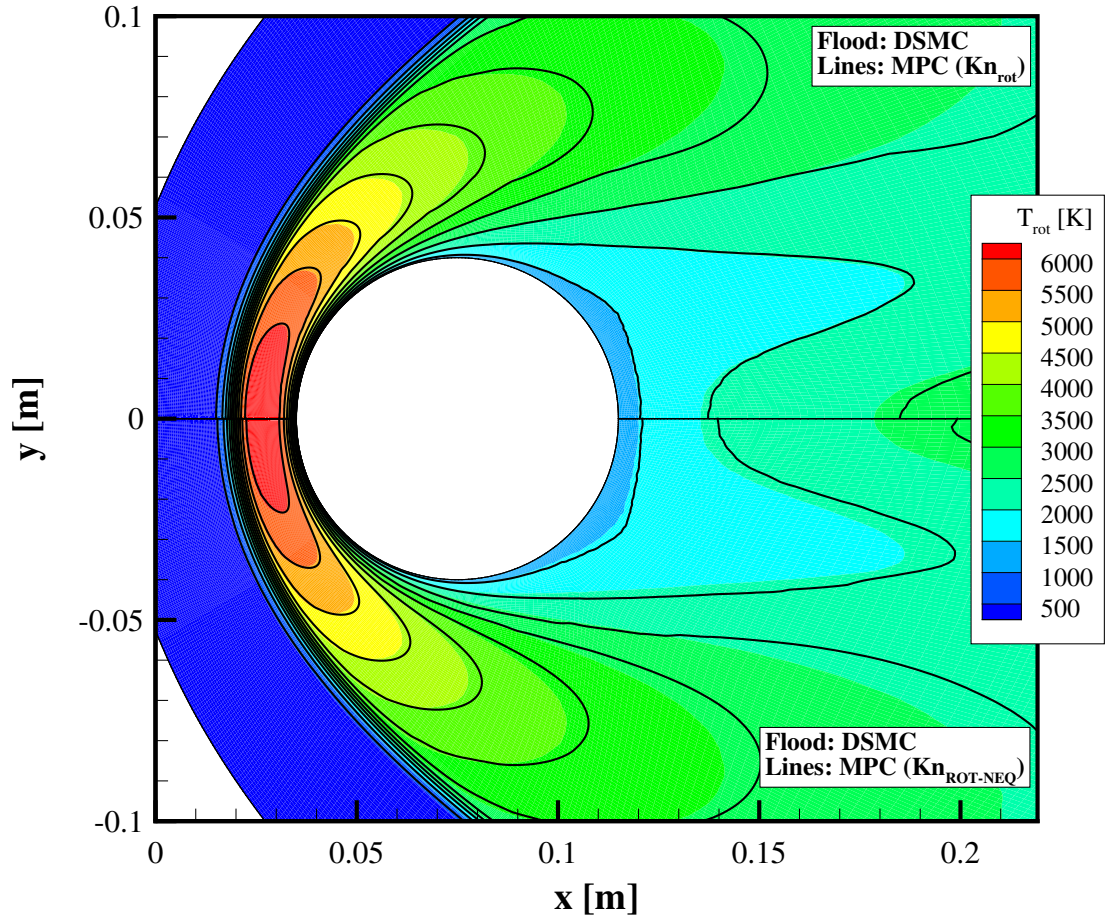


Figure 6.16: Contours of rotational temperature, with DSMC results shown as flooded contours, MPC results where Kn_{rot} is used as lines in the upper pane, and MPC results where $Kn_{ROT-NEQ}$ is used as lines in the lower pane.

contrast, translational and rotational temperature profiles obtained with the MPC hybrid method and the new Kn_{rot} parameter used in place of the $Kn_{ROT-NEQ}$ parameter are in much better agreement with full DSMC, as shown in Fig. 6.18.

Magnified views of the translational and rotational temperature profiles near the post-shock hybrid interface are shown in Figs. 6.19 and 6.20. The hybrid results plotted in Fig. 6.19 are obtained using the original $Kn_{ROT-NEQ}$ parameter. Although the MPC method is in reasonable agreement with full DSMC in terms of the translational temperature, there is a fairly large discrepancy between the rotational temperature profiles at this location. The hybrid results obtained using the new Kn_{rot} parameter are in much better agreement with full DSMC, as shown in Fig. 6.20.

Translational and rotational temperature profiles are also shown on a magnified scale in the region surrounding the pre-boundary layer hybrid interface in Figs. 6.21 and 6.22. It is observed that the full DSMC results are actually in better agreement with the full CFD results than with those given by the MPC method when the $Kn_{ROT-NEQ}$ parameter is used. Here, the MPC method under predicts the translational and rotational temperatures by approximately $200K$. Much closer agreement is achieved when the new Kn_{rot} parameter is used, as is evident in Fig. 6.22. Comparison of Figs. 6.21 and 6.22 also clearly illustrates that use of the new Kn_{rot} parameter in place of the original $Kn_{ROT-NEQ}$ parameter moves the pre-boundary layer hybrid interface upstream by $2.5mm$, whereas the other hybrid interfaces approximately retain their same locations.

A consistent and quantitative evaluation of the flow field results obtained using the MPC hybrid method is also performed in the same manner described in Chapter V. The errors incurred in translational temperature, rotational temperature, velocity magnitude, and mass density throughout the computational domain as a result of employing the MPC hybrid method and the new Kn_{rot} parameter are plotted in Figs. 6.23 through 6.26. The final hybrid interfaces are also plotted so that localized

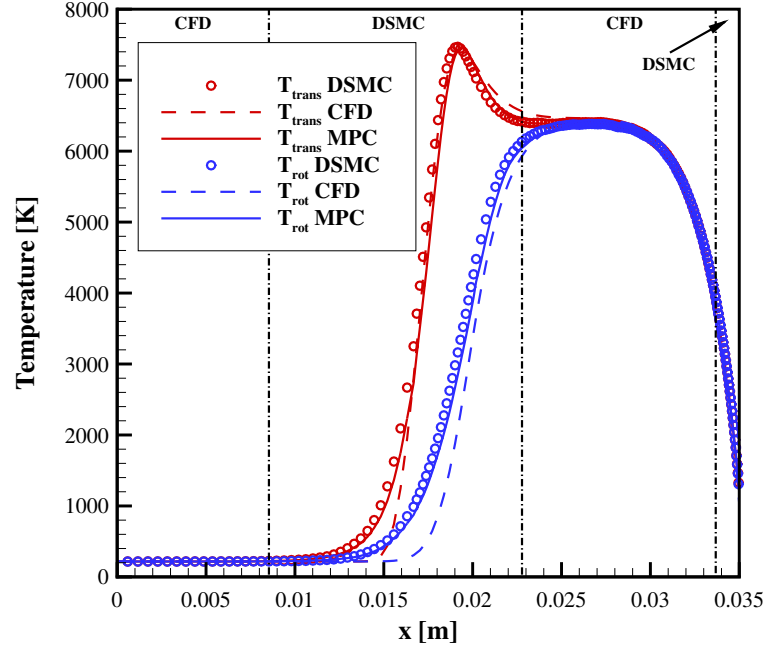


Figure 6.17: Translational and rotational temperatures along the stagnation streamline, with MPC results obtained using the original $Kn_{ROT-NEQ}$ parameter.

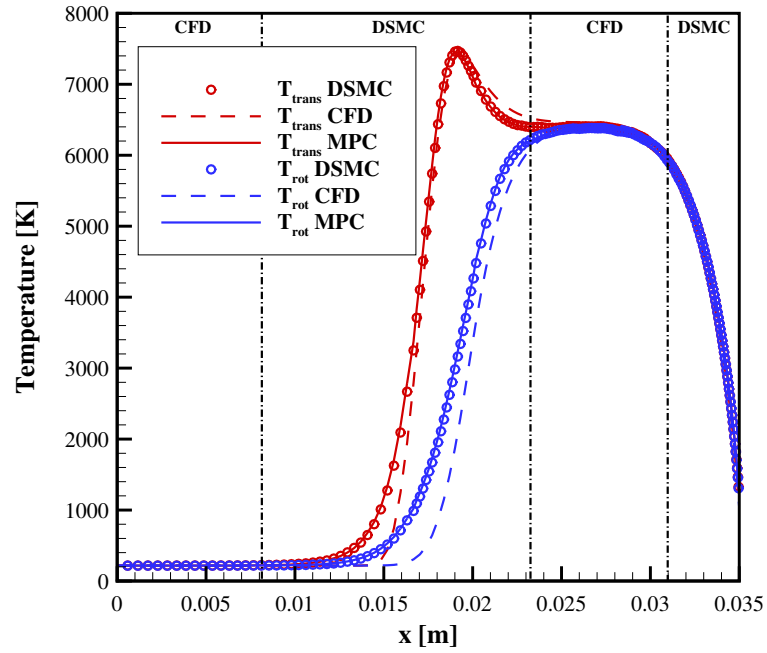


Figure 6.18: Translational and rotational temperatures along the stagnation streamline, with MPC results obtained using the new Kn_{rot} parameter.

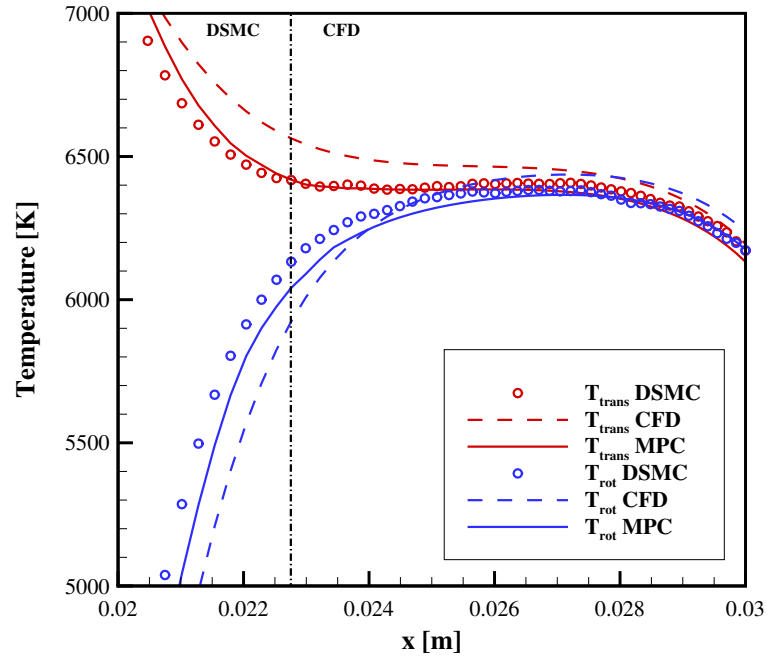


Figure 6.19: Translational and rotational temperatures along the stagnation streamline, with MPC results obtained using the original $Kn_{ROT-NEQ}$ parameter, near the post-shock hybrid interface.

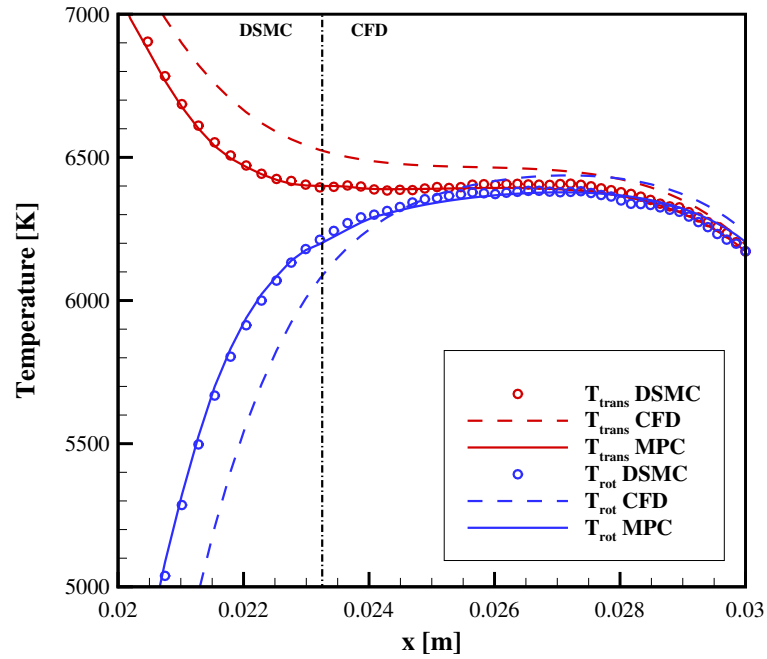


Figure 6.20: Translational and rotational temperatures along the stagnation streamline, with MPC results obtained using the new Kn_{rot} parameter, near the post-shock hybrid interface.

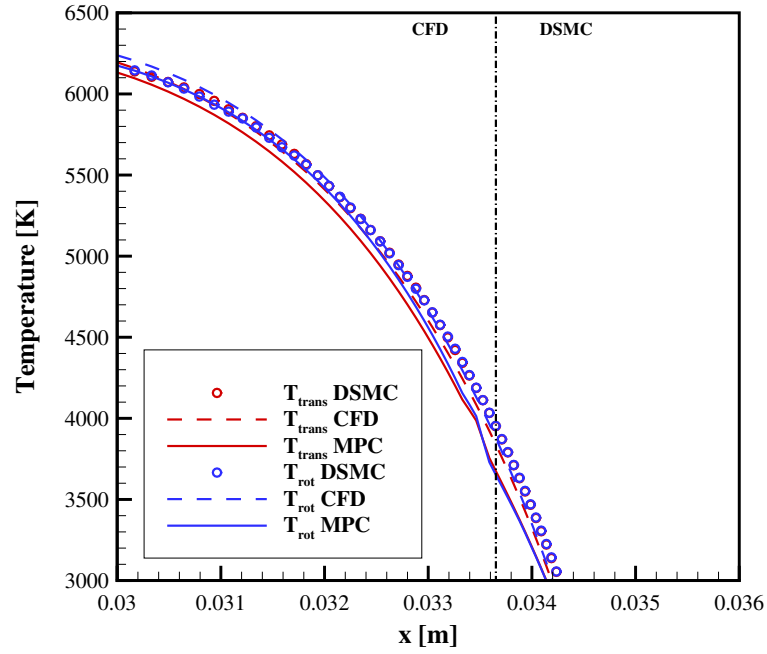


Figure 6.21: Translational and rotational temperatures along the stagnation streamline, with MPC results obtained using the original $Kn_{ROT-NEQ}$ parameter, near the pre-boundary layer hybrid interface.

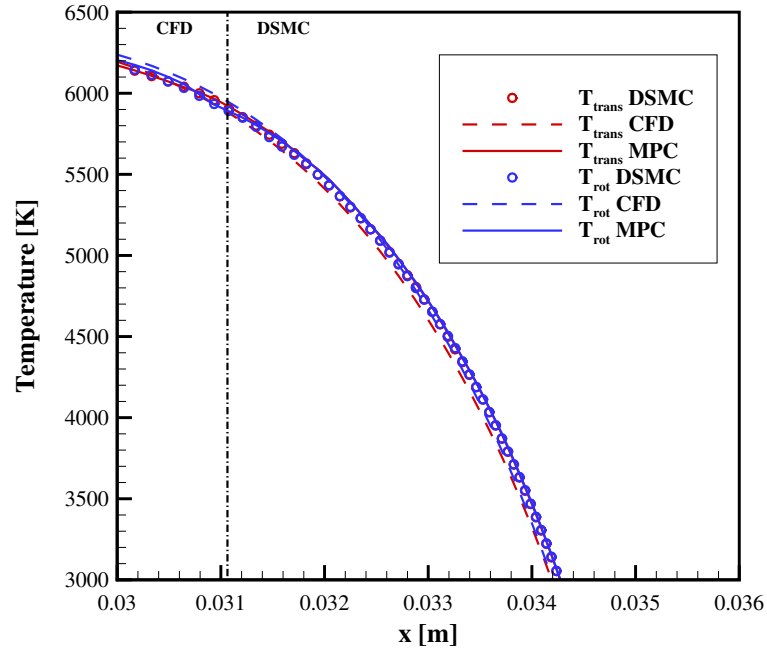


Figure 6.22: Translational and rotational temperatures along the stagnation streamline, with MPC results obtained using the new Kn_{rot} parameter, near the pre-boundary layer hybrid interface.

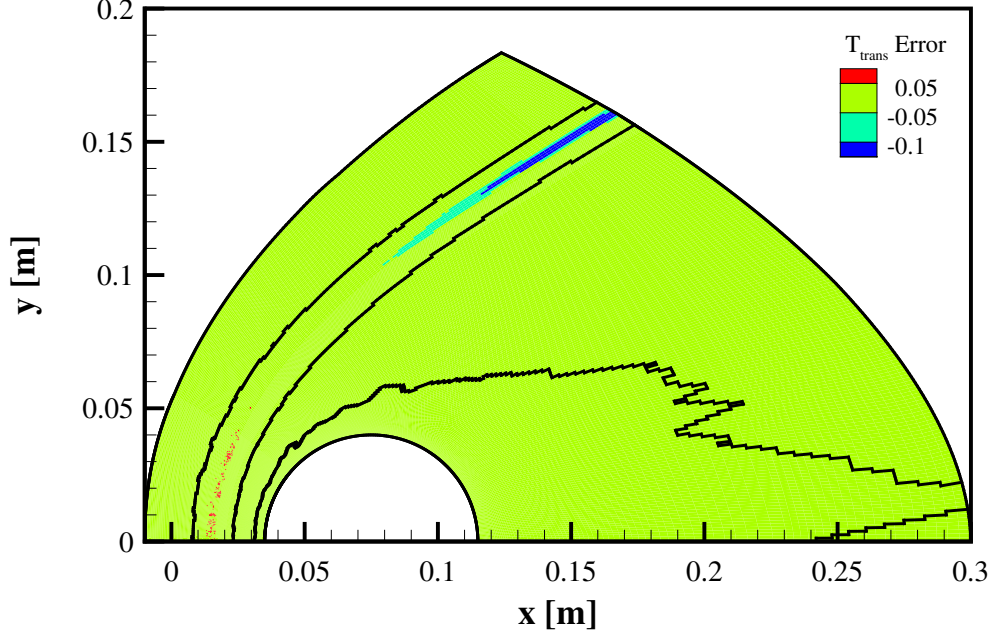


Figure 6.23: Contours of translational temperature errors of the MPC method relative to full DSMC when Kn_{rot} is used, with hybrid interfaces shown as black lines.

errors can be identified as being in either particle or continuum regions of the flow field. Both the physical extent and numerical ranges of these flow field errors, as provided in Table 6.1, have been reduced relative to the baseline accuracy results discussed in Section 5.3. The relative errors of these new MPC results measured in the L_2 norm, which are given in Table 6.2, have also been reduced.

The hybrid interfaces enveloping the shock wave in this Mach 12, Kn_∞ 12 flow of N_2 over a two-dimensional cylinder have remained virtually unchanged, despite the improvements made to the MPC hybrid method in Chapter V and the use of a new rotational nonequilibrium parameter explored in the current chapter. Even so, the physical accuracy of the MPC method relative to full DSMC in the upper shock wave region has improved with each successive development. This result is indicative of numerical errors generated in the fore body being propagated upwards along the shock wave, and highlights the far-reaching effects that the fore body flow has on the rest of the simulation domain.

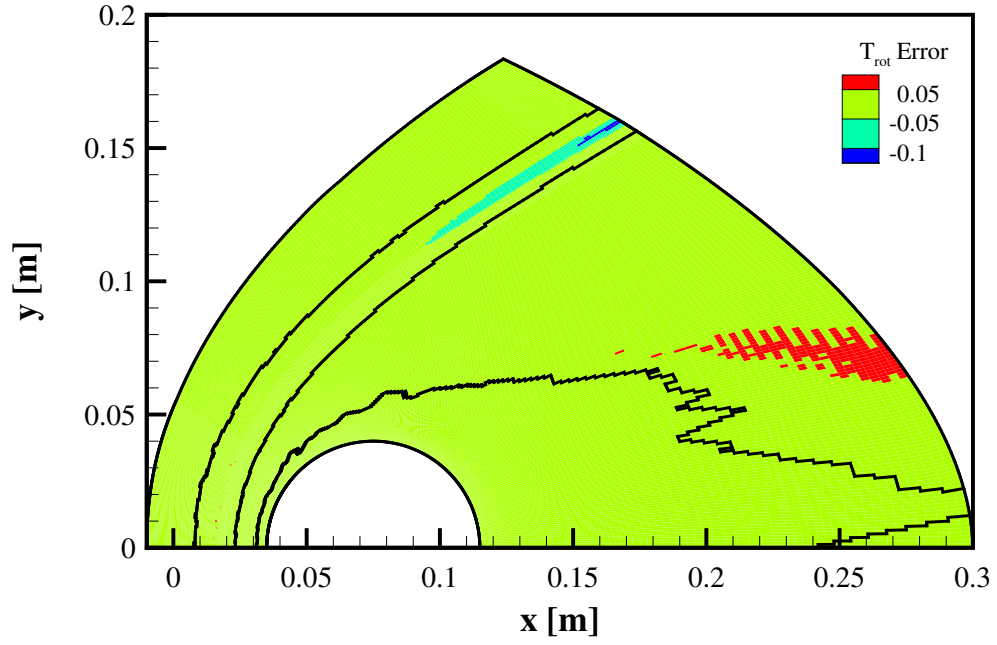


Figure 6.24: Contours of rotational temperature errors of the MPC method relative to full DSMC when Kn_{rot} is used, with hybrid interfaces shown as black lines.

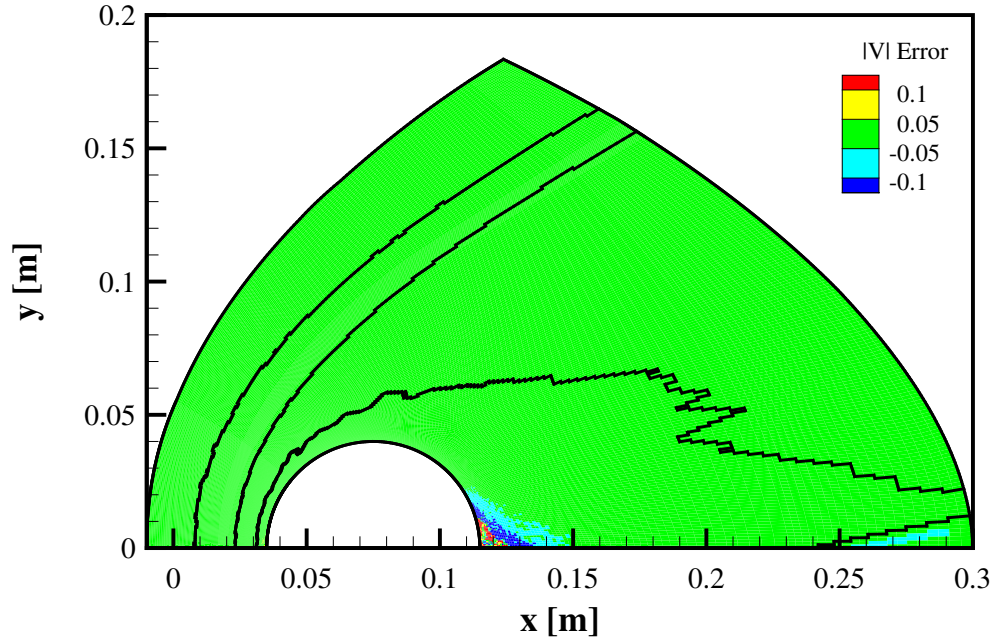


Figure 6.25: Contours of velocity magnitude errors of the MPC method relative to full DSMC when Kn_{rot} is used, with hybrid interfaces shown as black lines.

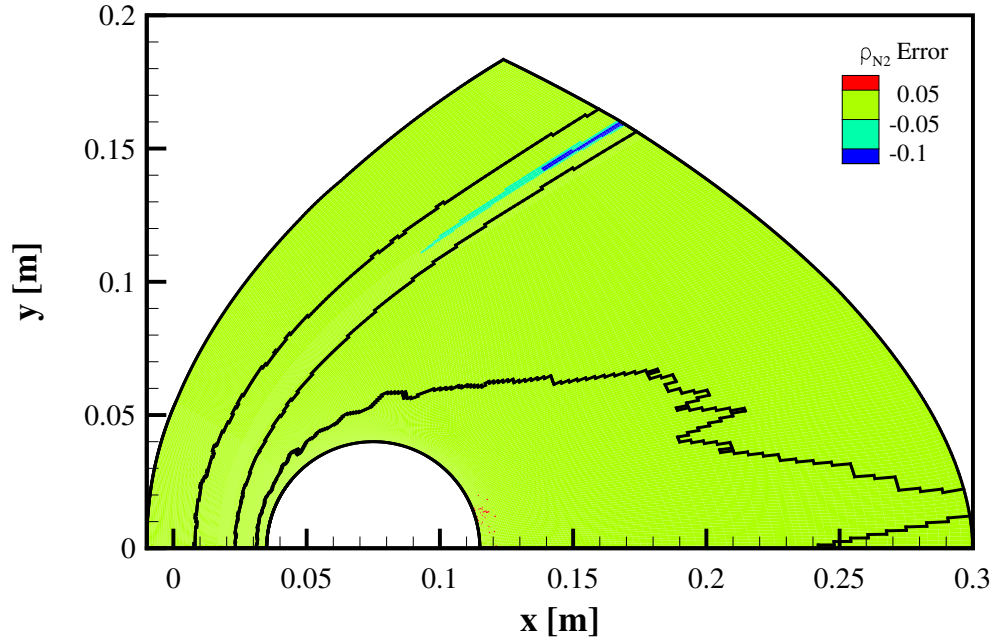


Figure 6.26: Contours of mass density errors of the MPC method relative to full DSMC when Kn_{rot} is used, with hybrid interfaces shown as black lines.

Table 6.1: Ranges of new MPC errors relative to full DSMC for the Mach 12, Kn_{∞} 0.01 flow of N_2 over a two-dimensional cylinder.

Property	New MPC Results
T_{trans}	$-0.15 \leq \epsilon \leq 0.08$
T_{rot}	$-0.11 \leq \epsilon \leq 0.06$
ρ_{N2}	$-0.14 \leq \epsilon \leq 0.06$

Table 6.2: Relative errors of new MPC results measured in the L_2 norm for the Mach 12, Kn_{∞} 0.01 flow of N_2 over a two-dimensional cylinder.

Property	New MPC Results
T_{trans}	0.008
T_{rot}	0.011
$ V $	0.005
ρ_{N2}	0.005

6.3.2 Surface Properties

Although it is important that use of the new Kn_{rot} parameter has significantly improved the agreement between MPC and full DSMC in terms of the flow field properties, as discussed in Section 5.3, the physical accuracy of the surface properties is of utmost importance. The profiles of surface pressure coefficient, heat transfer coefficient, and shear stress coefficient as predicted by the MPC method, full CFD, and full DSMC are plotted in Figs. 6.27 through 6.29. There is very little difference between the profiles of surface pressure coefficient predicted by the MPC method when the new Kn_{rot} parameter is used instead of the original $Kn_{ROT-NEQ}$ parameter, as seen in Fig. 6.27. However, there is a noticeable improvement in the profile of heat transfer coefficient when the new rotational nonequilibrium parameter is used. This is the reason why, in past MPC hybrid simulations, the particle region surrounding the boundary layer was forced to extend further upstream than that automatically dictated by the $Kn_{ROT-NEQ}$ parameter. Like the surface pressure coefficient, there is very little difference between MPC predictions of the shear stress coefficient along the cylinder surface, whether the original or new rotational nonequilibrium parameter is used.

The quantitative errors between the surface properties predicted by the MPC method using the new Kn_{rot} parameter and those predicted by a full DSMC simulation are plotted in Figs. 6.30 through 6.32. The largest error in surface pressure coefficient is approximately 5.1%, which is slightly less than the maximum error exhibited in previous results discussed in Section 5.3. A systematic positive error is seen in the wake, but overall, the level of accuracy in the surface pressure coefficient is maintained. The agreement between the heat transfer coefficient profile predicted by the MPC method and full DSMC has noticeably improved as a result of using the new Kn_{rot} parameter. The largest error here is approximately 5.2% and occurs in the wake, which is expected to be problematic because of the reduced number

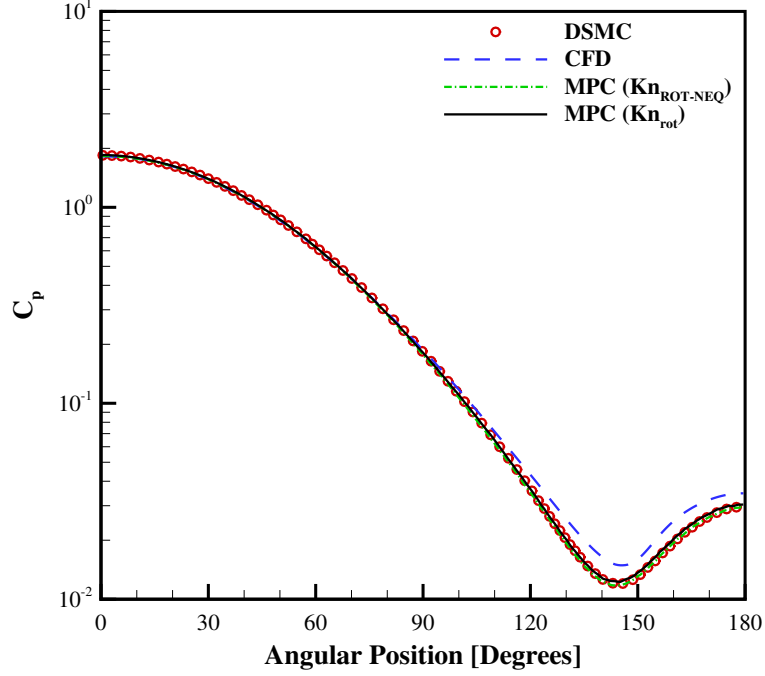


Figure 6.27: Surface pressure coefficient along the cylinder surface for the Mach 12, Kn_∞ 0.01 flow of N_2 over a two-dimensional cylinder.

of simulator particles in this region. The profile of shear stress coefficient also exhibits improved agreement relative to previous results. Whereas the errors between MPC and full DSMC results are still very large near the stagnation point and in the wake region due to near-zero velocity magnitudes, a relative accuracy of $\pm 5\%$ is maintained from an angular position of approximately 12° to 153° . This level of accuracy is maintained over a larger portion of the cylinder surface than when the original $Kn_{ROT-NEQ}$ parameter is used in conjunction with manually increasing the thickness of the boundary layer particle region, as seen in the results of Section 5.3.

6.3.3 Computational Performance

An MPC simulation using the new Kn_{rot} parameter to predict rotational nonequilibrium effects requires approximately 13.4 million DSMC simulator particles, whereas an MPC simulation using the original $Kn_{ROT-NEQ}$ parameter requires approximately 10.8 million particles. However, the latter of these simulations yields surface heat

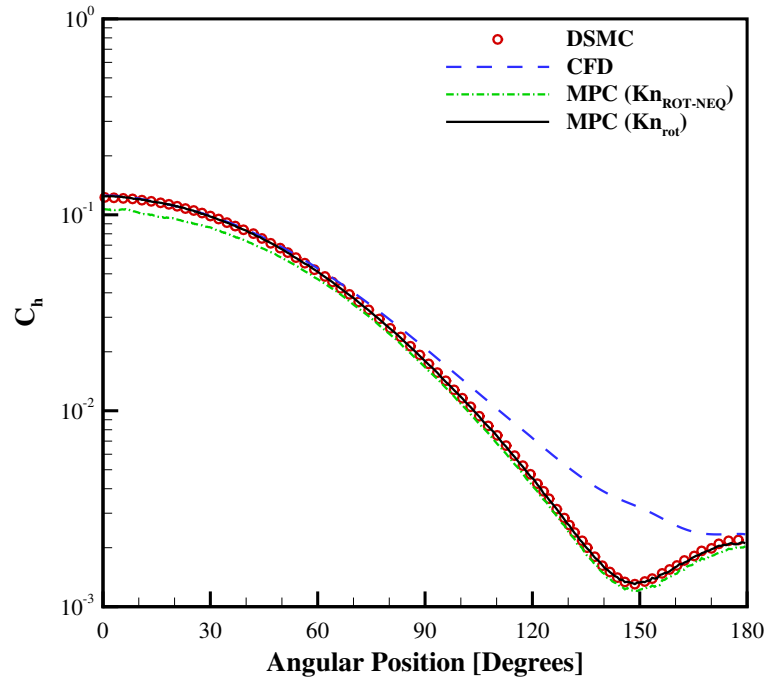


Figure 6.28: Heat transfer coefficient along the cylinder surface for the Mach 12, Kn_∞ 0.01 flow of N_2 over a two-dimensional cylinder.

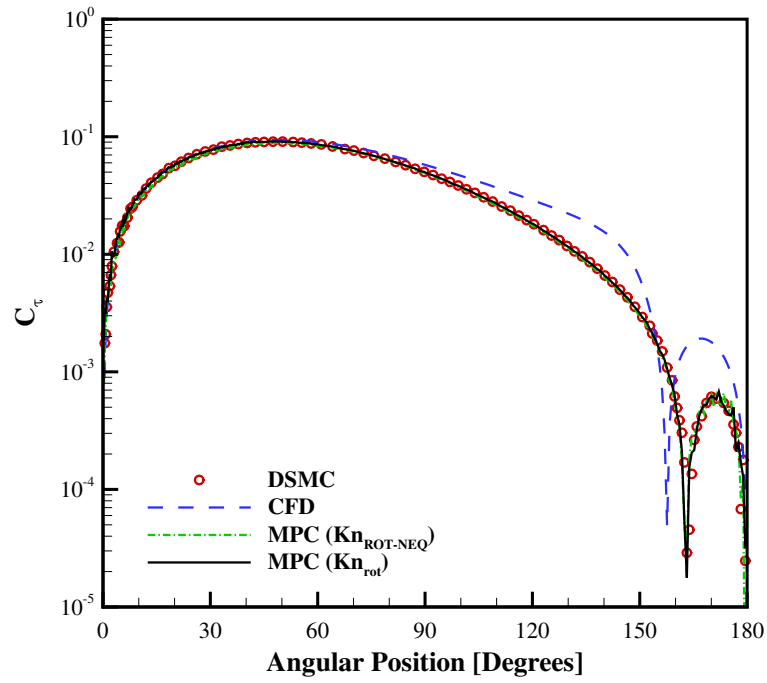


Figure 6.29: Shear stress coefficient along the cylinder surface for the Mach 12, Kn_∞ 0.01 flow of N_2 over a two-dimensional cylinder.

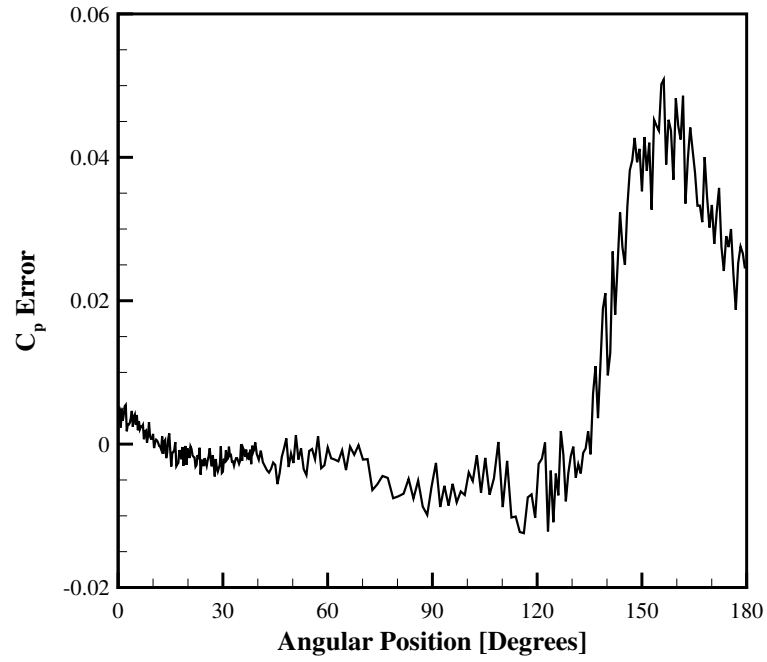


Figure 6.30: Surface pressure coefficient errors of the MPC method relative to full DSMC when Kn_{rot} is used.

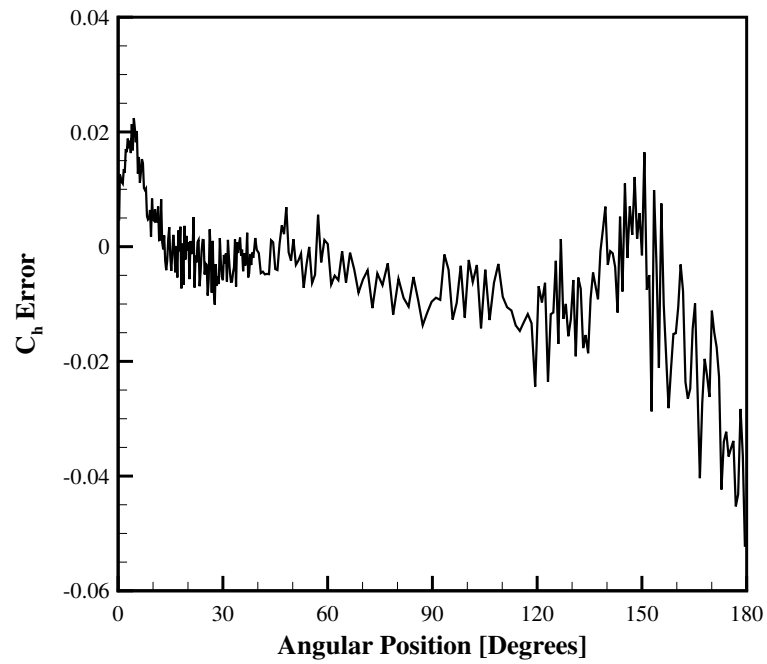


Figure 6.31: Heat transfer coefficient errors of the MPC method relative to full DSMC when Kn_{rot} is used.

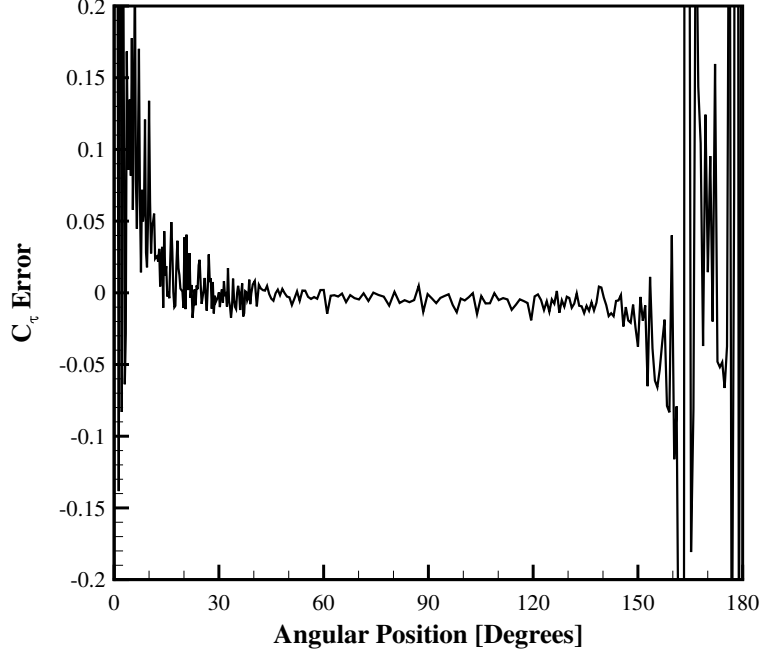


Figure 6.32: Shear stress coefficient errors of the MPC method relative to full DSMC when Kn_{rot} is used.

transfer coefficient results that are in very poor agreement with those from full DSMC, as seen in Fig. 6.28. Because of this, the more meaningful comparison is between those MPC results obtained using the new Kn_{rot} parameter, and those presented at the end of Chapter V, which were obtained by forcing DSMC to be used within $5mm$ of the cylinder surface. In that simulation, approximately 12.2 million particles were required. The particle region surrounding the wake in this most recent simulation is larger compared to that in Chapter V, and this accounts for the increase in the total number of particles.

Based on the number of particles required in this most recent MPC simulation and the number of particles required in the corresponding full DSMC simulation, an ideal speedup factor of 2.13 is calculated. The actual speedup factor as determined by comparing the total computational cost of the MPC simulation (288 hours) and the total computational cost of the full DSMC simulation (763 hours) is 2.65, and surpasses the ideal calculation. There are a couple of reasons why the current MPC

Table 6.3: Computational performance statistics for the Mach 12, Kn_∞ 0.01 flow of N_2 over a two-dimensional cylinder.

	CFD	DSMC	MPC
Normalized CPU Time	1.0	33.2	12.5
Normalized Memory	1.0	11.5	7.40
# Particles	-	28.5×10^6	13.4×10^6
# Continuum Cells	41,122	-	19,796
# Particle Cells	-	58,809	33,419
# Processors	4	22	10
Sampling/Total DSMC Steps	-	100,000/180,000	100,000/104,040

simulation, which requires a larger number of particles relative to the case presented in Chapter V, appears to require less computational time. For one, because the same number of processors are used in each simulation, there are more particles assigned to each processor in the most recent simulation, and therefore, less computational effort spent communicating between processors. In addition, to determine the variability in measured computational times, three identical DSMC simulations are performed. The resulting computational times differ by as much as 9%, depending on how the processors are divided among computing nodes and other factors. Similarly, the results of the memory profiling software also vary, but to a lesser degree. The computational performance statistics are summarized in Table 6.3.

6.4 Interim Conclusions

In this chapter, detailed comparisons of full DSMC and full CFD results for transitional, hypersonic, blunt-body flows of both a simple gas and a mixture of chemical species were performed. Various continuum breakdown parameters were then evaluated in terms of their ability to predict regions of excessive disagreement between these full DSMC and full CFD solutions along three flow field extraction lines. Although the gradient-length local Knudsen number was examined, too, this study was specifically aimed towards comparing the previously proposed $Kn_{ROT-NEQ}$ param-

ter for predicting rotational nonequilibrium effects and a new Kn_{rot} parameter. Upon determining a suitable threshold value of 0.2, this new Kn_{rot} parameter was implemented in the MPC method and found to be capable of accurately *and* automatically positioning both the post-shock hybrid interface and the hybrid interface surrounding the boundary layer of the simple gas test case presented earlier in Chapter V. These most recent MPC results exhibit improved accuracy throughout the flow field, including the upper shock region, compared to those results presented in Chapter V. In addition, surface properties are within approximately $\pm 5\%$ of those obtained with a full DSMC simulation, except in regions where macroscopic properties are particularly prone to statistical scatter. Therefore, in future simulations using the MPC method, continuum breakdown will be determined by calculating

$$Br = \max \left(Kn_{GLL-T_{trans}}, Kn_{GLL-\rho}, Kn_{GLL-|V|}, Kn_{GLL-T_{rot}}, Kn_{GLL-e_{vib}}, \frac{1}{4}Kn_{rot} \right), \quad (6.5)$$

and employing a threshold value of 0.05 to determine whether a computational cell is assigned to the particle or continuum domains.

CHAPTER VII

Hybrid Simulations of Mixtures of Chemical Species

One of the objectives of the present work is to extend the capabilities of the MPC hybrid method to include mixtures of chemical species. Such a development not only broadens the applicability of this hybrid approach to more realistic atmospheric flows, but also serves as a preliminary step towards the method's ability to accurately simulate thermochemical nonequilibrium effects in the future. It was shown in Chapter II that consideration of multiple chemical species further complicates the governing equations of fluid flow by requiring an additional transport coefficient that describes mass diffusion effects. A discussion of how the MPC method accommodates multiple chemical species in a gas mixture is first presented. In particular, the topics of continuum breakdown prediction and consistent exchange of information across hybrid interfaces are addressed. The ability of the MPC method to accurately and efficiently simulate gas mixtures is first demonstrated for the case of a Mach 10, Kn_∞ 0.01 flow of 50% N_2 /50% N (by mole) over a two-dimensional cylinder; this is the same case for which the new Kn_{rot} rotational nonequilibrium parameter was evaluated in Chapter VI. Next, a gas mixture composed of 80% N_2 /20% O_2 (by mole) is considered. Here, the rotational energy modes of N_2 and O_2 are allowed to relax at rates that are independent of one another by employing the particle selection method

for calculating translational-rotational energy exchange probabilities, as described in Chapter IV. Finally, a gas comprised of two species with very different molecular weights is simulated using the MPC hybrid method, and results are compared to both full CFD and full DSMC simulation results. This last case presents an interesting challenge to the MPC method and the assumptions made during its development.

7.1 Multispecies Considerations

In Chapter III, the particle generation procedure proposed by Garcia and Alder [26] for simple, monatomic gases was described. Stephani, *et al.* [75] proposed a similar approach for sampling particle properties—velocities *and* internal energies—from a generalized Chapman-Enskog distribution that is applicable to gas mixtures with internal energy modes. As was seen in Chapter II, the generalized Chapman-Enskog distribution function is much more involved than that describing a simple, monatomic gas. A rigorous derivation was presented, and the necessity of the generalized Chapman-Enskog formulation was evaluated in the context of hypersonic, flat-plate boundary layer flow and hypersonic flow over a two-dimensional cylinder involving a five-species air mixture. For these cases, the magnitudes of the other transport processes were much larger than that of mass diffusion. Therefore, it was determined that the effect of including the mass diffusion in both the prediction of continuum breakdown and the sampling of particle properties was negligible. In addition, although the rotational and vibrational heat fluxes were found to contribute substantially to continuum breakdown in the boundary layer flow, these specific transport terms were not required to accurately predict the onset of nonequilibrium effects upstream of the bow shock wave. The post-shock region and stagnation point were not examined in this analysis, however, so no valid conclusions could be drawn regarding the relative importance of the various perturbation terms of the generalized Chapman-Enskog distribution in these regions.

For this first application of the MPC hybrid method in simulating gas mixtures, several simplifying assumptions are made. Regarding the prediction of continuum breakdown that was explored in Chapter VI, besides accounting for the mass density of each component species separately, there are no additional terms considered in the breakdown calculation when a gas mixture is simulated. Any significant changes in mixture composition should be observable in the gradient-length local Knudsen number calculated for the density of each species. Also, as noted in Chapter IV, the particle domains of the MPC hybrid simulations and full DSMC simulations presented here employ the VHS collision model, which assumes that simulator particles are isotropically scattered upon colliding. Although capable of accurately reproducing the macroscopic coefficient of viscosity, the VHS model is not capable of accurately capturing mass diffusion effects. Therefore, it does not make sense at this stage of development to include the mass diffusion perturbation of the Chapman-Enskog distribution function when sampling particle properties along hybrid interfaces; the increased accuracy provided by this more rigorous approach cannot be sustained in the particle domains. Excluding the mass diffusion when generating new simulator particles is also consistent with the observations made by Stephani, *et al.* [75].

Based on these assumptions, the same particle generation procedure proposed by Garcia and Alder [26] is used for sampling particle properties in MPC simulations involving gas mixtures. The only difference is that the normalized shear stress and translational heat flux are now calculated using the mixture rules described in Chapter IV. This results in all newly generated particles for each species having the same average velocity, i.e. the diffusion velocity is assumed to be zero, while the differences in molecular weight are used to alter the spread of the distribution functions, resulting in different thermal velocities. For example, if a binary gas mixture comprised of species A and B is considered, the average velocity of all newly generated A particles will be the same as the average velocity of all newly generated B particles. However,

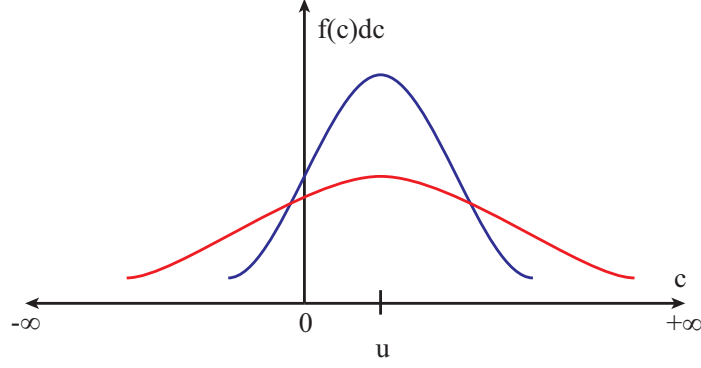


Figure 7.1: Illustration of two different VDFs, where the molecular weight of particles represented by the red line is less than that of the particles represented by the blue line.

if each A particle has a lower mass than each B particle, their individual molecular velocities will be sampled from a wider distribution, as illustrated in Fig. 7.1.

7.2 Verification of the MPC Method: 50% N_2 /50% N

Using the physical models described in Chapter IV, the Mach 10, Kn_∞ 0.01 flow of 50% N_2 /50% N (by mole) over a two-dimensional cylinder is simulated using the MPC hybrid method. In particular, the particle module employs the VHS model parameters for the N_2 - N_2 , N_2 - N , and N - N collision classes that were derived to be consistent with the Gupta Mixing Rule used in the continuum module. This is the same case examined in Section 6.2.2, where full CFD and full DSMC simulation results were compared in order to assess the merits of the various continuum breakdown parameters used in this work. For meaningful flow field, surface property, and computational performance comparisons, the same cell-based numerical weights that were used in the full DSMC simulation are also used in this hybrid simulation. The time step size and total number of sampled time steps are also specified to be the same.

The initial and final hybrid interfaces automatically determined by the MPC method for this flow field are plotted in Fig. 7.2. Again, the post-shock and pre-boundary layer hybrid interfaces remain relatively stationary throughout the course

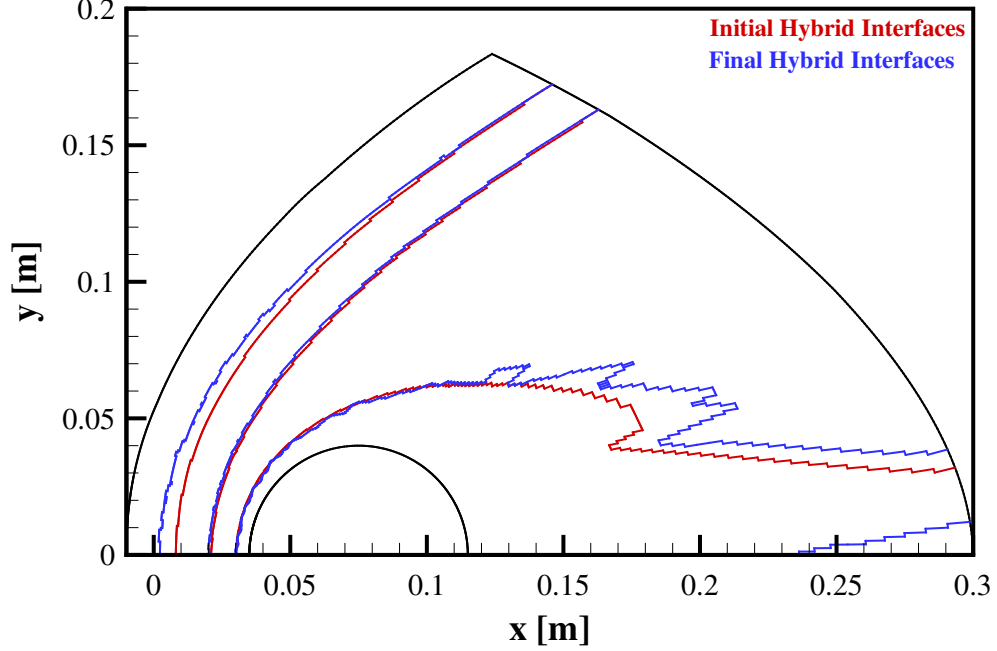


Figure 7.2: Initial and final hybrid interfaces for the Mach 10, Kn_∞ 0.01 flow of 50% N_2 /50% N over a two-dimensional cylinder.

of the simulation. However, as the initial CFD solution of the shock wave is improved by the DSMC method, the pre-shock hybrid interface moves upstream substantially. This accommodates the thicker, more diffuse shock wave that results when the strong nonequilibrium effects are accurately simulated. It should be reiterated that the continuum breakdown parameters used here, namely, the gradient-length local Knudsen number and the Kn_{rot} parameter introduced in the previous chapter, have automatically positioned these hybrid interfaces. The only user-defined parameters are the empirically determined threshold values that differentiate what are considered near-equilibrium and nonequilibrium computational cells.

7.2.1 Flow Field Properties

A comparison of the contours of velocity magnitude obtained with full DSMC, full CFD, and the MPC hybrid method is shown in Fig. 7.3. The results obtained with the MPC method are in excellent agreement with the full DSMC results, as ev-

idenced by the nearly indistinguishable flooded and lined contours in the upper pane of Fig. 7.3. There are slight discrepancies in the near-wake region, but the accuracy of the initial continuum solution has been greatly improved. For context, the contours of velocity magnitude predicted by the full DSMC and full CFD simulations are shown in the lower pane. As expected, the CFD solution indicates the shock onset to be much further downstream than in the DSMC solution, and the shock thickness is also under predicted. The CFD solution also exhibits a larger wake region, which will become more apparent in the surface properties discussed later in this section. Similar conclusions can be drawn from the contours of translational temperature and rotational temperature plotted in Figs. 7.4 and 7.5, respectively. One observation worth emphasizing is seen in the near-wake region of Fig. 7.5. There is an abrupt decline in the agreement between the results obtained with full DSMC and the MPC method that occurs along the hybrid interface. This may indicate that the flow field has not reached a true steady state at the time the hybrid interfaces are locked, which is possible considering the reduced collisionality in this region. This discrepancy may also be due to the manner in which rotational energies are sampled and assigned to newly generated particles along hybrid interfaces. Deschenes, *et al.* [22] proposed sampling from a Boltzmann distribution defined by the macroscopic rotational temperature, but the generalized Chapman-Enskog distribution may, in fact, be required to achieve the same physical accuracy as the full DSMC simulation. This discrepancy between contours of rotational temperature can also be observed in the simple gas results shown in Fig. 6.16.

The relative errors in macroscopic fluid properties between the MPC flow field results and those obtained with full DSMC are plotted in Figs. 7.6 through 7.10. The numerical ranges of these errors, which are given in Table 7.1, are consistent with those calculated for the simple gas case evaluated in Chapter VI. The relative errors measured in the L_2 norm for these MPC results are again much smaller than

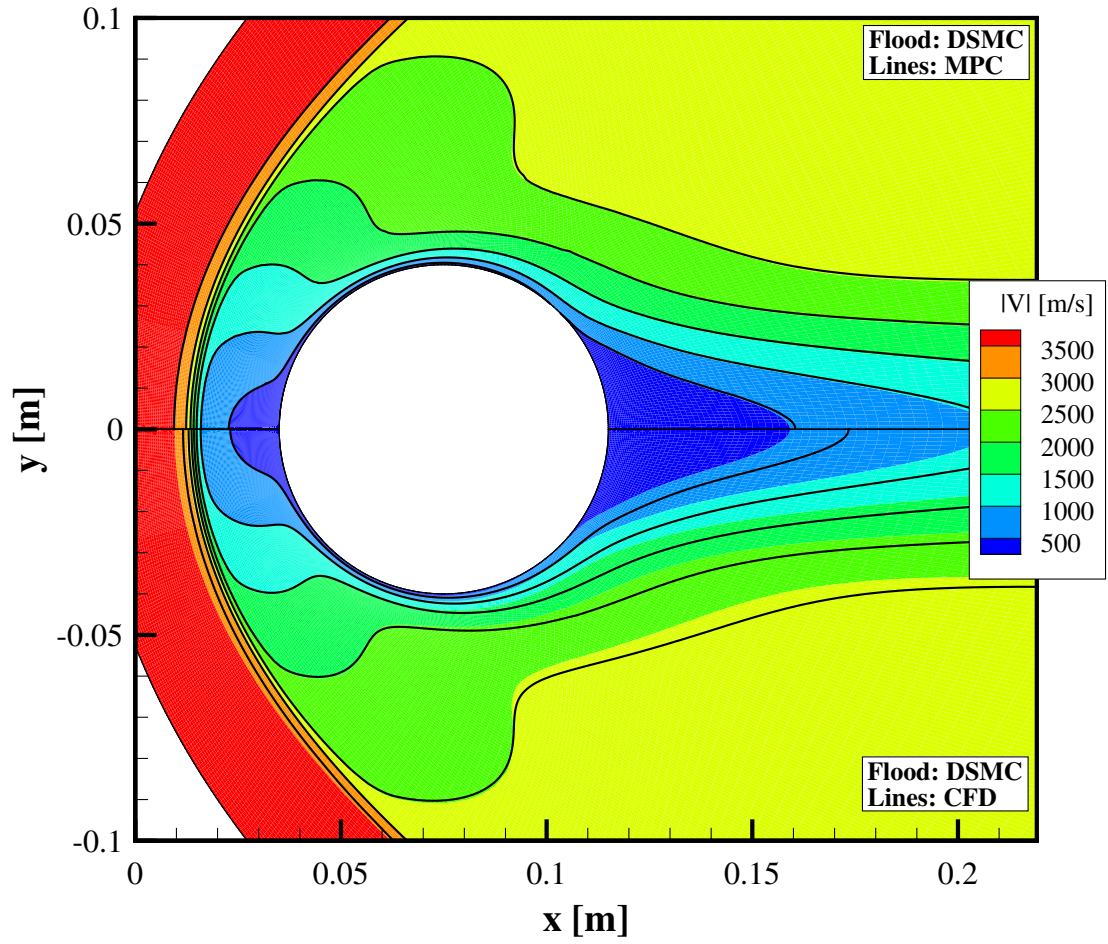


Figure 7.3: Contours of velocity magnitude for the Mach 10, Kn_∞ 0.01 flow of 50% N_2 /50% N over a two-dimensional cylinder.

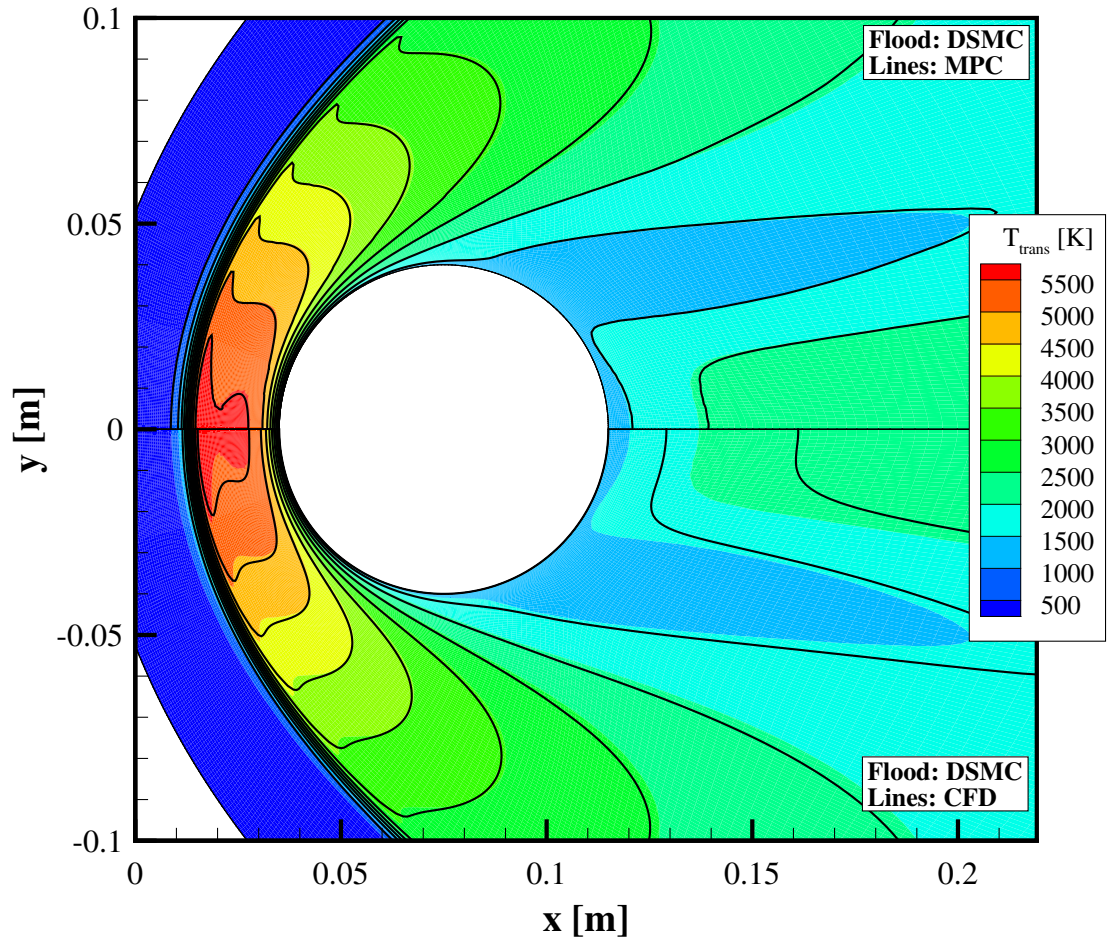


Figure 7.4: Contours of translational temperature for the Mach 10, Kn_∞ 0.01 flow of 50% N_2 /50% N over a two-dimensional cylinder.

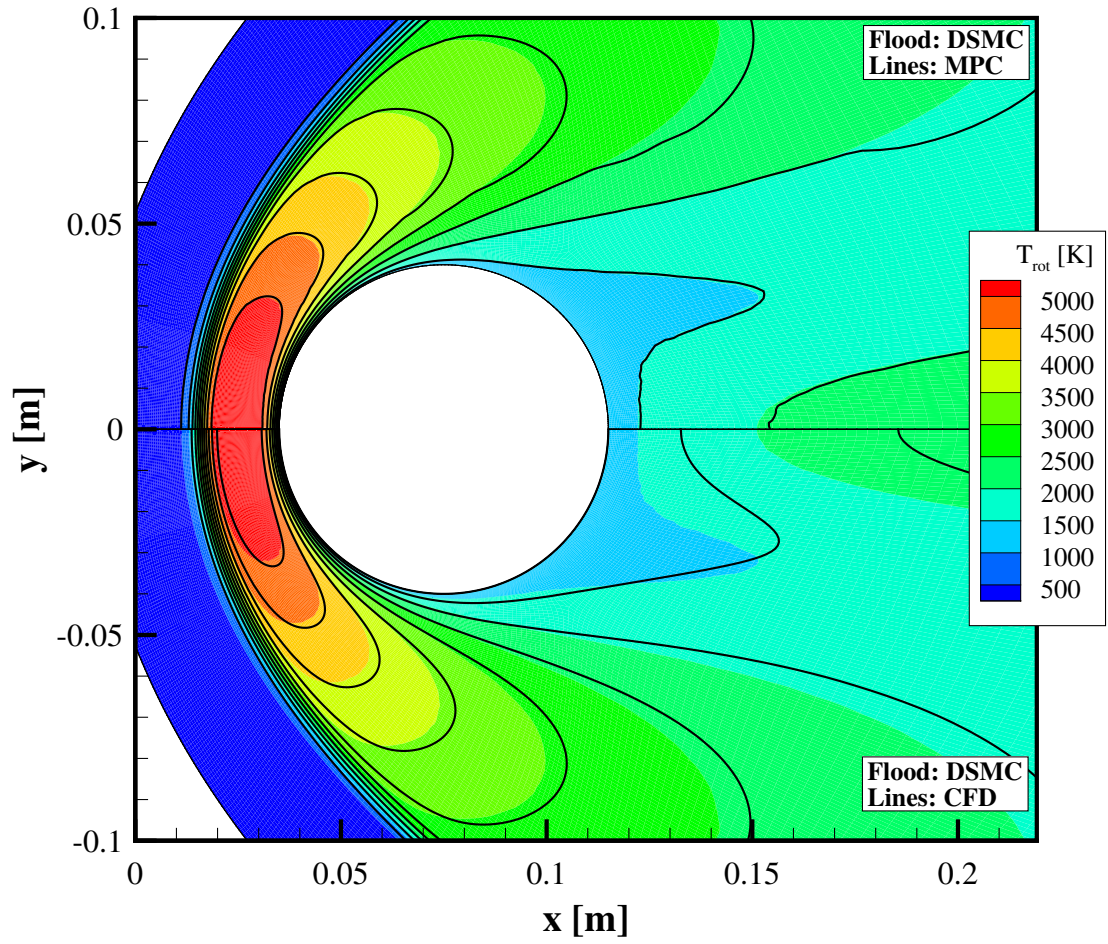


Figure 7.5: Contours of rotational temperature for the Mach 10, Kn_∞ 0.01 flow of 50% N_2 /50% N over a two-dimensional cylinder.

Table 7.1: Ranges of errors relative to full DSMC for the Mach 10, Kn_∞ 0.01 flow of 50% N_2 /50% N over a two-dimensional cylinder.

Property	MPC Results	CFD Results
T_{trans}	$-0.11 \leq \epsilon \leq 0.07$	$-0.76 \leq \epsilon \leq 0.17$
T_{rot}	$-0.09 \leq \epsilon \leq 0.07$	$-0.66 \leq \epsilon \leq 0.06$
ρ_{N2}	$-0.10 \leq \epsilon \leq 0.06$	$-0.05 \leq \epsilon \leq 0.61$
ρ_N	$-0.08 \leq \epsilon \leq 0.06$	$-0.13 \leq \epsilon \leq 0.36$

Table 7.2: Relative errors measured in the L_2 norm for the Mach 10, Kn_∞ 0.01 flow of 50% N_2 /50% N over a two-dimensional cylinder.

Property	MPC Results	CFD Results
T_{trans}	0.008	0.054
T_{rot}	0.010	0.061
$ V $	0.005	0.042
ρ_{N2}	0.011	0.035
ρ_N	0.012	0.175

those calculated for the full CFD results, as shown in Table 7.2. In terms of the locations of these errors throughout the computational domain, it appears that the extents of the errors in the fore body region are slightly more pronounced, while the extents of the errors in the upper shock region are slightly less pronounced, compared to the previous simple gas case. Again, because of the very large gradients in the shock wave, even very small discrepancies in the shock wave location can lead to remarkably large errors. Therefore, errors in this region are somewhat expected and may be unavoidable even in the most simple of simulations. As shown in Fig. 7.7, the most notable difference between the gas mixture and simple gas cases is observed in the rotational temperature prediction in the wake. Here, the MPC hybrid solution is within 5% of the full DSMC solution except for a few computational cells near the outflow boundary.

Although mass diffusion effects cannot be accurately simulated using the VHS collision model in DSMC, the variation of mixture composition as the flow of 50% N_2 /50% N traverses the shock wave and boundary layer is observed. To illustrate this, the mole fraction of N_2 is plotted along the stagnation streamline in Fig. 7.11. Of particu-

lar interest is the reduced population of N_2 molecules within the shock wave, which is caused by the N_2 molecules having a larger average velocity than the N atoms. This separation effect is due to baro-diffusion, which tends to *accelerate* heavier molecules, overcoming thermal diffusion, which tends to *decelerate* heavier molecules [69]. It should be noted that in the approximate diffusion flux used in the present continuum approach, baro-diffusion and thermal diffusion are neglected. The MPC method reproduces the same separation effect predicted by full DSMC in the shock wave, whereas the limited ability of CFD to accurately simulate strong nonequilibrium effects results in a minor depression in the N_2 mole fraction.

As shown in Fig. 7.11, even though there is a region between the shock wave and boundary layer particle regions where the continuum module is used, because of the improved boundary conditions provided by these particle regions, the MPC method is in better agreement with full DSMC than CFD is able to achieve alone. Therefore, rather than predicting the same N_2 mole fraction as the freestream value of 0.5, the MPC method and full DSMC predict a slightly higher post-shock N_2 mole fraction, which then decreases prior to increasing in the boundary layer. Although there is a noticeable discrepancy between full DSMC and the MPC method near the pre-boundary layer hybrid interface, this discrepancy is less than 2%. Again, the full CFD simulation yields a slight increase in the N_2 mole fraction in the boundary layer, whereas both full DSMC and the MPC method predict mole fractions of approximately 0.57.

7.2.2 Surface Properties

As they were defined in Eqs. 5.10 through 5.12, the surface pressure, heat transfer, and shear stress coefficients calculated along the cylinder surface are plotted in Figs. 7.12 through 7.14. The MPC method is able to reproduce full DSMC results for this gas mixture case to within the same accuracy observed in the simple gas case.

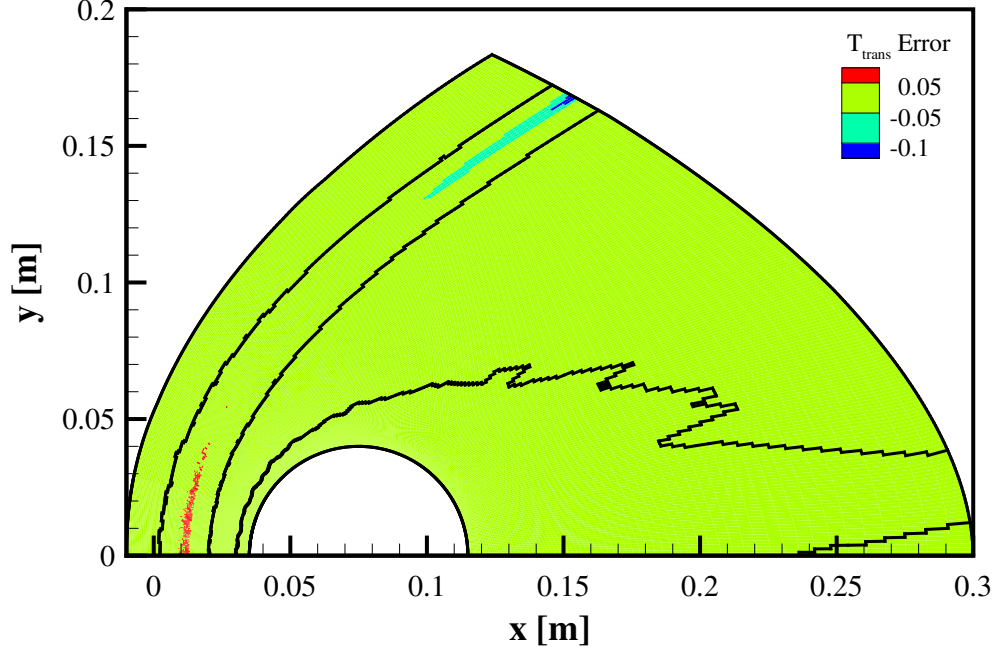


Figure 7.6: Contours of translational temperature errors of the MPC method relative to full DSMC for the Mach 10, Kn_∞ 0.01 flow of 50% N_2 /50% N over a two-dimensional cylinder; hybrid interfaces are shown as black lines.

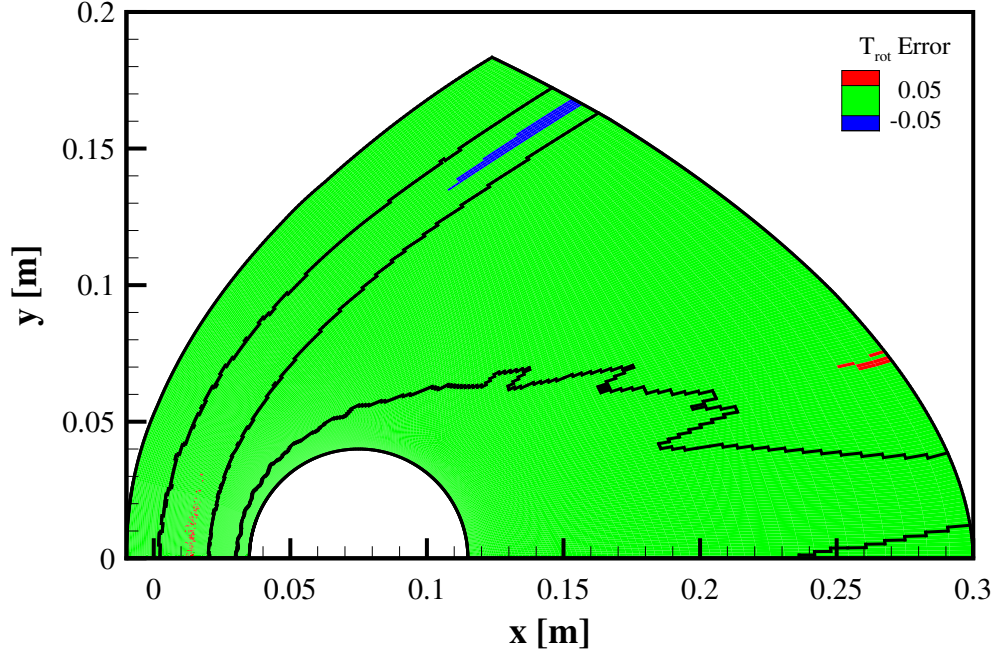


Figure 7.7: Contours of rotational temperature errors of the MPC method relative to full DSMC for the Mach 10, Kn_∞ 0.01 flow of 50% N_2 /50% N over a two-dimensional cylinder; hybrid interfaces are shown as black lines.

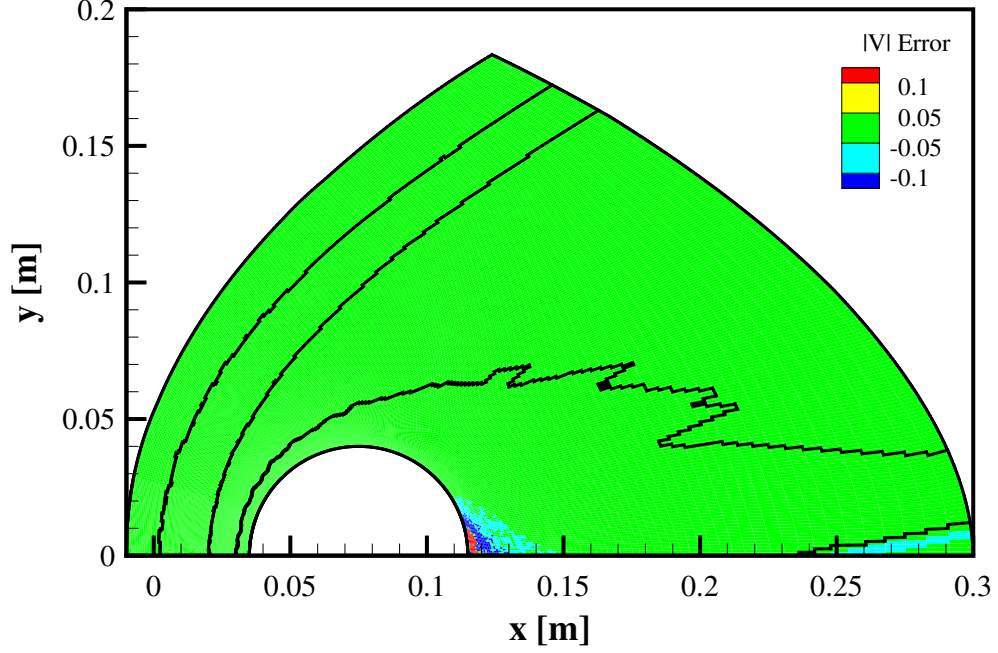


Figure 7.8: Contours of velocity magnitude errors of the MPC method relative to full DSMC for the Mach 10, Kn_∞ 0.01 flow of 50% N_2 /50% N over a two-dimensional cylinder; hybrid interfaces are shown as black lines.

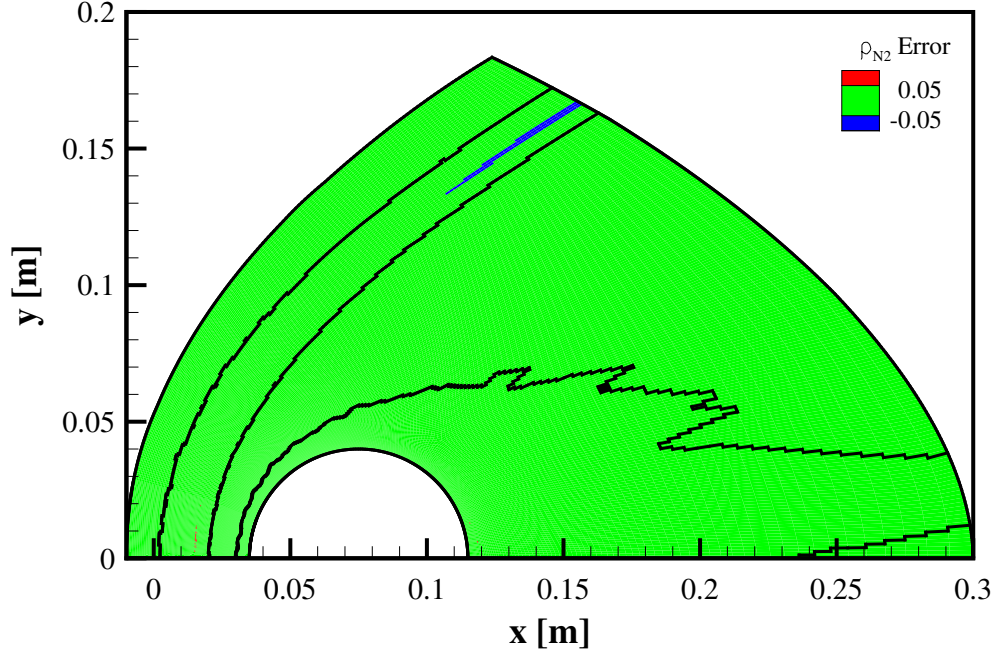


Figure 7.9: Contours of N_2 mass density errors of the MPC method relative to full DSMC for the Mach 10, Kn_∞ 0.01 flow of 50% N_2 /50% N over a two-dimensional cylinder; hybrid interfaces are shown as black lines.

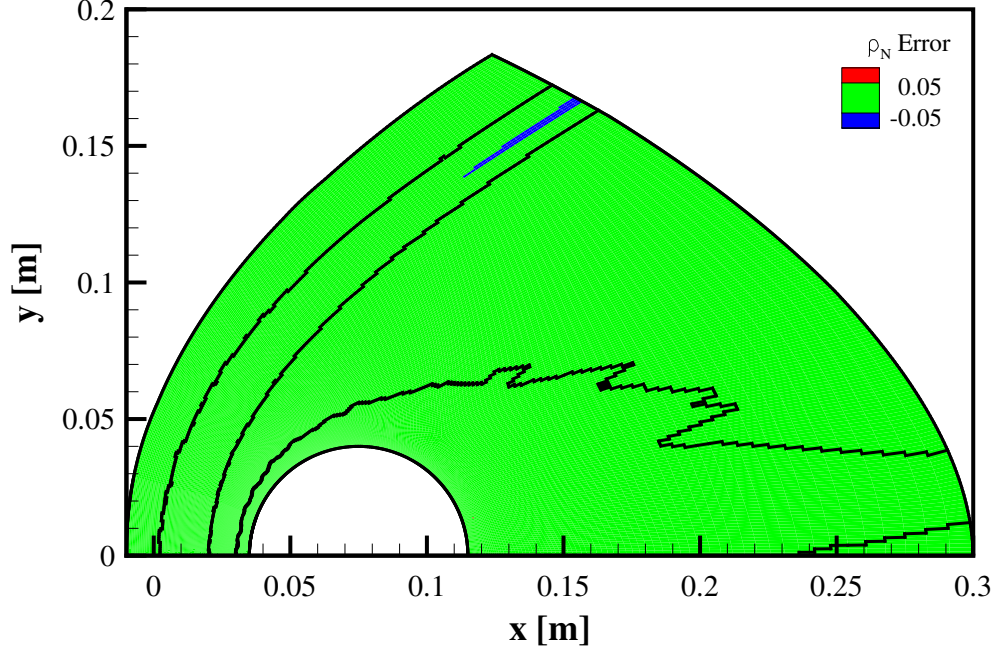


Figure 7.10: Contours of N mass density errors of the MPC method relative to full DSMC for the Mach 10, Kn_∞ 0.01 flow of 50% N_2 /50% N over a two-dimensional cylinder; hybrid interfaces are shown as black lines.

Whereas CFD results over predict the surface pressure coefficient over the entire aft body, the solution obtained using the MPC method is within $\pm 5\%$ of that obtained using the DSMC method throughout the entire computational domain. Because of the no-slip condition imposed in the CFD simulation, the resulting heat transfer coefficient profile is over predicted across the entire cylinder surface, as shown in Fig. 7.13. The MPC method is able to improve upon this initial continuum solution and recover the profile of the heat transfer coefficient predicted by full DSMC to within $\pm 5\%$. The profiles of shear stress coefficient along the cylinder surface are plotted in Fig. 7.14, where the larger wake region previously noted in the CFD solution is again illustrated. Because of the heightened level of statistical scatter observed near the fore stagnation point and in the wake, an accuracy of $\pm 5\%$ is maintained between the angular positions of 15° and 155° . The MPC method and full DSMC predict the point of incipient separation in the wake to occur within 1° of each other.

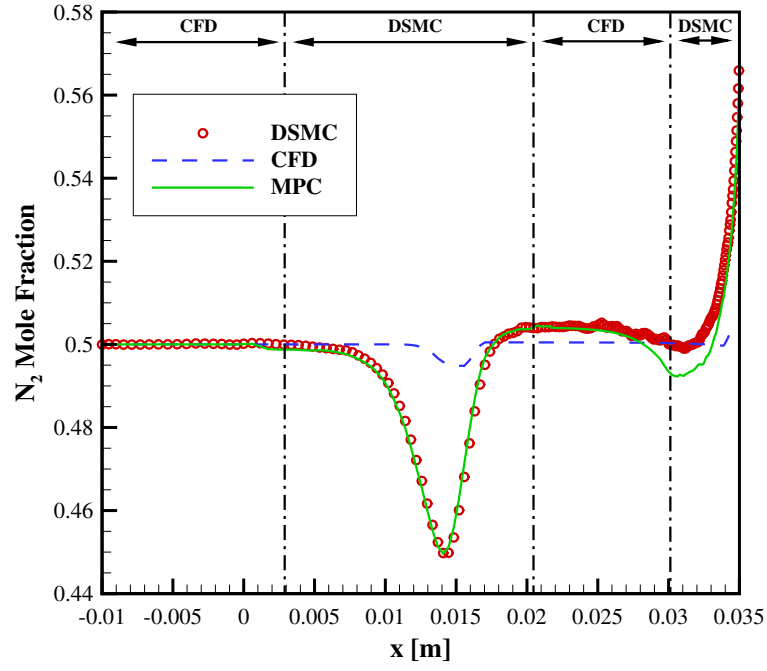


Figure 7.11: N_2 mole fraction along the stagnation streamline for the Mach 10, Kn_∞ 0.01 flow of 50% N_2 /50% N over a two-dimensional cylinder.

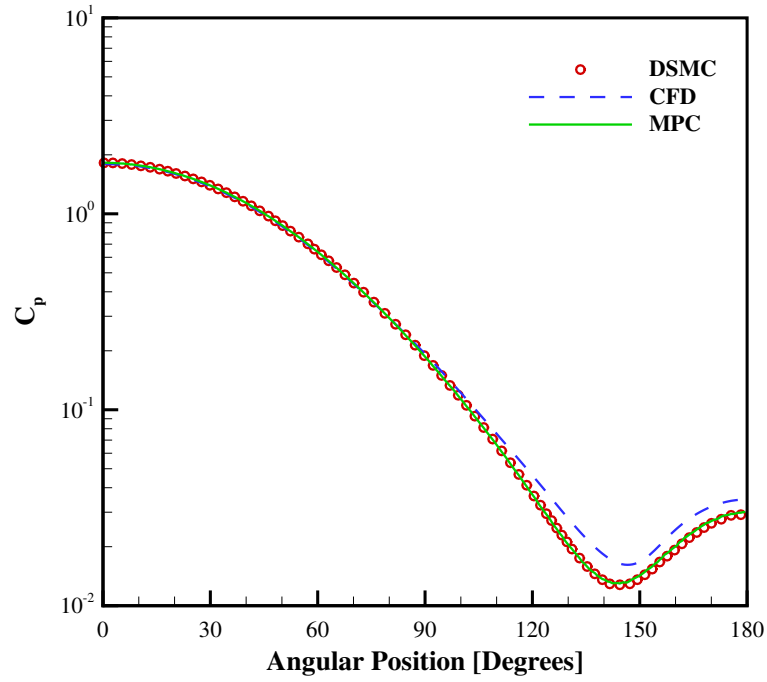


Figure 7.12: Surface pressure coefficient along the cylinder surface for the Mach 10, Kn_∞ 0.01 flow of 50% N_2 /50% N .

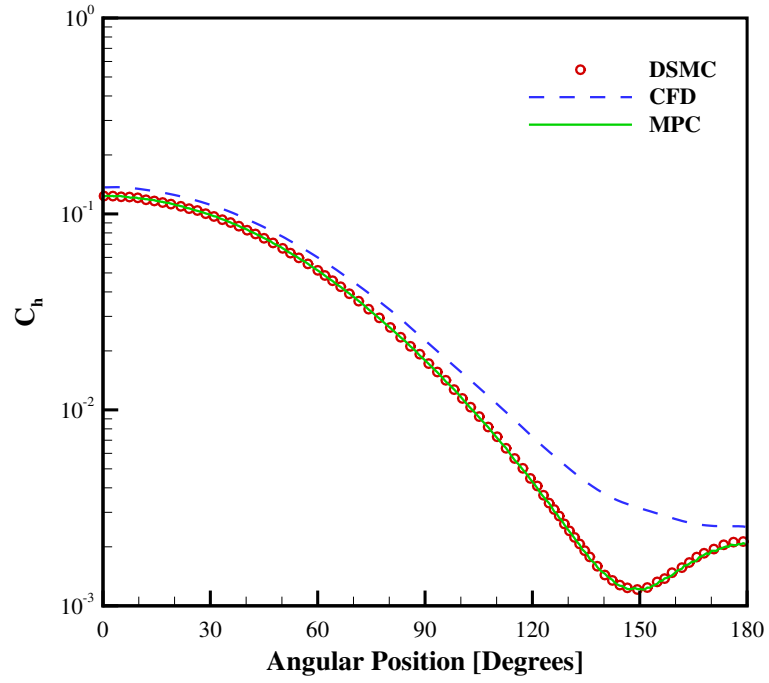


Figure 7.13: Heat transfer coefficient along the cylinder surface for the Mach 10, Kn_∞ 0.01 flow of 50% N_2 /50% N .

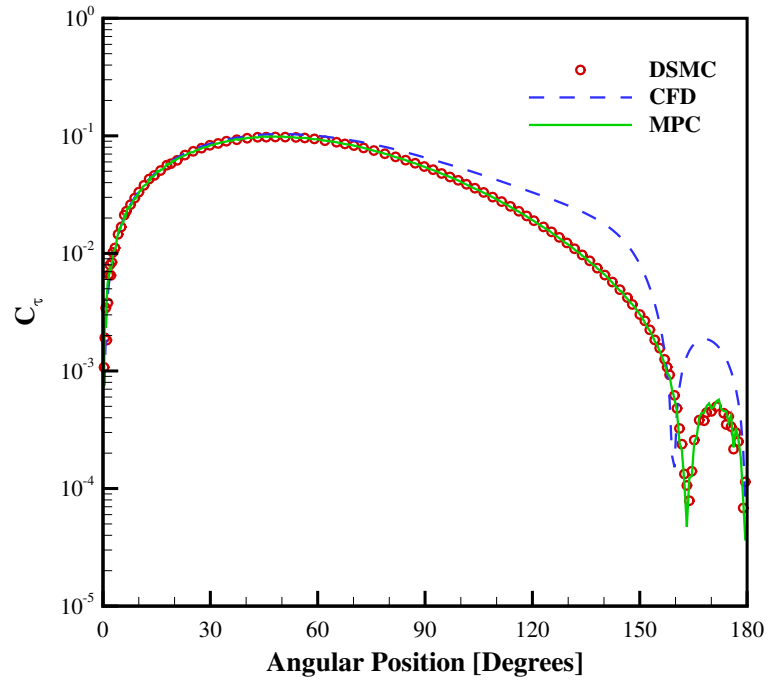


Figure 7.14: Shear stress coefficient along the cylinder surface for the Mach 10, Kn_∞ 0.01 flow of 50% N_2 /50% N .

Table 7.3: Computational performance statistics for the Mach 10, Kn_∞ 0.01 flow of 50% N_2 /50% N over a two-dimensional cylinder.

	CFD	DSMC	MPC
Normalized CPU Time	1.0	30.0	11.9
Normalized Memory	1.0	16.6	10.8
# Particles	-	47.1×10^6	21.3×10^6
# Continuum Cells	41,122	-	18,602
# Particle Cells	-	47,638	27,953
# Processors	4	40	18
Sampling/Total DSMC Steps	-	100,000/180,000	100,000/105,050

7.2.3 Computational Performance

Except for the computational cells near the cylinder surface, a constant numerical weight is specified throughout the simulation domain such that there are at least 40 particles per cell. Assuming the freestream mole fraction is maintained everywhere, this results in approximately 20 particles of each species per cell. As a result, the MPC hybrid simulation requires 21.3 million simulator particles, and the full DSMC simulation requires 47.1 million simulator particles, making this gas mixture case more computationally demanding than that for a simple gas. Therefore, the ideal speedup factor is approximately 2.21. Based on the total computational cost of each simulation, the actual speedup factor is approximately 2.52, which is higher than the ideal, as was the case with the simple gas simulation presented in Chapter VI. The number of processors was chosen such that the same number of particles are simulated on each processor. Whereas 80,000 time steps are required prior to sampling in the full DSMC simulation, the hybrid interfaces are locked and sampling begins after only 5,050 DSMC time steps in the hybrid simulation, which accounts for the better than ideal speedup factor. Also, the MPC simulation requires approximately 35% less memory than the full DSMC simulation. A summary of these computational performance statistics is provided in Table 7.3.

7.3 Verification of the MPC Method: 80% N_2 /20% O_2

In order to accommodate even the most simple atmospheric gas mixture, the MPC method must allow for each polyatomic species to experience rotational relaxation independently. This is accomplished through the use of the particle selection methodology described in Chapter IV, where each collision partner is examined sequentially to determine whether or not a rotational relaxation event occurs. Both the MPC method and the MONACO DSMC code used for verification now employ this selection methodology. In the current section, these modifications are verified by simulating a Mach 10, Kn_∞ 0.01 flow of 80% N_2 /20% O_2 (by mole) over a two-dimensional cylinder. Vibrational excitation is again neglected in this simulation, enabling a more straightforward assessment of the MPC method and its ability to accurately simulate mixtures of polyatomic species in rotational nonequilibrium. The global Knudsen number is calculated as the ratio of the freestream mean free path to the cylinder diameter, giving a freestream density of $6.415 \times 10^{-5} kg/m^3$ and $1.832 \times 10^{-5} kg/m^3$ for N_2 and O_2 , respectively, assuming a freestream temperature of 217.45K. The freestream velocity is specified to be 2965m/s, and the cylinder surface is maintained at a constant temperature of 1,000K. The physical models employed in the continuum and particle approaches are detailed in Chapter IV, and the relevant parameters for each species and collision class are provided in Appendix A.

The LeMANS finite volume CFD solver is first used to obtain a grid-independent continuum solution, which requires approximately 41,100 computational cells. The MPC method is then initialized with this continuum solution and mesh. The various continuum breakdown parameters defined in Eq. 6.5 are then calculated based on this initial continuum solution, and the computational domain is divided into particle and continuum regions, depending on the estimated level of thermodynamic nonequilibrium. Most importantly, the Kn_{rot} threshold value of 0.2 that was determined for the simple N_2 gas and the 50% N_2 /50% N gas mixture is verified to be adequate for

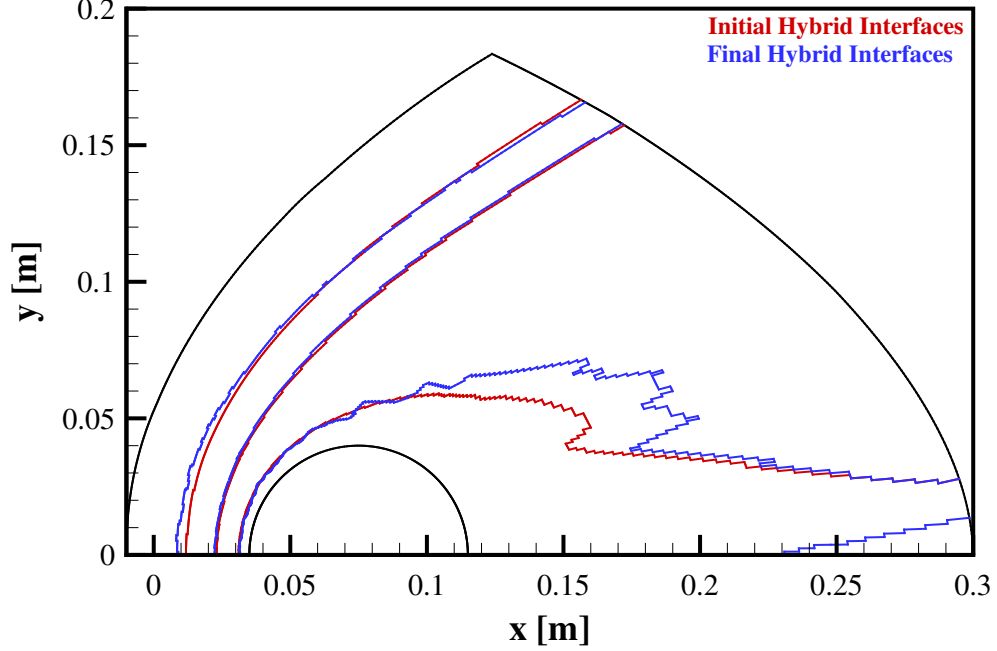


Figure 7.15: Initial and final hybrid interfaces for the Mach 10, Kn_∞ 0.01 flow of 80% N_2 /20% O_2 over a two-dimensional cylinder.

this mixture by executing the same procedure detailed in Chapter VI. The initial and final hybrid interfaces for this MPC simulation are plotted in Fig. 7.15, and are similar to those shown for the cases that have been previously discussed.

The particle regions are updated using a constant time step of $1 \times 10^{-8}s$, which is verified to be less than the local mean collision time throughout the computational domain; the maximum time step allowed in the continuum regions is $1 \times 10^{-7}s$. A constant numerical weight of 2×10^{12} is adequate to maintain at least 40 DSMC simulator particles per cell. However, reduced cell-based numerical weights are employed near the cylinder surface to increase the number of particles that contribute to the calculation of various surface properties. It should be noted that for this mixture composition, approximately 100 particles per cell would be required in order to maintain at least 20 particles representing O_2 in each cell. However, this would result in the full DSMC simulation requiring more than 100 million particles—a very computationally intensive simulation.

7.3.1 Flow Field Properties

Contours of various macroscopic fluid properties as predicted by full CFD, full DSMC, and the MPC hybrid method are presented in Figs. 7.16 through 7.18. There is excellent agreement between the MPC method and DSMC, with minor differences in the near-wake region, as was also the case with the 50% N_2 /50% N mixture. In addition, there appear to be discrepancies in both the translational and rotational temperatures in the fore body. Further investigation reveals, however, that this is merely an artifact of the chosen contour levels; although the full DSMC simulation predicts slightly higher post-shock temperatures along the stagnation streamline, the profiles are still in very good agreement. The numerical ranges of errors between the MPC method and full DSMC results are provided in Table 7.4, and the relative errors measured in the L_2 norm are given in Table 7.5. The locations of these errors throughout the simulation domain are plotted in Figs. 7.19 through 7.23. Comparisons of these error contours and those from the simple N_2 gas and the 50% N_2 /50% N gas mixture show that both the magnitudes and locations of these flow field errors are fairly consistent. There are, however, substantially higher errors in the mass densities predicted by the MPC method in the current simulation. It is interesting to note that the level of error seems to be correlated with the number of time steps used to update the particle domains prior to locking the hybrid interfaces. In addition, the O_2 species concentration is the lowest of any mixture component examined here, and the range of errors exhibited by the O_2 mass density is also the largest, suggesting that use of more simulator particles to represent O_2 molecules would increase the agreement between the MPC and full DSMC results. Finally, the mixture composition varies very little through the shock wave and in the boundary layer, so comparisons of the N_2 mole fraction are not shown for this case.

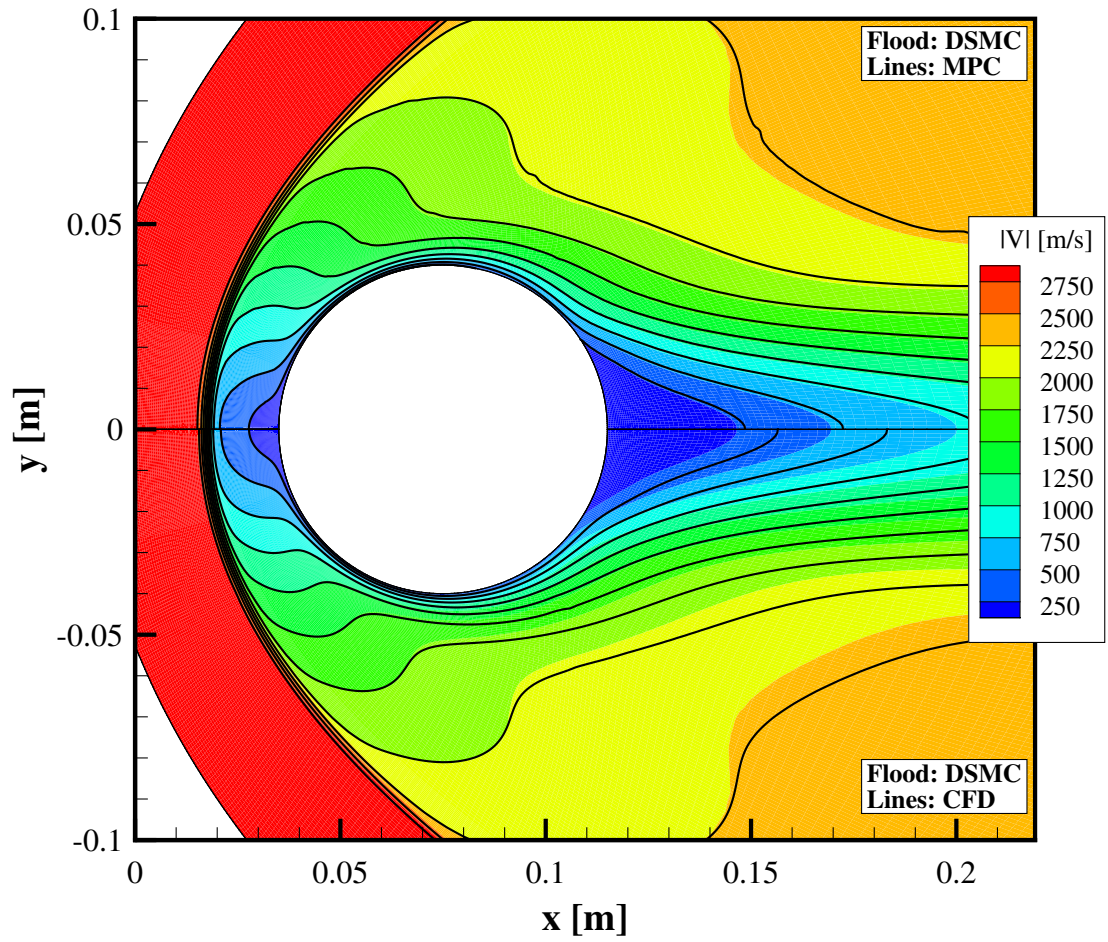


Figure 7.16: Contours of velocity magnitude for the Mach 10, Kn_∞ 0.01 flow of 80% N_2 /20% O_2 over a two-dimensional cylinder.

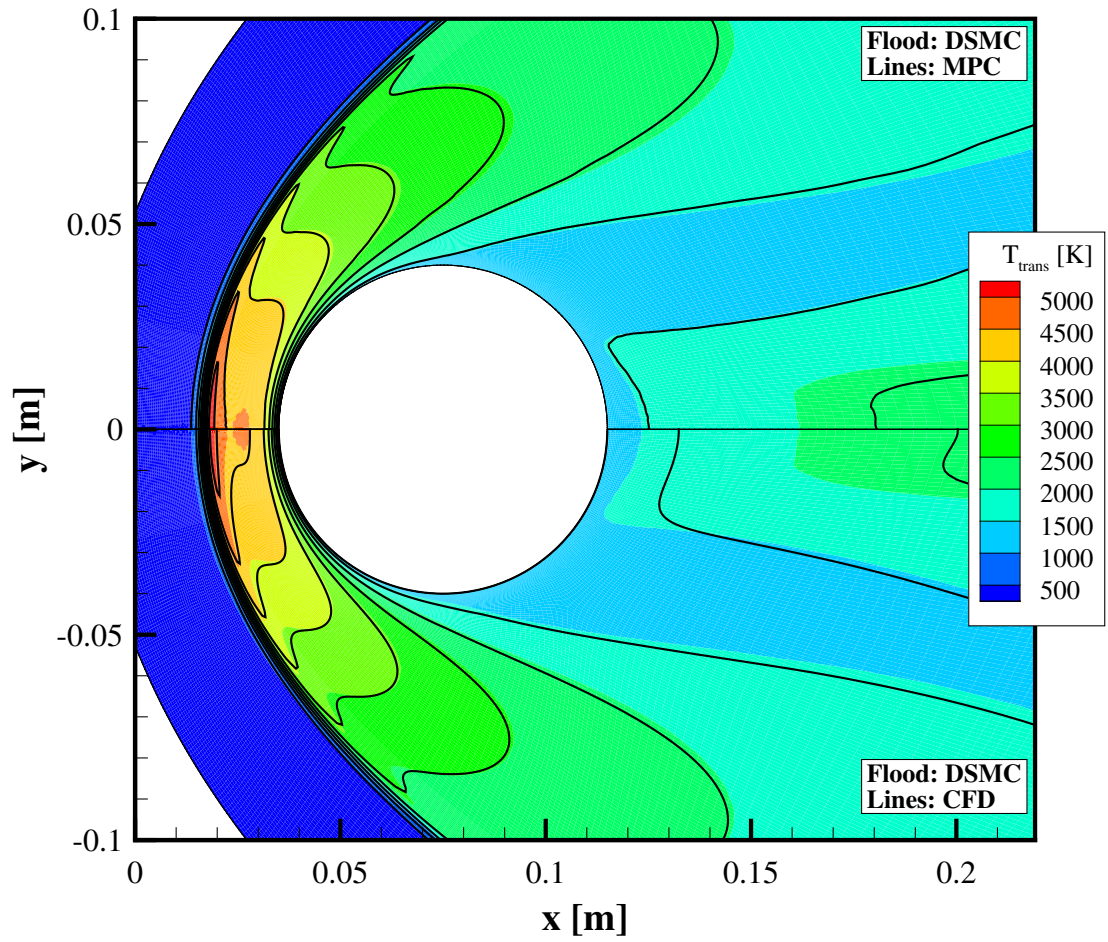


Figure 7.17: Contours of translational temperature for the Mach 10, Kn_∞ 0.01 flow of 80% N_2 /20% O_2 over a two-dimensional cylinder.

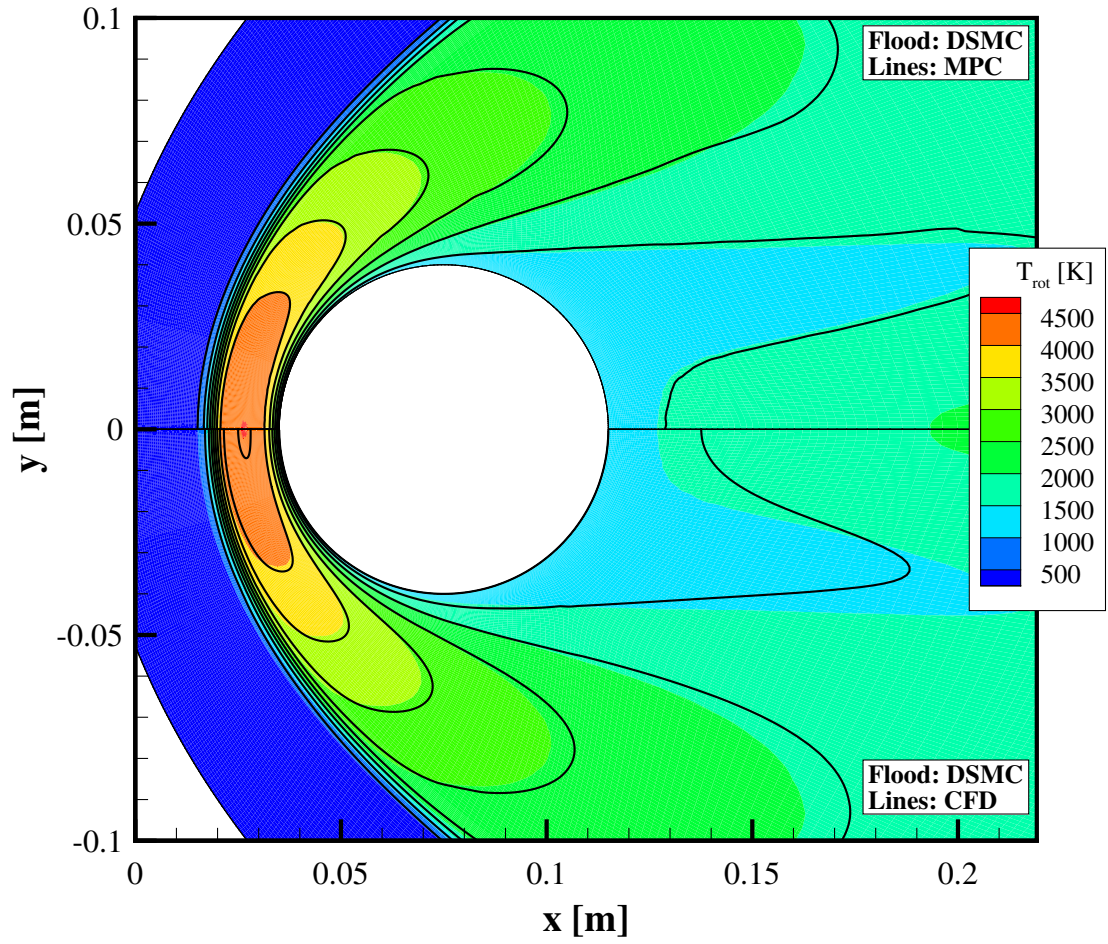


Figure 7.18: Contours of rotational temperature for the Mach 10, Kn_∞ 0.01 flow of 80% N_2 /20% O_2 over a two-dimensional cylinder.

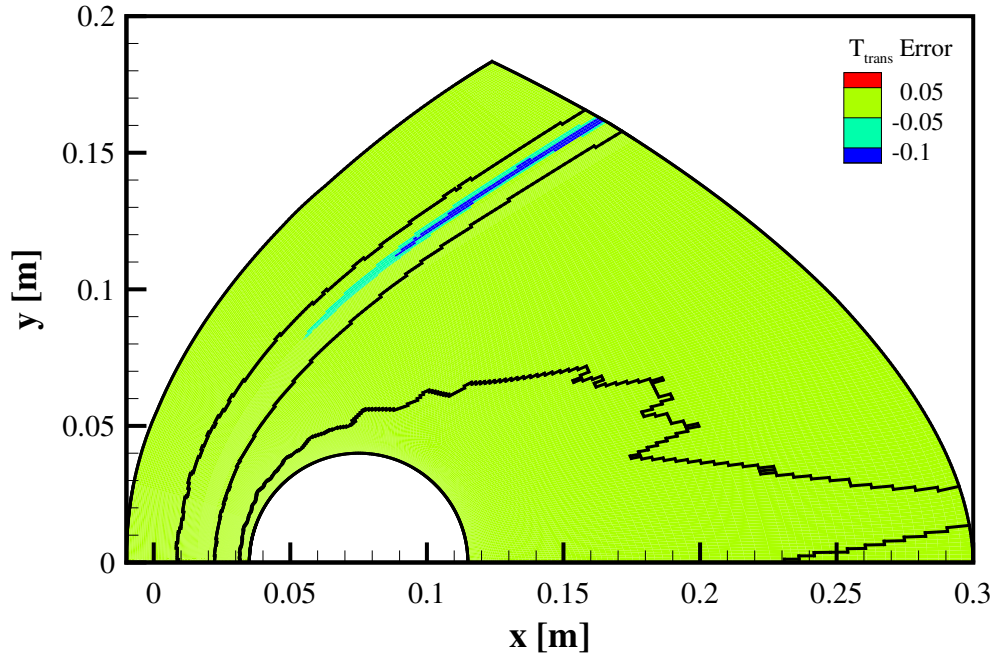


Figure 7.19: Contours of translational temperature errors of the MPC method relative to full DSMC for the Mach 10, Kn_∞ 0.01 flow of 80% N_2 /20% O_2 over a two-dimensional cylinder; hybrid interfaces are shown as black lines.

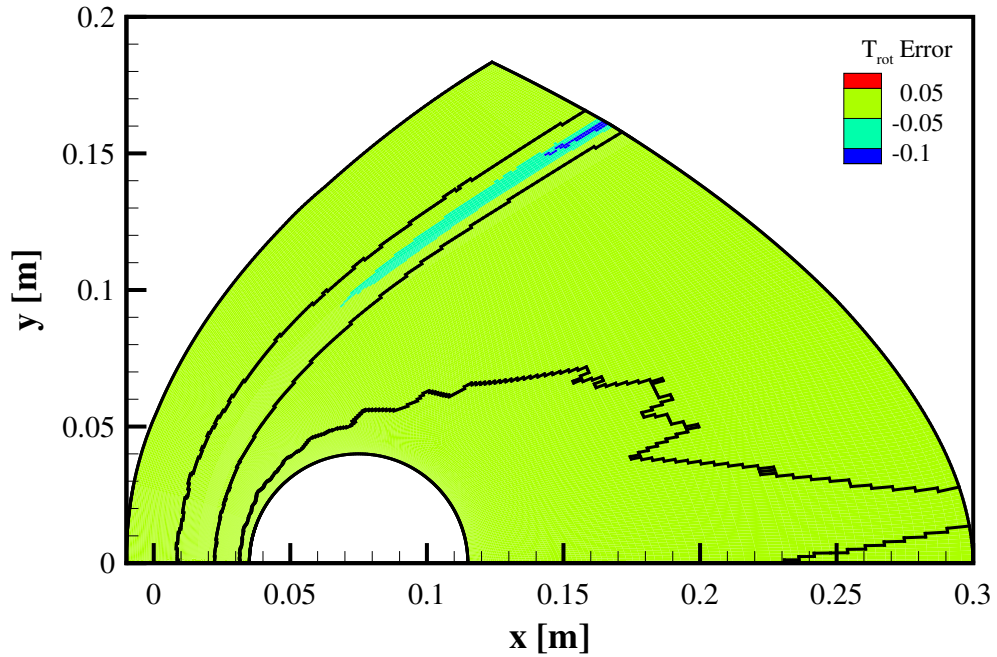


Figure 7.20: Contours of rotational temperature errors of the MPC method relative to full DSMC for the Mach 10, Kn_∞ 0.01 flow of 80% N_2 /20% O_2 over a two-dimensional cylinder; hybrid interfaces are shown as black lines.

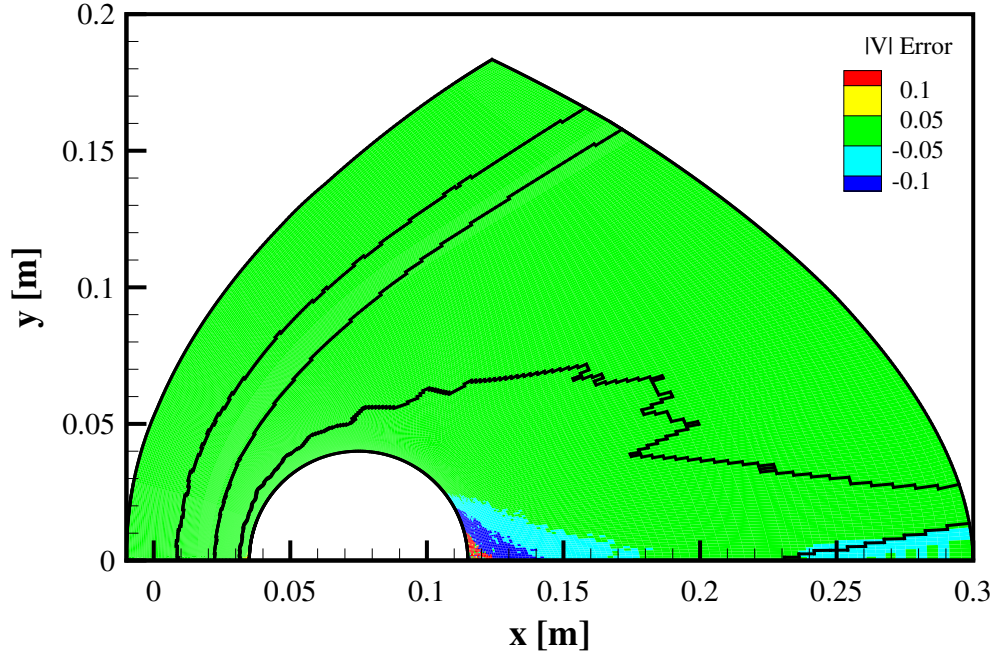


Figure 7.21: Contours of velocity magnitude errors of the MPC method relative to full DSMC for the Mach 10, Kn_∞ 0.01 flow of 80% N_2 /20% O_2 over a two-dimensional cylinder; hybrid interfaces are shown as black lines.

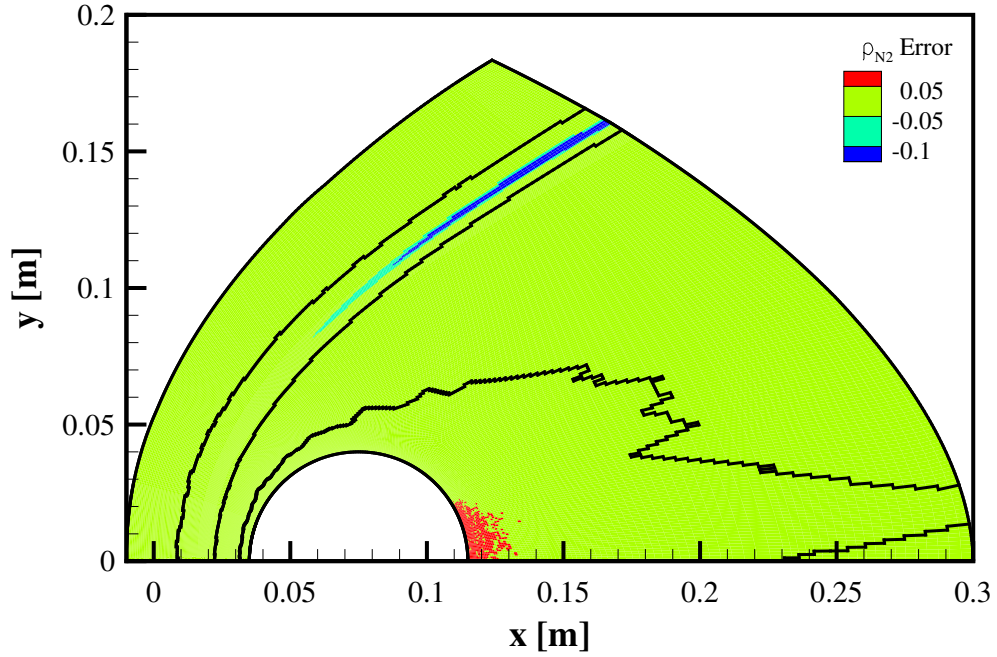


Figure 7.22: Contours of N_2 mass density errors of the MPC method relative to full DSMC for the Mach 10, Kn_∞ 0.01 flow of 80% N_2 /20% O_2 over a two-dimensional cylinder; hybrid interfaces are shown as black lines.

Table 7.4: Ranges of errors relative to full DSMC for the Mach 10, Kn_∞ 0.01 flow of 80% N_2 /20% O_2 over a two-dimensional cylinder.

Property	MPC Results	CFD Results
T_{trans}	$-0.14 \leq \epsilon \leq 0.04$	$-0.62 \leq \epsilon \leq 0.55$
T_{rot}	$-0.10 \leq \epsilon \leq 0.03$	$-0.63 \leq \epsilon \leq 0.07$
ρ_{N2}	$-0.20 \leq \epsilon \leq 0.08$	$-0.14 \leq \epsilon \leq 0.49$
ρ_N	$-0.20 \leq \epsilon \leq 0.10$	$-0.13 \leq \epsilon \leq 0.54$

Table 7.5: Relative errors measured in the L_2 norm for the Mach 10, Kn_∞ 0.01 flow of 80% N_2 /20% O_2 over a two-dimensional cylinder.

Property	MPC Results	CFD Results
T_{trans}	0.011	0.042
T_{rot}	0.011	0.071
$ V $	0.006	0.040
ρ_{N2}	0.012	0.082
ρ_N	0.012	0.064

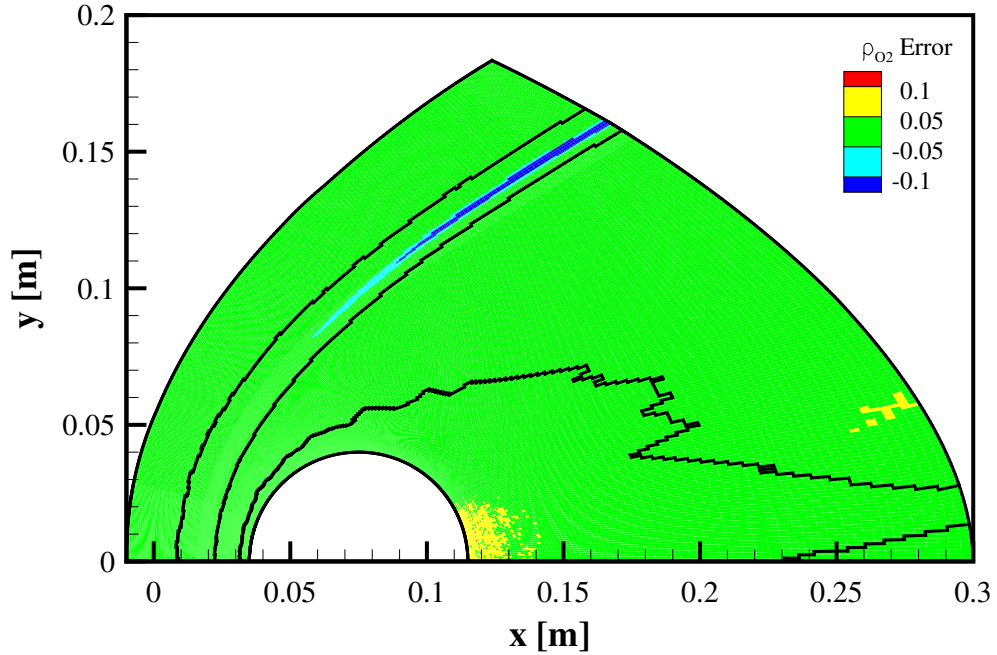


Figure 7.23: Contours of O_2 mass density errors of the MPC method relative to full DSMC for the Mach 10, Kn_∞ 0.01 flow of 80% N_2 /20% O_2 over a two-dimensional cylinder; hybrid interfaces are shown as black lines.

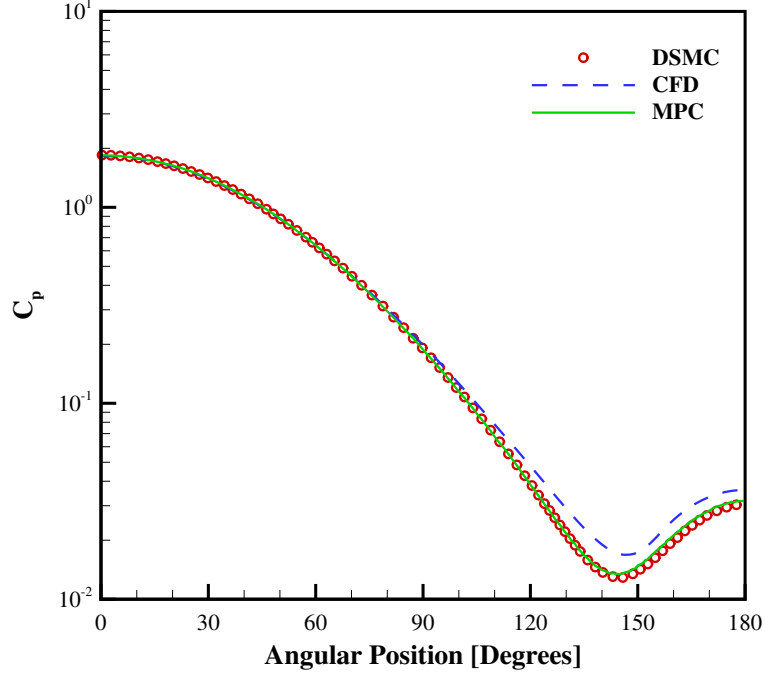


Figure 7.24: Surface pressure coefficient along the cylinder surface for the Mach 10, Kn_∞ 0.01 flow of 80% N_2 /20% O_2 .

7.3.2 Surface Properties

The surface pressure, heat transfer, and shear stress coefficients as calculated using CFD, DSMC, and the MPC hybrid method are plotted in Figs. 7.24 through 7.26. These results render conclusions that are very similar to those discussed regarding the 50% N_2 /50% N gas mixture. A slightly higher level of error is observed between the MPC and DSMC profiles of the surface pressure coefficient, with a maximum error of approximately 7.4%. Likewise, the maximum error between the profiles of heat transfer coefficient is approximately 6.2%. The errors between the profiles of shear stress coefficient are within the original goal of $\pm 5\%$ between the angular positions of 15° and 149° , with the statistical scatter of the DSMC simulation obscuring the level of error near the fore stagnation point and in the wake.

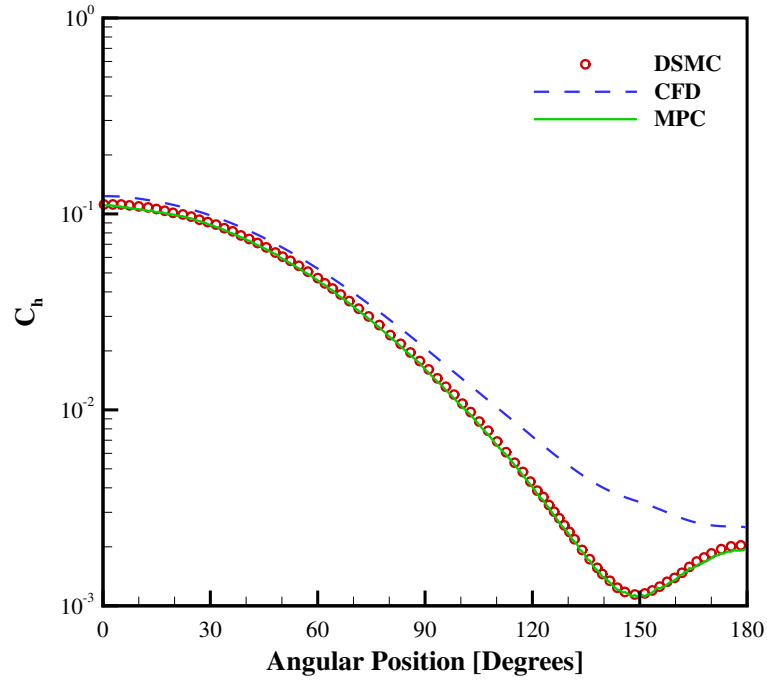


Figure 7.25: Heat transfer coefficient along the cylinder surface for the Mach 10, Kn_∞ 0.01 flow of 80% N_2 /20% O_2 .

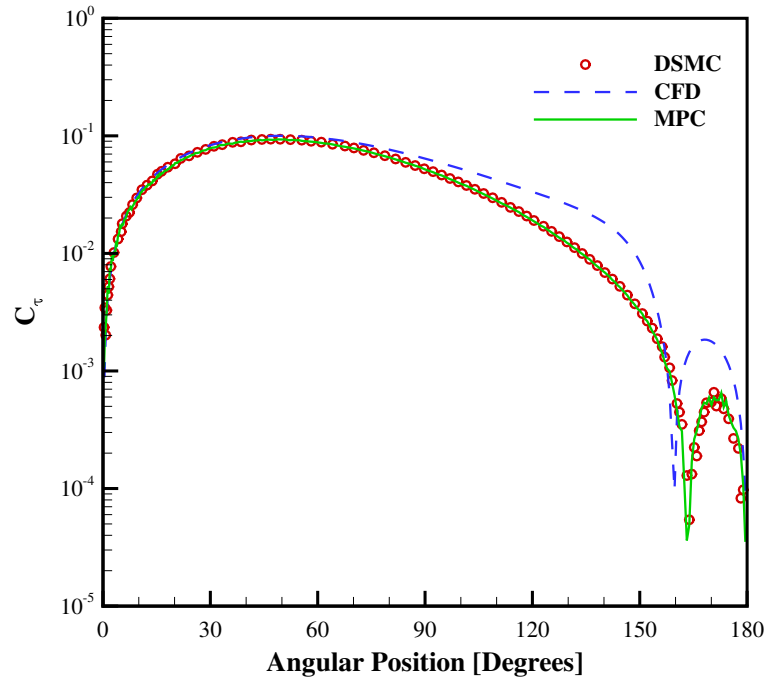


Figure 7.26: Shear stress coefficient along the cylinder surface for the Mach 10, Kn_∞ 0.01 flow of 80% N_2 /20% O_2 .

7.3.3 Computational Performance

By employing the more computationally involved DSMC method only where necessary to maintain physical accuracy, the MPC method is able to simulate this flow field using 17.9 million particles, whereas a full DSMC simulation requires 42.0 million particles. Therefore, an ideal speedup factor of 2.35 can be achieved. Upon comparing total computational times, it can be shown that the actual speedup factor is 2.22, which is slightly less than the ideal, despite the fact that each processor is assigned the same approximate number of particles in each simulation. However, this difference is of the order of the variation observed for repeated simulations, as discussed in Section 6.3.3. The MPC method also requires approximately 37% less memory than a full DSMC simulation.

Table 7.6: Computational performance statistics for the Mach 10, Kn_∞ 0.01 flow of 80% N_2 /20% O_2 over a two-dimensional cylinder.

	CFD	DSMC	MPC
Normalized CPU Time	1.0	18.6	8.36
Normalized Memory	1.0	15.3	9.64
# Particles	-	42.0×10^6	17.9×10^6
# Continuum Cells	41,122	-	20,668
# Particle Cells	-	52,912	28,601
# Processors	4	38	16
Sampling/Total DSMC Steps	-	100,000/180,000	100,000/103,030

7.4 A Challenge for the MPC Method: 50% N_2 /50% H

The largest difference between the molecular weights of constituent species in the gas mixtures analyzed thus far has been a factor of two. A gas mixture comprised of species with more disparate molecular weights presents an interesting challenge for the MPC method. To illustrate this, the case of a Mach 10, Kn_∞ 0.002 flow of 50% N_2 /50% H (by mole) over a two-dimensional cylinder is examined. Note the lower Knudsen number of this case relative to the previous simulations. As

mentioned in Chapter III, the MPC method is meant to provide a correction to an initial continuum solution. The bow shock wave formed in this flow is extremely diffuse, and a CFD solution provides a very poor approximation to the full DSMC solution. Reducing the Knudsen number improves the agreement between the full CFD and full DSMC solutions, facilitating the ability of the MPC method to bridge the difference.

Because of the small molecular weight of atomic hydrogen, and the resulting large molecular velocities of the simulator particles representing these atoms, the mean collision time is greatly reduced compared to the previous simulations. The DSMC time step is now required to be $1 \times 10^{-9}s$ for the decoupled advection and collision steps in the DSMC method to be valid. Such a small time step, in turn, leads to a longer transient period that must be simulated prior to sampling particle properties. For example, since 80,000 time steps were required before sampling in the previous full DSMC simulations, where a time step of $1 \times 10^{-8}s$ was used, the current simulation requires approximately 800,000 time steps prior to sampling. The very slow development of this flow field poses particular difficulty for the MPC method, which relies on changes in the flow field to determine when the hybrid interfaces should be locked.

Furthermore, with the continuum breakdown parameters defined as in Eq. 6.5, the shock wave is automatically encompassed in a particle region, but the particle region surrounding the boundary layer does not form until some distance away from the stagnation point. Therefore, even the new Kn_{rot} parameter with a threshold value of 0.2 fails to predict the onset of nonequilibrium in the boundary layer of this flow field. Even with extended particle regions surrounding the shock wave and boundary layer, which is enabled by reducing the threshold value of the Kn_{rot} parameter, the MPC method has limited success in reproducing full DSMC simulation results. Figure 7.27 shows the translational temperature profiles along the stagnation streamline

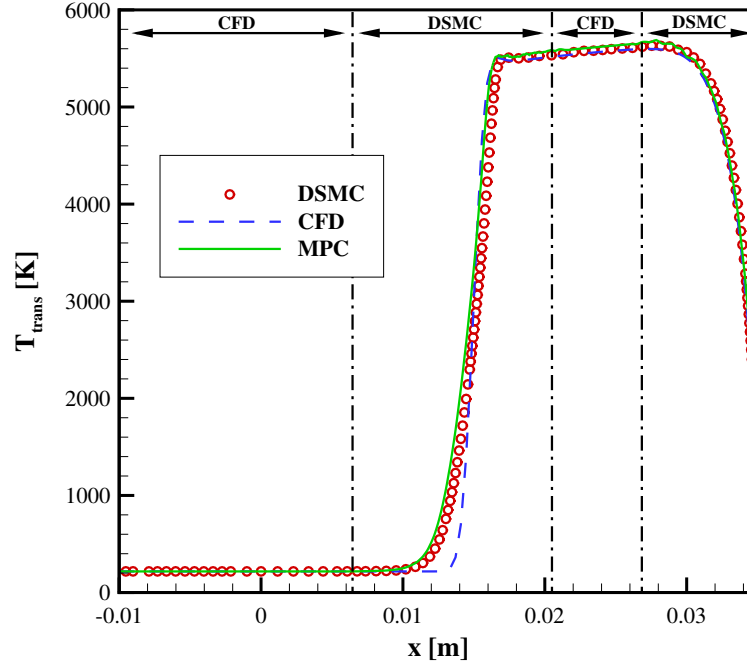


Figure 7.27: Translational temperature along the stagnation streamline for the Mach 10, Kn_∞ 0.002 flow of 50% N_2 /50% H .

as predicted by full CFD, full DSMC, and MPC hybrid simulations, while Fig. 7.28 shows the rotational temperature profiles. Relative to the agreement in the translational and rotational temperature profiles exhibited in Figure 6.18 of Chapter VI, and knowing that the errors for the 50% N_2 /50% N mixture are comparable, the current level of disagreement is quite high.

Perhaps the most compelling evidence that this particular mixture is problematic for the MPC method is provided by the surface properties plotted in Figs. 7.29 through 7.31. Even though it is apparent that more samples are needed to resolve these surface properties, the heightened level of disagreement between the MPC method and full DSMC is clear. The hybrid interfaces are automatically locked after 5,050 DSMC time steps, but it is estimated that an MPC simulation would have to be forced to run much longer in order to achieve improved physical accuracy relative to full DSMC results.

This simulation demonstrates the potential limitations of the automated MPC

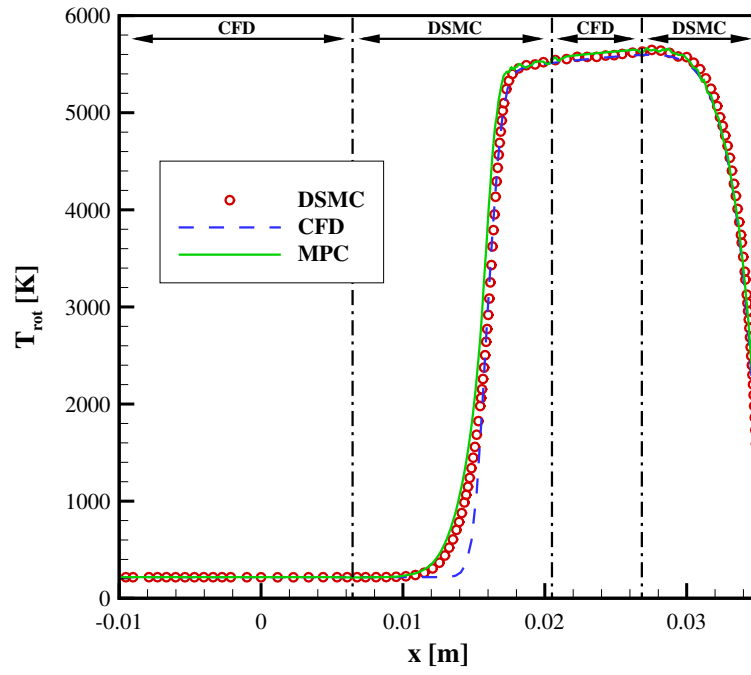


Figure 7.28: Rotational temperature along the stagnation streamline for the Mach 10, Kn_∞ 0.002 flow of 50% N_2 /50% H .

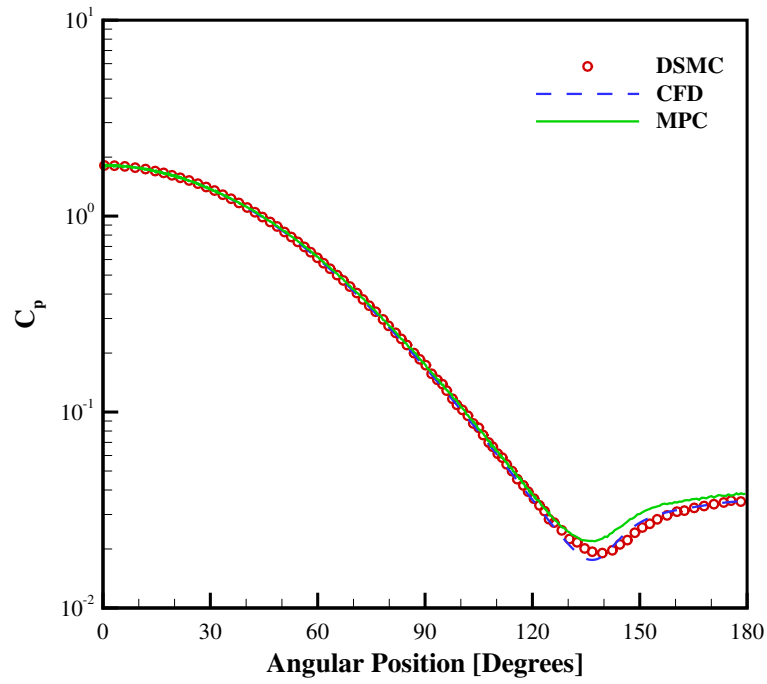


Figure 7.29: Surface pressure coefficient along the cylinder surface for the Mach 10, Kn_∞ 0.002 flow of 50% N_2 /50% H .

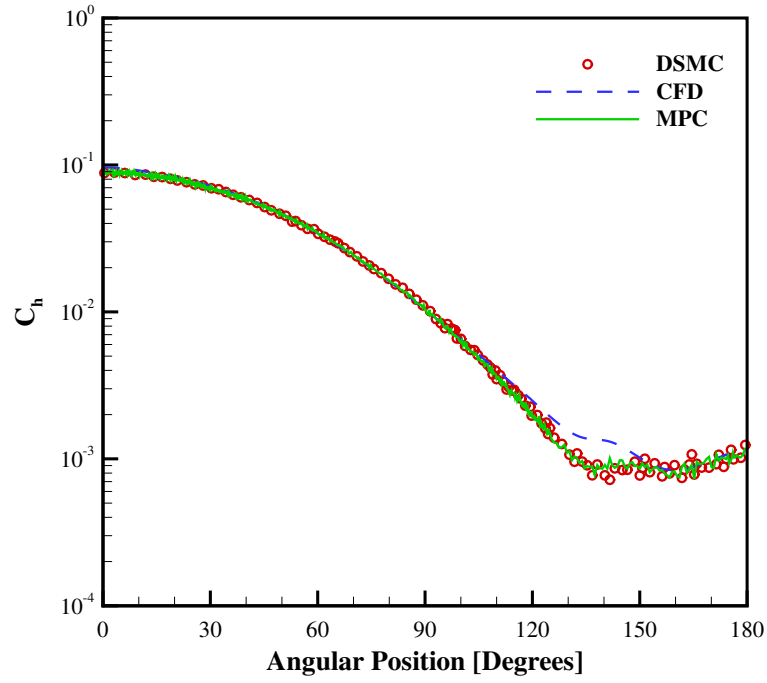


Figure 7.30: Heat transfer coefficient along the cylinder surface for the Mach 10, Kn_∞ 0.002 flow of 50% N_2 /50% H .

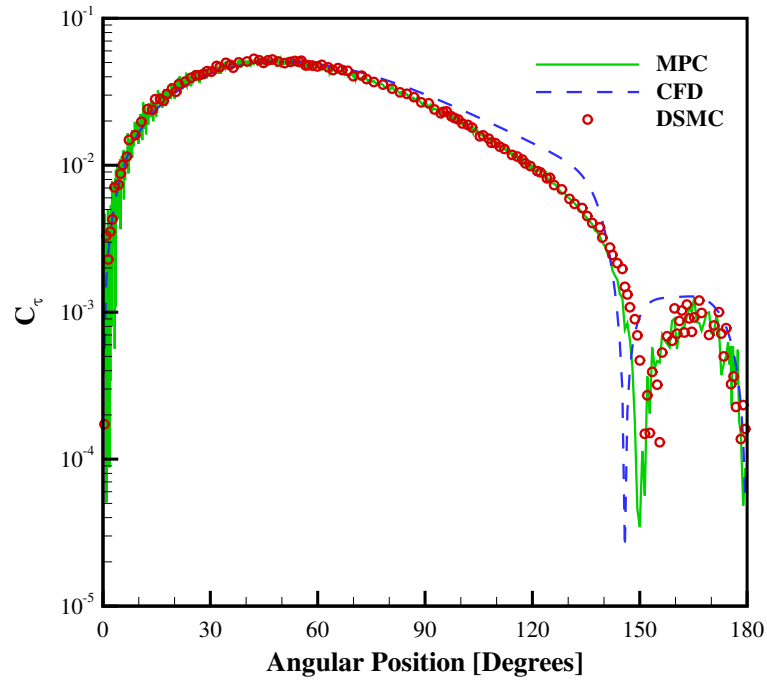


Figure 7.31: Shear stress coefficient along the cylinder surface for the Mach 10, Kn_∞ 0.002 flow of 50% N_2 /20% H .

algorithm in a subset of transitional, hypersonic flows. Future simulations of five-species air mixtures comprised of N_2 , O_2 , NO , N , and O should not pose such difficulties, since the molecular weights of the constituent species are not nearly as disparate as in this test case. However, more advanced chemical mechanisms for Earth’s atmosphere will include electrons, and atmospheric models for other planets include species with more widely varying molecular weights, so these obstacles will need to be overcome for the long-term development goals of the MPC hybrid method to be achieved.

7.5 Interim Conclusions

The MPC method was used to simulate three different gas mixtures in this chapter, with each case demonstrating either additional capabilities or potential limitations of the hybrid approach. First, the MPC method was shown to reproduce full DSMC results for a Mach 10, Kn_∞ 0.01 flow of 50% N_2 /50% N (by mole) over a two-dimensional cylinder. The maximum error exhibited in any macroscopic fluid property of interest throughout the entire flow field was approximately 11%, which is consistent with the level of error observed in the simple gas case of the previous chapter. Discrepancies in the rotational temperature, however, suggest that either the hybrid interfaces may have been locked prematurely, or the more rigorous generalized Chapman-Enskog distribution may be necessary when assigning rotational energies to newly generated particles along hybrid interfaces. Neglecting the fore stagnation point and wake region where statistical scatter is especially problematic, the surface properties predicted by the MPC method and those obtained from the corresponding full DSMC simulation differed by less than $\pm 5\%$. These hybrid results were obtained with a speedup factor that exceeded the ideal estimate based on the number of simulator particles, and required a fraction of the memory necessary for a full DSMC simulation.

The second simulation was quite similar except the gas mixture was comprised of 80% N_2 /20% O_2 (by mole), and each species was allowed to undergo rotational relaxation independently of the other. This represents a necessary step towards being able to accurately and efficiently simulate atmospheric flows with the MPC method. Although higher errors were observed for this case, results indicate that these errors could be reduced if a larger number of simulator particles were used. A final simulation of the Mach 10, Kn_∞ 0.002 flow of 50% N_2 /50% H (by mole) over a two-dimensional cylinder was performed, and highlighted a potential limitation of the automated MPC algorithm. In particular, a flow field that develops on a much longer time scale than can be detected by the automated algorithm may prove difficult for the MPC method to simulate accurately. This was also proposed as a possible cause for errors in the wake regions of previous simulations, where the low collisionality of the flow may result in the hybrid method prematurely locking the hybrid interfaces.

CHAPTER VIII

Conclusion

In this final chapter, the results and conclusions that have been presented are further summarized, and the implications of this work are discussed. The unique contributions made towards the ongoing development of a hybrid particle-continuum method for simulating transitional, hypersonic flows over blunt-body, re-entry vehicles are emphasized, and several areas where future research efforts should be focused are also proposed.

8.1 Summary of Dissertation

Chapter I provided a brief introduction to the complex, multiscale nature of transitional, hypersonic, re-entry flows, and motivated the development of hybrid numerical simulation approaches. The Knudsen and Damköhler numbers were shown to characterize the relative importance of microscopic length and time scales in these flows, indicating whether the assumption of a continuum is warranted, or if the molecular nature of the gas must be considered. Both translational and thermal nonequilibrium phenomena were introduced, along with their association with hallmark features of re-entry flows, such as the strong bow shock wave, boundary and shear layers, and low-density wake. The last several decades of spaceflight have ushered in a deeper understanding of hypersonic aerothermodynamics, and advances in computational

resources have enabled higher-fidelity mathematical modeling of the re-entry environment. However, the mixed rarefied/continuum nature of transitional, hypersonic flows presents a formidable challenge to even the most well developed simulation techniques, such as the numerical solution of the Navier-Stokes equations using CFD and the DSMC method. In terms of both physical accuracy and numerical efficiency, hybrid simulation approaches provide many advantages over either CFD or DSMC alone.

In Chapter II, an overview of the mathematical models and numerical simulation techniques used to analyze transitional, hypersonic flows was provided. Beginning with a description of dilute gases that is grounded in kinetic theory, the Boltzmann equation was introduced. The Boltzmann equation provided the foundation for deriving the Euler equations of mass, momentum, and energy conservation for a continuum flow in thermodynamic equilibrium. The Navier-Stokes equations were also derived by assuming the distribution of molecular properties is a first-order perturbation of the equilibrium distribution function. Inherent to this derivation is the assumption that mass diffusion, viscosity, and heat conduction are linear functions of density, velocity, and temperature gradients in the flow field. Because of the difficulties associated with numerical solution of the Boltzmann equation, especially for mixtures of polyatomic species, and the physical limitations of the Navier-Stokes equations, a number of alternative simulation approaches were also discussed. The DSMC method was presented as the method of choice for obtaining flow field solutions that converge to those of the Boltzmann equation. The last section of this chapter provided a review of the published work regarding hybrid computational approaches, which offer the benefit of physical accuracy and numerical efficiency.

Chapter III focused on describing the MPC method, a hybrid framework that loosely couples two existing CFD and DSMC simulation codes. The current capabilities of LeMANS, a finite volume CFD solver, and MONACO, a general cell-based

implementation of the DSMC method, were discussed, along with the recent development of the MPC method. A detailed description of the hybrid algorithm was presented. This included the means by which regions of thermodynamic nonequilibrium are identified from an initial continuum solution, and the subsequent refinement of the coarse, continuum mesh to comply with DSMC cell-size requirements in particle regions. In addition, the mechanisms used to transfer updated solution information across hybrid interfaces, between the continuum and particle simulation modules, were discussed. Specifically, the procedures used to sample DSMC particle properties from distribution functions defined by macroscopic properties and, thus, provide continuum solution information to the particle domains, were detailed. The various equations needed to calculate macroscopic fluid properties from these simulator particles were also provided, which enables updated boundary solution information from the particle regions to be transferred back to the continuum domains. Finally, the modular organization of the CFD, DSMC, and hybrid functions and data structures was illustrated, and the previously described steps of the hybrid algorithm were assembled in a description of a typical hybrid cycle and complete MPC simulation.

The mathematical models used to simulate various physical processes, such as transport phenomena and thermal relaxation, were discussed in Chapter IV. Particular emphasis was placed on the consistency of these physical models in near-equilibrium flows. Assuming the hybrid interfaces are placed in near-equilibrium regions of a flow field, where both CFD and DSMC are physically appropriate simulation techniques, the physical models used in each approach should predict the same flow field solution in these regions. By verifying that these physical models are consistent, through simplified Couette flow and heat bath simulations, it is known that information is being consistently exchanged across these hybrid interfaces. Therefore, any differences between full CFD, full DSMC, and hybrid simulation results must be due to the limitations of the numerical approaches themselves and not inaccurate

information exchange. In this chapter, pertinent physical models were verified to be consistent for both simple gases and mixtures of chemical species.

A detailed and consistent evaluation of the physical accuracy of the MPC method relative to full DSMC was presented in Chapter V. A mapping procedure that introduces no interpolation errors, yet allows for different computational meshes to be used by MPC and DSMC simulations enables cell-by-cell comparisons of macroscopic fluid properties of interest. In this way, both the magnitude and location of errors incurred by using the hybrid approach are known, leading to deeper insight into what challenges remain for the continued development of the MPC method. A previously simulated test case was revisited for this investigation, which involves the Mach 12 flow of N_2 over a two-dimensional cylinder at a global Knudsen number of 0.01. This more detailed approach to accuracy quantification revealed errors that were much higher than reported in earlier publications, and the locations of these errors suggested a number of improvements that were then implemented. Specifically, the vacuum outflow boundary condition employed in the particle regions of hybrid simulations and in full DSMC simulations was replaced by a supersonic boundary condition that is consistent with that used in the continuum approach. In addition, attempts were made to improve the definition of macroscopic properties along hybrid interfaces, where differences in mesh refinement may lead to a loss of information. This enabled newly generated DSMC simulator particles to be assigned properties that are more consistent with those that would naturally occur in a full DSMC simulation. A reduction in flow field errors was observed after these changes were implemented, and this level of error was contextualized by quantifying the statistical scatter of the corresponding full DSMC simulation. Additional causes for the remaining errors were also investigated.

In Chapter VI, a new parameter for detecting rotational nonequilibrium effects was proposed. As was done for the gradient-length local Knudsen number, which is

the primary tool for determining continuum breakdown in the MPC hybrid method, detailed comparisons of full DSMC and full CFD simulation results for two test cases were performed. The first case was that of a Mach 12, Kn_∞ 0.01 flow of N_2 over a two-dimensional cylinder, while the second case was very similar except that a Mach 10 flow of 50% N_2 /50% N was simulated. The magnitudes of the various continuum breakdown parameters, including the new rotational nonequilibrium parameter and that used in previous MPC simulations, were then calculated from the full CFD solution. The efficacy of these parameters was determined by how well their magnitudes correlated with the errors between the full DSMC and full CFD solutions. This new rotational nonequilibrium parameter was found to position the post-shock hybrid interfaces in these flows at the same approximate locations as the original parameter; failure of the gradient-length local Knudsen number to accurately predict continuum breakdown in this region is the reason why an additional parameter was initially proposed. In addition, the new rotational nonequilibrium parameter was shown to position the pre-boundary layer hybrid interfaces conservatively upstream of the stagnation points, where the other continuum breakdown parameters failed. An MPC hybrid simulation of the simple gas test case was then performed, and results obtained using the original and new rotational nonequilibrium parameters were compared. The agreement between hybrid and full DSMC results, in terms of both flow field and surface properties, was greatly improved through the use of this new rotational nonequilibrium parameter. In addition, the hybrid method achieved reductions in both computational time and memory usage relative to the corresponding full DSMC simulation.

Extension of the MPC method to include mixtures of chemical species was discussed and verified in Chapter VII. Additional considerations for accurately simulating gas mixtures using a hybrid approach were reviewed, including continuum breakdown detection and generation of DSMC simulator particles along hybrid in-

interfaces. Because of the simplifying assumptions made for these initial simulations involving gas mixtures, and additional findings published in the literature, very few changes to the hybrid algorithm were needed. The MPC method was first used to simulate the Mach 10, Kn_∞ 0.01 flow of 50% N_2 /50% N over a two-dimensional cylinder, which is the same mixture test case examined in Chapter VI. The maximum error in any macroscopic property throughout the entire flow field was calculated to be 11%, while errors in surface properties were, for the most part, limited to $\pm 5\%$. The MPC method was also shown to accurately predict the variation of mixture composition through the bow shock wave and in the boundary layer. A higher than ideal speedup factor was observed when computational times required by the MPC method and full DSMC were compared.

The particle selection methodology that allows for multiple polyatomic species to experience rotational relaxation independently was also verified by simulating a Mach 10, Kn_∞ 0.01 flow of 80% N_2 /20% O_2 over a two-dimensional cylinder. Although the errors between MPC and full DSMC results were generally higher than in the previous simulation, it is believed that these errors could be reduced by using more DSMC particles to represent the lower concentration of O_2 in this mixture. Finally, a mixture comprised of species with widely disparate molecular weights was simulated using the MPC method. The Mach 10, Kn_∞ 0.002 flow of 50% N_2 /50% H over a two-dimensional cylinder proved to be a challenge for the MPC method because of the much longer time required for this flow field to fully develop. Although this should not be problematic for future simulations of a five-species air mixture, for example, an appropriate solution will have to be determined for more complex air chemistry mechanisms.

8.2 Unique Contributions

As discussed in Chapter III, the MPC hybrid method was first developed by Schwartzentruber [64], and was shown to yield physically accurate results at a reduced computational cost for one-dimensional shock waves [65], two-dimensional and axisymmetric, steady, hypersonic blunt-body flows [66, 68], and shock-boundary layer interaction flows [67]. This initial demonstration of the loosely-coupled hybrid framework was limited to simple gases. Deschenes [19] later extended the capabilities of the MPC method to simple gases in rotational and vibrational nonequilibrium [21, 22]. The MPC algorithm was also parallelized to enable efficient simulation of more complicated physics and larger computational domains [20]. Building from these existing capabilities, this dissertation provides several unique contributions towards the ongoing development of the MPC hybrid method and its ability to simulate realistic atmospheric flows in an automated, numerically efficient, and physically accurate manner. A summary of these contributions and their implications is provided in this section, and additional details are provided in Refs. [79, 80, 81].

1. For the first time, a comprehensive assessment of the physical accuracy of the MPC hybrid method has been performed. Previous accuracy verification studies have been limited to comparisons between hybrid and full DSMC results along streamlines and other flow field extraction lines only. In this dissertation, hybrid and full DSMC results are quantitatively compared on a cell-by-cell basis without relying on interpolation procedures. As a result, both the magnitudes and locations of errors are known throughout the entire simulation domain. This enables a deeper level of understanding in terms of the causes of existing errors and potential improvements that should be made to the MPC method. These existing errors were also contextualized by quantifying the level of statistical scatter in a corresponding DSMC simulation, resulting in the conclusion that

the original accuracy objective of $\pm 5\%$ is unreasonable for typical simulations.

2. A commercial memory profiling software has been vetted in this dissertation, and provides a more accurate and detailed measure of the computational requirements of *parallel* MPC simulations. Profiling of the MPC code has also given insight into specific functions and subroutines that may impede further improvements in computational efficiency.
3. Improvements in the physical accuracy of the MPC method relative to full DSMC were achieved by implementing more consistent boundary conditions along the outflow boundary of the computational domain and hybrid interfaces. Most directly related to the ongoing development of hybrid particle-continuum methods, it was observed that differences in grid refinement along the hybrid interfaces contributes to a loss of information when newly generated simulator particles are generated from macroscopic fluid properties. By utilizing the gradients in these macroscopic fluid properties, better estimates of both particle properties and their positions can be obtained. Further investigation into the consistent exchange of information across hybrid interfaces also revealed that the transient nature of the DSMC method, especially in regions where the flow field develops more slowly, may lead to premature locking of the hybrid interfaces and inaccurate results.
4. The ability of the MPC hybrid method to *automatically* identify regions of thermodynamic nonequilibrium throughout the course of a simulation was also improved by the work presented in this dissertation. A new parameter for identifying rotational nonequilibrium effects was proposed and found to offer advantages over the gradient-length local Knudsen number and the previously employed rotational nonequilibrium parameter. Prior to this investigation, it was commonplace for these continuum breakdown parameters to fail to pre-

dict an adequately thick particle region surrounding the boundary layers of transitional, hypersonic, blunt-body flows. This new rotational nonequilibrium parameter was shown to obviate the need for human intervention in the MPC algorithm for a simple gas and two different gas mixtures.

5. This dissertation research enabled the accurate simulation of gas mixtures using the MPC method. Particle and continuum models for transport properties and thermal nonequilibrium were verified to be consistent for simple gases and gas mixtures. Specifically, a simple approach to calculating VHS collision model parameters that are consistent with the Gupta Mixing Rule in CFD was proposed, and was verified to give results that are comparable to those obtained using a more rigorous approach. Improved agreement between translational-rotational energy exchange models was obtained for both simple gases and gas mixtures through detailed heat bath simulations. To achieve consistent vibrational relaxation rates between CFD and DSMC when simulating gas mixtures, a new “mixture rule” was used in the continuum approach that is unlike others proposed in the literature.
6. The MPC method is now able to accommodate more realistic atmospheric flows in which multiple species are in rotational nonequilibrium and equilibrate at different rates. A particle selection methodology for calculating translational-rotational energy exchange probabilities was implemented and shown to yield relaxation rates that are consistent with the continuum approach.
7. This dissertation discussed the challenges of simulating gas mixtures comprised of species with widely disparate molecular weights. Simulated flow fields that develop on much longer time scales than were previously considered pose difficulties for the automatic detection of steady state in a hybrid simulation.

8.3 Future Work

The current capabilities of the MPC hybrid method enable the physically accurate and numerically efficient simulation of a large class of transitional, hypersonic flows over simple blunt bodies. However, continued research efforts are required to further develop the physical and chemical modeling capabilities, algorithm robustness, and general applicability of the method to more complex hypersonic vehicles of engineering interest. These recommended areas of future work are described in more detail in this section.

8.3.1 VSS Collision Model

In order to accurately simulate viscosity *and* mass diffusion effects in a gas mixture, the VSS collision model should be used in the DSMC method instead of the VHS collision model. The latter collision model was employed in these initial simulations of gas mixtures because the simple approach proposed in Chapter IV for determining collision parameters that are consistent with the Gupta Mixing Rule facilitated the calculation of only a reference diameter and temperature exponent for each collision class. The more rigorous Nelder-Mead simplex algorithm enables the minimization of functions of many independent variables, and provides a means to calculate a reference collision diameter, temperature exponent, and scattering parameter for each collision class in a gas mixture. Therefore, the capability already exists to perform MPC hybrid simulations of gas mixtures that account for all transport processes in a physically meaningful manner.

8.3.2 Generalized Chapman-Enskog Distribution

There is limited evidence to suggest that the mass diffusion and internal heat flux perturbation terms of the generalized Chapman-Enskog distribution are unimportant relative to other transport processes in transitional, hypersonic flows over blunt

bodies. In addition, when DSMC simulator particles are generated along hybrid interfaces in the MPC hybrid method, rotational energies are sampled from a Boltzmann equilibrium distribution. However, it is unclear how valid these approximations are until current MPC results are compared to those obtained when particle properties are sampled from the more rigorous generalized Chapman-Enskog distribution. Only after such a comparison is made can these approximations be eliminated as possible sources of the remaining errors between hybrid and full DSMC results. Of particular concern is the sudden disagreement between the contours of rotational temperature across the hybrid interfaces, as discussed in this dissertation. Also, when mass diffusion effects are accurately simulated through the use of the VSS collision model in particle domains, it will become even more important to determine the relative importance of the mass diffusion perturbation terms of the generalized Chapman-Enskog distribution throughout flow fields of interest.

8.3.3 Continuum Breakdown

One of the most challenging aspects of developing a hybrid particle-continuum method is the accurate and reliable prediction of continuum breakdown. Because one of the goals of the MPC method is to reduce the computational effort of obtaining physically accurate solutions of transitional, hypersonic flows, these measures of continuum breakdown are calculated from an initial continuum solution which is then improved throughout the course of the simulation. The downfall of such measures, however, is that a threshold value is required to distinguish computational cells that are in thermodynamic nonequilibrium from those that can be accurately simulated using CFD. Therefore, the generality of these continuum breakdown parameters and their associated threshold values is a concern. A more reliable mechanism for determining rotational nonequilibrium was proposed in this dissertation, but a deeper understanding of nonequilibrium phenomena and continuum breakdown is needed.

Until then, the efficacy of current measures of continuum breakdown should not be assumed in every situation. For example, even though a parameter for detecting vibrational nonequilibrium effects in the MPC method has already been proposed, a procedure similar to that presented in this dissertation for identifying rotational nonequilibrium effects should also be carried out.

8.3.4 Mesh Refinement Algorithm

Currently, the MPC method is able to accommodate structured computational meshes only, and does not allow for hanging nodes. This leads to more refinement in certain particle regions than is necessary to comply with DSMC cell-size requirements. Therefore, gains in efficiency may be achieved by allowing for hanging nodes in the computational mesh. Additional benefits could also be realized through more complex mesh refinement algorithms. For example, in a typical CFD simulation, the alignment of the computational mesh with the bow shock wave and boundary layer are essential because the numerical solution of the Navier-Stokes equations relies heavily on flow field gradients. Resolution of the viscous boundary layer also requires a very refined grid near simulated wall boundaries. A computational mesh that is optimized for a DSMC simulation will be quite different. Each cell is simply used for binning simulator particles for collision partner selection and calculating macroscopic averages. Use of an unstructured mesh is, thus, preferred because the grid generation process is greatly simplified without diminishing the accuracy of the simulation, as long as the computational cells are appropriately sized. Similar to the CFL condition in CFD, however, DSMC cells that are too small for a given time step can lead to a loss of accuracy; simulator particles do not spend enough time in these cells to obtain physically meaningful averages. This can easily happen when the current MPC algorithm is initialized with a continuum solution and corresponding mesh that is greatly refined to resolve the viscous boundary layer, for example. Through the use

of involved interpolation procedures, the particle and continuum regions of a hybrid simulation could employ computational meshes that are optimally suited for each approach. Such a complete separation of length scales between simulation domains is only advised after the basic hybrid algorithm is more thoroughly tested.

8.3.5 Chemical Reactions

In the case of high-enthalpy re-entry trajectories, chemical reactions among atmospheric species are expected to occur. Such chemical reactions, including dissociation of molecular species and ionization, may significantly alter the shock stand-off distance, heat loads, and aerodynamic forces on the vehicle, to name a few. Accurate simulation of chemical reactions is a long-term goal of the MPC hybrid method. Both the MONACO and LeMANS codes already account for atmospheric chemistry, but the *consistency* of these chemical models remains a formidable challenge for several reasons. For one, the interdependent nature of dissociative reactions, vibrational energy relaxation, and the temperatures that characterize each energy mode further complicates these already complex processes. In addition, chemical reactions usually introduce trace species which may require the use of species-based numerical weights in DSMC simulations; the effect of variable species-based and cell-based numerical weights on the statistics of the DSMC method is still an active area of research.

8.3.6 Three-Dimensional Geometries

The transitional, hypersonic flow over a two-dimensional cylinder provides a flow field that is rich in the same physics of a more realistic, blunt-body vehicle. However, to enable widespread use in the engineering community, the MPC method must be capable of simulating more complex, three-dimensional flows. Actual re-entry capsules, for example, even if they can be assumed axisymmetric, often fly at non-zero angles of attack and employ reaction control system thrusters or propulsive deceleration, so

that the three-dimensionality of the flow field cannot be ignored. The extension of the MPC method to include three-dimensional simulation domains becomes an issue of coding, since both MONACO and LeMANS already have this capability. Even larger improvements in computational savings are expected for the MPC method relative to full DSMC when three-dimensional simulations are performed because of the additional dimension. For example, neglecting any flow field gradients, if a single continuum cell must be refined to include two particle cells in one dimension to comply with the local mean free path, then the corresponding cell in a three-dimensional simulation will be comprised of eight particle cells, all of which must contain the required number of simulator particles.

APPENDIX

APPENDIX A

Physical Model Parameters

Table A.1: Variable Hard Sphere (VHS) collision model reference diameters, d_{ref} [Å].

	N_2	N	O_2	H
N_2	3.99	3.69	3.79	3.58
N	3.69	3.36	—	—
O_2	3.79	—	3.85	—
H	3.58	—	—	3.35

Table A.2: Variable Hard Sphere (VHS) collision model temperature exponents, ω .

	N_2	N	O_2	H
N_2	0.675	0.701	0.690	0.793
N	0.701	0.746	—	—
O_2	0.690	—	0.683	—
H	0.793	—	—	0.801

Table A.3: Molecular species constants.

	T^* [K]	$(Z_{rot})_\infty$	θ_{rot} [K]	θ_{vib} [K]
N_2	91.5	18.0	2.88	3395
O_2	113.5	16.5	2.07	2256

BIBLIOGRAPHY

BIBLIOGRAPHY

- [1] Allinea, *Allinea DDT and MAP User Guide, Version 4.2.2*, 2014.
- [2] Anderson, Jr., J. D., *Introduction to Flight*, McGraw-Hill, Inc., 1989.
- [3] Anderson, Jr., J. D., *Fundamentals of Aerodynamics*, McGraw-Hill, Inc., 2007.
- [4] Bergemann, F. and Boyd, I. D., “New Discrete Vibrational Energy Model for the Direct Simulation Monte Carlo Method,” *Rarefied Gas Dynamics: Experimental Techniques and Physical Systems*, edited by Shizgal, B. D., and Weaver, D. P., Vol. 158, 1994, pp. 174–183.
- [5] Bhatnagar, P. L., Gross, E. P., and Krook, M., “A Model for Collision Processes in Gases. I. Small Amplitude Processes in Charged and Neutral One-Component Systems,” *Phys. Rev.*, Vol. 94, No. 3, May 1954, pp. 511–525.
- [6] Bird, G. A., “Approach to Translational Equilibrium in a Rigid Sphere Gas,” *Phys. Fluids*, Vol. 6, No. 10, October 1963, pp. 1518–1519.
- [7] Bird, G. A., “Breakdown of Translational and Rotational Equilibrium in Gaseous Expansions,” *AIAA J.*, Vol. 8, No. 11, November 1970, pp. 1998–2003.
- [8] Bird, G. A., *Molecular Gas Dynamics and the Direct Simulation of Gas Flows*, Oxford University Press, 1994.
- [9] Bird, R. B., Stewart, W. E., and Lightfoot, E. D., *Transport Phenomena*, John Wiley and Sons, 1960.
- [10] Borgnakke, C. and Larsen, P. S., “Statistical Collision Model for Monte Carlo Simulation of Polyatomic Gas Mixture,” *J. Comput. Phys.*, Vol. 18, No. 4, August 1975, pp. 405–420.
- [11] Boyd, I. D., “Analysis of Rotational Nonequilibrium in Standing Shock Waves of Nitrogen,” *AIAA J.*, Vol. 28, No. 11, November 1990, pp. 1997–1999.
- [12] Boyd, I. D., “Rotational-Translational Energy Transfer in Rarefied Nonequilibrium Flows,” *Phys. Fluids*, Vol. 2, No. 3, March 1990, pp. 447–452.
- [13] Boyd, I. D., “Analysis of Vibrational-Translational Energy Transfer Using the Direct Simulation Monte Carlo Method,” *Phys. Fluids*, Vol. 3, No. 7, July 1991, pp. 1785–1791.

- [14] Boyd, I. D., Chen, G., and Candler, G. V., "Predicting Failure of the Continuum Fluid Equations in Transitional Hypersonic Flows," *Phys. Fluids*, Vol. 7, No. 1, January 1995, pp. 210–219.
- [15] Camberos, J. A. and Chen, P.-H., "Continuum Breakdown Parameter Based on Entropy Generation Rates," *AIAA Paper 2003-0157*, January 2003, presented at the 41st AIAA Aerospace Sciences Meeting and Exhibit, Reno, NV.
- [16] Chang, C. S. and Uhlenbeck, G. E., "Transport Phenomena in Polyatomic Gases," *Report No. CM-681*, July 1951, Engineering Research Institute, University of Michigan, Ann Arbor, MI.
- [17] Chapman, S. and Cowling, T. G., *The Mathematical Theory of Non-Uniform Gases*, Cambridge University Press, 1939.
- [18] Chen, G. and Boyd, I. D., "Statistical Error Analysis for the Direct Simulation Monte Carlo Technique," *J. Comput. Phys.*, Vol. 126, No. 2, July 1996, pp. 434–448.
- [19] Deschenes, T. R., *Extension of a Modular Particle-Continuum Method for Nonequilibrium, Hypersonic Flows*, Ph.D. thesis, University of Michigan, 2011.
- [20] Deschenes, T. R. and Boyd, I. D., "Parallelization of a Modular Particle-Continuum Method for Hypersonic, Near Equilibrium Flows," *AIAA Paper 2010-808*, January 2010, presented at the 48th AIAA Aerospace Sciences Meeting Including the New Horizons Forum and Aerospace Exposition, Orlando, FL.
- [21] Deschenes, T. R. and Boyd, I. D., "Extension of a Modular Particle-Continuum Method to Vibrationally Excited, Hypersonic Flows," *AIAA J.*, Vol. 49, No. 9, September 2011.
- [22] Deschenes, T. R., Holman, T. D., and Boyd, I. D., "Effects of Rotational Energy Relaxation in a Modular Particle-Continuum Method," *J. Thermophys. Heat Tr.*, Vol. 25, No. 2, April-June 2011.
- [23] Dietrich, S. and Boyd, I. D., "Scalar and Parallel Optimized Implementation of the Direct Simulation Monte Carlo Method," *J. Comput. Phys.*, Vol. 126, No. 2, July 1996, pp. 328–342.
- [24] Fallavollita, M. A., Baganoff, D., and McDonald, J. D., "Reduction of Simulation Cost and Error for Particle Simulations of Rarefied Flows," *J. Comput. Phys.*, Vol. 109, No. 1, November 1993, pp. 30–36.
- [25] Fan, J. and Shen, C., "Statistical Simulation of Low-Speed Rarefied Gas Flows," *J. Comput. Phys.*, Vol. 167, No. 2, March 2001, pp. 393–412.
- [26] Garcia, A. L. and Alder, B. J., "Generation of the Chapman-Enskog Distribution," *J. Comput. Phys.*, Vol. 140, No. 1, February 1998, pp. 66–70.

- [27] Garcia, A. L., Bell, J. B., Crutchfield, W. Y., and Alder, B. J., “Adaptive Mesh and Algorithm Refinement using Direct Simulation Monte Carlo,” *J. Comput. Phys.*, Vol. 154, No. 1, September 1999, pp. 134–155.
- [28] Gimelshein, N. E., Gimelshein, S. F., and Levin, D. A., “Vibrational Relaxation Rates in the Direct Simulation Monte Carlo Method,” *Phys. Fluids*, Vol. 14, No. 12, December 2002, pp. 4452–4455.
- [29] Gnoffo, P. A., Gupta, R. N., and Shinn, J. L., “Conservation Equations and Physical Models for Hypersonic Air Flows in Thermal and Chemical Nonequilibrium,” *NASA-TP-2867*, 1989.
- [30] Golse, F., “Applications of the Boltzmann Equation Within the Context of Upper Atmosphere Vehicle Aerodynamics,” *Comput. Method Appl. M.*, Vol. 75, 1989, pp. 299–316.
- [31] Grad, H., “On the Kinetic Theory of Rarefied Gases,” *Comm. Pure Appl. Math.*, Vol. 2, No. 4, 1949, pp. 331–407.
- [32] Gupta, R. N., Yos, J. M., Thompson, R. A., and Lee, K. P., “A Review of Reaction Rates and Thermodynamic and Transport Properties for an 11-Species Air Model for Chemical and Thermal Nonequilibrium Calculations to 30,000 K,” *NASA-RP-1232*, 1990.
- [33] Haas, B. L., Hash, D. B., Bird, G. A., Lumpkin, F. E., and Hassan, H. A., “Rates of Thermal Relaxation in Direct Simulation Monte Carlo Methods,” *Phys. Fluids*, Vol. 6, No. 6, June 1994, pp. 2191–2201.
- [34] Hadjiconstantinou, N. G., Garcia, A. L., Bazant, M. Z., and He, G., “Statistical Error in Particle Simulations of Hydrodynamic Phenomena,” *J. Comput. Phys.*, Vol. 187, No. 1, May 2003, pp. 274–297.
- [35] Hash, D. B. and Hassan, H. A., “Assessment of Schemes for Coupling Monte Carlo and Navier-Stokes Solution Methods,” *J. Thermophys. Heat Tr.*, Vol. 10, No. 2, April-June 1996.
- [36] Hash, D. B. and Hassan, H. A., “Two-Dimensional Coupling Issues of Hybrid DSMC/Navier-Stokes Solvers,” *AIAA Paper 1997-2507*, 1997, presented at the 32nd AIAA Thermophysics Conference.
- [37] Hirschfelder, J. O., Curtiss, C. F., and Bird, R. B., *Molecular Theory of Gases and Liquids*, John Wiley and Sons, 1954.
- [38] Holman, T. D. and Boyd, I. D., “Effects of Continuum Breakdown on the Surface Properties of a Hypersonic Sphere,” *J. Thermophys. Heat Tr.*, Vol. 23, No. 4, October-December 2009, pp. 660–673.

- [39] Holman, T. D. and Boyd, I. D., “Effects of Continuum Breakdown on Hypersonic Aerothermodynamics for Reacting Flow,” *Phys. Fluids*, Vol. 23, No. 2, February 2011, pp. 1–15.
- [40] Incropera, F. P., *Introduction to Molecular Structure and Thermodynamics*, John Wiley and Sons, 1974.
- [41] Jawahar, P. and Kamath, H., “A High-Resolution Procedure for Euler and Navier-Stokes Computations on Unstructured Grids,” *J. Comput. Phys.*, Vol. 164, 2000, pp. 165–203.
- [42] Jeans, J. H., *The Dynamical Theory of Gases*, Cambridge University Press, 1916.
- [43] Karypis, G. and Kumar, V., “METIS: A Software Package for Partitioning Unstructured Graphs, Partitioning Meshes, and Computing Fill-Reducing Orderings of Sparse Matrices,” University of Minnesota, MN, 1998.
- [44] Landau, L. and Teller, E., “Zur theorie der schalldispersion,” *Phys. Z. Sowjetunion*, Vol. 10, No. 14, 1936.
- [45] Lee, J. H., “Basic Governing Equations for the Flight Regimes of Aeroassisted Orbital Transfer Vehicles,” *AIAA Paper 1984-1729*, June 1984, presented at the 19th AIAA Thermophysics Conference, Snowmass, CO.
- [46] Lofthouse, A. J., Boyd, I. D., and Wright, M. J., “Effects of Continuum Breakdown on Hypersonic Aerothermodynamics,” *Phys. Fluids*, Vol. 19, No. 2, February 2007, pp. 1–12.
- [47] Lofthouse, A. J., Scalabrin, L. C., and Boyd, I. D., “Velocity Slip and Temperature Jump in Hypersonic Aerothermodynamics,” *J. Thermophys. Heat Tr.*, Vol. 22, No. 1, January-March 2008.
- [48] Lumpkin, F. E., Haas, B. L., and Boyd, I. D., “Resolution of Differences Between Collision Number Definitions in Particle and Continuum Simulations,” *Phys. Fluids*, Vol. 3, No. 9, 1991, pp. 2282–2284.
- [49] MacCormack, R. W. and Candler, G. V., “The Solution of the Navier-Stokes Equations using Gauss-Seidel Line Relaxation,” *Computers and Fluids*, Vol. 17, 1989, pp. 135–150.
- [50] Martin, A., Scalabrin, L. C., and Boyd, I. D., “High Performance Modeling of Atmospheric Re-Entry Vehicles,” *J. Phys.: Conf. Ser.*, Vol. 341, No. 012002, 2012.
- [51] Millikan, R. C. and White, D. R., “Systematics of Vibrational Relaxation,” *J. Chem. Phys.*, Vol. 39, No. 12, December 1963, pp. 3209–3213.
- [52] Mott-Smith, H. M., “The Solution of the Boltzmann-Equation for a Shock Wave,” *Phys. Rev.*, Vol. 82, No. 6, 1951, pp. 885–892.

- [53] Nagnibeda, E. and Kustova, E., *Non-Equilibrium Reacting Gas Flows: Kinetic Theory of Transport and Relaxation Processes*, Springer-Verlag, Berlin, Germany, 2009.
- [54] Nelder, J. A. and Mead, R., "A Simplex Method for Function Minimization," *Comput. J.*, Vol. 7, 1965, pp. 308–313.
- [55] Palmer, G. E., Pulsonetti, M., Wood, W. A., Alter, S., Gnoffo, P., and Tang, C., "Computational Assessment of Thermal Protection System Damage Experienced During STS-118," *J. Spacecraft Rockets*, Vol. 46, No. 6, November-December 2009, pp. 1110–1116.
- [56] Palmer, G. E. and Wright, M. J., "A Comparison of Methods to Compute High Temperature Gas Thermal Conductivity," *AIAA Paper 2003-3913*, June 2003, presented at the 36th AIAA Thermophysics Conference, Orlando, FL.
- [57] Palmer, G. E. and Wright, M. J., "Comparison of Methods to Compute High-Temperature Gas Viscosity," *J. Thermophys. Heat Tr.*, Vol. 17, No. 2, April-June 2003, pp. 232–239.
- [58] Park, C., "Problems of Rate Chemistry in the Flight Regimes of Aeroassisted Orbital Transfer Vehicles," *AIAA Paper 1984-1730*, June 1984, presented at the 19th AIAA Thermophysics Conference, Snowmass, CO.
- [59] Parker, J. G., "Rotational and Vibrational Relaxation in Diatomic Gases," *Phys. Fluids*, Vol. 2, No. 4, July-August 1959, pp. 449–462.
- [60] Ramshaw, J. D., "Self-Consistent Effective Binary Diffusion in Multicomponent Gas Mixtures," *J. Non-Equilib. Thermodyn.*, Vol. 15, No. 3, 1990, pp. 295–300.
- [61] Ried, R. C., "Orbiter Entry Aerothermodynamics," *NASA CP-2342, Part 2*, 1983, pp. 1051–1061.
- [62] Roveda, R., Goldstein, D. B., and Varghese, P. L., "Hybrid Euler/Particle Approach for Continuum/Rarefied Flows," *J. Spacecraft Rockets*, Vol. 35, No. 3, May-June 1998, pp. 258–265.
- [63] Scalabrin, L. C., *Numerical Simulation of Weakly Ionized Hypersonic Flow over Reentry Capsules*, Ph.D. thesis, University of Michigan, 2007.
- [64] Schwartzenruber, T. E., *A Modular Particle-Continuum Numerical Algorithm for Hypersonic Non-Equilibrium Flows*, Ph.D. thesis, University of Michigan, 2007.
- [65] Schwartzenruber, T. E. and Boyd, I. D., "A Hybrid Particle-Continuum Method Applied to Shock Waves," *J. Comput. Phys.*, Vol. 215, No. 2, July 2006, pp. 402–416.

- [66] Schwartzentruber, T. E., Scalabrin, L. C., and Boyd, I. D., “A Modular Particle-Continuum Numerical Method for Hypersonic Non-Equilibrium Gas Flows,” *J. Comput. Phys.*, Vol. 225, No. 1, July 2007, pp. 1159–1174.
- [67] Schwartzentruber, T. E., Scalabrin, L. C., and Boyd, I. D., “Hybrid Particle-Continuum Simulations of Hypersonic Flow over a Hollow-Cylinder-Flare Geometry,” *AIAA J.*, Vol. 46, No. 8, August 2008, pp. 2086–2095.
- [68] Schwartzentruber, T. E., Scalabrin, L. C., and Boyd, I. D., “Multiscale Particle-Continuum Simulations of Hypersonic Flow over a Planetary Probe,” *J. Spacecraft Rockets*, Vol. 45, No. 6, November-December 2008, pp. 1196–1206.
- [69] Sherman, F. S., “Shock-Wave Structure in Binary Mixtures of Chemically Inert Perfect Gases,” *J. Fluid Mech.*, Vol. 8, No. 3, July 1960, pp. 465–480.
- [70] Stallcop, J. R., Levin, E., and Partridge, H., “Transport Properties of Hydrogen,” *J. Thermophys. Heat Tr.*, Vol. 12, No. 4, October-December 1998.
- [71] Stallcop, J. R., Partridge, H., Walch, S. P., and Levin, E., “H-N₂ Interaction Energies, Transport Cross Sections, and Collision Integrals,” *J. Chem. Phys.*, Vol. 97, No. 5, September 1992, pp. 3431–3436.
- [72] Steger, J. L. and Warming, R. F., “Flux Vector Splitting of the Inviscid Gasdynamics Equations with Application to Finite-Difference Methods,” *J. Comput. Phys.*, Vol. 40, 1981, pp. 263–293.
- [73] Stephani, K. A., *Development of a Hybrid DSMC/CFD Method for Hypersonic Boundary Layer Flow over Discrete Surface Roughness*, Ph.D. thesis, University of Texas at Austin, 2012.
- [74] Stephani, K. A., Goldstein, D. B., and Varghese, P. L., “Consistent Treatment of Transport Properties for Five-Species Air Direct Simulation Monte Carlo/Navier-Stokes Applications,” *Phys. Fluids*, Vol. 24, No. 7, July 2012, pp. 1–23.
- [75] Stephani, K. A., Goldstein, D. B., and Varghese, P. L., “A Non-Equilibrium Surface Reservoir Approach for Hybrid DSMC/Navier-Stokes Particle Generation,” *J. Comput. Phys.*, Vol. 232, 2013, pp. 468–481.
- [76] Sun, Q. and Boyd, I. D., “Evaluation of Macroscopic Properties in the Direct Simulation Monte Carlo Method,” *J. Thermophys. Heat Tr.*, Vol. 19, No. 3, July-September 2005, pp. 329–335.
- [77] Sutton, K. S. and Gnoffo, P. A., “Multi-Component Diffusion with Application to Computational Aerothermodynamics,” *AIAA Paper 1998-2575*, 1998, presented at the 7th AIAA/ASME Joint Thermophysics and Heat Transfer Conference.
- [78] Tannehill, J. C., Anderson, D. A., and Pletcher, R. H., *Computational Fluid Mechanics and Heat Transfer*, Taylor and Francis, 1997.

- [79] Verhoff, A. M. and Boyd, I. D., “Extension of a Hybrid Particle-Continuum Method for a Mixture of Chemical Species,” *28th International Symposium on Rarefied Gas Dynamics*, AIP Conf. Proc. 1501, 2012, pp. 342–349.
- [80] Verhoff, A. M. and Boyd, I. D., “Consistent Modeling of Rotational Nonequilibrium in a Hybrid Particle-Continuum Method,” *AIAA Paper 2013-3145*, June 2013, presented at the 44th AIAA Thermophysics Conference, San Diego, CA.
- [81] Verhoff, A. M. and Boyd, I. D., “Further Development of a Hybrid Particle-Continuum Method for Transitional Hypersonic Flows,” *29th International Symposium on Rarefied Gas Dynamics*, AIP Conf. Proc. 1628, 2014, pp. 510–518.
- [82] Vincenti, W. G. and Kruger, C. H. J., *Introduction to Physical Gas Dynamics*, John Wiley and Sons, 1965.
- [83] Wadsworth, D. C. and Erwin, D. A., “One-Dimensional Hybrid Continuum/Particle Simulation Approach for Rarefied Hypersonic Flows,” *AIAA Paper 1990-1690*, June 1990, presented at the 5th AIAA/ASME Joint Thermophysics and Heat Transfer Conference.
- [84] Wadsworth, D. C. and Erwin, D. A., “Two-Dimensional Hybrid Continuum/Particle Approach for Rarefied Flows,” *AIAA Paper 1992-2975*, July 1992, presented at the 23rd AIAA Plasmadynamics and Lasers Conference.
- [85] Wagner, W., “A Convergence Proof for Bird’s Direct Simulation Monte Carlo Method for the Boltzmann Equation,” *J. Stat. Phys.*, Vol. 66, No. 3, 1992, pp. 1011–1044.
- [86] Wang, W.-L. and Boyd, I. D., “A New Energy Flux Model in the DSMC-IP Method for Nonequilibrium Flows,” *AIAA Paper 2003-3774*, June 2003, presented at the 36th AIAA Thermophysics Conference, Orlando, FL.
- [87] Wang, W.-L. and Boyd, I. D., “Hybrid DSMC-CFD Simulations of Hypersonic Flow over Sharp and Blunted Bodies,” *AIAA Paper 2003-3644*, June 2003, presented at the 36th AIAA Thermophysics Conference, Orlando, FL.
- [88] Wang, W.-L. and Boyd, I. D., “Predicting Continuum Breakdown in Hypersonic Viscous Flows,” *Phys. Fluids*, Vol. 15, No. 1, January 2003, pp. 91–100.
- [89] Wijesinghe, H. S., *Hybrid Atomistic-Continuum Formulations for Gaseous Flows*, Ph.D. thesis, Massachusetts Institute of Technology, September 2003.
- [90] Wright, M. J., Bose, D., Palmer, G. E., and Levin, E., “Recommended Collision Integrals for Transport Property Computations, Part 1: Air Species,” *AIAA J.*, Vol. 43, No. 12, December 2005, pp. 2558–2564.
- [91] Wu, J. S., Lian, Y.-Y., Cheng, G., Koomullil, R. P., and Tseng, K.-C., “Development and Verification of a Coupled DSMC-NS Scheme Using Unstructured Mesh,” *J. Comput. Phys.*, Vol. 219, No. 2, December 2006, pp. 477–1014.

- [92] Zhang, C. and Schwartzentruber, T. E., “Inelastic Collision Selection Procedures for Direct Simulation Monte Carlo Calculations of Gas Mixtures,” *Phys. Fluids*, Vol. 25, No. 10, October 2013, pp. 1–13.